

# Investigations on the Mobility of the Na,K-ATPase in Cell Membranes Probed by Fluorescence Microscopy

vorgelegt von

**Dipl.-Phys.**

**Cornelia Junghans**

geb. in Berlin

von der Fakultät II - Mathematik und Naturwissenschaften  
der Technischen Universität Berlin  
zur Erlangung des akademischen Grades

**Doktor der Naturwissenschaften**

**- Dr. rer. nat. -**

genehmigte Dissertation

**Promotionsausschuss:**

**Vorsitzende: Prof. Dr. Ulrike Woggon**

**Gutachter: Prof. Dr. Thomas Friedrich**

**Gutachter: Prof. Dr. Jan Koenderink**

Tag der wissenschaftlichen Aussprache: 19. Juli 2016

Berlin 2016



# Contents

<b>Deutsche Zusammenfassung</b>	<b>1</b>
<b>Abstract</b>	<b>3</b>
<b>1 General Introduction</b>	<b>5</b>
<b>2 Biological Materials and Molecular Biological Methods</b>	<b>9</b>
2.1 Cellbiology and Cell Lines . . . . .	9
2.1.1 About the Cell . . . . .	9
2.1.2 Structure of the Plasma Membrane . . . . .	13
2.1.3 Cell Cultures . . . . .	14
2.2 Na,K-ATPase . . . . .	15
2.2.1 Overview . . . . .	15
2.2.2 Subunits and Isoforms of the Na,K-ATPase . . . . .	18
2.2.3 Na,K-ATPase Associated Human Diseases . . . . .	20
2.2.4 Na,K-ATPase and Cellular Interaction Partners . . . . .	21
2.2.5 Generation of Sequence Variants of the Na,K-ATPase . . . . .	22
2.3 Fluorescent Proteins used as Marker Proteins . . . . .	25
2.3.1 Green Fluorescent Protein . . . . .	25
2.3.2 Red Fluorescent Protein . . . . .	26
2.3.3 Photoswitchable Fluorescent Protein Dreiklang . . . . .	27
2.4 Molecular Biological Methods . . . . .	28
2.4.1 Mutagenesis in the Human Na,K-ATPase $\alpha_2$ -Subunit in pIRES Expression Vector . . . . .	28
2.4.2 Different Mutations of the Human Na,K-ATPase $\alpha_2$ -Subunit Labeled with Dreiklang . . . . .	29
2.4.3 Fusion Constructs with Different Fluorescent Protein Marker .	30
2.4.4 Production of Purified Dreiklang and eGFP Protein . . . . .	31
2.4.5 Production of cRNA for Expression in Oocytes . . . . .	32
2.4.6 Examination of the Functionality of the Na,K-ATPase by Rb <sup>+</sup> Uptake Measurements . . . . .	33

2.5	Cell Culture and Transient Transfection . . . . .	36
2.5.1	Transient Transfection for Imaging, Lifetime and FRAP Measurements . . . . .	37
2.5.2	Transient Transfection for FCS Measurements . . . . .	37
2.5.3	Cell Treatment for Studies at Different Incubation Temperatures . . . . .	38
2.5.4	Cell Preparation for pH Measurements . . . . .	38
<b>3</b>	<b>Microscopy Techniques and the used Spectroscopic Setups</b>	<b>39</b>
3.1	Introduction . . . . .	39
3.2	Theoretical Background . . . . .	39
3.2.1	Introduction . . . . .	39
3.2.2	Wide-field and Confocal Fluorescence Microscopy . . . . .	42
3.2.3	Time-Correlated Single Photon Counting . . . . .	45
3.2.4	Fluorescence Correlation Spectroscopy . . . . .	47
3.2.5	Fluorescence Recovery after Photobleaching . . . . .	50
3.3	Experimental Setups . . . . .	53
3.3.1	Multiparameter Microscopy Setup . . . . .	53
3.3.2	The PML-16C Setup for Lifetime Studies and Emission Measurements . . . . .	54
3.3.3	ConfoCorr3 Setup for Confocal Fluorescence Microscopy and FCS . . . . .	56
3.3.4	TCS SP5 Setup for Confocal Fluorescence Microscopy and FRAP . . . . .	57
<b>4</b>	<b>Expression Studies on the Na,K-ATPase FHM2 Mutation P979L at Different Incubation Temperatures</b>	<b>59</b>
4.1	Introduction . . . . .	59
4.2	Measurement Procedure and Data Analysis . . . . .	60
4.3	Discussion . . . . .	63
<b>5</b>	<b>Spectroscopic Characterization of the Fluorescent Protein Dreiklang</b>	<b>67</b>
5.1	Introduction . . . . .	67
5.2	Absorption and Fluorescence Emission Spectra . . . . .	67
5.3	Excitation Spectrum and Emission Spectrum at different Excitation Wavelength . . . . .	69
5.4	Fluorescence Lifetime Studies at Different pH-Values . . . . .	72
5.5	Fluorescence Lifetime Kinetics at Different Temperatures . . . . .	75
5.6	Investigations on the OFF-Switching Process . . . . .	77
5.7	Discussion . . . . .	81

<b>6</b>	<b>Investigations on the Mobility of the Na,K-ATPase in the Plasma Membrane</b>	<b>83</b>
6.1	Introduction . . . . .	83
6.2	Fluorescence Correlation Spectroscopy . . . . .	84
6.2.1	Adjustment and Calibration for FCS Measurements . . . . .	84
6.2.2	Comparison of Diffusion Studies with Different Fluorescence Labels (eGFP and Dreiklang) . . . . .	86
6.2.3	FCS with DRK-/eGFP-labeled Na,K-ATPase on all Mutants . . . . .	92
6.2.4	Total Number of Particles in the Observation Volume . . . . .	100
6.3	Fluorescence Recovery after Photobleaching . . . . .	102
6.3.1	Image-, Data Analysis and Fitting Procedure . . . . .	102
6.3.2	FRAP with DRK-labeled Na,K-ATPase . . . . .	104
6.3.3	FRAP with eGFP-labeled Na,K-ATPase . . . . .	106
6.4	Discussion . . . . .	107
6.4.1	Differences between DRK- and eGFP-labeling for the Diffusion Measurements by FCS . . . . .	107
6.4.2	Mobility in the Plasma Membrane Probed by FCS . . . . .	112
6.4.3	Total Number of Molecules in the Confocal Volume for Different Na,K-ATPase Constructs . . . . .	119
6.4.4	Mobility in the Plasma Membrane Studied by FRAP . . . . .	120
<b>7</b>	<b>Summary</b>	<b>127</b>
	<b>Appendix</b>	<b>131</b>
	<b>List of Abbreviations</b>	<b>135</b>
	<b>List of Figures</b>	<b>145</b>
	<b>List of Tables</b>	<b>147</b>
	<b>List of Publications</b>	<b>150</b>
	<b>Bibliography</b>	<b>165</b>
	<b>Acknowledgments</b>	<b>167</b>



# Deutsche Zusammenfassung

Die Natrium-Kalium-ATPase (Na,K-ATPase) ist eine spannungsabhängige Ionenpumpe und eines der bedeutendsten Membrantransport-Proteine, welche insbesondere in erregbaren Zellen des zentralen Nervensystems von hoher physiologischer Bedeutung sind. Die Na,K-ATPase transportiert, gegen den chemischen Konzentrationsgradienten unter ATP Hydrolyse, drei Natriumionen aus der Zelle und zwei Kaliumionen in die Zelle. Diese beiden Prozesse sind strikt aneinander gekoppelt und halten somit die elektrochemischen Gradienten für  $\text{Na}^+$ - und  $\text{K}^+$ -Ionen über die Plasmamembran der Zelle aufrecht. Mutationen in den Genen der verschiedenen Isoformen der Na,K-ATPase  $\alpha$ -Untereinheit können zu schweren Erkrankungen wie familiärer hemiplegischer Migräne (FHM Typ 2), *alternating hemiplegia of childhood* (AHC) oder Epilepsie führen. Viele der bereits bekannten Mutationen führen zum Verlust ihrer Funktion auf molekularer Ebene, wohingegen andere die Funktion des Enzyms nicht verändern oder beeinflussen. Stattdessen verursachen diese Mutationen eine reduzierte Proteinstabilität, verringern die Proteinexpression oder führen zur defekten zellulären Lokalisation.

In dieser Arbeit wurden verschiedene Mutationen in der Na,K-ATPase  $\alpha_2$ -Untereinheit untersucht, die mit der Bindung der Na,K-ATPase an andere membranständige Proteine, wie z.B. Caveolin-1 (NaK- $\Delta$ C, NaK- $\Delta$ N), oder an Bindungsproteine des Zytoskeletts, wie Ankyrin B (NaK-K456E) assoziiert werden sowie der Fixierung innerhalb der Plasmamembran dienen. Es wird angenommen, dass diese Mutationen zu veränderter Zielsteuerung des Enzyms, Veränderung der Lokalisierung in der Plasmamembran und damit zur Änderung des Diffusionsverhaltens des Enzyms führen.

Das Diffusionsverhalten der verschiedenen Konstrukte in der Plasmamembran von lebenden HEK293 Zellen wurde mit zwei verschiedenen Messtechniken untersucht, zum einen mit der Fluoreszenzkorrelationsspektroskopie (FCS) und zum anderen mit *Fluorescence recovery after photobleaching* (FRAP). Beide Verfahren erfordern die Markierung der zu beobachtenden Proteine mit geeigneten Fluoreszenzmarkern. Da in der Literatur beschrieben ist, dass genetisch kodierte Fluoreszenzproteine wie das grün fluoreszierende Protein (GFP) zu Artefakten durch Photoschalten in FRAP-Messungen führen, wurde außerdem das reversibel schaltbare Dreiklang Protein (DRK) als Marker verwendet. Es konnte gezeigt werden, dass DRK als Marker für FCS-Messungen nicht geeignet ist, da das Protein unbekannte photophysikalische Prozesse durchläuft, welche sich auf der gleichen Zeitskala, wie die zu erwartenden Diffusionsänderungen, abspielen und somit diese überlagern. Die ver-

schiedenen eGFP-Na,K-ATPase Mutanten zeigten im Vergleich zum Wildtyp signifikante Unterschiede bei FCS-Messungen. Alle Mutanten wiesen eine deutlich schnellere Diffusion auf als der Wildtyp, was auf eine gelockerte Bindung an der Membran zurückgeführt werden kann.

FRAP-Messungen unter Verwendung von eGFP als Fluoreszenzmarker zeigten deutlich eine sehr schnelle Diffusionskomponente, welche auf das reversible Photoschalten der Proteine zurückzuführen ist und damit die Messung für kleine Unterschiede im Diffusionsverhalten unmöglich machen. Die gleichen Ergebnisse wurden auch für DRK markierte Zellen unter Standard FRAP Bedingungen beobachtet. Dieses Problem konnte mit Hilfe von reversiblen FRAP-Messungen umgangen werden, indem DRK in seinen ausgeschalteten Zustand gebracht wurde, anstatt DRK irreversibel zu bleichen. Anhand dieser Messungen konnten signifikante Unterschiede der DRK-Na,K-ATPase Mutanten im Vergleich zum Wildtyp beobachtet werden. Es muss aber hier angemerkt werden, dass diese Messungen nur als qualitative Untersuchung angesehen werden können, da DRK durch thermische Reaktivierung wieder in den eingeschalteten Zustand zurückkehren kann und dieser Prozess die zu beobachtenden Diffusionsprozesse überlagert.

Die in dieser Arbeit durchgeführten Messungen eröffnen eine neue Sichtweise für die Untersuchung der Na,K-ATPase und lassen Rückschlüsse auf die Fixierung innerhalb der Plasmamembran und die Bindung an andere Adapter- oder Matrixproteine zu. Dadurch kann in zukünftigen Untersuchungen die FCS Messtechnik genutzt werden um unbekannt Mutationen zu studieren, welche mit verschiedenen Krankheiten assoziiert werden und somit einen wertvollen Beitrag zur Erforschung deren Ursachen leisten können.

# Abstract

The Na,K-ATPase is a plasma membrane ion transporting enzyme, which is of high physiological importance especially in excitable cells of the central nervous system. It converts the energy from ATP hydrolysis to electrochemical gradients of Na<sup>+</sup> and K<sup>+</sup> ions across the cell membrane. The enzyme transports three sodium ions out of the cell and two potassium ions into the cell for each hydrolyzed ATP molecule.

Mutations in genes coding for Na,K-ATPase isoforms lead to severe human pathologies like familial hemiplegic migraine (FHM), alternating hemiplegia of childhood (AHC) or epilepsy. Many of the reported mutations lead to loss-of-function effects on the molecular level, but others do not alter the function of the enzyme. Instead, to e.g. reduced protein stability, reduced protein expression or defective cellular localization may result. Therefore, the overall understanding of the implementation of the Na,K-ATPase into the plasma membrane is of great interest. By mutational disruption of binding sites of the Na,K-ATPase with ankyrin B (NaK-K456E) and caveolin-1 (NaK- $\Delta$ C, NaK- $\Delta$ N) it could be expected to observe changes in the plasma membrane targeting of the enzyme and changes of the localization within the plasma membrane and, consequently, of the diffusion behavior of the enzyme.

The diffusion behavior of the different Na,K-ATPase constructs in the plasma membrane of living HEK293T cells was studied with fluorescence correlation spectroscopy (FCS) and as well with fluorescence recovery after photobleaching (FRAP). Both methods require labeling of the observed proteins with suitable fluorescent markers. Since from the literature it is known that common genetically encoded fluorescent proteins, e.g. eGFP, lead to artifacts in diffusion studies by FRAP due to photoswitching, the reversibly photoswitchable fluorescent protein Dreiklang (DRK) was used in addition as fluorescent marker.

FCS studies on the Na,K-ATPase labeled with DRK lead to the conclusion that DRK is unsuitable for FCS analysis. It seems that DRK undergoes photophysical quenching processes, which occur on the same time scale as the observed diffusion times and, thus, small differences in diffusion are not measurable. The different Na,K-ATPase mutants labeled with eGFP exhibit significant differences in the diffusion behavior within the plasma membrane compared with the Na,K-ATPase wild-type.

FRAP measurements on the Na,K-ATPase labeled with eGFP do not show significantly different results, but affirm the problems mentioned above. On the other side, DRK as fluorescence marker studied with standard FRAP settings also exhibits artificially shortened diffusion components, which can be attributed to reversible photoswitching of the

fluorescent proteins and, therefore, these data are biased by photophysical artifacts. This problem is overcome by reversible FRAP experiments with DRK as fluorescence marker. However, these reversible FRAP data should be considered as a first qualitative result and gives a hint about the different diffusion behavior of the various Na,K-ATPase constructs, because a thermally reactivation of the OFF-switched proteins into the ON-state is possible.

These measurements open another view on the study of the implementation of the Na,K-ATPase into the plasma membrane and provides the opportunity to gain a deeper understanding of the binding or fixation of this enzyme within the membrane. FCS measurements can be therefore used in future investigations on Na,K-ATPase mutants linked to several diseases.

# 1 General Introduction

Every life on earth begins with the formation of a cell. It is the smallest unit that is autonomously capable for reproduction and self-preservation and almost all known living organisms or systems are constructed from it.

Living systems rely on the integrity of biological membranes, which enclose cells and are crucial to many cellular processes such as membrane transport, sensing and signaling as well as energy transduction and catalysis.

The Na,K-ATPase is one of the most important membrane transporter proteins in animal cells since its active transport mode of exporting 3 Na<sup>+</sup> ions in exchange for the import of 2 K<sup>+</sup> ions per hydrolyzed ATP molecule is the main mechanism to energize animal cell membranes. This is particularly important in electrically active tissues like the cardiac muscle or in cells of the central nervous system (CNS), in which the contribution of the Na,K-ATPase to total energy consumption can reach values of up to 50 %. The minimal functional unit of the Na,K-ATPase is composed of a large, catalytic  $\alpha$ -subunit and a smaller  $\beta$ -subunit, which stabilize the complex in the plasma membrane. Depending on the tissue, a third,  $\gamma$ -subunit is present, which belongs to the family of FXYD-domain containing ion transport regulator proteins, from which *FXYD2* is the originally identified  $\gamma$ -subunit. A still unresolved controversy exists, whether higher oligomeric assemblies (such as  $\alpha\beta$ - $\beta\alpha$ ) are formed within a physiological context [1]. In humans, four isoforms of the  $\alpha$ - and three of the  $\beta$ -subunit exist, of which  $\alpha_1$  is ubiquitously expressed, whereas  $\alpha_2$  is present e.g. skeletal, heart and vascular smooth muscle, or in the adult brain mainly in glial cells,  $\alpha_3$  is typical for neurons, and  $\alpha_4$  is only found in male sperm. In recent years, several human inherited diseases have been linked to Na,K-ATPase  $\alpha$ -isoforms. Mutations in the  $\alpha_2$  gene *ATP1A2* result in familial hemiplegic migraine type 2 (FHM2) [2–5], whereas mutations in the  $\alpha_3$  gene *ATP1A3* have been linked to rapid dystonia parkinsonism (RDP) [6, 7], alternating hemiplegia of childhood (AHC) [8], and CAPOS syndrome [9]. It is well established that the Na,K-ATPase can form higher heteromeric protein complexes with other membrane proteins such as the Na<sup>+</sup>/Ca<sup>2+</sup> exchanger (NCX) or the inositol-1,4,5-trisphosphate receptor IP3R [10], and with scaffolding proteins like ankyrins, tubulins or caveolins. Of note, mutations in in-

teraction motifs associated with ankyrin B are implicated in the cardiac long-QT syndrome LQT4, presumably by causing misrouting of Na,K-ATPase and NCX1 in heart muscle cells [11]. Thus, it can be expected that also FHM2, RDP and AHC mutations may not only affect protein function, but have also an impact on targeting of the enzyme to specific membrane microdomains or anchoring to the cytoskeleton meshwork or cellular matrix proteins, which would largely influence the dynamic behavior of the protein. Since these effects are currently out of the scope of conventional functional studies of Na,K-ATPase mutants, assays need to be developed that allow for the monitoring of the dynamic properties of individual Na,K-ATPase enzymes in the membranes of living cells. These methods should be able to discriminate between the fraction of mobile and immobile Na,K-ATPase molecules and provide data about the diffusion behavior of the Na,K-ATPase within the plasma membrane, which can best be performed by fluorescence correlation spectroscopy (FCS) or by fluorescence recovery after photobleaching (FRAP) techniques.

On the one hand, fluorescence correlation spectroscopy (FCS) is an experimental technique to measure thermodynamic fluctuations on a molecular level as a function of time or frequency, so that e.g. diffusion constants or, more importantly, the rates for forward and backward chemical reactions can be determined under conditions of chemical equilibrium. FCS was first introduced in 1972 by Magde, Webb and Elson [12] to study the kinetics of a fluorescent molecule binding to DNA. This method, which was common in the 1970ies, laid strong focus on its use as a relaxation technique that allowed for the determination of rates of individual reaction steps of a physico-chemical process. It soon emerged that FCS equally well allows for the determination of concentration (below the nanomolar range), translational and rotational diffusion times in two- or three-dimensions, singlet-triplet state conversion and conformational fluctuations [13–21], even within living cells or in fluidic systems [22].

On the other side, another very common technique to study the mobility of membrane-embedded proteins is the fluorescence recovery after photobleaching (FRAP). FRAP was firstly introduced in 1970s by Axelrod *et al.* [23] and become more and more popular in the field of medicine and biology since commercial confocal laser scanning microscopes (CLSM) are available (early 1990s). This technique measures the diffusion of fluorophores in a region of interest after a strong bleaching pulse and allows the determination of mobile and immobile fractions as well as the calculation of the diffusion coefficients [24–29].

In conclusion, FRAP observes the diffusion of chromophores in a photobleached area of some square micrometers and measures the recovery time of the fluorescence signal. On the other side, FCS observes the fluorescence intensity fluctuations of

---

molecules diffusing across a confocal volume of about 1 fL. FCS allows the simultaneous observation of multiple fast-diffusing molecular species, while FRAP is limited to a temporal scale of the diffusion time above 1 ms.

Both methods (FCS and FRAP) require labeling of the observed proteins with appropriate fluorescent markers that need to match photophysical constraints depending on the used application.

A suitable class of markers for diffusion assays are genetically encoded fluorescent proteins (FPs) due to the very high labeling specificity. In the last two decades following the discovery of the green fluorescent protein (GFP) from the jellyfish *Aequorea victoria* by O. Shimomura [30], GFP and its spectral variants, including homologs from many other species (corals, sea pens, sea squirts, and sea anemones), have become indispensable tools in modern molecular, cellular and developmental biology, medicine and biophysics. Molecular engineering approaches have created a large variety of chemical sensors along with spectroscopic probes e.g. for protein tracking, or for the investigation of protein-protein interactions as well as conformational changes by fluorescence resonance energy transfer (FRET). Furthermore, the design of optically switchable FPs has been demonstrated, which coexist in multiple fluorescent and dark isoforms. These have been proven particularly useful for improving imaging contrast or for the application of optical super-resolution techniques on the single molecule level such as STORM (stochastic optical reconstruction microscopy, [31]), STED (stimulated emission depletion, [32–34]) or PALM (photoactivated localization microscopy, [35]). However, the potential of photoswitchable molecules is limited if photoactivation or deactivation can be performed only once, which impedes repeated measurements with the same molecule. Moreover, early FP-derived photoswitches suffered from significant spectral overlap between the ON-/OFF-switching and the fluorescence excitation spectral bands. For example, the excitation of the fluorophores was simultaneously triggering the switching into the dark state (rsTagRFP) [36]. The first photoswitchable FP derivative to overcome these limitations was Dreiklang (DRK), in which - for the first time - the spectral bands for ON- and OFF-switching, as well as excitation, are sufficiently separated to selectively trigger the fluorescence signal of the switching process. The unique molecular switching mechanism of DRK relies on a reversible, light-induced water addition/elimination reaction in the proximity of the chromophore [37]. In contrast to Citrine, the fluorophore from which DRK was derived, nearly 100 % photoswitching efficiency was obtained at a greatly improved photostability, compared to other photoswitchable FPs like rsTagRFP or Dronpa.

From literature it is known that FRAP measurements under commonly used FRAP settings with standard fluorescent proteins (e.g. eGFP, eYFP or Citrine) used as

marker can lead to significant artifacts in the experiments. These artifacts show up as a short component which could be attributed to a photoswitching process of the chromophores and often leads to an overestimation of the mobility and to false conclusions about the diffusion behavior [38–40].

Since the photoswitchable FP Dreiklang seems to be a promising tool for both experimental schemes, this study aims at a comparison between DRK with the conventional, nonswitchable eGFP in FCS and FRAP applications on membrane proteins. Furthermore, different mutations on the Na,K-ATPase, which are involved in mediating the fixation of the enzyme within the plasma membrane are studied in diffusion measurements.

This thesis starts with the biological materials, which contains a short introduction about cell biology, the Na,K-ATPase and the different utilized fluorescent proteins, following by the used molecular biological methods (chapter 2). In chapter 3 the theoretical background of different microscopy techniques is given and the experimental setups are presented. Expression studies of the Na,K-ATPase FHM2 mutation P979L and the WT at different incubation temperatures is presented and exhibited results discussed in chapter 4. Chapter 5 reveals a spectroscopic characterization of the fluorescent protein Dreiklang like absorption and emission studies at various pH-values. Finally, diffusion studies of different Na,K-ATPase constructs in the plasma membrane of living cells were performed with two different measurement techniques (FCS and FRAP) and were compared. Also for these measurements two different fluorescent labels (eGFP and DRK) were tested (chapter 6).

# 2 Biological Materials and Molecular Biological Methods

## 2.1 Cellbiology and Cell Lines

### 2.1.1 About the Cell

The cell is the smallest living unit from which all creatures and plants are composed. In general, a distinction is made between two types of cells, prokaryotic cells and eukaryotic cells. Prokaryotic cells have no nucleus and are the simplest cell form. They are composed of two groups, bacteria and archaea.

For this work, eukaryotic cells are of interest, which differ from the prokaryotic cells, because they have a nucleus in which the deoxyribonucleic acid (DNA) molecules are included. For these reasons, eukaryotic cells are also larger and more complicated than prokaryotic cells. These cells are mostly multicellular organisms to which plants and animals belong. This type of cells has a very similar construction and differs only in some small parts. Figure 2.1 shows the scheme of a typical animal or human cell with the different main components and organelles.

Every cell is surrounded by a plasma membrane, which is composed of a double layer of lipid molecules and is approximately 5 nm thick. The membrane separates the cell interior from the environment and serves as a barrier. Nevertheless, to ensure an exchange of nutrients and waste products, the membrane is interspersed with highly selective channels and pumps. These are made of special protein molecules that allow specific substances to be taken up and others to be transported to the outside. More details on these proteins are given in section 2.1.2. In addition, membranes contain sensors that can receive information about external changes and thus react to them. Membranes can be adapted to the cell size, by inflicting membrane parts and are able to deform without tearing. If the membrane is damaged it does not collapse back upon itself, but the membrane seals the concerned area.

Archaic bacterial forms have only one membrane, the plasma membrane. In contrast, eukaryotic cells have in addition many internal membranes, which enclose in-

tracellular compartments. This results in many organelles, such as the endoplasmic reticulum (ER), the Golgi apparatus and the mitochondria. The inner membranes have a similar composition and function as the outer plasma membrane, and they serve also as barriers between areas of different molecular compositions. The subtle differences that exist, give the respective organelles their special properties.

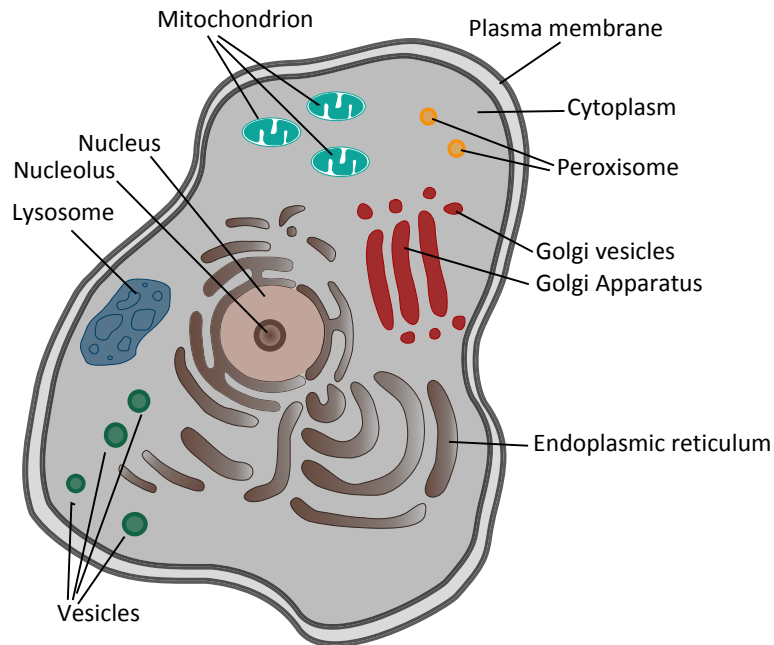


Figure 2.1: Components of a typical animal/human cell.

The most prominent organelle of an eukaryotic cell is the nucleus. It has a diameter of about 4  $\mu\text{m}$  to 6  $\mu\text{m}$ , and is enclosed by two concentric membranes the so-called nuclear envelope. The core is containing the DNA molecules, which are extremely long polymers, in which the genomic information of the organism is encrypted. The core forms the control center of a cell. Furthermore, the nucleus contains one or more nucleoli, which do not have an own membrane. The number of contained nucleoli depends on the cell type, but the ribonucleic acid (RNA) and additional proteins are stored in all of them. The nucleolus is mainly involved in the assembly of ribosomes. Moreover, the core has a network which strengthens its mechanical structure, similar to the cytoskeleton in the cell. The surrounding double membranes are not uniform, but they merge into one membrane at several places. A direct exchange of material with the cytosol is possible through pores in this area.

The lumen contained by the membrane structure of the nucleus is in direct communication with the three-dimensional channel system of the endoplasmic reticulum (ER). The ER is an irregular, branched labyrinth of elongated membrane vesicles and extends through the entire cytoplasm. Most cell membrane components and substances for active and passive transport from the cell are produced in it. These

ER membranes are often occupied on the outside by ribosomes, which are commonly referred as rough endoplasmic reticulum. The synthesized proteins are usually packaged in vesicles and then pinched out of the membrane. They move then to the Golgi apparatus, where they fuse again with the membrane system. The Golgi apparatus forms a separate membrane system on its own and consists of flattened membrane-bound sacs that are arranged in stacks and they chemically modify partially the captured proteins. After transport through the Golgi system the proteins are passed to different locations in the cell, or even further to the outside. The Golgi apparatus is also involved in the formation of the plasma membrane and of the membrane of lysosomes. Lysosomes are small, irregular and individual vesicles in which the intracellular digestion of substances is done. Escaping nutrients from food particles and unwanted molecules are degraded in lysosomes. In addition, the lysosomes take also a part in the lysis of cell components, especially during the cell death. Other small membrane-enclosed vesicles are the peroxisomes, which prevail in the interior an ideal environment for oxidising chemical reactions. In these reactions, hydrogen peroxide is generated, and also removed again. Furthermore, many other different types of vesicles can be found in the cytoplasm, which are involved in the transport of materials between the different organelles. This ensures a constant exchange of proteins and other materials between the ER, the Golgi apparatus, the lysosomes, and the remaining cell environment. One of the most prominent organelle besides the nucleus, are the mitochondria, which are found nearly in all eukaryotic cells. Mitochondria are worm-like factories, which can be one to several microns in length and one micron in diameter. They are surrounded by two different membranes and the inner one form wrinkles, the so-called cristae, in the interior. Mitochondria contain their own DNA and accrete themselves by bisection. Furthermore, they are responsible for the oxidative final degradation of the nutrients and the adenosine triphosphate (ATP) generation. They are therefore usually referred as the power plants of the cell, because they partially use the released energy from the respiratory chain reaction to synthesize ATP. This is the most basic energy vector that drives almost all cell activities.

In addition to the various organelles mentioned above, the cytoplasm is the basic structure, which fills the whole cell. The cytoplasm consists of the liquid cytosol and the fixed cytoskeleton. The biggest compartment in the cell is the cytosol, which contains the liquid constituents that are not separated by a membrane. It contains small as well as large molecules, which are so densely packed that it acts more like a gel than an aqueous solution. Many essential reactions take place in the cytosol, such as the first steps in setting up and dismantling nutrients and the protein production. The fixed part of the cytoplasm is called cytoskeleton and is a filament assembly, which consists of proteins. It is tightened in a criss-crossed manner in the

cell and responsible for movement and shape of the cell. Furthermore, it enables the transport of organelles and molecules from one place to another in the cytoplasm. There are three types of filaments with different tasks. The thinnest filaments are the actin filaments and they are found in all cells, but preferably in muscle cells. Microtubules are the thickest filaments and carry their name because they look like tiny hollow tubes. They are involved in cell division and deliver the chromosomes to the daughter cells. For the mechanical strength of the cell the intermediate filaments are responsible, they are in the range between the other two filaments. The whole filament system is always on move and permanently undergoes restructuring [41, 42].

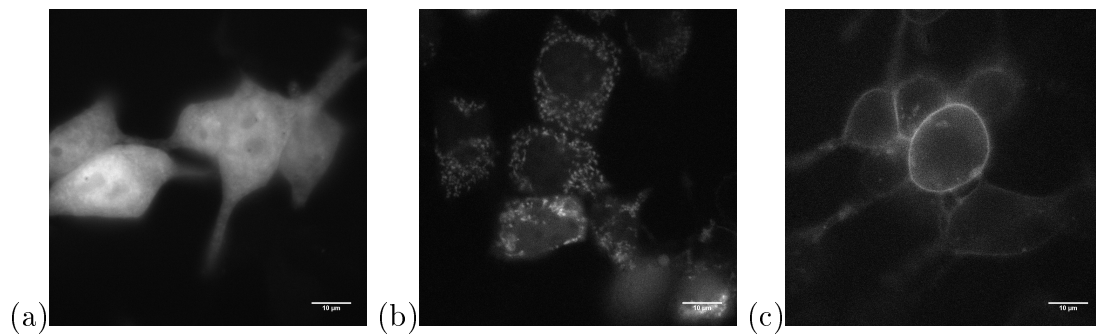


Figure 2.2: Illustration of different compartments in living HEK293 cells. The different areas are marked with the fluorescent protein Dreiklang. As expected, the fluorescence in the cytoplasmically labeled cells is distributed over the entire cell **(a)**. The middle image shows the mitochondria and the nucleus is also clearly recognizable, which occupies more than half of the cell **(b)**. **(c)** A typical transmembrane protein, the Na,K-ATPase, is shown. A typical membrane staining and some intracellular staining from moving vesicles are visible.

To get a first impression about the different compartments of a cell, Figure 2.2 shows some fluorescence pictures of HEK293 cells transfected with Dreiklang targeted to different compartments. The first image shows cytoplasmically labeled cells (Figure 2.2 (a)), the fluorescence signal is distributed across the whole cell including the nucleus, as expected. In the middle image the mitochondria (Figure 2.2 (b)), the power plants of the cell are tagged by the fluorescent protein. One can see that the mitochondria are distributed over the entire cell, as described above. It is also evident that they are not found in the nucleus. This stands out as a dark hole in the cell, which takes up more than half of the total volume of the cell. In Figure 2.2 (c), the transmembrane protein Na,K-ATPase (see section 2.2) was tagged showing a dominant fluorescence signal from the plasma membrane. In addition, there is some intracellular staining also visible, which results from transporter vesicles on the way to the membrane.

## 2.1.2 Structure of the Plasma Membrane

As mentioned in section 2.1, each cell is surrounded by a plasma membrane. All cell membranes are composed of both lipids and proteins and are similar in their structure. The lipids are arranged in two closely assembled layers, forming the so-called double layer. This forms the basic structure of every membrane and acts as a permeability barrier for water-soluble molecules. Most membrane functions are performed by the protein molecules contained in the plasma membrane and give the membrane its individual characteristics.

### Lipid Bilayer

Each lipid has a hydrophilic head and one or two hydrophobic hydrocarbon tails. Most lipids in the cell membrane are phospholipids in which the hydrophilic head is connected to the rest by a phosphate group. Molecules containing both hydrophilic and hydrophobic properties are referred as amphipathic. These properties play an important role in the spontaneous formation of lipid bilayers by the lipid molecules in aqueous solutions. The formation of the double layer is the lowest energy state for these molecules. All heads are located on the surface and are in contact with water, while the hydrophobic tails are in the interior close to each other and are thus protected from water. The aqueous environment also prevents that the membrane lipids may escape from the bilayer. The double layer is not rigid, but rather the molecules can move within the plane of the membrane in each direction and also change places. Thus the membrane acts as a two-dimensional liquid.

### Membrane Proteins

Most membrane functions are not performed by the lipid double layer itself, but from membrane proteins, which are embedded in it. These proteins not only transport certain nutrients, metabolites and ions through the membrane, but also fulfill many other functions. Some of these proteins anchor macromolecules to the membrane which can be fixed on each side of the plasma membrane. Others act as receptors, which detect chemical signals in the cell environment and transmit them to the cell interior. Still others are working as enzymes to catalyze certain reactions.

The membrane proteins can thus be classified into different functional classes, transport proteins, anchor proteins, receptors and enzymes. They differ in the way how they are connected to the membrane. The most important in this case are the trans-membrane proteins, which extend through the lipid bilayer from the inside to the

outside. These proteins can exist as a single  $\alpha$ -helix, multiple  $\alpha$ -helices or even as rolled beta sheets in the double layer. Others are completely found in the cytosol and are connected only by an amphipathic  $\alpha$ -helix to the inner layer of the lipid bilayer. There are also proteins that are completely inside the cytoplasm and only connected by one or more lipid groups covalently linked to one side of the membrane. All of them are called integral membrane proteins and can only be detached by destroying the lipid bilayer. On the other hand, peripheral membrane proteins exist, which are only indirectly connected with the membrane and maintained in place by interactions with other proteins. These proteins can be separated by careful extraction of the membrane and without damaging the lipid bilayer.

### 2.1.3 Cell Cultures

There are many different types of cell cultures, which can be differentiated in two groups, adherent and non-adherent cells. Non-adherent cells grow in solution and are thus easier to be cultivated. The adherent cells grow attached to the surface of a culture flask. Therefore, they must be detached to subcultivate them. In this work only adherent cell cultures are used as expression system.

#### **Human Embryonic Kidney Cells 293 (HEK293)**

The cell line Human Embryonic Kidney Cells 293 was produced in 1973 in the laboratory of A. J. van der Eb and is a human cell line [43, 44]. The HEK293 is a transformation product of an embryonic kidney cell with some DNA parts of the human adenovirus 5. In this cell culture, 4.5 kilo base pairs of the viral genome were specifically incorporated into the genome of renal cells. Nowadays this cell line is a very common and easy to culture for biological experiments and to solve medical questions.

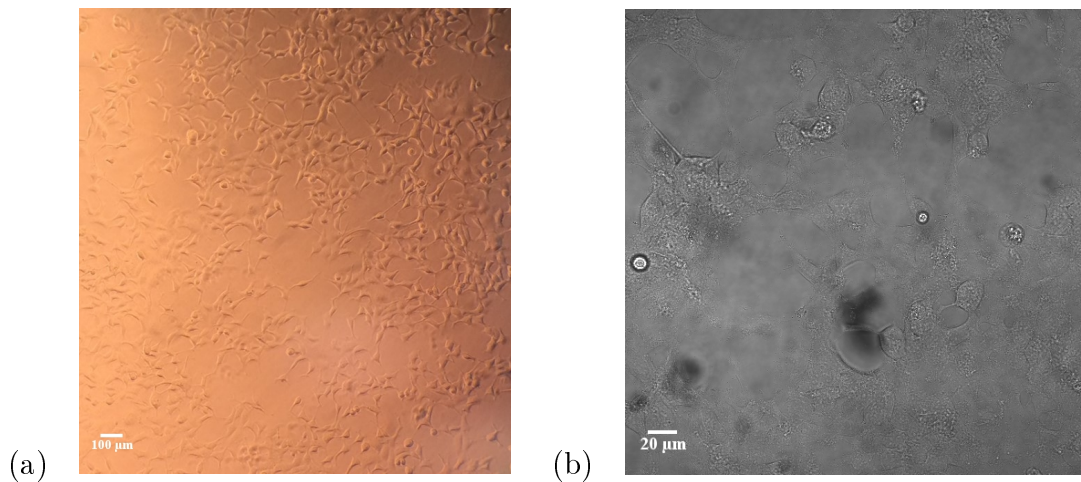


Figure 2.3: The pictures show an untransfected HEK293T cell culture under a microscope with 20x magnification **(a)** and the same cell culture by bright-field microscopy at a higher resolution **(b)**.

For this work, mostly HEK293T cell cultures were used for the experiments. HEK293T cells are derived from HEK293 cells but stably express the SV40 large T antigen, which binds to SV40 enhancers of expression vectors to increase protein production. This cell line is mostly used for virus production. However, these properties have no effect on the experiments performed in here.

## 2.2 Na,K-ATPase

### 2.2.1 Overview

The Na,K-ATPase is an integral membrane protein, which typically resides in the plasma membrane of essentially any animal cell. Within the enzymes class, it is one of the most extensively studied proteins. It was firstly described in 1957 by J.C. Skou [45], who was awarded with the Nobel prize in chemistry in 1997. It is an active ion transporter and is also called Na pump or sodium potassium pump. The enzyme transports three sodium ions ( $\text{Na}^+$ ) out of the cell and two potassium ions ( $\text{K}^+$ ) into the cell against the chemical concentration gradient for each hydrolyzed adenosine triphosphate (ATP) molecule (see Fig. 2.4). Both processes are strictly coupled with each other and provide the maintenance of the electrochemical gradients of  $\text{Na}^+$  and  $\text{K}^+$  ions across the plasma membrane.

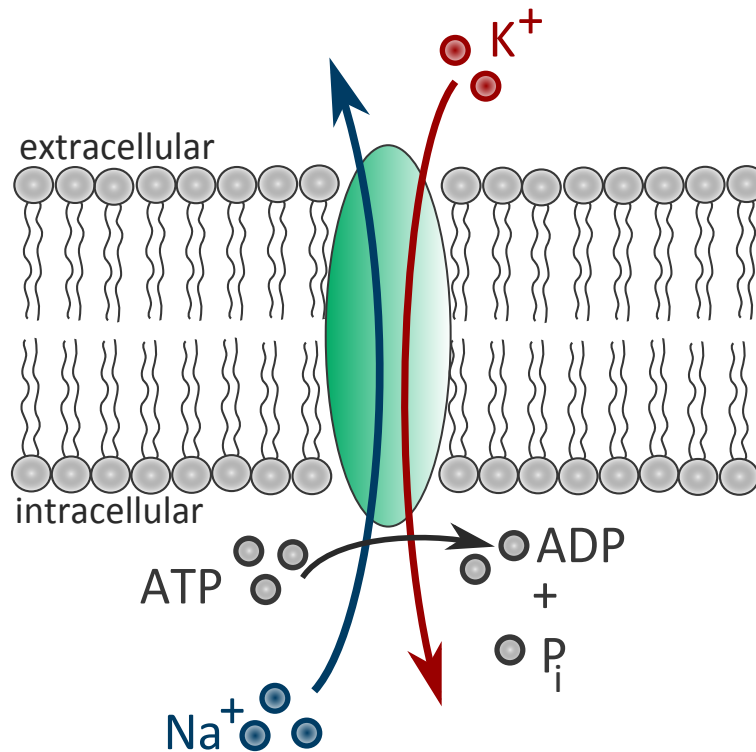


Figure 2.4: The Na,K-ATPase enzyme located in the plasma membrane with the mode of active ion transport upon hydrolysis of ATP.

ATPases are found everywhere in membranes of prokaryotic cells and mostly in all higher eukaryotic cells. They all catalyze the hydrolysis of ATP to adenosine diphosphate (ADP) and use the liberated energy for the transport of ions or other substrates. The ATPases can be divided into membrane-bound and non-membrane-bound ATPases. The membrane-bound types thereby can be categorized in F-, P-, V- and ABC-ATPases. For this work, the class of P-type ATPases is of interest, for which formation of a phosphorylated intermediate during the transport cycle is characteristic for all members of this protein family. Furthermore, the superfamily of P-type ATPases is featured by several characteristic key sequences one of them is the DKTG-motif. In this motif, the central aspartate is found to which the terminal phosphate of ATP is bound upon hydrolysis. In addition to this motif, there are two other highly conserved regions in P-type ATPases, which are mentioned in here. Firstly, the TGES-motif, which is just in front of the phosphorylation sequence, and the GDGXNDXP-motif, which is located just behind the DKTGT sequence. The P-type ATPases have a kind of core structure, which includes the three mentioned sequences and three pairs of associated hydrophobic transmembrane sequences. From here on the TGES-containing region and the DKTG region are named with actuator domain (A domain) and phosphorylation domain (P domain). It is also important to note that the N-terminus constitutes a part of the A domain [46]. Furthermore, nucleotide binding occurs in the N domain.

The P-type ATPases are categorized according to their substrate specificity into five groups and in total nine subgroups. In this class, the Na,K-ATPase and H,K-ATPase are the only ones, which are composed of more than one subunit. These enzymes are hetero-oligomeric membrane proteins and contain a catalytic  $\alpha$ - and an accessory  $\beta$ -subunit, which are present in a one-to-one ratio. Depending on the tissue, a third,  $\gamma$ -subunit is present in the functional unit of the complex, which belong to the family of FXYD-domain containing ion transport regulator proteins, from which *FXYD2* is the originally identified  $\gamma$ -subunit

A major advance in the study of the Na,K-ATPase was achieved in 2007 when the X-ray crystal structure of the oligomeric Na,K-ATPase in E<sub>2</sub>P-like conformation was published [47]. The used Na,K-ATPase was isolated from pig kidney. Meanwhile, there are other structures published with higher resolution [48], one of them is shown in Figure 2.5 and represents the overall structure of the Na,K-ATPase.

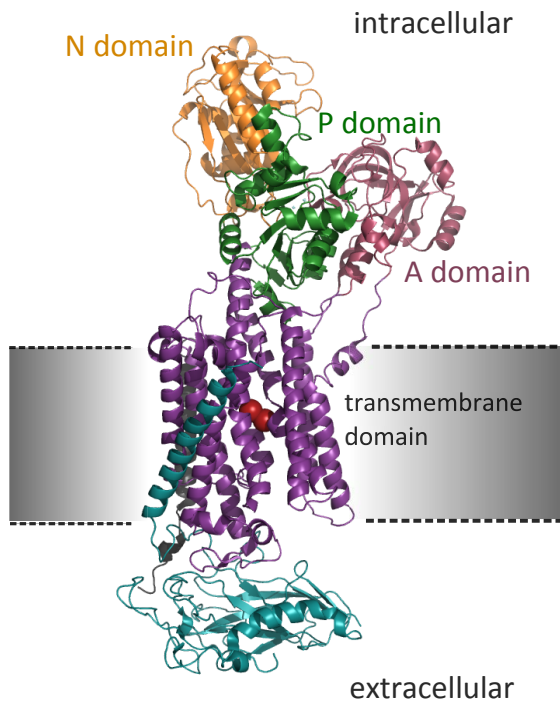


Figure 2.5: X-ray crystal structure of the Na,K-ATPase in E<sub>2</sub> conformation and at 2.4 Å resolution (reconstructed from PDB entry 3A3Y) [48]. The  $\alpha$ -subunit consists of ten transmembrane segments (purple) and contains intracellular the N- (orange), P- (green) and A domain (light red). The two bound K<sup>+</sup> ions in the transmembrane segments of the  $\alpha$ -subunit (red) are also illustrated. The  $\beta$ -subunit with one transmembrane cylinder and the corresponding extracellular domain are painted in cyan. The  $\gamma$ -subunit is depicted in black.

It is also known that the P-type ATPases undergo extensive conformational changes during the catalytic cycle, in which two principal states are distinguished, E<sub>1</sub> and E<sub>2</sub>. The E<sub>1</sub> and E<sub>2</sub> state differ in the orientation and specificity of the binding sites for Na<sup>+</sup> and K<sup>+</sup>. Since these different conformations are not of interest further for this work it is not outlined in details. For more details see [46, 49].

### 2.2.2 Subunits and Isoforms of the Na,K-ATPase

The  $\alpha$ -subunit is responsible for the catalytic activity of the enzyme and undergoes a reversible phosphorylation and characteristic conformational transitions that are coupled to ATP hydrolysis and the cation transport. The  $\beta$ -subunit is required for the normal activity of the enzyme and for the structural and functional maturation of the  $\alpha$ -subunit. Four  $\alpha$ - ( $\alpha_1$ ,  $\alpha_2$ ,  $\alpha_3$ , and  $\alpha_4$ ) and three  $\beta$ -isoforms ( $\beta_1$ ,  $\beta_2$ , and  $\beta_3$ ) have been identified in humans. Different isoforms combine to form Na,K-ATPase isozymes with distinct kinetic properties, which can be regulated in a tissue- and developmental-specific manner.

All  $\alpha$ -subunits have a molecular weight of around 110 kDa [46] and consist of approximately 1000 amino acid residues. The number of amino acids varies within the same species. Additionally, different types of regulatory proteins exist too, which vary depending on the tissue and the organism where they originate from. The  $\alpha_1$ -isoform is the most essential subunit, because it is found in almost all tissues. The other isoforms are only expressed in specific cells and tissues, e.g. the  $\alpha_2$  is predominantly expressed in skeletal, heart and vascular smooth muscle as well as mostly glia cells in the brain. The  $\alpha_3$  is found in larger amounts in neurons and the  $\alpha_4$  exclusively in testicular tissues especially in spermatozoa.

The  $\alpha$ -subunit comprises ten transmembrane segments M1 to M10, which are interconnected by four intracellular and five extracellular amino acid loops. In all  $\alpha$ -isoforms both the C- and the N-terminus are located on the cytosolic side (Figure 2.6). Within the  $\alpha$ -subunit, three cytoplasmic domains are present, the actuator (A), the phosphorylation (P) and nucleotide binding domain (N). The A domain is composed of the N-terminal tail and the loop segment between M2 and M3. It contains the TGES-motif and plays a major role in the dephosphorylation of the protein. The P domain consists of the initial and final segment of the loop between M4 and M5 and contains also the DKTGT-motif to which the phosphate is transferred. The main segment of the loop between M4 and M5 forms the ATP binding site (N domain), and thus the catalytic center.

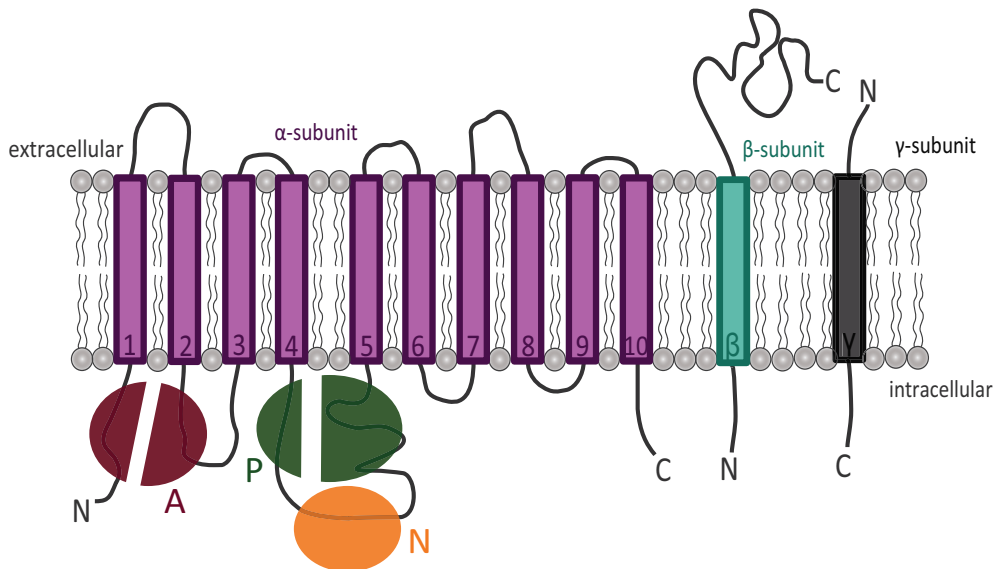


Figure 2.6: The topological arrangement of the Na,K-ATPase  $\alpha$ -,  $\beta$ - and  $\gamma$ -subunits is shown. The purple cylinders represent the ten transmembrane segments (M1 - M10) of the  $\alpha$ -subunit, which are located in the transmembrane domain. The small extracellular and the larger intracellular loops with the three cytoplasmic domains (A, P and N) are also shown. The  $\beta$ -subunit (cyan cylinder) comprises only one transmembrane segment, like the  $\gamma$ -subunit painted in dark grey.

The  $\beta$ -subunit comprises just one transmembrane segment, in contrast to the  $\alpha$ , and thus belongs to the type II membrane proteins. Type II membrane protein indicates that the N-terminus is stored intracellularly and the C-terminus extracellularly. The subunit is made of about 370 amino acids and has an overall molecular weight of around 55 kDa. Naturally, the  $\beta$ -subunit is located near the M7 and M8 segments of the  $\alpha$ -subunit and possesses an extracellular domain with multiple glycosylation sites. The exact function of the  $\beta$ -subunit at the molecular level is not fully understood. It is known that it plays no role in the ATP hydrolysis, but it is necessary for expression, transport to the plasma membrane, the folding of the protein and affects ion transport [50].

The smallest subunit is, as already mentioned above, the  $\gamma$ -subunit (illustrated in Figure 2.6 in dark grey). As the  $\beta$ -subunit, the  $\gamma$ -subunit contains only one transmembrane segment and consists of around 65 amino acids with a molecular weight of approximately 7 kDa. It contains a FXDY-motif typical for this class of membrane proteins. Tissue-specific regulatory functions relating to the cation affinities and the cellular targeting of the protein are attributed to the  $\gamma$ -subunit [51]. It binds exclusively to an  $\alpha/\beta$ -complex and not to individual subunits.

### 2.2.3 Na,K-ATPase Associated Human Diseases

The physiological importance of Na,K-ATPase is underlined by the fact that mutations in the genes coding for Na,K-ATPase isoforms lead to severe human pathologies like familial hemiplegic migraine (FHM), alternating hemiplegia of childhood (AHC) [52], rapid dystonia parkinsonism (DYT12) or epilepsy.

One of the most common neurological diseases in the world is migraine, which affects 10 % to 15 % of the population. Migraine is divided into different subtypes, by criteria of the International Headache Society (IHS) [53]. The two main groups which are distinguished between is migraine with aura and migraine without aura. An aura is a series of different movement disorders, as well as sensory disturbances and this phases precede the actual headache. Most forms of migraine are induced by the environment with a genetic disposition, which means that they occur frequently familial. The only type of migraine, which is classified as a hereditary disease, is the familial hemiplegic migraine (FHM) that is caused by mutations in four different genes (*ATP1A2*, *CACNA1A*, *SCN1A* and *PPRT2*). It is a rare autosomal dominant disease, belonging to the more general phenotype of migraine with aura, but with a particularly severe clinical form. This type of migraine is independent of gender. For FHM diagnosis three criteria must be fulfilled. First, there must be at least one affected relative in first or second degree, and it must be a hemiplegia in the aura phase. Furthermore other aura symptoms must occur, which often are accompanied by complications such as fever, consciousness disorder or epileptic seizures.

Until now four different variants of FHM are identified, which are related to four different gene mutations. Two mutations in genes encoding neuronal voltage-gated channels (termed *CACNA1A*), encoding the  $\alpha_1$ -subunit of a calcium channel (FHM1) are mostly found in neurons. The other one is termed *SCN1A* (FHM3) coding the neuronal voltage-gated sodium channel. Lately, a third variant was identified, which is attributed to mutations in the *PPRT2* gene (FHM 4), that encodes a proline-rich transmembrane protein of as yet unknown function [54].

The fourth variant is FHM type 2 (FHM2), that is caused by mutations in the gene *ATP1A2* coding for the human Na,K-ATPase  $\alpha_2$ -subunit, which in the brain is mostly expressed in glial cells especially in astrocytes. Until now, there are more than 80 *ATP1A2* mutations known, which are associated to FHM or SHM, a sporadic form characterized by *de novo* mutations in single patients [2, 4, 55].

### 2.2.4 Na,K-ATPase and Cellular Interaction Partners

The impact of sub-cellular targeting of the Na,K-ATPase and its enzymatic role in health and disease is largely enigmatic so far. There are a couple of reports indicating that the human Na,K-ATPase enzyme interacts with other structural proteins or constituents of the cytoskeleton for sub-compartment localization.

One interesting example for an interaction partner for the Na,K-ATPase is ankyrin B. Ankyrins are cytoskeletal proteins that interact via dynamic covalent bonds with integral membrane proteins and take part in their distribution in the cell membrane. Three classes of ankyrins are distinguished, ankyrin R in which R stands for "restricted" and is encoded by *Ank1* on human chromosome 8p11. It was firstly found in erythrocytes, but it is also expressed in certain neurons and striated muscle cells. Another class is encoded by *Ank2* on human chromosome 4q25-27 and termed as ankyrin B, because it is "broadly expressed" in most cell types. The third type of protein is ankyrin G, which is encoded by *Ank3* on human chromosome 10q21 and expressed in nearly all cell types. In this context G means "giant size" and "generally expressed". All ankyrins are composed of four functional groups, a membrane-binding domain at N-terminus consisting of 24 ankyrin-repeats, a central domain that binds to the cytoskeletal protein spectrin, a death domain as well as a regulatory domain at the C-terminus, which differs for different ankyrin proteins. Ankyrin B is with 440 kDa a particularly large ankyrin and has an additional tail domain between spectrin and death domain, which consists of a 220 kDa random coil. Also the membrane-binding domain differs from other proteins, which has specialized functions in unmyelinated axons and e.g. targeting of voltage-dependent channels. Ankyrin B and G are required for the polar distribution of many membrane proteins, like the Na,K-ATPase. The interaction between Na,K-ATPase and ankyrin B is intrinsically associated with the stabilization of the Na,K-ATPase in the plasma membrane and also enables the transportation from ER to Golgi.

Some examples for interaction partners of ankyrin and mutations, which lead to several diseases are given in the following. One example is the involvement of mutations in the gene coding for ankyrin B in Long-QT syndrome type 4 (LQT4), a severe autosomal-dominant form of cardiac arrhythmia. Ankyrin B serves as adapter protein, and LQT4 mutations disrupt cellular organization of Na,K-ATPase, Na,Ca-exchanger, and inositol-1,4,5-trisphosphate receptors, which are all ankyrin B binding proteins. In effect they reduce the targeting of these proteins to transverse tubules as well as causing a reduction of the overall protein level. In cardiac cells, it is mainly the  $\alpha_2$ -isoform that is located in t-tubules, whereas the general "house-keeping"  $\alpha_1$ -isoform is more evenly distributed across the sarcolemma membrane.

Similar considerations apply for the  $\alpha_2$ -subunit in the central nervous system (CNS). The  $\alpha_2$ -subunit is found mainly in glial cells (astrocytes) and co-localizes in distinct subdomains of the plasma membrane with the Na,Ca-exchanger (NCX). They are located close to ER as intracellular  $\text{Ca}^{2+}$  storage compartment, in very restricted geometries dubbed PLasmERosomes [10, 56–58].

Another well-known Na,K-ATPase interaction partner is caveolin-1 (cav.-1), which has been characterized in detail and which plays an important role in many caveolin-dependent cellular processes. Caveolins are structure proteins that form caveolae membrane domains. So far, three different caveolin forms in mammalian cells are known that encode five different protein isoforms, wherein the caveolin-1 is the most well characterized form. The expression and distribution of the various forms are tissue-specific, but all of them serve as protein markers for caveolae [59]. Caveolin-1 is found mostly in the plasma membrane and in Golgi-derived vesicles. The highest expression of cav.-1 is found in fibroblasts, endothelial cells and smooth muscle cells. This protein forms complexes of around 13 to 16 monomers of high molecular weight and is also interacting with caveolin-2 (cav.-2), which is mostly co-expressed with cav.-1 to form hetero-oligomers. The third form is caveolin-3 that is expressed in the majority of cases in striated muscle cells [60].

Caveolin-1 is an important structural element of caveolae, building invaginations with a typical size of 50 nm up to 100 nm in the plasma membrane e.g. of endothelial cells visible in the electron microscope. This membrane protein has a molecular weight of about 18 kDa up to 24 kDa and forms the scaffold of caveolae. Many cellular functions were associated with caveolae and caveolin-1, such as membrane transport and endocytosis. They are also linked to the regulation of calcium metabolism and also to lipid metabolism, as well as to signal transduction during cellular proliferation and programmed cell death. The Na,K-ATPase has been attributed to the regulation of caveolin trafficking and stabilization of caveolin-1 in the plasma membrane. Disruptions of caveolin targeting have been linked to several human pathologies such as dystrophies, disruption of cellular signaling cascades or endocytosis defects [61, 62].

### 2.2.5 Generation of Sequence Variants of the Na,K-ATPase

For expression studies at different incubation temperatures a FHM2 mutant P797L was created by mutagenesis. This single point mutation in the *ATP1A2* gene was firstly described by Jurkat-Rott *et al.* [55].

Binding motifs, which are conserved in all human isoforms of the Na,K-ATPase  $\alpha$ -subunit were mutated in this work in order to elucidate the consequences of interactions of the Na,K-ATPase  $\alpha_2$ -isoform with other proteins. These proteins might influence the cellular distribution pattern or the mobility of the enzyme in the plasma membrane. The following sequence variants were generated.

Two caveolin-1 binding motifs are described in the literature by Wang *et al.* [63]. One at the N-terminus the FCRQLFGGF motif around amino acid 90 and the second at the C-terminus the WWFCAFPY motif around amino acid 990 (see Fig. 2.8). The two caveolin-1 binding motifs were disrupted by mutagenesis with replacement of the most critical aromatic amino acids by poly-alanine stretches.

There is one motif known from the literature by Jordan *et al.* [64], by which the Na,K-ATPase  $\alpha_2$ -subunit mutant can interact with ankyrin B. This motif comprises a positively charged lysine, therefore, the introduction of a negative charge by mutation to a glutamate should drastically interfere with the interaction. Following this reasoning, a mutation was introduced onto the ALLK motif around amino acid 450 in the nucleotide binding domain (see Fig. 2.8), mutated to ALLE now termed DRK-NaK-K456E.

All binding motifs (orange points) are located in highly conserved regions of the Na,K-ATPase  $\alpha_2$ -subunit and their positions were illustrated in Figure 2.7.

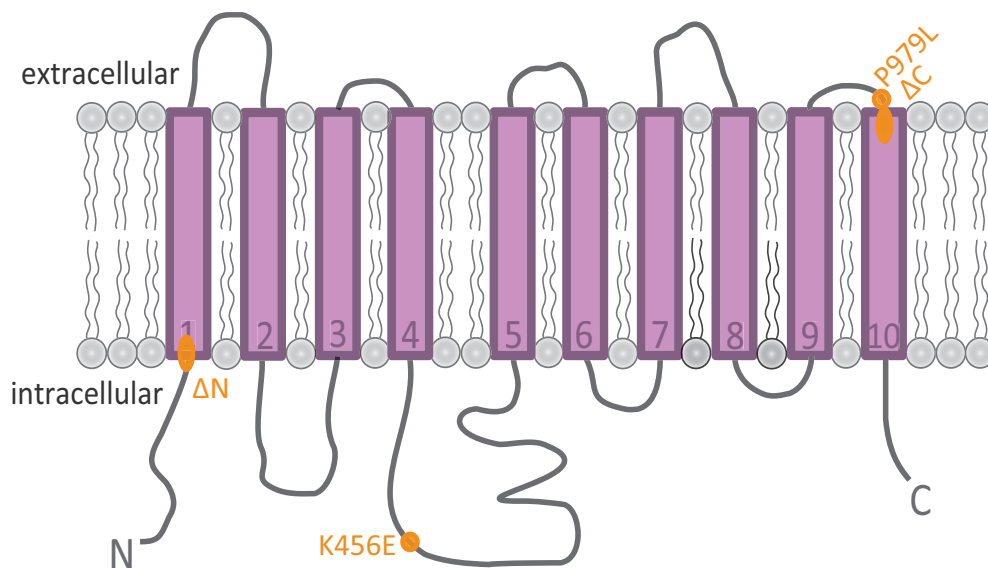


Figure 2.7: Scheme of the Na,K-ATPase  $\alpha_2$ -subunit with the positions of the desired mutations (orange points).

The template for all mutations is the human Na,K-ATPase  $\alpha_2$ -subunit carried a fluorescence label at the N-terminus. For more details about the fluorescence marker see section 2.3. As expression vector for Dreiklang- and eGFP (see details in section 2.3) mutations and fluorescence-labeled Na,K-ATPase constructs always a pcDNA3.1x vector suitable for mammalian cell expression was used. In addition, the in this work used Na,K-ATPase is carrying a double mutation Q116R/N127D, which produces  $IC_{50}$  values for ouabain in the hundred micromolar range [65].

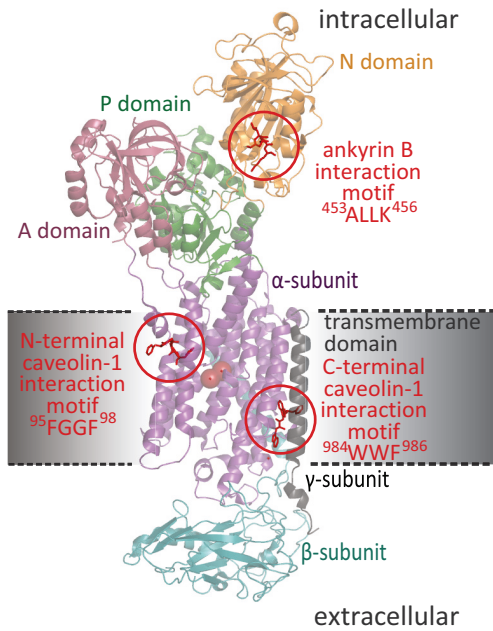


Figure 2.8: X-ray crystal structure of the Na,K-ATPase in  $E_2$  conformation at 2.4 Å resolution (reconstructed from PDB entry 3A3Y) [48] with the positions of the two interaction motifs associated with caveolin-1 (NaK- $\Delta C$ , NaK- $\Delta N$ ) and the interaction motif associated to ankyrin B (NaK-K456E).

For studies with the P979L mutant, the bicistronic pIRES vector was used, because of the ability to express two separate proteins from a single vector due to the presence of an internal ribosomal entry site between two multiple cloning regions. In this case eGFP and TagRFP were used as fluorescent markers. Table 2.1 shows a list of the used primers, the sequences for the mutation production and the subsequently utilized construct names. All constructs were created by mutagenesis, as described in more details in sections 2.4.2 and 2.4.3.

Table 2.1: List of the used primers, the sequences for the mutation production and the utilized construct names. DRK and eGFP are the used fluorescent marker.

Primer	Function	Sequence	Name
delCCav-for delCCav-rev	deletion deletion	CGCTCAAAGTCACCGCGTGGGCTGCGCCTTCCCC GGGGAAGGCGCAGGCCACGCGGTGACTTTGAGCG	DRK-NaK- $\Delta C$ / eGFP-NaK- $\Delta C$
delNCav-for delNCav-rev	deletion deletion	GCCGTCAGCTTGCCGGGGGGGCTCCATCCTGC GCAGGATGGAGCCCCCGGCAAGCTGACGGC	DRK-NaK- $\Delta N$ / eGFP-NaK- $\Delta N$
K456E-a K456E-r	point mutation point mutation	GAGTCAGCTCTGCTCGAGTGCATTGAGCTC GAGCTCAATGCACTCGAGCAGAGCTGACTC	DRK-NaK-K456E / eGFP-NaK-K456E
P979L-a P979L-r	point mutation point mutation	CAT GTA CCT GCT CAA AGT CAC GTG ACT TTG AGC AGG TAC ATG CGG	P979L

The same mutants of the Na,K-ATPase were also labeled with the eGFP fluorescent marker (see section 2.4.3). They are named in the following sections and chapters eGFP-NaK-WT, eGFP-NaK- $\Delta$ C, eGFP-NaK- $\Delta$ N and eGFP-NaK-K456E.

Additionally, two special mutants were produced. The first one is a double mutant, which combines both caveolin-1 interaction motifs, and the latter is a threefold mutant that unifies all three interaction motifs of caveolin-1 (NaK- $\Delta$ C and NaK- $\Delta$ N) and ankyrin B (NaK-K456E). These two mutants were labeled with eGFP and referred as eGFP-NaK- $\Delta$ C $\Delta$ N and eGFP-NaK- $\Delta$ C $\Delta$ NK456E.

## 2.3 Fluorescent Proteins used as Marker Proteins

Nowadays there is a broad spectrum of genetically-encoded fluorescent proteins available that can be used as markers for compartments or proteins in living cells and as chemical sensors. In addition, they offer the possibility to observe processes in the cell, such as protein localization, dynamics and interactions and offers the opportunity for high resolution microscopy studies.

Beside common fluorescent proteins like GFP and its variants, several reversibly photoswitchable fluorescent proteins have been recently developed, such as Dronpa or rsTagRFP [36, 66]. These proteins provide reversible photoswitching between a fluorescent ON-state and nonfluorescent OFF-state. Thus they provide many benefits and applications for research studies in living organisms. In the following the relevantly fluorescent proteins (eGFP, TagRFP, DRK) for this work are introduced and described in more detail. A direct comparison of all spectral properties is given in Table A.3 in the appendix.

### 2.3.1 Green Fluorescent Protein

The green fluorescent protein (GFP) is one of the most commonly used fluorescent markers and was originally identified in the jellyfish *Aequorea victoria*. In these days there are many different types of GFP variants available. The importance of this fluorescent protein in many scientific fields is also reflected by the award of the Nobel Prize in 2008 to O. Shimomura, M. Chalfie and R. Tsien.

The primary structure of GFP comprises a total number of 238 amino acids, which are arranged in 11  $\beta$ -sheets with a molecular mass of around 26.9 kDa. The protein looks like a barrel, also named as  $\beta$ -barrel (see Fig. 2.9). GFP and other fluorescent proteins for itself have no chromophore. They receive the fluorescent properties by an autocatalytic process, which forms a chromophore. This fluorophore arises from the

three consecutive amino acids Ser<sup>65</sup>, Tyr<sup>66</sup> and Gly<sup>67</sup>, which are post-translationally modified and a cyclic system of conjugated double bonds is formed [67].

The wild-type GFP has two excitation maxima, the first at 396 nm and the second at 475 nm. The emission wavelength is at 504 nm, which is in the green wavelength range. The wild-type GFP exhibits an extinction coefficient ( $\epsilon$ ) between 25,000 M<sup>-1</sup> cm<sup>-1</sup> and 30,000 M<sup>-1</sup> cm<sup>-1</sup> for excitation wavelengths between 395 nm and 397 nm. For excitation wavelengths between 470 nm - 475 nm, the extinction coefficient is only 9,500 M<sup>-1</sup> cm<sup>-1</sup> to 14,000 M<sup>-1</sup> cm<sup>-1</sup>. The fluorescence quantum yield ( $Q_y$ ) of the wild-type GFP is 0.79 as reported by previous investigations in the literature [67, 68].

For this work, an improved variant of GFP was used the so called enhanced green fluorescent protein eGFP. This carries the Ser<sup>65</sup>-Thr and Phe<sup>64</sup>-Leu point mutations. eGFP has an extinction coefficient of 55,000 M<sup>-1</sup> cm<sup>-1</sup> up to 57,000 M<sup>-1</sup> cm<sup>-1</sup> at an excitation wavelength of 488 nm and exhibits a quantum yield of 0.60. An advantage of eGFP is that it is 35 times brighter ( $\epsilon \cdot Q_y$ ) than wild-type GFP after excitation at about 470 nm [69, 70]. It is also more photostable and shows no photoswitching compared to the wild-type GFP.

### 2.3.2 Red Fluorescent Protein

TagRFP is a monomeric red-emitting fluorescent protein firstly derived from the sea anemone *Entacmaea quadricolor*. The protein is a GFP-like protein and has a very similar structure (Figure 2.10). Only the fluorophore has a slightly different composition, because the amino acid trio forming the chromophore consists of Met-Tyr-Gly.

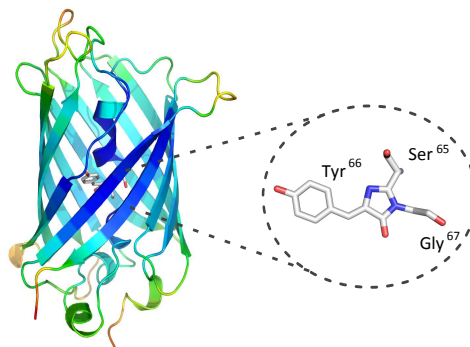


Figure 2.9: Structure of the green fluorescent protein (GFP) and the chromophore formed within. The picture is reconstructed from PDB entry 1GFL. The  $\beta$ -barrel and the  $\alpha$ -helices are shown in cartoon representation and the chromophore as sticks. Carbons are displayed in light grey, nitrogen in blue and oxygen in red.

It shows an excitation maximum at 555 nm and emission at around 584 nm. The protein is characterized by a high brightness in comparison to other red-emitting fluorescent proteins, a complete chromophore maturation, an extended lifetime of 2.2 ns/2.3 ns and a high pH stability.

TagRFP has an extinction coefficient of  $100,000 \text{ M}^{-1}\text{cm}^{-1}$  and a quantum yield of 0.48. Because of these characteristics, this fluorescence protein is very useful as a marker for localization studies in living cells or as a Förster resonance energy transfer (FRET) partner of eGFP [71].

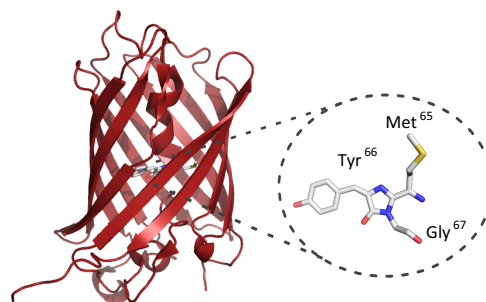


Figure 2.10: Structure of the fluorescent protein TagRFP (reconstructed from PDB entry 3M22). The  $\beta$ -barrel and the  $\alpha$ -helices are shown in cartoon representation and the chromophore as sticks.

### 2.3.3 Photoswitchable Fluorescent Protein Dreiklang

The fluorescent protein Dreiklang is a new reversibly photoswitchable GFP-like protein, which exhibits decoupled fluorescence excitation and optical switching spectra [37]. The overall structure of Dreiklang (DRK) resembles that of GFP-like protein Citrine and the difference to the parental GFP is only 9 mutations. The chromophore of DRK is also formed autocatalytically, but from the three amino acids Gly65-Tyr66-Gly67. They reside in an  $\alpha$ -helical segment, which is surrounded by an 11-stranded  $\beta$ -barrel. Figure 2.11 shows the overall structure of Dreiklang in its fluorescent equilibrium state and the inner structure of the chromophore.

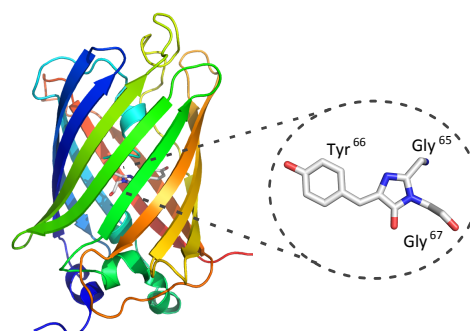


Figure 2.11: Structure of the photoswitchable fluorescent protein Dreiklang in the equilibrium state (reconstructed from PDB entry 3ST2). The  $\beta$ -barrel and the  $\alpha$ -helices are shown in cartoon representation and the chromophore as sticks.

Dreiklang provides a major advantage compared to other switchable fluorescent proteins. It can be reversibly switched and, therefore offers many benefits for many different measuring techniques and is suited for many biological samples. Figure 2.12 a) to c) shows three different possible states of the chromophore. At thermal equilibrium at 300 K, the chromophore structure is arranged in a plane. In this state, the chromophore is indistinguishable from the fluorescent ON-state. Dreiklang can

be switched from the equilibrium in the nonfluorescent OFF-state by irradiation of light at a wavelength of 405 nm. This switching process occurs by hydration due to a structural change of the chromophore. In this state, the planarity of the chromophore is distorted.

Using UV light (365 nm) the protein is switched back in an ON-state by a dehydration process and thus resulting again in a change in the chromophore structure. This switching process can proceed over several hundred cycles, without undergoing any irreversible photobleaching processes. To observe the protein fluorescence in different states a monitoring wavelength of 515 nm can be used, because of the limited switching rate between the ON- and OFF-states. In the fluorescent ON-state, Dreiklang provides an extinction coefficient of  $83,000 \text{ M}^{-1}\text{cm}^{-1}$  and a quantum yield of 0.41 at pH 7.5 [37]. Therefore, Dreiklang and eGFP exhibit a similar brightness of about  $34,000 \text{ M}^{-1}\text{cm}^{-1}$  ( $\epsilon \cdot Q_y$ ).

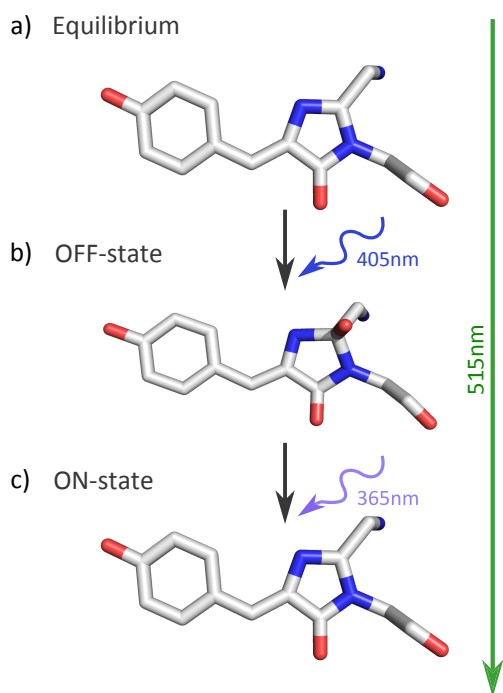


Figure 2.12: Scheme of the Dreiklang chromophore in different states and with the different switching wavelengths. a) shows the equilibrium, b) the OFF-state and c) the ON-state (all chromophores are reconstructed from PDB entry 3ST2, 3ST3 and 3ST4). The chromophore is represented as sticks.

## 2.4 Molecular Biological Methods

### 2.4.1 Mutagenesis in the Human Na,K-ATPase $\alpha_2$ -Subunit in pIRES Expression Vector

The various mutations of the human Na,K-ATPase  $\alpha_2$ -subunit (P979L and FS(S966fs)) as well as the wild-type (WT) were generated by polymerase chain reaction (PCR) prepared by N. N. Tavraz at TU Berlin [72]. The PCR fragments

were ligated into a pIRES vector suitable for mammalian cell expression (Clontech Laboratories, Inc.). The vector allows for a high expression level for two different genes of the same bicistronic mRNA transcript. The first gene is the particular Na,K-ATPase  $\alpha_2$ -subunit mutant labeled with eGFP and the second with TagRFP, which is expressed in the cytoplasm and serves as an expression reference.

### 2.4.2 Different Mutations of the Human Na,K-ATPase $\alpha_2$ -Subunit Labeled with Dreiklang

The targeted mutagenesis by the QuickChange method allows for a simple and precise introduction of a mutation in a double-stranded plasmid deoxyribonucleic acid (DNA). All mutations were done by using the QuickChange<sup>®</sup> II XL Site-Directed Mutagenesis Kit (Stratagene). The reaction approach for the PCR reaction, which was always used is shown in the following:

- 2.0  $\mu\text{l}$  Template DNA (10 ng/ $\mu\text{l}$ )
- 0.5  $\mu\text{l}$  dNTP-Mix (10 mM total concentration)
- 2.5  $\mu\text{l}$  Polymerase-Buffer
- 1.0  $\mu\text{l}$  forward-Primer (10 pmol/ $\mu\text{l}$ )
- 1.0  $\mu\text{l}$  reverse-Primer (10 pmol/ $\mu\text{l}$ )
- 0.5  $\mu\text{l}$  DNA-Polymerase
- 1.5  $\mu\text{l}$  QuickSolution
- 17.0  $\mu\text{l}$  ddH<sub>2</sub>O

In this case Dreiklang-NaK-WT was utilized as template DNA. For polymerase chain reaction (PCR) the following temperature protocol program was used (see Table 2.2). A PCR is done in three steps, which are repeated cyclically. In the first step, the denaturation step, the double strand of the DNA templates is separated. Secondly, the used oligonucleotide primer hybridizes on DNA single strands (annealing). In the last step of a PCR, the elongation, the primers become extended and each template is synthesized to the complementary DNA strand.

Table 2.2: Used PCR protocol with the three steps (denaturation, annealing and elongation), number of cycles, used temperature and the needed time for each cycle step.

cycle	temperature	length	
1	95 °C	1 min	(denaturation)
18	95 °C	50 s	(denaturation)
18	60 °C	50 s	(annealing)
18	68 °C	5 min	(elongation)
1	68 °C	7 min	(elongation)
1	4 °C	$\infty$	(storage)

Afterwards the PCR product was mixed with 0,5  $\mu\text{l}$  DpnI and incubated for 1 hour at 37 °C. In this step methylated, nonmutated template DNA is digested.

For transformation of the mutated DNA chemically competent cells of the bacterial host strain *E.coli* (XL10-Gold-ultracomp. cells, Stratagene) were used. In the use of XL10-Gold cells it is necessary first to mix 1  $\mu\text{l}$   $\beta$ -Mercaptoethanol with 22.5  $\mu\text{l}$  of competent cells and melt them for 10 minutes on ice. Afterwards cells were mixed with 1  $\mu\text{l}$  of DpnI-digested DNA and incubated for another 30 minutes on ice. The next step is a 30 second heat shock at 42 °C, which is essential for a successful transformation followed by a cooling down for another 2 minutes on ice. After addition of 250  $\mu\text{l}$  preheated NZY-medium (37 °C) the cell suspension was incubated for 1 hour at 37 °C and 225 - 250 rpm (UFO) in an air bath shaker. The cell suspension was plated out on agar plates, which contained an antibiotic to select only those bacteria which taken up the vector. In this case the pcDNA3.1x vector was used, which needs ampicillin as antibiotic. After an incubation period of 16 h to 20 h at 37 °C in a plate incubator LB overnight cultures were arranged. Therefore 8 ml LB-medium with ampicillin were inoculated with a clone of the agar cultures and cultured for 16 h to 20 h at 37 °C and 225 - 250 rpm in an air bath shaker.

During the following mini preparation the plasmid DNA was isolated from transformed bacteria with the alkaline lysis method. The AxyPrep Plasmid Miniprep Kit (Axygen Biosciences) was used and all steps were done as described in the protocol. In the last step, the DNA was eluted in 50  $\mu\text{l}$  of ddH<sub>2</sub>O. The DNA concentration was determined photometrically (BioPhotometer<sup>®</sup>, Eppendorf) for all samples. In the next step, the samples for a complete sequencing were chosen, which was done by Eurofins MWG operon. This step is important to confirm the desired mutation and to make sure that no unwanted mutations in the plasmids are present. All plasmids were successful generated and purified for transfection. In some cases, it was necessary to generate more plasmid DNA, therefore midi preparations were performed, which generate up to 100  $\mu\text{g}$  of plasmid DNA. For all of these preparations the Quiagen Plasmid Midi Kit (Quiagen) or the JetStar 2.0 Plasmid Purification Midi Kit (Genomed) were used.

### **2.4.3 Fusion Constructs with Different Fluorescent Protein Marker**

For later measurements the fluorescent label of the human Na,K-ATPase constructs was changed from Dreiklang to eGFP. Therefore, a plasmid cloning by a restriction enzyme digestion was done. From all constructs (eGFP-NaK-WT, DRK-NaK- $\Delta\text{C}$ ,

DRK-NaK- $\Delta$ N and DRK-NaK-K456E) 1  $\mu$ g of the plasmid DNA was digested with the restriction enzymes BamHI and BsrGI for two hours at 37 °C. The same enzymes were used, since the expression vector used by all constructs is the same (pcDNA3.1x). Afterwards the vector fragments (NaK- $\Delta$ C, NaK- $\Delta$ N and NaK-K456E) were digested with alkaline phosphatase for another 10 minutes at 37 °C. In order to isolate the vector and insert fragments, the digested DNA fragments were run on a 1 % agarose gel stained with ethidium bromide and carefully sliced out.

The following purification of the fragments from the gel was carried out by using the High Pure Purification Kit (Roche) and the respective concentrations were determined photometrically (BioPhotometer<sup>®</sup>, Eppendorf) to optimize the ligation process for a one to three molar ratio of vector to insert (eGFP). The ligation process fused the inserts into the plasmid vectors and was done using the Rapid DNA Ligation Kit (Thermo Scientific). The ligated DNA was then transformed into competent XL-Gold cells and plated on ampicillin agar plates. From all plates, colonies were picked and overnight cultures for DNA purification were inoculated.

Finally the plasmid DNA was purified with another mini preparation kit (peq Gold Plasmid Miniprep Kit I, peQlab). A test digestion of the plasmids was taken for determining the plasmids which have been successfully cloned and run on a 1 % agarose gel labeled with ethidium bromide. Based on the results of the gel separation the samples for sequencing (Eurofins MWG Operon) were chosen.

#### 2.4.4 Production of Purified Dreiklang and eGFP Protein

In order to express and purify the fluorescent proteins Dreiklang and eGFP in *E. coli*, it was necessary to subclone the respective cDNAs from the plasmids Dreiklang-pcDNA3.1x and peGFP-N1 (Life Technologies). The cDNA of eGFP was excised from peGFP-N1 by BamHI and NotI and ligated in-frame into a modified pQE81L-Amp vector (Qiagen) carrying an additionally engineered NotI restriction site. The cDNA of DRK was excised from pcDNA3.1x by BamHI and XhoI and ligated in-frame into the pQE81L-Kan vector (Qiagen) carrying a kanamycin resistance gene, which was cut with the restriction enzymes BamHI and SalI. These resulted in protein sequences with an N-terminal 6xHis-tag preceding the first methionine. The remaining cloning work was performed using the same method as described already in chapter 2.4.2 and plasmid constructs were verified by sequencing.

After transformation of the generated recombinant plasmid constructs in *E.coli*, 400 ml LB-medium with appropriate antibiotic (50 µg/mL kanamycin or 50 µg/mL ampicillin) were inoculated from a starter culture to 0.1 optical density (OD) and grown at 37 °C in an orbital shaker with 200 rpm to an OD of 0.6. After induction with 1 mM IPTG, cells were grown for 48 h at 22 °C. Cells were harvested by centrifugation yielding brightly green-colored pellets. Cell pellets were resuspended in phosphate-buffered saline (PBS) and lysed by two passages through a French press using a pressure of about 20,000 psi. Afterwards, the cell debris was removed from the sample by 15 min centrifugation at 10,000 g and 4 °C. The clarified supernatant is then isolated and purified by using medium pressure liquid chromatography (MPLC) with Ni<sup>2+</sup>-Sepharose columns (GE-Healthcare) according to the manufacturer instructions (20 mM imidazole was supplemented to the supernatant, as recommended). Figure 2.13 reveals the obtained proteins after the MPLC in a glass tube. In connection to the MPLC, the purest sample fractions obtained were pooled and dialysed against 50 ml Tris/HCl, 300 mM NaCl, 5 mM EDTA (pH 7.8). The protein concentration was determined for Dreiklang to be 1.01 mg/ml by using the Bradford test Roti<sup>®</sup>-Quant (Roth). Bovine serum albumin (BSA) was used as calibration standard.

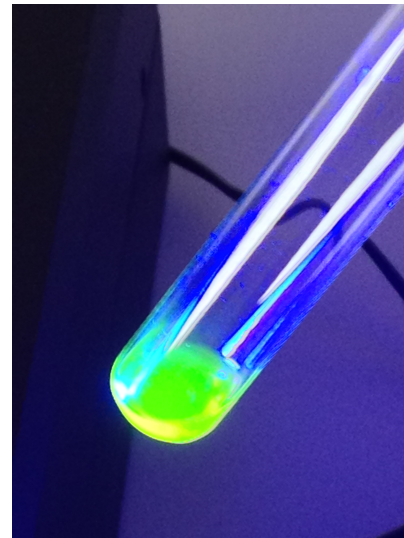


Figure 2.13: The received purified Dreiklang protein after MPLC in a glass tube illuminated with UV light.

#### 2.4.5 Production of cRNA for Expression in Oocytes

cRNA of the different Dreiklang constructs was also generated from the plasmid DNA to express the fusion proteins in oocytes. First of all, the circular plasmid DNA must be linearized. This can be done by cutting the DNA with the restriction enzyme XbaI (Fermentas). Then, 3 µg of the plasmids were mixed with 5 µl of "Tango" buffer (Fermentas) and 1 µl of the enzyme. The mixture is then filled up with water to a volume of 50 µl and is incubated for one hour at 37 °C. The subsequent purification of the DNA is carried out using the High Pure PCR Product Purification Kit (Roche). The resulting DNA is then concentrated with a vacuum centrifuge (Concentrator 5301, Eppendorf) to approximately 15 µl. The subsequent cRNA synthesis is done using the T7 mMessage mMachine Kit (Ambion), since the used pcDNA3.1 vector contains a T7 promoter. The cRNA is then stored at -20 °C.

### 2.4.6 Examination of the Functionality of the Na,K-ATPase by Rb<sup>+</sup> Uptake Measurements

The general functionality of the Na,K-ATPase of the various mutants labeled with Dreiklang was checked with cation uptake measurements by atomic absorption spectrophotometry (AAS) using a Perkin Elmer AAnalyst800. Under normal conditions, the Na,K-ATPase uses the released energy from the hydrolysis of ATP to actively transport Na<sup>+</sup> out of the cell and K<sup>+</sup> in the cell. During this transport, K<sup>+</sup> can be replaced by a suitable alkaline congeners, such as, for example, Rb<sup>+</sup>. This allows the determination of the activity of the Na,K-ATPase using AAS measurements. This technique offers the advantage with respect to the direct measurement of K<sup>+</sup>, since the rubidium concentration is negligible in the cell [73].

Therefore, oocytes of the clawed frog *Xenopus laevis* were used as a well-known expression system [74, 75]. The oocytes were surgically removed from frogs under anesthesia with 0.1 % tricaine (see Fig. 2.14 (a) and (b)). To isolate the oocytes gently from the ovary tissue, a collagenase digest was done using a calcium free ORI solution with 2 mg/ml collagenase and 10 mg/ml trypsin inhibitor. The oocytes were then incubated for 3 to 5 hours at 18 °C. Afterwards, the oocytes were rinsed with ORI solution and stored at 18 °C in a calcium containing ORI solution with 50 µg/ml gentamicin.

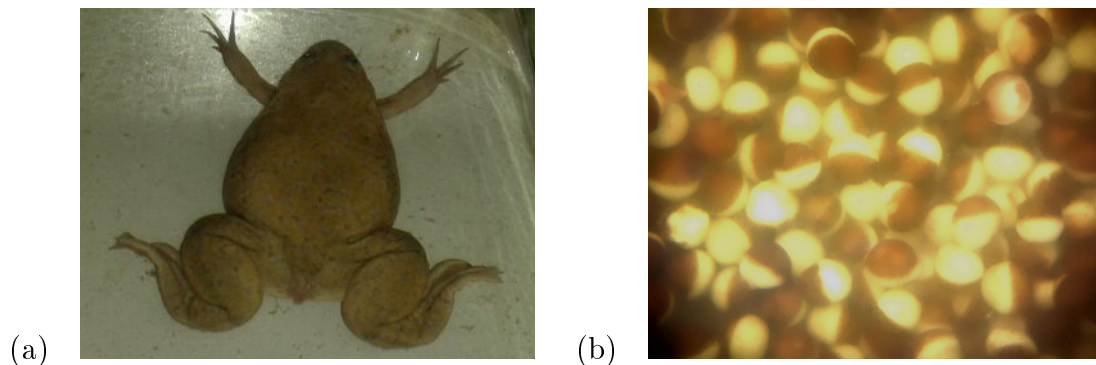


Figure 2.14: Pictures of a female clawed frog *Xenopus laevis* (a) and digested oocytes (b).

In the following, the oocytes were injected with the cRNA mixture of the respective Na,K-ATPase  $\alpha_2$ - and  $\beta_1$ -subunits. Afterwards, the oocytes were kept in a Ca<sup>2+</sup> containing ORI solution with 50 µg/ml gentamicin at 18 °C for three days. Before measurements, the intracellular concentration of Na<sup>+</sup> in all oocytes has to be increased to foster the activity of the enzyme. Therefore, the cells were incubated for 45 min in a Na<sup>+</sup>-loading solution and then for another 30 min in Na<sup>+</sup>-buffer (pH 7.4).

Finally the oocytes were incubated for 3 min with 1 mM  $\text{Rb}^+$  in 100 mM NMDG<sup>+</sup>-buffer, and were subsequently three times washed in Milli-Q<sup>®</sup> water. A detailed composition of all used buffers is given in Table A.1 in the appendix. All individual oocytes were homogenized in 1 ml Milli-Q<sup>®</sup> water for AAS measurements. As negative control, water-injected oocytes and uninjected oocytes were also prepared for measurements and serve as reference.

For each measurement, 20  $\mu\text{l}$  from the sample volume of the homogenized oocytes were transferred automatically to a transversely heated graphite furnace (THGF) and processed with the temperature protocol written in Table 2.3. During the atomization process the absorption was measured with a rubidium vapor cathode lamp at a wavelength of 780 nm and using a slit to select a spectral width of 0.7 nm. A standard calibration has to be performed before sample measurements, for values between 0  $\mu\text{g/l}$   $\text{Rb}^+$  and 50  $\mu\text{g/l}$   $\text{Rb}^+$  and the AAnalyst800 device is equipped with an assembly of high-field magnets for Zeeman correction.

Table 2.3: Temperature protocol for THGF-AAS measurements with rubidium.

Program Step	Temperature / °C	Ramp Time / s	Hold Time / s
Dry 1	110	1	30
Dry 2	130	15	30
Pyrolysis	700	20	20
Atomization	1620	0	4
Clean Out	2450	1	3

Figure 2.15 (a) and (b) shows the normalized rubidium uptake for the different Dreiklang-labeled Na,K-ATPase constructs (DRK-NaK-WT, DRK-NaK- $\Delta\text{C}$ , DRK-NaK- $\Delta\text{N}$  and DRK-NaK-K456E) measured with AAS after 4 minutes incubation time. More than 10 oocytes were measured for all constructs and the values were then averaged. All data were normalized to the mean value of the h.NaK $\alpha_2$ -WT or to the mean value of the eGFP-NaK-WT with corresponding standard deviation. The number N of oocytes, which were used for the analysis is given in the diagram.

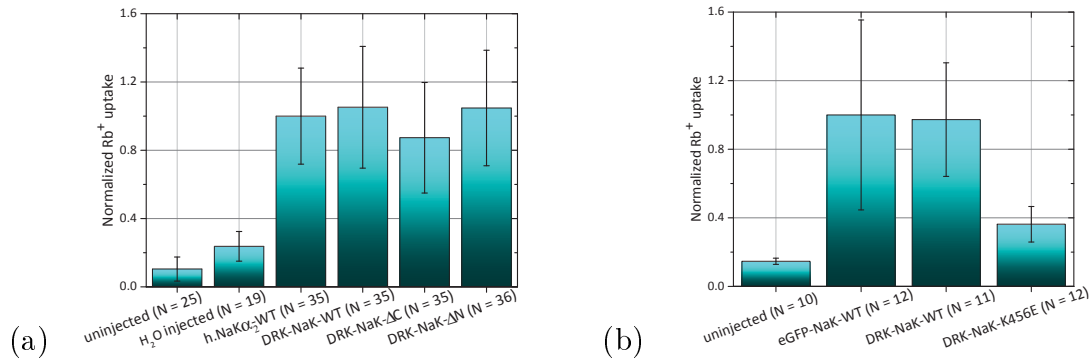


Figure 2.15: **(a)** Normalized Rb<sup>+</sup> uptake of the caveolin-1 associated mutants labeled with Dreiklang (DRK-NaK-ΔC, DRK-NaK-ΔN) in comparison with the DRK-NaK-WT, human Na,K-ATPase wild-type, water injected and uninjected oocytes. The number N of measured oocytes is also shown. Data are given as means  $\pm$  S.D. **(b)** Normalized Rb<sup>+</sup> uptake of the mutant DRK-NaK-K456E compared with eGFP-NaK-WT and DRK-NaK-WT.

The data in Fig. 2.15 show that the Rb<sup>+</sup> uptake in all Na,K-ATPase mutants is present, which is indicated by the comparable amount of Rb<sup>+</sup> uptake for the Na,K-ATPase WT and the mutants. This leads to the conclusion that the functionality of the active transport of the Na,K-ATPase is not impaired by the introduced mutations. This is also underlined by the control samples of water-injected oocytes and uninjected oocytes, both show a very small normalized Rb<sup>+</sup> uptake since the buffers contain 10  $\mu$ M ouabain to inhibit the endogenous Na,K-ATPase (see the two left bars of Fig. 2.15 (a)). Instead, the constructs labeled with Dreiklang showed a normalized Rb<sup>+</sup> uptake around one, five to ten times higher. Only the ankyrin B associated mutant (DRK-NaK-K456E) exhibits a decreased rubidium uptake and seems to be not completely functional, or the ion pump activity is slowed down, or plasma membrane expression is reduced. In comparison, eGFP- and Dreiklang-labeled enzymes show a very similar activity. This confirms that both labels do not disturb the enzyme activity.

Figure 2.16 shows the measured normalized Rb<sup>+</sup> uptake for all available eGFP-labeled Na,K-ATPase  $\alpha_2$ -subunit constructs, which were measured to see if they are as functional as the Dreiklang constructs. Since only the fluorescent label was exchanged and no other mutations were generated it can be assumed that no differences in the activity by the Rb<sup>+</sup> uptake measurements are visible. Additionally, the threefold mutant (eGFP-NaK-ΔCΔNK456E), which comprises all single point mutations described in section 2.2.5, has been measured.

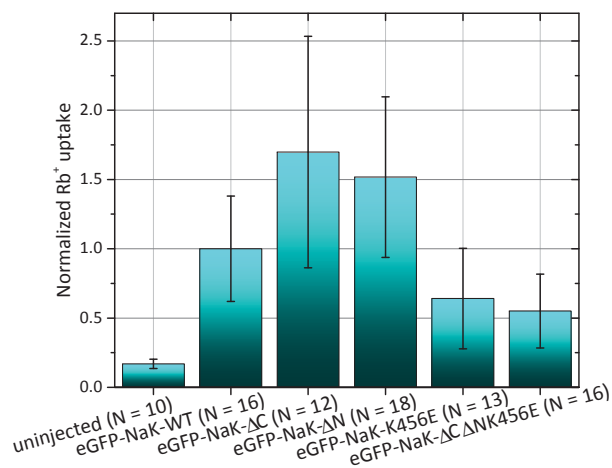


Figure 2.16: Normalized Rb<sup>+</sup> uptake of all eGFP-labeled Na,K-ATPase mutations in comparison with the eGFP-labeled Na,K-ATPase wild-type and uninjected oocytes. Also the number N of measured oocyte is shown in each bar. Data are given as means ± S.D.

Clearly, all eGFP-labeled Na,K-ATPase mutants seems to be functional compared to the uninjected oocytes, which serve as a reference for non-specific Rb<sup>+</sup> uptake. As already mentioned for DRK-NaK-K456E, also the eGFP-NaK-K456E mutant shows a reduced Rb<sup>+</sup> uptake, which leads to a reduced activity. The threefold mutant exhibits more or less the same reduced uptake like the Na,K-ATPase construct carrying a mutation in the ankyrin B binding motif. In this experiment the double mutant (eGFP-NaK-ΔCΔN) was not measured, because it is an intermediate form of the threefold mutant. If the threefold mutant is functional one can also assume that the twofold mutant is functional. In conclusion, it can be confirmed that all prepared Na,K-ATPase  $\alpha_2$ -subunit constructs are functional independent of the fluorescence label (eGFP or DRK).

## 2.5 Cell Culture and Transient Transfection

HEK293 cells were cultured at 37 °C with 5 % CO<sub>2</sub> in Dulbecco's Modified Eagle Medium (DMEM, Gibco) with phenol red dye supplemented with 5 % fetal bovine serum (FBS) and 1 % penicillin/streptomycin in 25 cm<sup>2</sup> culture flasks from neo-Lab<sup>®</sup>. The whole medium is changed twice a week. Depending on the confluence of the cells in the flask, the cell cultures were split once or twice per week.

For splitting, the complete old medium was removed and the cells were rinsed with 5 ml pre-warmed phosphate-buffered saline (PBS). Afterwards, 1 ml of trypsin-EDTA was added to the culture flask containing the adherent cells and the flask was placed for 1 minute back in the incubator. As a next step, the detached cells were resuspended in 5 ml pre-warmed medium and their concentration was estimated.

The new culture flask was labeled and filled with 5 ml fresh, pre-warmed medium, incubated and aerated for the whole working process in the incubator. From the old culture flask one takes a sample of the cell solution that corresponds to  $2 \cdot 10^5$  cells per ml and the cell solution was transferred into a new flask.

### 2.5.1 Transient Transfection for Imaging, Lifetime and FRAP Measurements

For all measurements in living HEK293 cells, a transient transfection was always used. Therefore, 2 ml of cells were seeded in 35 mm Glass Bottom Culture Dishes, which are Poly-d-lysine coated (MaTek Corporation). For transient transfection 1  $\mu$ g of the plasmid-DNA was diluted in 200  $\mu$ l PBS. After adding 3  $\mu$ l TransFect transfection reagent (Thermo Scientific) to the dilution, the mixture was incubated for 20 minutes at room temperature. Afterwards, the cells were overlaid with the mixture and incubated for another 36 h to 48 h. Before measurements the cells were washed with PBS buffer to reduce the fluorescent background generated by the phenol red and the FBS.

### 2.5.2 Transient Transfection for FCS Measurements

For fluorescence correlation spectroscopy (FCS) measurements, 300  $\mu$ l of cells per well were seeded in eight-well Nunc™ Lab-Tek™ Chamber Coverglass with 1.0 borosilicate bottom (Thermo Scientific). 24 h after seeding, transient transfection was performed, by diluting 400 ng of the plasmid DNA per transfection (per well) in 30  $\mu$ l serum-free OPTI-MEM medium (Gibco). After adding 2.6  $\mu$ l Lipofectamine (Invitrogen™) reagent to the dilution, the mixture was incubated for 30 min at room temperature. In the meantime, the seeded cells were washed with 300  $\mu$ l of serum-free OPTI-MEM and subsequently left without any medium in the well. In each tube containing the lipid-DNA complexes, 120  $\mu$ l of serum-free OPTI-MEM was added. After gentle mixing, the diluted complex solution was added to the washed cells. Subsequently, the cells were incubated for 2 h before adding 150  $\mu$ l DMEM Fluoro Brite (Gibco) supplemented with 10 % fetal bovine serum and 1 % penicillin/streptomycin. 18 h to 24 h after start of transfection, the complete medium was replaced by DMEM Fluoro Brite (Gibco) with 5 % FBS and 1 % penicillin/streptomycin. Measurements were performed 36 h to 48 h after transfection.

### 2.5.3 Cell Treatment for Studies at Different Incubation Temperatures

The transient transfection for studies of living HEK293 cells at different incubation temperatures was done as described in 2.5.1. After transfection some cells were then incubated at 28 °C with 5 % CO<sub>2</sub> in DMEM medium and other cells under the usual experimental conditions (T = 37 °C). Experiments were always started 36 h after transfection.

### 2.5.4 Cell Preparation for pH Measurements

For the pH dependence measurements in living cells, the cultures were washed with PBS buffer at the desired pH and were then overlaid with 2 ml buffer. To improve the pH equilibration between cytoplasm and buffer ionophores were added. Ionophores are molecules, which increase the permeability of the plasma membrane for ions and lead to a collapse of the natural ion gradient and as a consequence to a pH shift. Two different types of ionophores were used. The first one is *Monensin*, which is an carrier for Na<sup>+</sup>/H<sup>+</sup>. The other one is *Nigericin* that exchanges the cations K<sup>+</sup>/H<sup>+</sup>. Measurements were always performed after 20 minutes incubation time.

# 3 Microscopy Techniques and the used Spectroscopic Setups

## 3.1 Introduction

Modern spectroscopy techniques provide a minimal invasive observation of the structure and organization of living organisms. Therefore, a wide range of different fluorescence microscopy techniques and detection systems are available. This chapter is partitioned in two main parts, a theoretical background and an experimental section. The theoretical section gives a short introduction about fundamental physical phenomena and their representations like fluorescence and the Jablonski scheme. The essential experimental methods for this work are also described in detail as time-correlated single photon counting (TCSPC), fluorescence correlation spectroscopy (FCS) and fluorescence recovery after photobleaching (FRAP). All the described spectroscopic setups are presented in detail with the common measurement settings.

## 3.2 Theoretical Background

### 3.2.1 Introduction

In order to observe the emission of fluorescence, a molecule must be transferred into an excited state as a prerequisite. This can occur by absorption of a photon, where the energy of the photon must satisfy the Bohr frequency condition:

$$\Delta E = E_A - E_G = h \cdot \nu = h \cdot \frac{c}{\lambda} \quad , \quad (3.1)$$

in which  $h$  is the Planck constant,  $\nu$  describes the frequency and  $\lambda$  the wavelength of the photon, and  $c$  stands for the light velocity. Thus, the energy of the absorbed photon corresponds to the energy difference ( $\Delta E$ ) between the two involved electronic states ( $E_A$ ,  $E_G$ ). A medium is irradiated with light of a suitable frequency so that light is partially absorbed. The amount of light, which is absorbed, is described

by the Lambert-Beer law. If a light beam of an initial intensity  $I_0$  passes a medium containing absorbing molecules at the concentration  $[c]$  and sample thickness  $d$  the following formula applies:

$$A = \ln \frac{I_0}{I} = \epsilon(\lambda) \cdot [c] \cdot d \quad . \quad (3.2)$$

Here,  $A$  describes the absorption,  $I$  the transmitted intensity and  $\epsilon(\lambda)$  the molar extinction coefficient. Furthermore, from the Beer-Lambert law the formula for the absorption cross section of a molecule is derived. This cross section is the virtual active area of a molecule, which describes the probability of the absorption of a photon:

$$\sigma(\lambda) = \frac{\epsilon(\lambda) \cdot 1000 \cdot \ln(10)}{N_A} \quad , \quad (3.3)$$

with  $N_A$  the Avogadro constant and  $\epsilon(\lambda)$  the molar extinction coefficient. The extinction coefficient depends on the excitation wavelength and indicates how efficiently the light is absorbed by a target molecule.

After optical excitation, the excited molecule relaxes to the ground state after a certain time. This can occur, for example by spontaneous emission of a photon. To illustrate the transitions that can take place in relaxation processes one uses the so-called Jablonski diagram (see Figure 3.1).

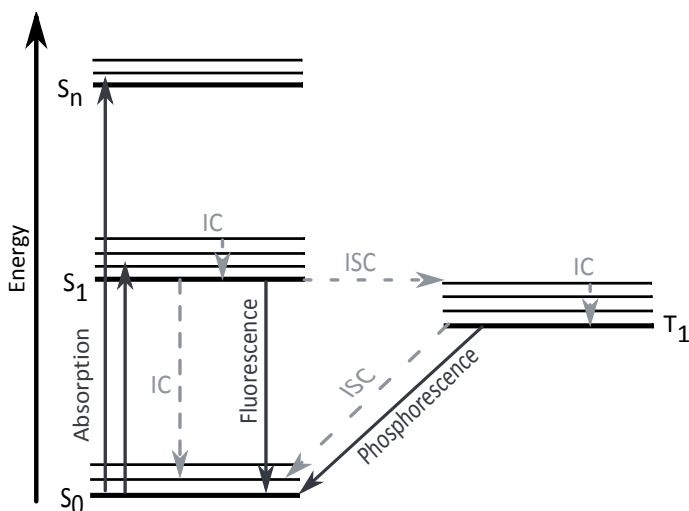


Figure 3.1: The Jablonski diagram shows the different electronic states of a molecule (singlet state S, triplet state T) with possible transitions between them. Radiative transitions are indicated by solid arrows in dark grey. Light grey dashed lines represent non-radiative transitions, such as intersystem crossing (ISC) and internal conversion (IC).

By absorption of a photon, the molecule is excited from the ground state  $S_0$  to a vibronic state of a higher energy singlet state  $S_1 - S_n$ . As these transitions occur within  $10^{-15}$ s, the assumption is made that the heavy nuclei do not change their relative position in the time scale of excitation during a transition. The equilibrium distance between the nuclei changes with some delay due to the inertia, because the ratio of electron mass to proton mass is 1 to 1800. The Franck-Condon principle assumes that the transition takes place without a shift in the nuclear coordinates

and thus is vertically in the diagram (compare with Fig. 3.1). In this case, the vibrational states of the electronic wave functions, which shows a high overlap with the ground state are preferably excited. Figure 3.2 illustrates the Frank-Condon principle more in detail.

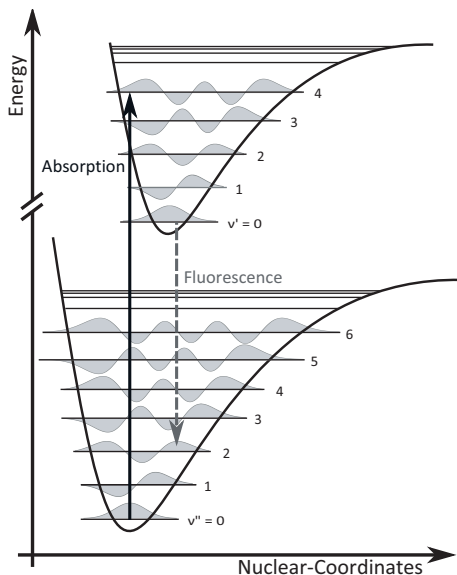


Figure 3.2: Scheme of the Franck-Condon principle. The vibrational levels of the electronic ground state and the first excited state as a function of the nuclear coordinates are plotted.

The electrons relax rapidly from the higher vibrational states to the energetically lowest vibrational level of the first excited singlet state  $S_1$  by generating heat. This is a non-radiative process and is known as internal conversion (IC). From this state, the electron can return to the ground state on different ways. Firstly, by fluorescence, also named spontaneous emission back to the singlet ground state  $S_0$ , but also by various non-radiative processes, such as intersystem crossing (ISC). Here, the electron relaxes in a radiation-less process from an excited singlet state to a lower energy triplet state under a spin flip. The electron can eventually return to the singlet ground state from the metastable triplet state by a reverse spin flip. This transition is referred to as phosphorescence and proceeds much slower than fluorescence. The lifetime of phosphorescence is in the range of milliseconds to seconds, because the relaxation from triplet to singlet under a spin reversal occurs only with a low probability. The lifetime of the triplet states is thus much longer than the lifetime of the singlet states. The Jablonski scheme (see Fig. 3.1) shows that the fluorescence emission has a lower energy compared to the absorption. This shift of the fluorescence transition to longer wavelengths is called Stokes shift.

Although the Jablonski diagram shows possible transition pathways, the probability of the different transitions has not been considered here yet. Probabilities are usually expressed by considering transition rates  $k$ , which indicate a likelihood per time unit. The fluorescence quantum yield  $\phi_f$  is specified when these transition rates are

known. The fluorescence quantum yield of a dye molecule describes the number of absorbed photons that are converted into fluorescence photons and is therefore a ratio of emitted to absorbed photons:

$$\Phi_f = \frac{\text{Number of emitted photons}}{\text{Number of absorbed photons}} = \frac{k_f}{k_f + k_w} \quad . \quad (3.4)$$

Here,  $k_f$  represents the rate of fluorescence emission and  $k_w = k_{IC} + k_{ISC}$  the rate of nonradiative deactivation of the first excited singlet state  $S_1$ . A quantum yield of 1 would mean that no nonradiative processes take place and the deactivation proceeds exclusively by fluorescence.

Another important parameter is the fluorescence lifetime  $\tau_f$ , which gives the average time between excitation to the first excited singlet state  $S_1$  of a molecule and relaxation to the ground state  $S_0$ . It is defined as follows:

$$\tau_f = \frac{1}{k_f + k_{IC} + k_{ISC}} \quad , \quad (3.5)$$

and therefore corresponds to the reciprocal value of the sum of the rate constants of the non-radiative transitions ( $k_{IC} + k_{ISC}$ ), and the rate of fluorescence emission  $k_f$ . If no non-radiative processes are present, the fluorescence lifetime  $\tau_f$  corresponds to the natural fluorescence lifetime  $\tau_0$ :

$$\tau_0 = \frac{1}{k_f} \quad . \quad (3.6)$$

In the ideal case, the fluorescence kinetics follows a mono-exponential decay function after excitation at  $t = 0$  by a short light pulse. This can be written as:

$$I(t) = I_0 \cdot e^{-\frac{t}{\tau_f}} \quad , \quad (3.7)$$

where  $I_0$  correspond to the intensity at time  $t = 0$ . The lifetime  $\tau_f$  thus corresponds to a decrease in the initial intensity to  $1/e$  of its initial value. Since most of the biological systems are much more complex and can not be described by a single exponential deactivation kinetics, multi-exponential models have to be assumed.

### 3.2.2 Wide-field and Confocal Fluorescence Microscopy

The most conventional and oldest microscopy technique is the wide-field microscopy. A scheme of the optical pathway of a wide-field fluorescence microscope is illustrated in Figure 3.3. The sample is excited by a laser or Hg lamp in a large area typically

in a range between some square micrometers up to millimeters by a collimated light beam. This can be achieved by focusing the excitation beam on the back focal plane of the objective as depicted in Fig. 3.3.

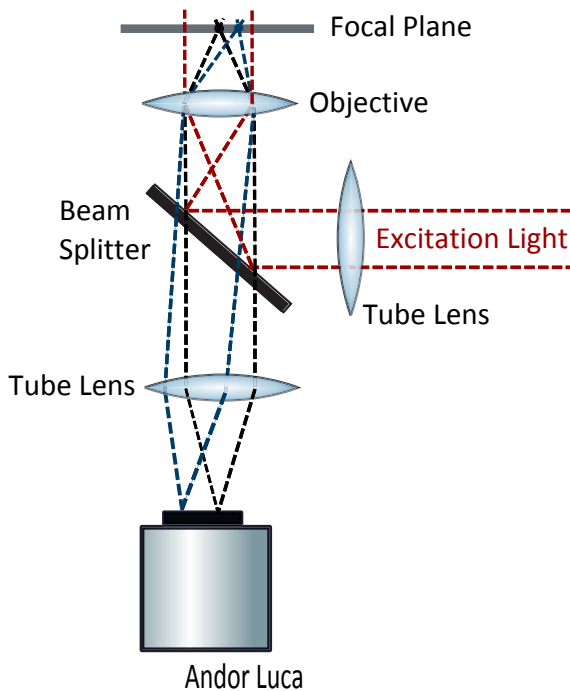


Figure 3.3: Scheme of the optical pathway of a wide-field fluorescence microscope. The dashed blue line shows the effect, when the observed signal is shifted from the optical axis.

With this technique, only two-dimensional structures can be resolved. Structures that are located outside the focal plane of the objective are no longer sharply projected on the detector plane, but lead to an increase in the fluorescence background and blurred images result. This microscopy method is common for studies with sensitive biological samples that can not be illuminated with high laser intensities and also for simple imaging procedures.

Later on in 1955, the method of confocal fluorescence microscopy was developed by Marvin Minsky [76] and extended in the last years to commercially available confocal scanning microscopy systems. This technology is becoming increasingly important, since it gives the opportunity to observe individual molecules and allows for the observation of small structures in biological organism. It offers in contrast to the conventional wide-field microscopy several advantages, such as the suppression of the background fluorescence by reducing the focal volume and therefore an increase in resolution for imaging. Roughly speaking, the two methods differ in the type of excitation and detection. In the confocal microscopy, only a diffraction-limited spot in the sample is mostly excited by focusing the light beam with an objective. This gives the possibility to get a better discrimination along the optical axis of the spatial distribution of the fluorescence signal and to increase the lateral resolution.

The obtained three-dimensional resolution is described as follows:

$$\Delta r_{\text{FWHM}} = \frac{\lambda}{2n \sin \alpha} \quad (\text{axial resolution}) \quad (3.8)$$

$$\Delta z_{\text{FWHM}} = \frac{\lambda}{n \sin^2 \alpha} \quad (\text{lateral resolution}). \quad (3.9)$$

Thereby  $n \cdot \sin \alpha = NA$  corresponds to the numerical aperture of the used objective,  $\alpha$  corresponds to the half angle of the light cone, which is acquired by the objective and  $n$  is the refractive index of the medium in front of the first lens of the used objective. Furthermore,  $\lambda$  describes the used wavelength [77].

The principle of a confocal fluorescence microscope is illustrated in Figure 3.4. A laser is used as light source and a focused beam in the sample is realized by an objective with a high numerical aperture. The same lens collects the resulting fluorescence light, which can be then separated by a dichroic beam splitter from the excitation light. Afterwards, the light passes through the tube lens, which focuses the fluorescent light in the intermediate image plane of the microscope. There, a pinhole is placed, which blocks fluorescence signals that do not originate from the focal plane, of the detection path. Behind the aperture, a detector is placed, which generates an electric signal according to the intensity of the light signal. This optical system generates an observation volume of about 1 fL, which offers the possibility to measure the diffusion of single molecules in solutions up to several hundredths nanomolars.

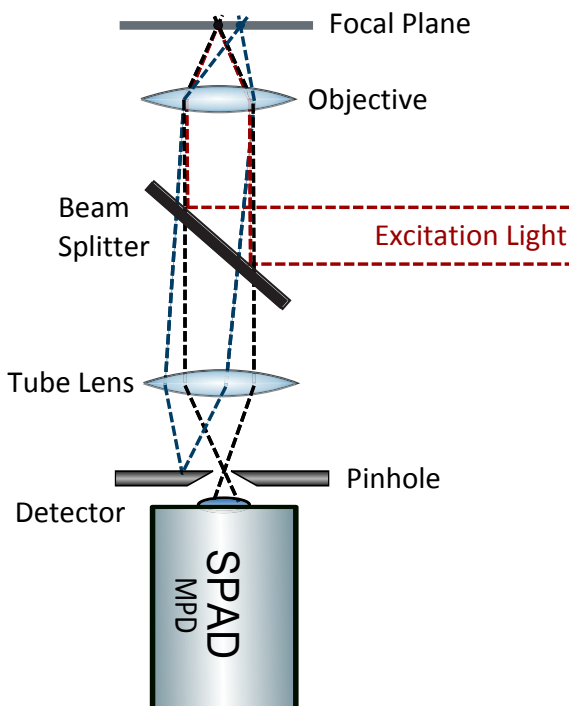


Figure 3.4: Scheme of the light beam path from a confocal microscope. The dashed blue line shows the effect, when the observed signal is shifted from the optical axis.

The observation volume consists of the product between the excitation and the detection volumes. The excitation volume is described by the laser beam profile (FWHM) and is collimated to a diffraction limited spot by the used objective. The detection volume depends on both, the size of the pinhole used, as well as the magnification of the objective. The observation volume is usually approximated by a three-dimensional Gaussian profile and the spatial distribution of the observation volume is then described as:

$$w(x, y, z) = e^{\left(-2\frac{(x^2+y^2)}{w_0^2}\right)} \cdot e^{\left(-2\frac{z^2}{z_0^2}\right)} \quad . \quad (3.10)$$

The different dimensions of the confocal volume in the  $w_0$  radial (xy-plane) and  $z_0$  axial (z-axis) directions must be considered in which the excitation intensity has dropped to  $1/e^2$ . The result is an ellipsoidal observation volume, which is simply calculated by rewriting the equation in cylindrical coordinates and integrating.

$$V = \frac{4}{3} \cdot \pi \cdot z \cdot \frac{d^2}{4} \quad (3.11)$$

Here,  $z$  corresponds in a first approximation to the FWHM in the axial direction, and  $d$  is approximately the ratio of the diameter of the aperture used and the magnification factor of the lens.

### 3.2.3 Time-Correlated Single Photon Counting

The method of time-correlated single photon counting (TCSPC) allows for the direct measurement of the fluorescence lifetime. In this process the sample is excited by short laser pulses with high repetition frequencies  $>1\text{MHz}$  and only the arrival time of the first incoming fluorescence photon is measured. Since only one incoming photon can be measured by the electronics, only low laser excitation intensities are required. All other photons that reach the detector during the same pulse are discarded, due to the dead-time of the system. If several photons could reach the detector within one cycle of excitation, it leads to the pile-up-effect, which shortens artificially the measured fluorescence kinetics.

The working principle of SPC is shown in Fig. 3.5. The first incoming photon starts the time-to-amplitude-converter (TAC), which will be stopped by the next incoming excitation pulse. The TAC output gives a voltage pulse which is proportional to the time delay between the first arrival of a photon and the stopping laser pulse. This analog signal is then converted to a digital value by an analog-to-digital converter (ADC) and accumulated in a histogram. This measurement process is repeated until

the signal-to-noise ratio (see equation 3.21) is sufficiently high. The measured frequency distribution of the time periods occurring between excitation and detection of a photon corresponds to the fluorescence kinetics. For more details see [78, 79].

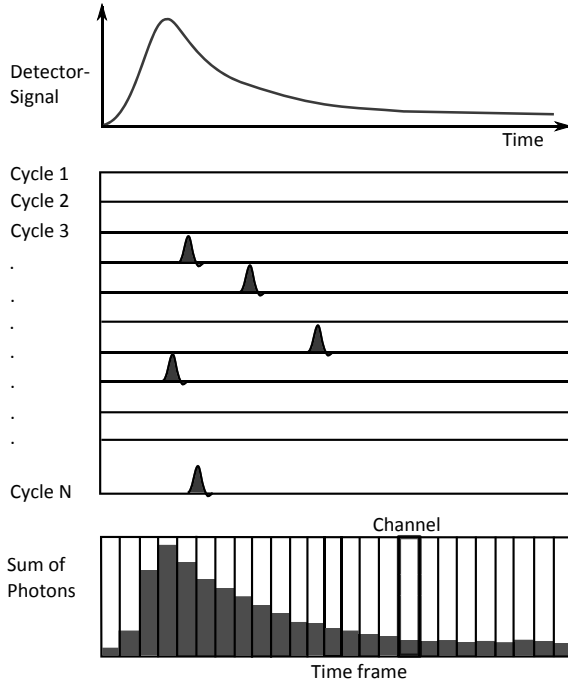


Figure 3.5: Working principle of time-correlated single photon counting (TCSPC) measurements. The photon arrival times of multiple cycles are summed up in a histogram (reconstructed from [80]).

The number of measured photons in a given time channel is a statistical value. The probability distribution around the expected value is following a Poisson distribution. The probability for the arrival of  $l_i$  photons in the time interval  $t_i$  is given by:

$$p_{l_i} = \frac{(z_i)^{l_i}}{l_i!} \cdot e^{-z_i} \quad \text{mit} \quad \sum_{l_i=0}^{\infty} p_{l_i} = 1 \quad . \quad (3.12)$$

Thereby  $z_i$  corresponds to the expected number of measured photons at time  $t_i$ . The probability for a certain number of incident photons  $l_i$  in the time interval  $t_i$  can then be specified as the following:

$$p_{0_i} = e^{-z_i} \quad (3.13)$$

$$p_{1_i} = z_i \cdot e^{-z_i} \quad (3.14)$$

$$p_{l_i > 1} = 1 - p_{0_i} - p_{1_i} = 1 - (1 + z_i) \cdot e^{-z_i} \quad . \quad (3.15)$$

Now the total number of photon events  $N_i$  in the time interval  $t_i$  is determined by equation 3.15. If the measurements were done over a time period  $t$  with a repetition frequency  $f$ :

$$N_i = ft(p_{1_i} + p_{l_i > 1}) = ft(1 - e^{-z_i}) \quad . \quad (3.16)$$

In the limiting case that the average number of fluorescence photons  $z_i$  in the time interval  $t_i$  is much smaller than 1, the probability values are approximated by

$$p_{0_i} \approx 1 - z_i \quad (3.17)$$

$$p_{1_i} \approx z_i \quad (3.18)$$

$$p_{t_i > 1} \approx z_i^2 \approx 0 \quad . \quad (3.19)$$

It follows with approximation  $z_i \ll 1$  for the total number of photon events  $N_i$  in the time interval  $t_i$ :

$$N_i \approx ftz_i \quad . \quad (3.20)$$

Thus, the average number of incoming photon events after a time period  $t$  in the time interval  $t_i$  is approximately proportional to the expected total number of photons emitted in this time interval.

The time-correlated single photon counting technique is also characterized by a large signal-to-noise ratio (SNR), which has the advantage to work with low intensities, whereby the light pollution is minimized on the sample. This can be described using the following formula:

$$SNR = \sqrt{N_i} \quad , \quad (3.21)$$

where  $SNR$  is the signal-to-noise ratio and  $N_i$  is the number of photons in the  $i$ -th time channel.

### 3.2.4 Fluorescence Correlation Spectroscopy

Fluorescence correlation spectroscopy (FCS) was developed in the 70s of the last century by E. Elson and W. Webb [12]. It is a measuring method, which obtains information from fluctuations of the fluorescence intensity. Furthermore, it gives the opportunity to observe dynamic processes of individual molecules, which can be caused by various phenomena. Firstly, photophysical processes, such as inter-system crossing (ISC) or changing the quantum yield from quenching effects due to conformational changes are observed. Another reason for fluctuations may be local variations in the fluorophores concentration which occur from diffusing particles through the observation volume element.

To describe a FCS measurement the autocorrelation function  $G(\tau)$  is used, see equation 3.22. It describes the correlation of the fluorescence signal at different times and is a product of the intensity at the time  $t$ ,  $F(t)$ , and the intensity after a delay

time  $\tau$ ,  $F(t + \tau)$ , averaged over a large number of measurements and weighted by the average square of the total fluorescence.

$$G(\tau) = \frac{\langle F(t)F(t + \tau) \rangle}{\langle F^2 \rangle} = 1 + \frac{\langle \delta F(0)\delta F(\tau) \rangle}{\langle F^2 \rangle} \quad (3.22)$$

In this case, the time  $t$  describes the current time at which the intensity is measured, and it may range from seconds to minutes. The delay time  $\tau$  is the difference in real time between measurement of  $F(t)$  and  $F(t + \tau)$ . It is usually in the range of  $10^{-2}$  ms to  $10^2$  ms. The fluorescence fluctuation  $F(t)$  describes the averaged fluorescence signal of a large number of molecules, which diffuse through the confocal volume element. If the average intensity is irrespective of the delay time  $\tau$ ,  $\langle F(t) \rangle = \langle F(t + \tau) \rangle$  and the autocorrelation function is then  $G(\tau) = 1$ . The fluorescence signal is then said to be uncorrelated.

Thereafter, the experimentally obtained autocorrelation curves have to be compared to a theoretically predicted autocorrelation function to identify an appropriate model. The three-dimensional autocorrelation function for dye molecules, which diffuse freely through the confocal volume element is shown in equation 3.23 [81, 82].

$$G_{3dim}(\tau) = \frac{1}{N} \cdot \left[ 1 + \frac{\tau}{\tau_D} \right]^{-1} \cdot \left[ 1 + \frac{\tau}{S^2 \cdot \tau_D} \right]^{-1/2} \quad \text{with} \quad S = \frac{z_0}{r_0} \quad (3.23)$$

The first term describes the average number of molecules  $N$  in the observation volume.  $\tau_D$  corresponds to the characteristic decay time of the correlation function. If  $\tau_D$  can only be determined by the residence time of molecules in the excitation volume then it corresponds to the diffusion time, i.e. the time required for a molecule to pass through the observation volume element.

$$\tau_D = \frac{r_0^2}{4 \cdot D} \quad (3.24)$$

$\tau_D$  depends on the diffusion coefficient  $D$  and the extension of the excitation volume in the radial direction  $r_0$ .

In order to describe the observation volume element (OVE) for FCS measurements the geometrical volume of an ellipsoid is no longer used (see section 3.2.2), but rather the effective volume, see eq. 3.25. The effective volume depends strongly on the detection volume and is larger than the geometric volume [83].

$$V_{eff} = \pi^{\frac{3}{2}} \cdot z_0 \cdot r_0^2 \quad (3.25)$$

Here,  $r_0$  stands for the expansion in radial direction (perpendicular to beam axis) and  $z_0$  for the axial component. Both components are given by the  $1/e^2$  radius of the Gaussian intensity profile, which has to be accurately determined by calibration measurements. The ratio  $S = z_0/r_0$  is defined as structure parameter, which describes the geometry of the focus.

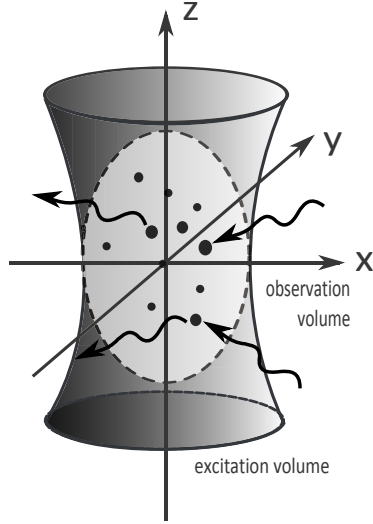


Figure 3.6: Scheme of a confocal volume element with freely diffusion molecules.

In the case of two-dimensional diffusion (like in a planar membrane), the square root term in eq. 3.23 is not present, since the exit pathway out of the plane is no longer available to the molecules, which yields:

$$G_{2dim}(\tau) = \frac{1}{N} \cdot \left[1 + \frac{\tau}{\tau_D}\right]^{-1} = \frac{1}{N} \cdot \left[1 + \frac{4 \cdot D\tau}{r_0^2}\right]^{-1} . \quad (3.26)$$

In both cases, the intercept of  $G(\tau)$  at  $\tau = 0$  is equivalent to the reciprocal of the mean number of molecules  $N$  in the OVE. The concentration of the fluorophore can be determined almost exactly by the amplitude of the autocorrelation function at the time point  $\tau = 0$ , if the geometry of the OVE is precisely known. Equation 3.27 shows the relationship between OVE,  $G(0)$ , and the average concentration of molecules  $\langle C \rangle$ .

$$G(0) = \frac{1}{N} = \frac{1}{V_{\text{eff}} \cdot \langle C \rangle} \quad (3.27)$$

That means that the amplitude is inversely proportional to the sample concentration. This can be explained by stronger fluctuations at lower concentrations resulting from molecules passing the focal volume than for higher numbers of molecules.

The diffusion coefficient  $D$  can be derived from the Stokes-Einstein equation:

$$D = \frac{k_B \cdot T}{6 \cdot \pi \cdot \eta \cdot R_{hyd}} \quad , \quad (3.28)$$

where  $k_B$  is the Boltzmann constant,  $T$  the absolute temperature,  $\eta$  the dynamic viscosity of the solvent and  $R_{hyd}$  the hydrodynamic radius of the diffusing molecule.  $R_{hyd}$  is proportional to the cubic root of the particle volume, that is in turn proportional to the mass and hence also to the molecular weight [83].

Equation 3.23 and 3.26 assume that no change of the fluorescence properties of the fluorophore during the passage through the confocal volume element are present. This is no longer true for most dyes and especially at high excitation intensities as used in confocal illumination schemes. A common reason for the change in the fluorescence properties is the ISC transition to the first excited triplet state. This process is quantum mechanically forbidden, and accordingly the relaxation of this triplet state to the ground state takes a long time. During this time, the dye can not emit any fluorescence and is, therefore, no longer available for the measurement. This effect must be taken into account in the autocorrelation function. So the function is extended by a triplet term, which leads to a modified autocorrelation function for three- and two-dimensional diffusion:

$$G_{3dim}(\tau) = \frac{1}{N} \cdot \left[1 + \frac{\tau}{\tau_D}\right]^{-1} \cdot \left[1 + \frac{\tau}{S^2 \cdot \tau_D}\right]^{-1/2} \cdot \left(1 + \frac{T}{1-T} \cdot e^{-\tau/\tau_T}\right) \quad (3.29a)$$

$$G_{2dim}(\tau) = \frac{1}{N} \cdot \left[1 + \frac{\tau}{\tau_D}\right]^{-1} \cdot \left(1 + \frac{T}{1-T} \cdot e^{-\tau/\tau_T}\right) \quad . \quad (3.29b)$$

Where  $T$  denotes the relative proportion of the molecules in the triplet state. These molecules do not generate any fluorescence signal and the data thus tend to a lower sample concentration, resulting in a higher amplitude  $G(0)$ . Furthermore,  $\tau_T$  denotes rapid fluctuations, which result from the transition to the triplet state and typically results in a shoulder of the autocorrelation curves at short correlation times  $\tau$ .

### 3.2.5 Fluorescence Recovery after Photobleaching

A further very common microscopy technique to measure the diffusion of fluorophores, binding interaction and mobility in living cells is the method of fluorescence recovery after photobleaching (FRAP). It has been established in the 70s of the last century [23, 84]. For the original FRAP technique, an epi or wide-field

fluorescence microscope was used to focus an excitation beam to a small spot (about  $1\ \mu\text{m}$ ) in a region of interest (ROI) in the cell (see Fig 3.7). This beam is used both for the bleaching of the molecules in the region of interest at  $t = 0$ , as well as to probe the fluorescence signal in the same region (prebleach ( $t < 0$ ) and postbleach ( $t > 0$  up to  $t = \infty$ )). This technique was utilized to observe the diffusion of fluorescent molecules in the bleached region and thereby to determine the diffusion coefficient  $D$ . This has been especially designed for the investigation of diffusion processes in the membrane [85, 86].

Since the 90s, FRAP technique was getting more popular, because of the introduction of confocal laser scanning microscopes (CLSM), which are more user-friendly and also accessible for non-specialists. More details about confocal microscopy are provided in section 3.2.2. In addition, commercial CLSM systems offer the advantage that they allow for a fast switch between bleach and monitor modes, which results in more accurate recovery curves.

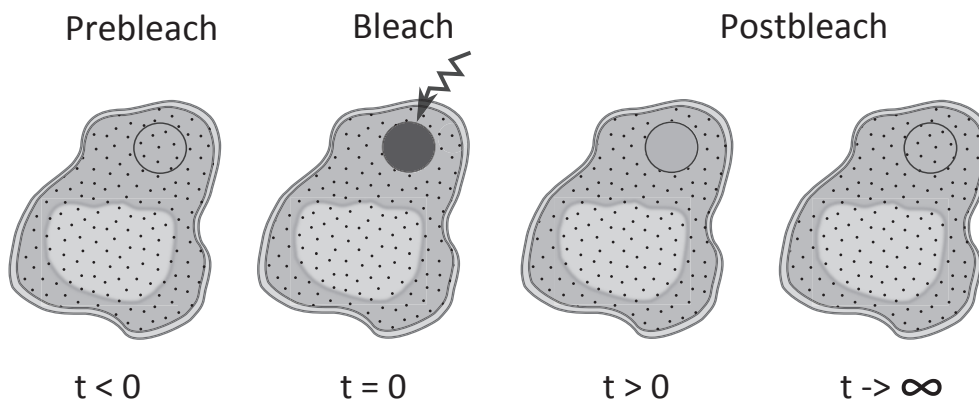


Figure 3.7: Schematic representation of a common FRAP experiment with an intense laser beam in a living cell.

FRAP experiments consists of three steps (see Fig. 3.7 and Fig. 3.8). In the first step the fluorescence before bleaching in the region of interest is monitored at a low laser intensity (prebleach,  $I_I$ ). In the next step, the fluorescent molecules in a small spot are bleached with a high power excitation beam ( $t = 0$ ). Usually the used spot has a size of a few micrometers to tens of micrometers in diameter. This bleaching process leads to a local concentration gradient in this area and causes bleached molecules to diffuse out from the ROI and fluorescent molecules from other regions to diffuse into the bleached area. This diffusion ( $t > 0$ ) is observed after the bleaching process, i.e. postbleach, with low laser excitation intensity. A typical fluorescence recovery curve is constructed by plotting the fluorescence intensity  $I(t)$  of the ROI as a function of time  $t$ , as seen in Fig. 3.8. In this case, the bleaching time is defined as time zero ( $t = 0$  with  $I_0(0)$ ). By properly fitting of the measured recovery the diffusion coefficient  $D$  of the fluorescently labeled molecules can be determined in the considered area.

Since not all molecules are mobile in the cell, the recovery of the fluorescence usually is not complete and the fluorescence intensity prebleach value  $I_I$  will not be reached ( $I_\infty$ ) again. The difference of  $I_I - I_\infty$  describes the fraction of immobile molecules in the ROI during the experiment, which can not be replaced by intact fluorescent molecules. Thus, the fraction which is located under the curve  $I(t)$ , stands for the mobile fraction of molecules in the observed area. FRAP measurements as a result offer the possibility to determine the local mobile and immobile fractions.

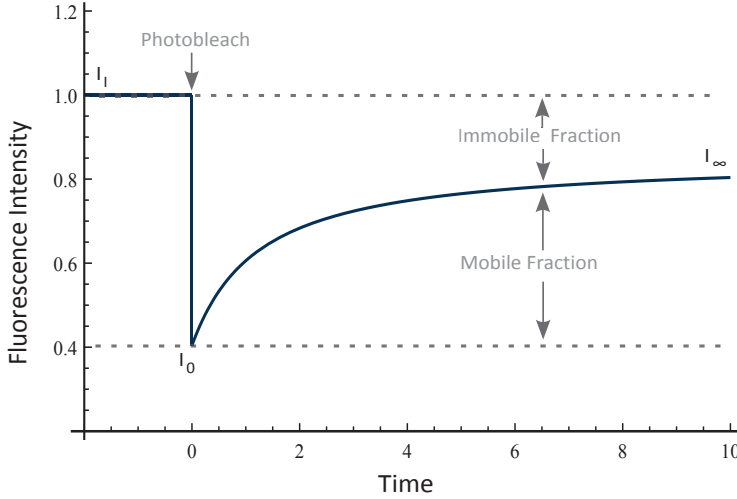


Figure 3.8: Typical monitored fluorescence recovery curve before ( $I_I(t)$ ) and after bleaching ( $I_\infty(t)$ ) in a region of interest over the time  $t$ .

A simple equation that is often used to determine the amount of the mobile fraction ( $M$ ) and the diffusion constant  $D$  from quantitative FRAP data are given in eq. 3.30.

$$M = \frac{I_\infty - I_0}{I_I - I_0} \quad (3.30)$$

$I_\infty$  indicates the fluorescence in the ROI after full recovery,  $I_I$  denotes the fluorescence before bleaching and  $I_0$  just after bleaching. In order to calculate the diffusion constant  $D$  the formula described by Axelrod *et al.* [23] could be used in the case of a small bleached spot in a two-dimensional area like the plasma membrane.

$$\tau_D = \frac{r^2 \cdot \gamma}{4 \cdot D} \quad (3.31)$$

In this equation  $r$  is the radius of the bleached spot,  $\gamma$  is introduced as a correction factor for the amount of bleaching and  $\tau_D$  is the diffusion time. For three dimensional diffusion, the equations are much more complex. All FRAP experiments are based on this approach, but the data analysis varies widely in the literature [24–29].

## 3.3 Experimental Setups

### 3.3.1 Multiparameter Microscopy Setup

Biophysical investigations on living cells require complementary experimental techniques to fully characterize complex protein interactions. The setup used for the measurements performed in this work combines suitable time-, wavelength-, and spatially resolved fluorescence techniques for different applications. It allows to switch between wide-field fluorescence lifetime imaging microscopy (FLIM), time-correlated single photon counting (TCSPC) in confocal mode and also fluorescence correlation spectroscopy (FCS).

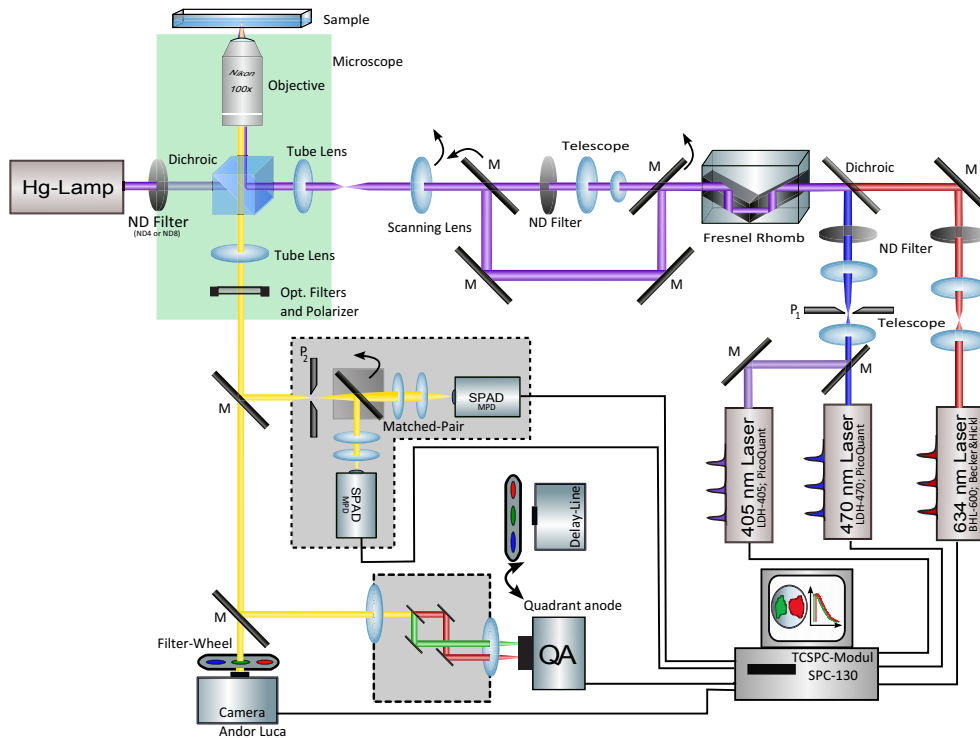


Figure 3.9: Scheme of the whole fluorescence microscopy setup

The setup based on a Nikon TI Eclipse microscope is arranged with different pulsed diode lasers for the excitation (LDH-405 and LDH-470 from PicoQuant Berlin; BHL-600 from Becker & Hickl Berlin), which are collimated by a telescope, consisting of two convex lenses to ensure an optimal illumination of the sample and the excitation pathway cleaned spatially with a 30  $\mu\text{m}$  pinhole (P1). The optics is designed in a way to allow fast switching between confocal and wide-field illumination. For wide-field illumination it is also possible to excite the samples with a mercury lamp. In addition the setup is equipped with several fully automated optical add-ons to switch between different operation modes (see Fig. 3.9) and detectors.

For imaging with wide-field or confocal illumination, the setup is equipped with an Andor Luca R<sup>EM</sup> Camera, which is an electron multiplying CCD camera (EMCCD). The peak quantum efficiency of the photo detector is 65 % at 600 nm. The camera has a pixel size of 8  $\mu\text{m}$  x 8  $\mu\text{m}$  with 1004 (H) x 1002 (V) active pixels and a maximal frame rate of 124 frames per second.

For TCSPC and FCS measurements, the detection pathway is equipped with a 50  $\mu\text{m}$  pinhole (P2) in the image plane to block fluorescence light out of the focal region enhancing the axial resolution. Afterwards the emission light is focused on a Single-Photon-Avalanche-Diode (SPAD). The used SPAD (MPD; Bolzano; Italy) has a quantum efficiency of approximately 40% and a time resolution of about 35 ps (FWHM). The setup offers the possibility for cross-correlation spectroscopy by using a second SPAD (Fig. 3.9). Data acquisition and processing is done with a SPC130 measuring board from Becker & Hickl Berlin [78].

For FLIM measurements with wide-field illumination the microscopic setup is equipped with a novel quadrant anode (QA) single photon counting detector with high photon throughput (up to  $2 \cdot 10^6$  counts per second) and very low noise ( $< 10$  photons/sec) for ultra sensitive wide-field observations with high temporal- and spatial resolution. The detector offers an active area of 25 mm with a spatial resolution of  $< 40 \mu\text{m}$  FWHM. The time resolution is  $< 49$  ps FWHM with a dead time of  $< 400$  ns.

The presented setup is capable of switching between several microscopic techniques, and therefore it is suitable to measure a wide range of optically accessible properties of molecular complexes with only small changes in the setup. From this data, structural parameters are gathered to achieve a comprehensive characterization of the sample. Dynamical processes after direct manipulation of the sample are analyzed in relation to the underlying functional mechanisms covering several orders of magnitude in time and therefore to obtain the possibility to observe the temporal dynamics (s-resolution) of the fluorescence decay time (ps-resolution) and fluorescence intensities in living samples.

#### 3.3.2 The PML-16C Setup for Lifetime Studies and Emission Measurements

The PML-16C setup is useful to measure fluorescence lifetimes at different emission wavelengths and temperatures. It can measure lifetimes using the time-correlated single photon counting (TCSPC) technique. For excitation different pulsed lasers are available. Mostly, the diode laser (LDH-470 from PicoQuant; Berlin; Germany)

with 470 nm was used as excitation wavelength, which has a repetition frequency of 8 MHz and a pulse duration of around 90 ps FWHM. The laser beam is focused by a lens on the sample contained in a holder and excites the fluorescence. In most cases, the sample holder consists of a quartz cuvette, while a glass tube is used only for temperature-dependent measurements. The emitted fluorescence light is collected by a lens in a 90 ° angle with respect to the excitation beam. Thus, excitation light transmitted or reflected by the sample is strongly suppressed. The whole setup is shown in Figure 3.10.

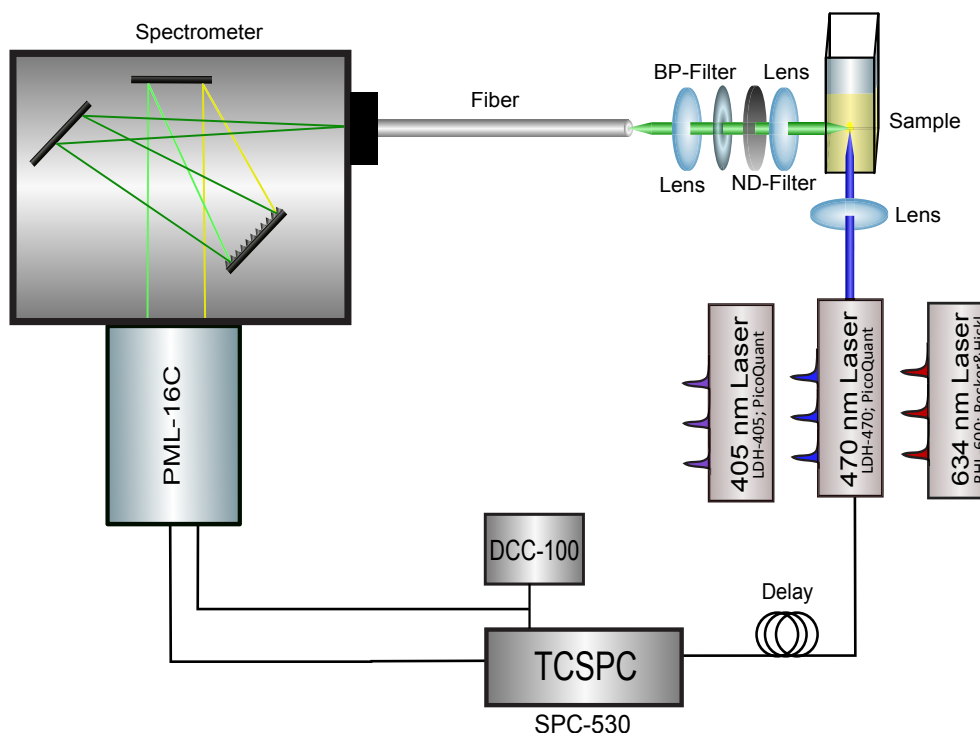


Figure 3.10: The PML-16C setup with the different available lasers is shown.

By means of a further lens, the gathered fluorescence light can be focused on the entrance slit of a monochromator or coupled to it by an optical fiber. Between the two lenses, grey filters for intensity attenuation or long-pass filters for removal of the excitation laser stray light from the beam path can be introduced.

For detection of time-resolved spectra, a commercial PML-Spec (Becker& Hickl; Berlin) is utilized, which is composed of a spectrometer and a PML-16C detector. Depending on the grid used the spectrometer delivers a spectral resolution of 6.25 nm, 12.5 nm or 25 nm. The PML-16C consists of a 16 channel multi-anode photo-multiplier-tube with 16 separate output elements (R5900; Hamamatsu) and a cathode dynode system for signal gain. It is controlled by a DCC-100 controller (Becker& Hickl; Berlin) that provides the power supply voltages and the shut off at the overload of the detector. The PML-16C is connected to a SPC530 measuring board (Becker& Hickl; Berlin), which provides the whole signal processing. For more

details about single-photon counting see also section 3.2.3 and [78–80].

For temperature dependent studies, a home-built variable-temperature cryostat (10 K-300 K, CTI-Cryogenics 8001/8300) as mobile cryostatic system was used for controlling sample temperature. The sample temperature was adjusted in the range between 10 K and 300 K. For more details see [87].

For steady state emission measurements, the PML-16C was replaced by a fiber-coupled CCD-spectrometer (BLACK-Comet-C Spectrometer; StellarNet). The spectrometer consists of a grating (590 grooves/mm), which enables detection in the spectral range from 185 nm up to 850 nm. Depending on the slit width at the entrance of the spectrometer, a spectral resolution between 0.75 nm and 6 nm was obtained. As detector a Sony ILX511 CCD-Chip (Sony) with 2048 pixels was used. Data acquisition was done with the software SpectraWiz<sup>®</sup> (StellarNet).

### 3.3.3 ConfoCorr3 Setup for Confocal Fluorescence Microscopy and FCS

Confocal imaging and FCS measurements were performed using a 510 META Laser Scanning Microscope equipped with a ConforCor 3 system (Carl Zeiss, Jena, Germany) as described in [88, 89]. For imaging and FCS, the cw ArKr laser intensity was set to 50 % of the 30 mW maximum power, and further attenuated by an Acousto Optic Tunable Filter (AOTF) to the indicated value. A 40x (1.2W) water-immersion objective (C-Apochromat, Carl Zeiss) was used throughout. Dreiklang-labeled samples were excited using the 514 nm laser line. The excitation light was separated from the fluorescence emission by a HFT 485/514 main dichroic beam splitter (Carl Zeiss), and the resulting emission passed a 530 nm long pass filter before detection by an avalanche photodiode. For imaging, the laser attenuation was set to 10 %, yielding 40  $\mu$ W at the objective lens. For eGFP-labeled cells, the 488 nm laser line was used and attenuated by AOTF to 2 % of the maximum intensity, yielding 12  $\mu$ W power after the objective. The main dichroic beam splitter HFTKP 700/488 was used to separate the incident and emitted light, and a 505 nm long pass filter was used to collect the fluorescence signal.

For FCS measurements in living HEK293T cells, the laser intensity was set to 0.5 % up to 0.7 % to avoid destruction of the sensitive biological material. FCS data were collected through a 70  $\mu$ m pinhole (PH70) in front of the avalanche photodiode. Only in some characteristic experiments, the pinhole size was varied (between 70  $\mu$ m and 280  $\mu$ m, e.g. 80  $\mu$ m denoted by PH80) in order to ascertain whether the characteristic decay time of the correlation function is changing or not, and to

distinguish if the fluctuations in fluorescence intensity are generated by molecular diffusion or by a kinetic process. Furthermore, the intensity of the laser was changed for some characterization measurements between 0.5 % and 4 %. Laser intensity at a given wavelength ( $I_\lambda$  in  $\mu\text{W}$ ) was measured after the objective lens and scaled linearly with the attenuation ( $\text{atn} = 0 - 100$ ),  $I_{488} = 5.76 \cdot \text{atn}$  and  $I_{514} = 3.96 \cdot \text{atn}$ . All experiments were carried out at 22 °C.

### 3.3.4 TCS SP5 Setup for Confocal Fluorescence Microscopy and FRAP

Fluorescence recovery after photobleaching and confocal image series were taken using a Leica TCS SP5 II microscope and LAS AF acquisition Software (Leica Microsystems; Wetzlar; Germany). The confocal scanning microscope was equipped with an 63x water-immersion objective with a numerical aperture ( $NA$ ) of 1.4. For image series a cw Ar laser was used and the laser intensity was set to 25 mW of the 30 mW maximum power in focal plane. For cells expressing Dreiklang (DRK), the 514 nm argon line was used for monitoring ( $I = 8 \%$  to  $11 \%$ ) and bleaching ( $I = 100 \%$ ). Experiments on eGFP-labeled samples were always performed using the 488 nm laser line ( $I = 6 \%$  to  $10 \%$  or  $100 \%$ ). The utilized emission range of the detectors was set between 520 nm and 600 nm suitable for Dreiklang and 500 nm up to 600 nm suitable for eGFP.

Reversible FRAP measurements were performed using an upright TCS SP5 with LAS AF Software (Leica Microsystems; Wetzlar; Germany) confocal scanning microscope with a 20x water-immersion objective with a  $NA$  of 1.0. For excitation of the DRK-labeled samples, the 514 nm argon laser line ( $I = 8 \%$  to  $11 \%$  of the full intensity) was used. For the OFF-switching process (see therefore section 2.3) instead of bleaching a 405 nm laser diode ( $I = 100 \%$ ) was chosen.

FRAP image series were recorded using the Leica FRAP Wizard of the Leica TCS NT Software with an image size of (1024 x 128) pixels and 1400 Hz acquisition speed. A focused single laser shot representing a diffraction-limited spot was chosen as bleaching pulse. Alternatively, the fluorescence of a region of interest (ROI) was bleached with a single 50 ms laser scan at 100 % laser intensity. Prebleach and postbleach image sequences were acquired with 7 % up to 11 % laser intensity (Gain 100 %) depending on fluorescence intensity of the cell. Prebleach image series consists of 10 images taken every 0.112 s. Postbleach image sequences were composed of 750 images taken every 0.112 s and followed by 100 images taken every 0.52 s using 2x line-averaging and bidirectional scanning.

A whole FRAP series took about 137 s and was performed for more than 10 cells per construct. The reversible FRAP studies with DRK consist also of an 860 image sequence, but images were acquired every 0.099 s instead of 0.112 s, which leads to a total duration of around 127 s per sequence. The bleaching / OFF-switching (see section 2.3) was performed with a single 5 ms bleach at 100 % laser intensity. All experiments were carried out at room temperature.

# 4 Expression Studies on the Na,K-ATPase FHM2 Mutation P979L at Different Incubation Temperatures

## 4.1 Introduction

The physiological importance of Na,K-ATPase is underlined by the fact that mutations in the genes coding for Na,K-ATPase isoforms lead to severe human pathologies like familial hemiplegic migraine (FHM), alternating hemiplegia of childhood (AHC) rapid dystonia parkinsonism (DYT12) or epilepsy (as described in more detail in section 2.2.3). Many of the reported mutations lead to loss-of-function effects, whereas others do not largely change the function of the enzymes but lead e.g. to reduced protein stability, reduced protein expression or defective cellular localization.

Whereas most mutations identified in FHM2 (and RDP or AHC as well) lead to distinct functional changes of the Na,K-ATPase that converge on the notion of a loss-of-function effect, several FHM2 mutations fail to exhibit functional alterations when assayed in a particular type of cells [3]. This is especially true for the FHM2 mutation P979L, that shows no functional changes in electrophysiological or biochemical experiments using *Xenopus laevis* oocytes as expression system. However, it turned out that the enzyme P979L is thermodynamically less stable in transfected mammalian cells (grown at 37 °C) than in frog oocytes (cultivated at 20 °C) [3]. Thus, in order to completely address all possible reasons for pathophysiological effects upon Na,K-ATPase mutations in humans, functional studies must not only include electrophysiological and biochemical experiments in various relevant cell models, but should also try to assess effects regarding cellular quality control mechanisms,  $\alpha$ -/ $\beta$ -subunit assembly, plasma membrane targeting, protein degradation, protein phosphorylation and importantly interactions with other proteins that might interfere with the aforementioned processes. Two major points on this

list, which have not been scrutinized thoroughly yet are the determinants of plasma membrane targeting as well as the influence of temperature on this process and processes that are critical for the recruitment of Na,K-ATPase to distinct sub-domains of the plasma membrane.

## 4.2 Measurement Procedure and Data Analysis

Fluorescence microscopy studies were carried out on HEK293 cells expressing an eGFP-labeled human Na,K-ATPase  $\alpha_2$ -subunit, expressed from a bicistronic vector harboring TagRFP cDNA for using the latter as internal expression standard, images were recorded with the multiparameter microscopy setup, described in detail in chapter 3. Cell illumination and excitation was performed with two different wavelength ranges of a mercury lamp under the use of a filter cube for blue light (FITC; 465 nm - 495 nm) and a filter cube for green light (TRITC; 540/25). For all cells three images were taken with an electron multiplying CCD camera (see section 3.3.1). For all samples one brightfield image, another in the wavelength range for eGFP (BrightLineHC 520/35; Semrock) as well as a picture in the red range (D605/55M; Chroma) were taken. All images were recorded with same camera settings such as exposure time and gain.

To investigate, if temperature-dependent protein degradation occurs for the Na,K-ATPase  $\alpha_2$ -subunit mutant P979L HEK293 cells were transfected with cDNA from the Na,K-ATPase  $\alpha_2$ -subunit (WT or P979L) and  $\beta_1$ -subunit in a 1:1 ratio. Further information about sample production, transient transfection and cell treatment is given in chapter 2. The Na,K-ATPase  $\alpha_2$ -subunit frameshift mutant (FS), which refers to another FHM2 mutation (S966fs) leading to premature termination of the protein that should lead to misfolding and subsequent to protein degradation, as shown in Tavraz *et al.* [3] served as another control for measurements.

Fluorescence images were subsequently analyzed with the software *ImageJ*. For every cell, the same size of the region of interest (ROI) was taken (100 x 20 pixels) in order to read out the maximum intensity. This was done for eGFP in the plasma membrane and cytoplasm, and for TagRFP only in the cytoplasm. For illustration, some pictures of measured HEK293 cells expressing Na,K-ATPase WT and mutant P979L at different incubation temperatures are shown in Figure 4.1. Measurements are performed for more than  $N = 10$  cells and repeated several times.

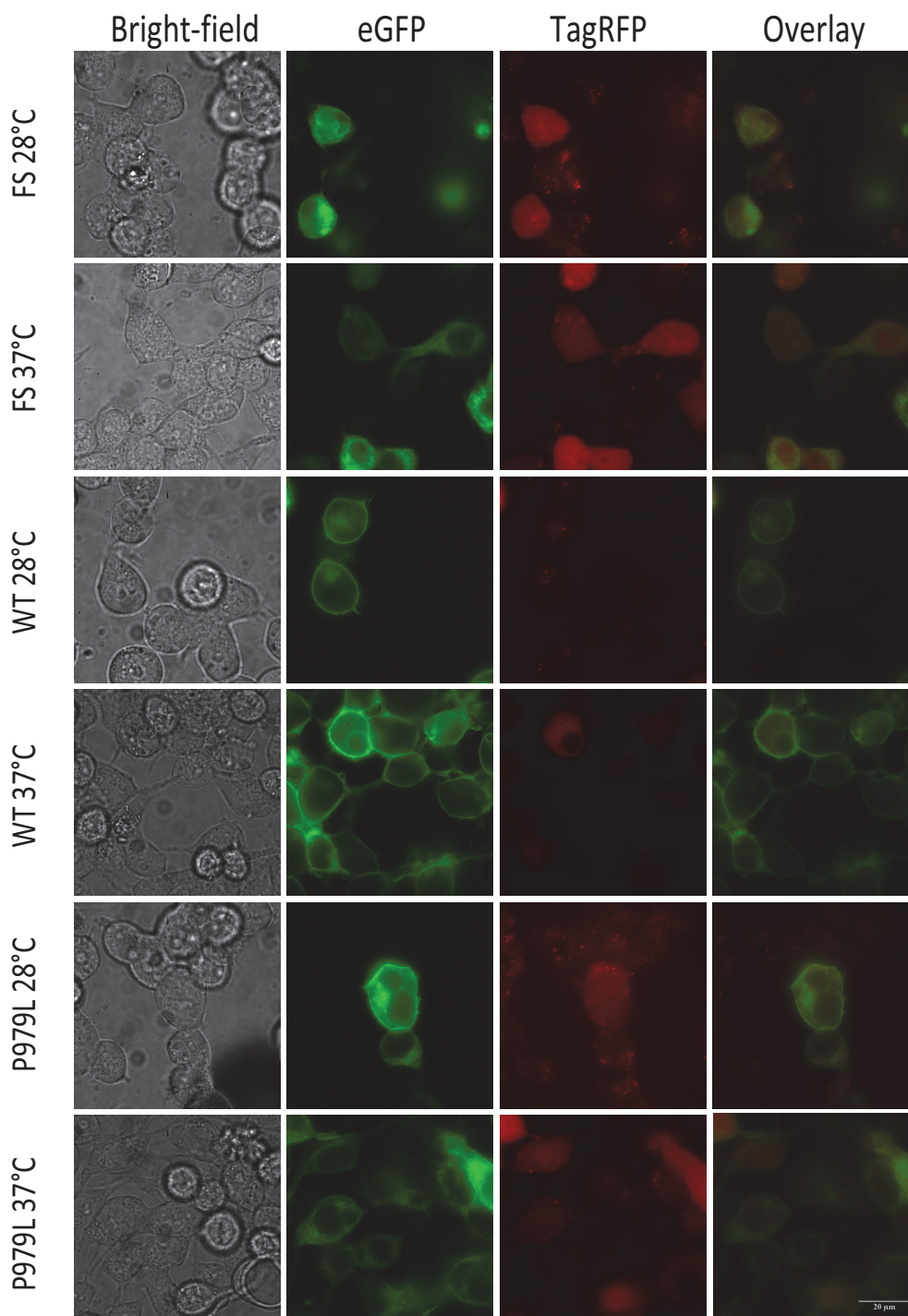


Figure 4.1: Comparison between the different mutations of Na,K-ATPase labeled with eGFP and TagRFP in living HEK293 cells (P979L, WT and FS) at different incubation temperatures. In the first row, bright-field pictures, then eGFP channel, the TagRFP channel and at least an overlay of eGFP and TagRFP is shown.

In Fig. 4.1, HEK293 cells expressing the eGFP-labeled human Na,K-ATPase  $\alpha_2$ -subunit (wild-type and FHM2 mutant P979L) together with TagRFP from a bicistronic vector are shown. In addition, bright-field images, the eGFP and TagRFP fluorescence, and at last an overlay of the latter are displayed. Furthermore, TagRFP expression permits to use its fluorescence as internal standard of protein expression

to normalize the fluorescence signal from eGFP-labeled Na,K-ATPase constructs (see data in Fig. 4.2). The cells in Fig. 4.1 were grown at 28 °C and at 37 °C in order to explore, whether the plasma membrane targeting of the Na,K-ATPase constructs are temperature-dependent, which would give a hint for a difference in protein stability. The Na,K-ATPase WT can be found at both incubation temperatures (28 °C and 37 °C) almost exclusively in the plasma membrane (see second column in Fig. 4.1), as expected. In contrast, the FHM2 mutant at a temperature of 37 °C, corresponding to human body temperature, is diffusely distributed throughout the whole cell. However, at an incubation temperature of 28 °C the P979L mutant shows the same plasma membrane staining as the WT at both incubation temperatures.

Figure 4.2 shows the ratio of fluorescence intensities between the green fluorescence of eGFP-labeled Na,K-ATPase constructs (WT: wild-type, PL: mutant P979L, FS: S966fs frameshift mutant) and the red fluorescence intensity of TagRFP in the cytoplasm, which is used as expression standard. For measuring the green fluorescence, either the intensity in the plasma membrane (blue columns) or in the cytoplasm (red columns) was taken.

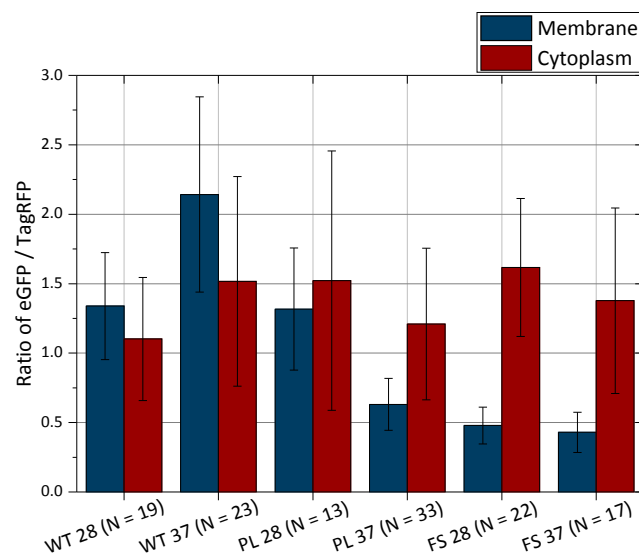


Figure 4.2: Ratio of fluorescence intensities between the green fluorescence of eGFP-labeled Na,K-ATPase constructs (WT: wild-type, PL: mutant P979L, FS: S966fs frame shift mutant) and the red fluorescence intensity of TagRFP in the cytoplasm, which is used as expression standard. For measuring the green fluorescence, either the intensity in the plasma membrane (blue columns) or in the cytoplasm (red columns) was taken. Also the number of sample cells measured is given.

The data in Fig. 4.2 show that at 28 °C, the FHM2 mutant P979L exhibits the same plasma membrane expression as the WT enzyme. However, the plasma membrane expression is significantly reduced at 37 °C for the mutant P979L. As a control, the

S966fs (frame shift) mutation, which leads to premature termination of the protein, exhibits profoundly reduced expression at both temperatures. In contrast to that, it is clearly visible that the ratio of eGFP/TagRFP in the cytoplasm for all mutations (WT, P979L, S966fs) at both incubation temperatures (28 °C and 37 °C) exhibits nearly the same amount. In order to get a better view to the data Fig. 4.3 shows a bar diagram of the ratio of the normalized eGFP signal in membrane and cytoplasm (TagRFP fluorescence used for normalization).

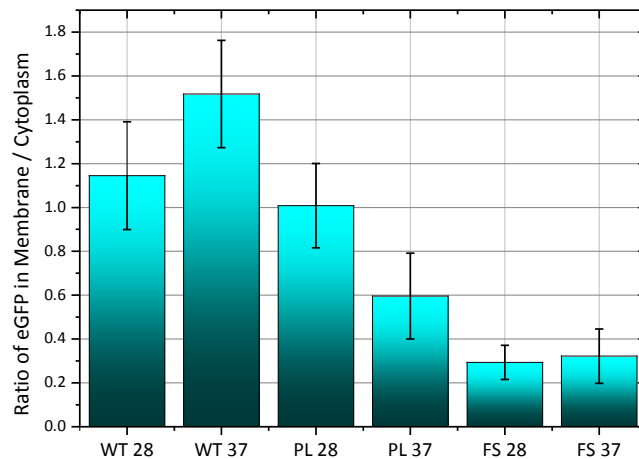


Figure 4.3: Ratio of the normalized eGFP-Na,K-ATPase signal (TagRFP fluorescence used for normalization) in the membrane vs. the signal in the cytoplasm.

Additionally, in Figure 4.3 the reduced amount of eGFP for the Na,K-ATPase mutant P979L in the plasma membrane of living HEK293 cells at 37 °C is clearly visible.

### 4.3 Discussion

In this chapter, the protein expression of the FHM2 mutant P979L of the Na,K-ATPase  $\alpha_2$ -subunit in dependence of the incubation temperature in living mammalian cells was studied and compared with the wild-type. The P979L mutant is a single point mutation in the extra cellular region at the beginning of the tenth transmembrane segment (M10) and located closely to the C-terminus. As already mentioned in the introduction, former studies on the Na,K-ATPase mutant P979L exhibit no differences in functionality compared to the WT studied with electrophysiological methods in *Xenopus laevis* oocytes cultivated at 20 °C, although the mutation can be clearly assigned to the FHM2 [3, 5, 55]. Also, no differences in protein expression and targeting between P979L and WT were observed by the use of

oocytes as expression system at room temperature. In order to study, if temperature dependence protein degradation can occur for the FHM2 mutant, the expression system was changed to mammalian HEK293FT cells, which were cultivated at 37 °C. From this, western blot analysis of total cell lysates grown at different incubation temperatures (28 °C or 37 °C) exhibit that the mutant P979L apparently leads at body temperature to a reduced amount of protein in the plasma membrane as detected by a surface biotinylation assay on HeLa cells [5, 72].

In this work, living HEK293 cells expressing the Na,K-ATPase  $\alpha_2$ -subunit WT and the FHM2 mutant (P979L) have been observed, and fluorescence emission images were recorded. Thereby, a better view insight the cell can be gained and a statement about the distribution of the plasma membrane protein inside the cell can be made. It could be shown that FHM2 mutation P979L significantly reduces the amount of  $\alpha_2$  proteins in the plasma membrane in living HEK293 cells at 37 °C, but not at 28 °C. This corroborates to a temperature-dependent effect on protein folding or stability, which results in reduced targeting to the plasma membrane, although the total amount of protein does not seem to be affected.

The lifetime of proteins in cells is highly variable, ranging from less than an hour up to days. The reason for protein degradation can be the misfolding of proteins or to the maintenance of the amino acid pool. Other factors for protein degradation are the processing of precursor proteins, immune response and cell proliferation as well as the programmed cell death. The degradation of a protein can occur over several pathways, but the two main pathways are the lysosomal and the proteasomal proteolysis. Typically, most of the endogenous, cytoplasmic and degenerated proteins are abolished on the proteasomal pathway that is performed by a two step process. In the first step, a protein that has to be decomposed is marked by a covalent attachment of multiple ubiquitin molecules. Ubiquitin is a 76 amino acid long protein with a weight of 8.5 kDa. The ubiquitination reaction proceeds in a three step mechanism, activation, conjugation and ligation of the enzyme. The importance of the discovery of the ubiquitin-mediated protein degradation is also reflected in the award of the Nobel Prize for chemistry in 2004 to the scientists A. Ciechanover, A. Hershko and I. Rose. More details about the ubiquitination process can be found here [42, 90, 91]. The ubiquitin chains serve as a signal for recruitment to the proteasomes. Proteasomes are protein complexes of one core complex and two regulatory subunits, which were found in the cytoplasm as well as in the cell nucleus of all eukaryotic organisms. In the second step the eukaryotic proteasomes break down ubiquitylated proteins and thus they are special types of proteases. Due to the regulatory subunits of the proteasome it can act on a variety of cellular processes.

Furthermore, exogenous proteins, which enter into the cell by endocytosis, are decomposed by lysosomal proteases (e.g. cathepsine), which are located inside the lysosomes. Lysosomes are acidic compartments of the cell, which contain numerous of hydrolases like nucleases, proteases, lipases and phosphatases that are working in an acidic environment (pH ~ 5.2). The acidic environment is generated and maintained by a V-type ATPase, which pumps two protons ( $H^+$ ) into the lysosome per ATP molecule. Also some endogenous proteins can be decomposed by the lysosomal pathway, this process is then described as autophagy. Furthermore, also transmembrane proteins can be degraded by the lysosomal pathway, which is coupled to the process of endocytosis [92, 93]. The group of Hicke *et al.* showed that also in the lysosomal pathway probed for plasma membrane receptors ubiquitination can signal protein degradation by inducing endocytosis. But in contrast to the ubiquitination proteasomal pathway, which uses multiple ubiquitin molecules as label, just one ubiquitin as marker was found in the work from Hicke *et al.* [94]. Therefore, it is easy to understand that the degradation of proteins across the lysosomal pathway takes longer than in the proteasomal pathway using a multiple ubiquitination.

From the literature it is known that the Na,K-ATPase  $\alpha_1$ - and  $\alpha_2$ -subunit expressed in COS-7 cells were degraded under the influence of a poly-ubiquitination process and therefore is degraded at least partially by the proteasome [95]. On the other side, Yoshimura *et al.* showed that the different subunits of the Na,K-ATPase in the plasma membrane are degraded on different pathways. They found that the  $\alpha$ -subunit is depleted within the lysosomal pathway and the  $\beta$ -subunit is decomposed by the proteasomal degradation [96]. A more recent study from Cherniavsky-Lev and co-workers showed that ouabain-induced internalized Na,K-ATPase pumps in the human lung carcinoma cell line H1299 are also destined for lysosomal degradation [97]. This leads to the assumption that the degradation process is maybe also dependent on the used cell line. It has to be also mentioned here that protein degradation can also occur over the proteasomal way without ubiquitination. This process usually happens for misfolded proteins, which were directly transferred back to the cytoplasm and decomposed there by the proteasome. In order to see, if the degradation of the P979L mutant occurs by the proteasomal pathway Tavraz *et al.* tested two different proteasome inhibitors [72], which should lead to an accumulation of the plasma membrane protein in the corresponding cell compartments. Since, no differences were visible the assumption can be made that the Na,K-ATPase  $\alpha_2$ -subunit mutant maybe does not undergo an ubiquitination process or the decomposition of the protein does not occur by the proteasomal pathway.

Starting from the obtained fluorescence images (see Fig. 4.1), one can assume that an incubation temperature of 37 °C leads to a premature degradation of the P979L

mutant, as has been already suggested by Tavraz *et al.* Comparing the fluorescence images of the mutant at 37 °C with those from wild-type at 28 °C or 37 °C it is clearly evident that the plasma membrane protein is diffusely distributed over the whole cell. If the plasma membrane proteins were on the way to the plasma membrane one would suggest to see small, fluorescent spots, which can be assigned to the transport vesicles. Another aspect which should be considered is that the protein is apparently expressed, because in every cell the TagRFP can be seen in the cytoplasm and therefore the plasmid vector is read correctly. In the constructs TagRFP serves as an internal standard of protein expression. This assumption is also underlined by the obtained diagrams (see Fig. 4.2), which show nearly the same amount in the ratio of eGFP and TagRFP in the cytoplasm for all Na,K-ATPase constructs (WT, P979L, FS) at all incubation temperatures (28 °C and 37 °C). It could also be that the mutant P979L is misfolded at body temperature and thus removed directly into the cytoplasm with following degradation by the proteasome.

Thus, the protein expression of the P979L mutant needs to be monitored in much more detail, in order to understand if the mutant protein reaches the plasma membrane and is degraded from there much faster than the WT protein or if it is degraded before reaching the plasma membrane in future studies. In addition, it would be interesting to see, if the protein is visible in the Golgi apparatus or in transport vesicles before reaching the plasma membrane or in lysosomal compartments, which could be done by co-localization experiments with fluorescent markers for these cellular compartments. This can be done by monitoring the protein expression in short time steps or the whole time after transient transfection. In this work measurements were always performed 36 h after transient transfection, since the WT protein exhibits in this time slot a bright plasma membrane staining. Another interesting aspect is the use of inhibitors, which perhaps can inhibit the lysosomal pathway for protein degradation such as chloroquine or leupeptin. Also inhibitors, which prevent the protein transport in different compartments of the cell would be interesting for future investigations. More details and understanding for the causes for the temperature-dependent protein degradation of the P979L mutant can lead to a better explanation of the molecular origin of FHM2.

# 5 Spectroscopic Characterization of the Fluorescent Protein Dreiklang

## 5.1 Introduction

For further studies, the fluorescence emission of the photoswitchable protein Dreiklang was firstly characterized under various environmental conditions such as different pH-values, excitation intensities or temperatures. Therefore the purified Dreiklang protein and cDNA plasmids suitable for HEK293 cell expression of Dreiklang were generated (see section 2.4). These studies were performed with different microscopy and spectroscopic techniques, as described in more detail in chapter 3. An introduction to Dreiklang and other common fluorescence proteins is given in section 2.3.

## 5.2 Absorption and Fluorescence Emission Spectra

Absorption measurements were performed using a spectrometer from Perkin Elmer (Lambda 19; 190 nm - 3.2  $\mu\text{m}$ ) with a wavelength range from 200 nm to 600 nm and a scanning speed of 480 nm/min. The PML-16C setup was used for steady-state emission investigations, which has been described in detail in section 3.3.2. Here, a 470 nm laser diode was used to excite the samples and the fluorescence emission was observed in a wavelength range of 450 nm up to 700 nm. All measurements were done at room temperature and for each measurement method the same sample concentration ( $c_{Abs.} = 8.4 \mu\text{g/ml}$  and  $c_{Em.} = 19.9 \mu\text{g/ml}$ ) was used. Figure 5.1 shows the normalized absorption and fluorescence emission spectra of purified Dreiklang proteins in phosphate-buffered saline (PBS) solutions at physiological pH.

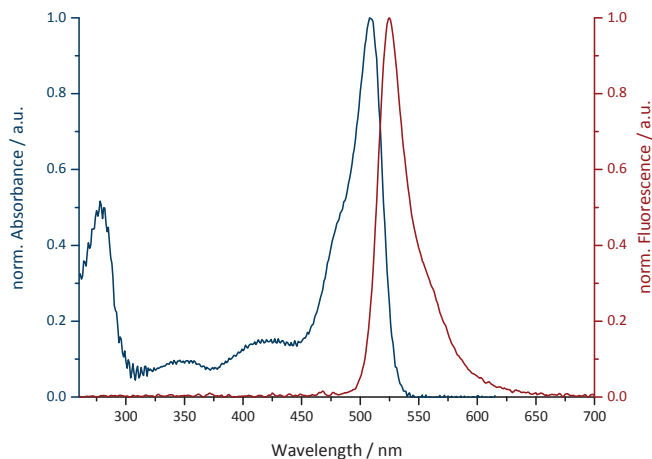


Figure 5.1: Normalized absorption and fluorescence emission spectra of purified Dreiklang proteins in PBS at pH 7.4.

Fig. 5.1 clearly shows that Dreiklang has three absorption bands and shows in addition a fourth peak from the protein at 280 nm. Two small peaks, one unusual in the UV range at around 340 nm and another in the blue range at around 412 nm and a major peak in the green range at 511 nm at a pH of 7.4 were observed. These absorption bands can be associated to the different states of Dreiklang. In the ON-state DRK exist in a protonated form and a deprotonated form, which have been assigned to the absorption bands at 412 nm and 511 nm. The absorption band at 340 nm corresponds to the OFF-state of DRK. The maximum of the fluorescence emission spectrum is found at 525 nm and as expected shifted to longer wavelength due to the Stokes shift. The normalized absorption and emission spectra of the purified Dreiklang proteins diluted in PBS at various pH-values are presented in Fig. 5.2. Normalization was performed by setting the maximum observed intensity to 1 and scaling the other curves in each plot by the same factor.

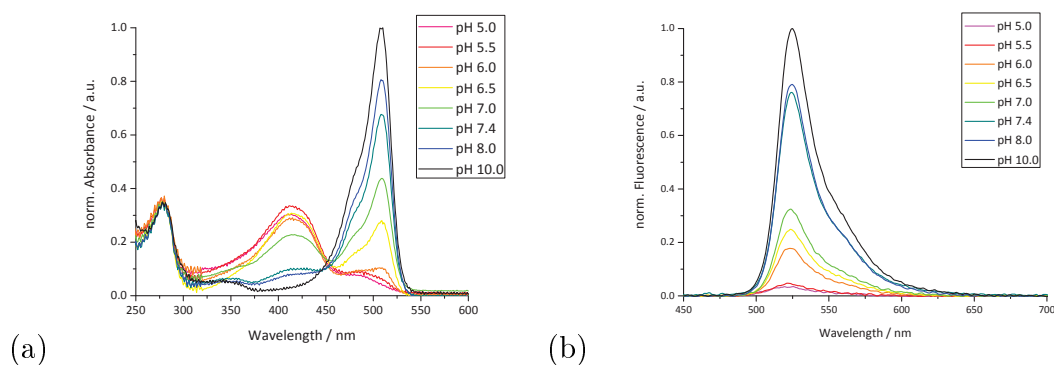


Figure 5.2: Absorption- **(a)** and emission spectra **(b)** of purified Dreiklang protein in PBS at various pH-values. Fluorescence emission spectra were taken with excitation at 470 nm.

The protein is efficiently excited at all selected pH-values, which is shown by a clear peak at 280 nm in all absorption curves related to the absorption of the amino acids with aromatic rings, which are present within the protein (mainly tryptophanes contribute to the 280 nm absorption) (Fig. 5.2 (a)). As already mentioned above, the absorption spectra of Dreiklang at different pH-values show a major peak at 511 nm and a minor peak at 412 nm. The amplitude of the 511 nm peak decreased in increasingly acidic solutions, whereas the 412 nm peak increased concomitantly, with a clear isosbestic point at around 455 nm. The minor peak at around 412 nm that increased with lower pH corresponds to a neutral form of the chromophore, also termed protonated form. Higher pH-values convert the chromophore in an deprotonated form, which absorbs at 511 nm and leads mostly to formation of a reactive anionic form of the chromophore. Similar to other FPs, Dreiklang shows a minor absorption peak blue-shifted to the main peak. This has been associated to a second deprotonated form of the chromophore as shown by Cotlet *et al.* [98]. The steady-state emission spectra of Dreiklang at different pH with excitation at 470 nm are characterized by a dominant peak at 525 nm and a small shoulder at about 560 nm (see Fig. 5.2 (b)). As the pH increases, the intensity of the fluorescence emission signal increases. These results are in good agreement with the data shown by Brakemann *et al.* [37]. Additionally, other fluorescent proteins, e.g. GFP, show also pH-dependent absorption and emission spectra as already described in several works [16, 36, 67, 99].

## 5.3 Excitation Spectrum and Emission Spectrum at different Excitation Wavelength

In order to understand, to which extent the absorption of radiation by Dreiklang results in emission of light or fluorescence, an excitation spectrum was taken.

The absorption spectrum measures the wavelength at which a molecule absorbs light. However, many compounds do not emit light after absorption of radiation and the energy dissipates in the molecule or its environment without resulting in the emission of photons. In contrast, an excitation spectrum determines the efficiency, by which excitation by light of different wavelengths leads to fluorescence emission of the observed molecules, as monitored at a fixed detection wavelength. If every absorbed photon results in fluorescence emission with quantum yield determined only by the wavelength-dependent absorption (extinction) coefficient, the excitation and absorption spectra are similar.

Excitation spectra and steady-state emission measurements with different excitation wavelength were performed using a FluoroMax-2 (Horiba Jobin Yvon GmbH) spectrometer with 2 nm resolution. For all measurements the same sample concentration of  $c = 16.6 \mu\text{g/ml}$  was used. An excitation spectrum of purified Dreiklang proteins diluted in PBS at pH 7.4 was taken between 300 nm and 516 nm. The emission wavelength was set to 525 nm. The results are shown Fig. 5.3. Additionally, the absorption spectrum of DRK at physiological pH from measurements above is depicted in the same diagram.

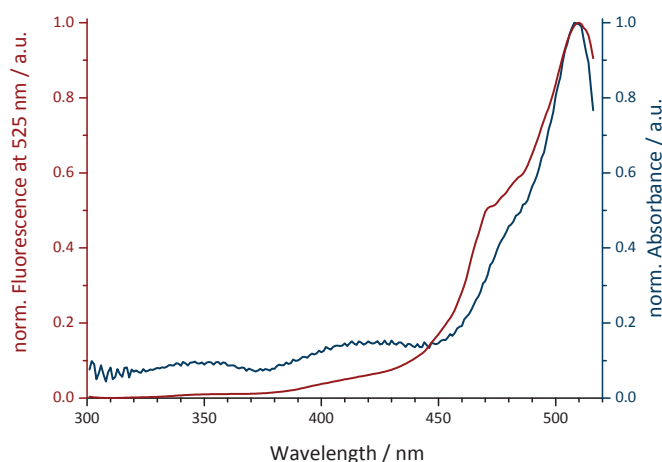


Figure 5.3: Overlay of the excitation spectrum of Dreiklang taken at an emission wavelength of 525 nm and the absorption spectrum. Both spectra were taken at physiological pH and have been normalized to a maximal amplitude of 1.

Clearly, the excitation spectrum of Dreiklang has a similar shape as the absorption spectrum of Dreiklang at a pH of 7.4 (see Fig. 5.3). Both spectra show a major peak at 511 nm with a prominent shoulder at about 475 nm and minor bands at 415 and 345 nm. At physiological pH the chromophore is mostly found in the deprotonated form, which is well excited at 511 nm and results in fluorescence emission at 525 nm. The protonated form of the chromophore, which can be excited at 412 nm and, as described above, is weakly fluorescent. This wavelength range is explicitly responsible for the OFF-switching of the fluorophore. So no peaks but clear bands are visible in fluorescence emission at 525 nm for lower excitation wavelength at around 440 nm, in contrast to the the absorption spectrum. Another possible reason for that is that the protonated state has a very low quantum yield or this state emits at wavelength below 510 nm and is therefore filtered out in this measurement.

Steady-state emission spectra of Dreiklang at various pH-values were performed by excitation with 412 nm and emission range between 480 nm - 650 nm (Fig. 5.4 (a)) or

505 nm and emission range of 510 nm to 650 nm (Fig. 5.4 (b)). Normalization is done by setting the maximum observed intensity to 1 and scaling the other measurements at the same excitation wavelength of the same factor under the premise that the same protein concentration was used in all experiments.

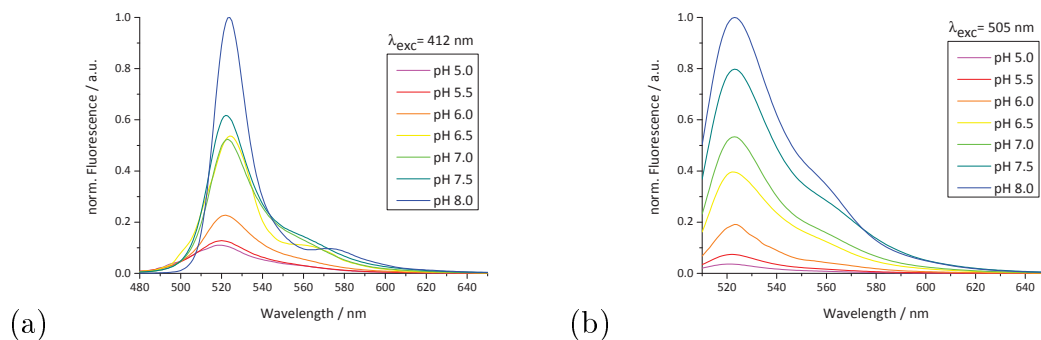


Figure 5.4: Steady-state emission spectra of purified Dreiklang protein at various pH-values for excitation with 412 nm (a) and 505 nm (b).

When Dreiklang is excited at 412 nm, the fluorescence spectra display a narrow and fairly invariant peak at 525 nm, and the emission amplitude is increasing with rising pH and a shoulder at longer wavelengths, which develops into a second emission band centered at 575 nm at pH 8. At this excitation wavelength mainly the neutral form of the chromophore is excited, as already shown in the absorption spectra of Fig. 5.2 (a). For excitation at 505 nm, which is associated with the wavelength range for direct excitation of the anionic form of the chromophore, the peak at 525 nm is broadened and a pronounced shoulder at longer wavelengths is observed. The pH dependence is also clearly visible in the emission spectra upon excitation with 412 nm. Another aspect, which has to be discussed is that the unnormalized curves for the two different measurements (excitation with 412 nm and excitation with 505 nm) show large differences in the amplitude of fluorescence intensity although for both measurements the same concentrations were used (data not shown). This effect is also found for other fluorescent proteins, for example like eGFP [98–100] and could be explained by the fact that by excitation with 412 nm mainly the protonated form of the chromophore is excited, which is not fluorescent. On the other hand, at 505 nm mainly the deprotonated form is excited and shows a broad fluorescence spectra as described above. By normalization of the fluorescence emission spectra to their respective maximum one clearly recognizes a shift of the maximum to the blue range for lower pH-values (see Fig. 5.5). This effect is visible for both excitation wavelengths.

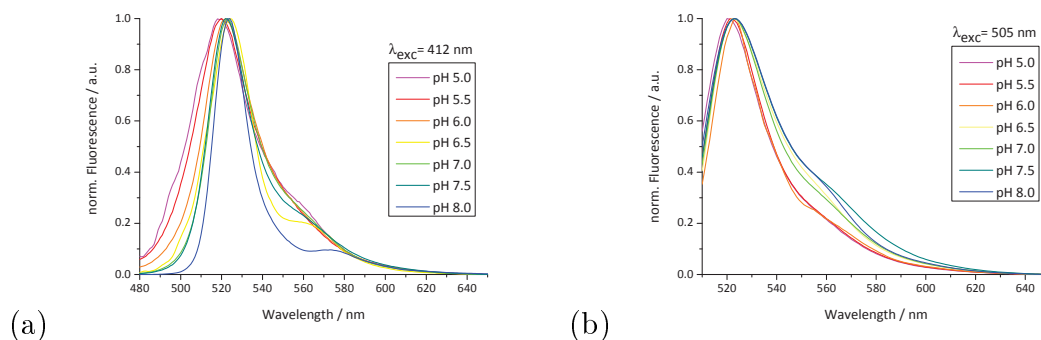


Figure 5.5: Normalized emission spectra to their respective maximum of Dreiklang protein at various pH-values for excitation with 412 nm **(a)** and 505 nm **(b)**.

This effect could be explained by the fact that at lower pH the protein is much more protonated than for higher pH. This is also underlined by the bigger visible shift for measurements at 412 nm, which is associated for the excitation of the neutral or protonated form of the chromophore.

## 5.4 Fluorescence Lifetime Studies at Different pH-Values

The lifetime of the excited state of purified Dreiklang proteins at different pH-values was studied using the confocal multiparameter setup coupled with the SPAD as detector (see section 3.3.1). A 470 nm laser diode with 20 MHz pulse repetition rate was used to excite the sample and emission was selected with a 570lp filter. The adaptation of all measured fluorescence decay kinetics with a time increment of 12.2 ps/channel were carried out using the program Globals Unlimited<sup>®</sup>. Thus, a multi-exponential fit with deconvolution of the instrument response function (IRF) were performed using a Levenberg-Marquardt algorithm for minimization of the mean square error  $\chi^2$ . Figure 5.6 (a) shows raw fluorescence decay curves obtained at various pH-values and the measured instrument response function. The calculated lifetimes with the respective amplitudes are shown in the right panel. The recorded fluorescence decay kinetics could be fitted using a global three exponential model with lifetimes of 80 ps, 740 ps and 2.7 ns. Decay associated spectra (DAS) were constructed, which represents the effect of different pH-values on the amplitudes of the exponential components of the model.

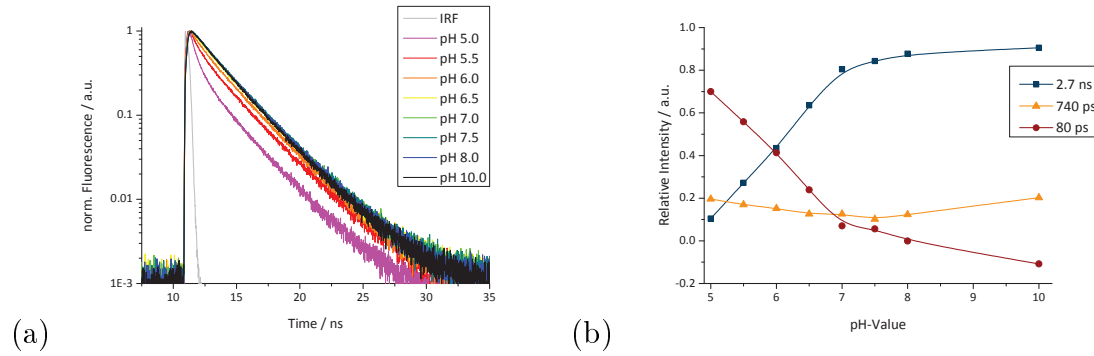


Figure 5.6: **(a)** Fluorescence decay curves of purified Dreiklang proteins at different pH-values and the measured IRF. **(b)** Decay associated spectra with lifetimes and respective amplitudes of Dreiklang as a function of the pH.

Fig. 5.6 (a) shows that a short lifetime (80 ps) increases in amplitude with decreasing pH. This is also underlined by the calculated lifetimes and amplitudes (see Fig. 5.6 (b)). In contrast, the amplitude of the long 2.7 ns component decreases with decreasing pH. Furthermore, the 740 ps component has an almost constant contribution over all pH-values. As already mentioned in section 5.2, fluorescent proteins, exist in two forms at physiological pH, in a first approximation, a protonated form and a deprotonated. These two states have, as already indicated, various spectroscopic properties and show overlapping absorption spectra. This assumption excludes mono-exponential models for the decay of the fluorescence. At least a bi-exponential model is required. Many different groups [98, 100–103] have already shown that various fluorescent proteins like GFP can not be described with a mono-exponential model and typical lifetimes for the protonated state are found between 150 ps and 250 ps. The lifetime for the deprotonated state of the chromophore is usually reported from 2.7 ns to 3.3 ns. Since Dreiklang is a GFP-like fluorescent protein, it can be compared in a first approximation to GFP. Therefore, it can be assumed that the measured 80 ps component represents the protonated form of the chromophore, which is supported by the increase in the amplitude at lower pH-values. On the other hand, the long 2.7 ns component could be associated with the fluorescence lifetime of the deprotonated form of the chromophore. This component dominates the fluorescence decay at alkaline pH.

The work of Cotlet *et al.* [98] distinguishes a third state, which is also deprotonated and it is associated to immature proteins, as well as to the local oxygen concentration. This form emits above 550 nm. This state could not be observed with excitation at 470 nm and observation around 520 nm. Additionally, it shows a lifetime of the excited state close to 3 ns, which makes it very hard to be distinguished from the 2.7 ns component. The 740 ps component with a small constant amplitude is found in these measurements for all different pH-values can not be explained so far.

However, several works [100, 101] found a similar unexplained lifetime component of around 850 ps for GFP.

In order to get an impression about the spatial distribution of the average lifetime and effects at different pH-values in living cells the averaged lifetime were measured with the fluorescence lifetime imaging microscopy (FLIM) setup based on a QA detector (see section 3.3.1 and [104, 105]). For illumination and excitation of living HEK293 cells expressing cytoplasmic DRK the 470 nm laser diode was used and emission selected with a 565ALP filter. For more details of cell treatment see section 2.5. Figure 5.7 (a) shows the spatial distribution of the average lifetime of cytoplasmic Dreiklang in HEK293 cells with an intracellular pH of 5.0, 6.0, 7.4 and 8.0. Color scale bar on the left side represents the average lifetime (Fig. 5.7 (a)). The lower panel of Fig. 5.7 (b) gives the corresponding normalized fluorescence decay curves of the measured cells at different pH read out in a region of interest.

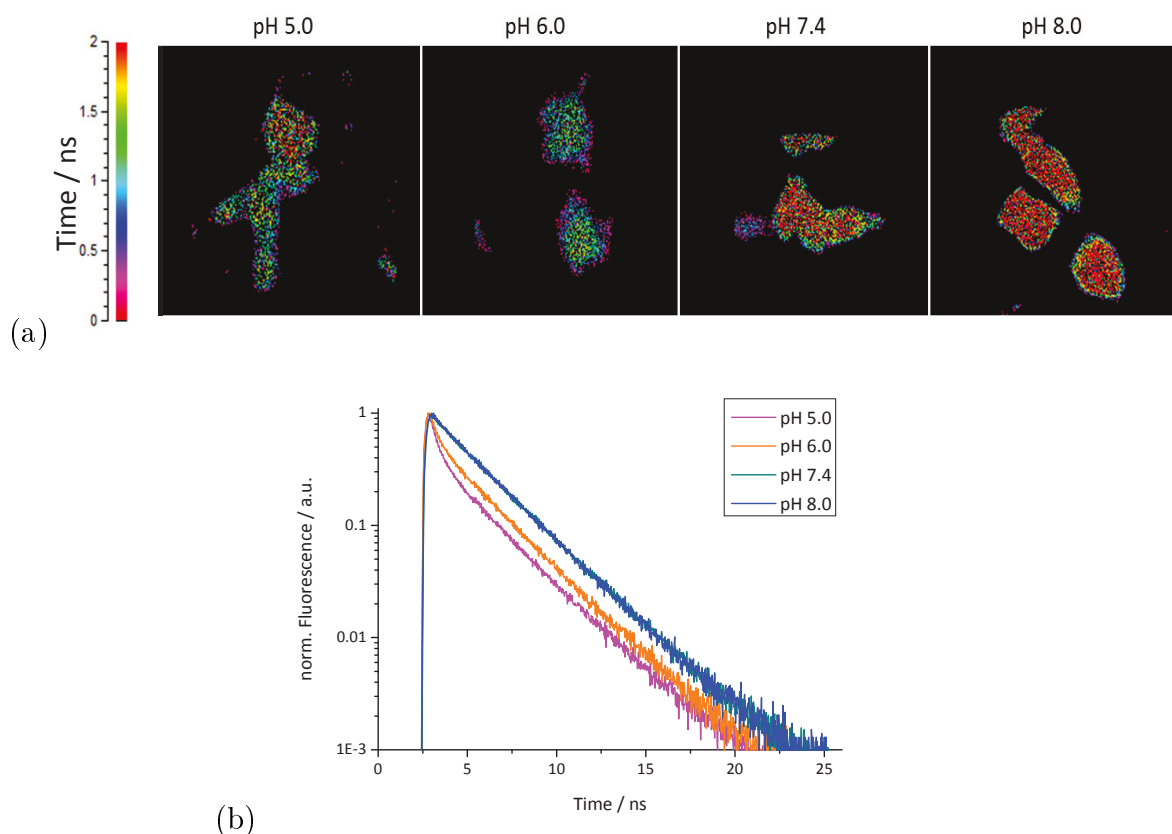


Figure 5.7: **(a)** FLIM images of living HEK293 cells expressing cytoplasmic DRK after illumination at 470 nm and emission selection above 565 nm at various pH-values. The color scale bar encode the average lifetime. Lower panel shows the corresponding normalized measured lifetime decay curves **(b)**.

It is clearly visible that the average lifetime increases with increasing intracellular pH, as already shown in Fig. 5.6 for the long lifetime component of the purified protein. The FLIM pictures (see Fig. 5.7 (a)) also show that the average lifetime increases with higher pH-values, which is indicated in Fig. Fig. 5.7 (a) by changing the colors from blue (~ 0.5 ns) to red at pH 8.0 corresponding to a lifetime of around 2 ns. These results are underlined by the given normalized decay curves (Fig. 5.7 (b)), which show clearly a rising contribution of the fast component with decreasing pH. All of these results are in good agreement with the obtained data from the lifetime studies at different pH-values.

## 5.5 Fluorescence Lifetime Kinetics at Different Temperatures

Temperature dependence of the lifetime and fluorescence emission spectra were performed using purified Dreiklang proteins diluted in PBS buffer (pH 7.4) containing 70 % glycerol and measured with the PML-16C setup (see section 3.3.2). The 470 nm laser diode with a repetition rate of 8 MHz was used to excite the sample. The fluorescence emission signal was separated from laser light using a 488lp filter. Fluorescence decay curves were taken in 16 channels with a spectral resolution of 12.5 nm in a fluorescence emission range from 450 nm to 640 nm. The analysis of all measured fluorescence decay kinetics with a time increment of 6.1 ps/channel were carried out using Global Unlimited<sup>®</sup> software. The recorded data was fitted with a mono-exponential function for the sake of simplicity for different emission wavelengths and temperatures. Simultaneously, time integrated emission spectra were taken at steps of 5 K in the wavelength range from 400 nm to 800 nm. Measurements were started at room temperature (291 K) and stopped at 250 K. Normalization for time integrated spectra is done by setting the maximum observed intensity to 1 (here at 291 K) and scaling the other measurements at the same excitation wavelength of the same factor.

Normalized time integrated fluorescence spectra at different temperatures (291 K - 250 K) of DRK protein are shown in Figure 5.8 (a), exhibiting a fluorescence maximum at 525 nm as expected for Dreiklang. Clearly, it is visible that the intensity of the fluorescence emission decreases with decreasing temperature, but the shape of the emission curve does not change. Fluorescence spectra for temperatures below 250 K could not be taken, because the fluorescence emission signal vanished.

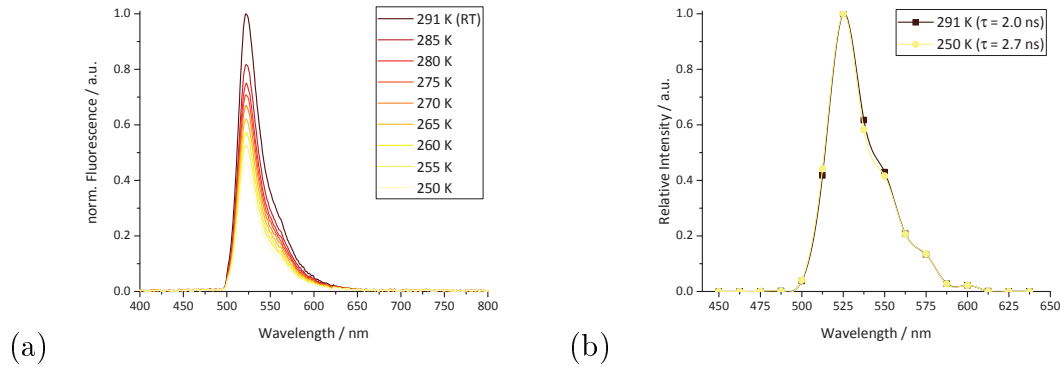


Figure 5.8: **(a)** Normalized fluorescence emission spectra of purified DRK proteins (pH 7.4) in dependence of the temperature after excitation with 470 nm. **(b)** The obtained DAS spectra from DRK at room temperature (291 K) and 250 K after excitation with 470 nm and fitting with a single exponential model are shown on the right.

One would expect that the fluorescence emission signal increases with freezing of the sample due to a higher scattering by working in a perpendicular mode (see section 3.3.2) and since the distribution of vibronic modes in the excited state occur according to the Boltzmann statistic a clear change also in the shape of the fluorescence emission spectra in dependence of the temperature is expected, which sharpens the emission band with decreasing temperature. At lower temperatures one would expect a narrower or sharper spectrum, a stronger signal and also a shift of the emission peak to shorter wavelengths (blue range), due to the different population of the vibrational levels. These effects were observed for eGFP (data not shown). So, it can be speculated that DRK switches by freezing under continuous illumination into an OFF-state or a not clearly identified dark state. The switching process from the fluorescence equilibrium state or ON-state of DRK to the OFF-state occurs normally by illumination with 405 nm light, and it requires a hydration process. One possibility would be that by the freezing process the necessary water molecule for a hydration process moves closer to the chromophore and thus switch it in the OFF-state without illumination of 405 nm. This is also underlined from the fact that the DRK fluorescence turns back with nearly same amount after heating the sample to room temperature again. Another option could be that the water mobility is restricted due to freezing and the surrounding environment is distorted, which is also influenced by the 70 % glycerol in the solution. This could lead to an accumulation of the protein in a nonfluorescent dark state. Similar effects were also observed for other switchable proteins like derivatives of IRFP in our group. The decay associated spectra from obtained lifetime data at room temperature (291 K) and at 250 K are plotted together to visualize the relative amplitudes of the calculated lifetimes at different emission wavelengths (see Fig. 5.8 (b)). An averaged lifetime of 2.0 ns was observed for Dreiklang at room temperature, which is faster than the

obtained lifetimes ( $\sim 2.7$  ns) in former measurements (see section 5.4). This could be explained by the presence of glycerol in the PBS buffer (pH 7.4), which leads to a change in the lifetime. The comparison of the obtained lifetimes at room temperature with the lifetimes calculated at 250 K shows a clear increase of the lifetime, but no changes or shifts in the wavelength of the emission peak at low temperatures. Similar effects were visible for temperature dependence lifetime measurements on eGFP in a 70 % glycerol-containing PBS solution (data not shown).

## 5.6 Investigations on the OFF-Switching Process

To get more information about the photoswitching mechanism of Dreiklang the OFF-switching process was studied at different excitation intensities and for various pH-values. All measurements were performed with the multiparameter setup, and using a mercuryarc lamp as light source. The fluorescence emission signal was then detected by the Andor Luca R<sup>EM</sup> camera. Measurements were taken with purified Dreiklang in PBS and for living HEK293 cells expressing cytoplasmic Dreiklang protein (for more details about used cDNA plasmids and cell treatment see section 2.5).

In order to monitor the OFF-switching process and its dependence on the local environmental pH, two emission lines of the mercuryarc lamp were selected for excitation. The first was a DAPI filter set for UV light and a filter set for 405 nm to monitor the OFF-switching. The emission range was selected by a 570lp filter. Series of 200 images were taken with 0.1 s exposure time without EM gain and auto-scaling. The samples were firstly illuminated for 5 s with UV light and then monitored for up to 40 s under 405 nm light excitation. The cycles were repeated for the whole series. Experiments were always carried out at room temperature.

Data analysis were done with *Image J* software by selecting a region of interest (ROI) of 1,000 pixels and reading out the mean fluorescence intensity over time. The resulting OFF-switching curves were subsequently analyzed with *Origin* software and were fitted independently with a single exponential function in order to calculate the OFF-switching time. All measurements were repeated several times for more than 5 curves per intensity or pH-value. The averaged switching time with corresponding standard error is given.

Firstly, the dependence of the used light intensity on the switching process was characterized. OFF-switching studies with the purified protein were done with a 5  $\mu\text{l}$  PBS solution droplet on a coverslip, and measured with a 10x objective. Intensities of the mercury lamp could be selected with different neutral density filters (None, ND4, ND8, ND4 + ND8). The corresponding optical power were measured after the 10x objective with a power meter (Nova; Ophir Photonics) for the 405 nm excitation light and the resulting intensities calculated to be 30  $\text{W}/\text{cm}^2$  (None), 8  $\text{W}/\text{cm}^2$  (ND4), 4  $\text{W}/\text{cm}^2$  (ND8) and 1  $\text{W}/\text{cm}^2$  (ND4 + ND8).

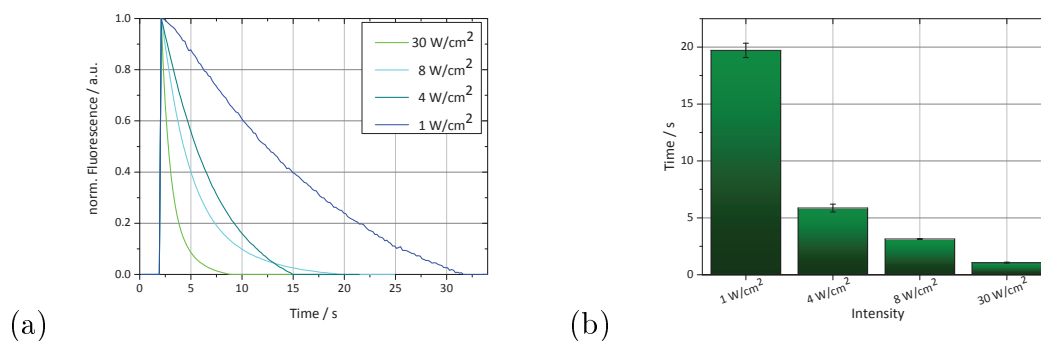


Figure 5.9: **(a)** Normalized OFF-switching process of Dreiklang protein diluted with PBS at a pH of 7.4 by illumination with different intensities of 405 nm and fluorescence collected through a 570lp filter. **(b)** Calculated switching times at different intensities.

In Figure 5.9 (a) and (b) it is significantly shown that the OFF-switching time is strongly dependent on the used light intensity. For all following measurements, the excitation intensity was chosen very carefully not to modify the acquired data with additional quenching effects other than the photophysical processes under investigation. Since, the switching reaction of DRK is light-driven, one has to ensure always a constant excitation intensity. Even if the used excitation is far away from the OFF-switching peak, one will always trigger the switching process. It is just a matter of time. From these results, the following measurements were performed using the minimum excitation intensity of 1  $\text{W}/\text{cm}^2$  for the 405 nm light.

OFF-switching studies with the purified protein at different pH-values were done under same conditions as described above. Normalized OFF-switching curves of the purified Dreiklang protein at different pH-values are given in Fig. 5.10 (a).

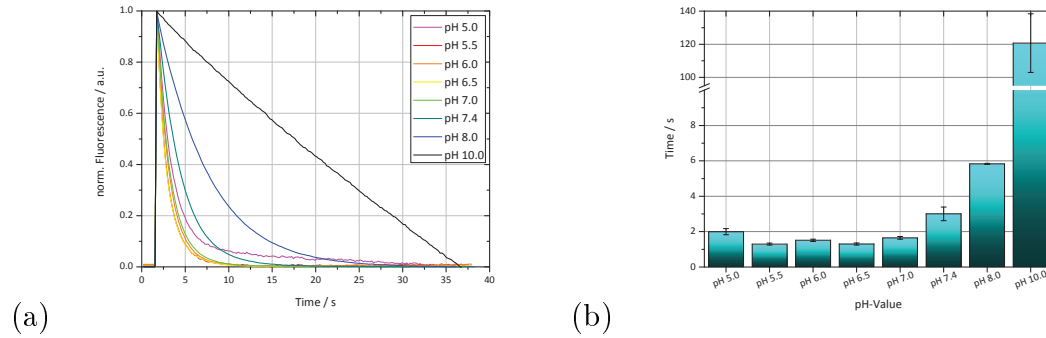


Figure 5.10: **(a)** Normalized OFF-switching curves of purified Dreiklang protein at different pH-values by illumination with 405 nm and fluorescence collected through a 570lp filter. **(b)** OFF-switching time in dependence of the pH estimated with an exponential fit.

Clearly, a dependence between the OFF-switching time and utilized pH is visible. For lower pH the curves decay faster that means the switching rate is increased. This is better visualized by the histogram in Fig. 5.10 (b) presenting the calculated OFF-switching times in dependence of the used pH. Between pH 5.0 and 7.0 the switching time is unchanged, but above pH 7.4 it increases clearly. It must be noted, that the absolute value of the measured time constants was not very accurate and changed significantly in different measurement sets. However, in all measurements the same trend for different pH-values was obtained.

To confirm that the behavior of the switching process in living organisms remains unchanged, experiments were performed on HEK293 cells expressing cytoplasmic Dreiklang. Before measurements, the cells were treated with ionophores in order to change and adapt the intracellular pH (see section 2.5).

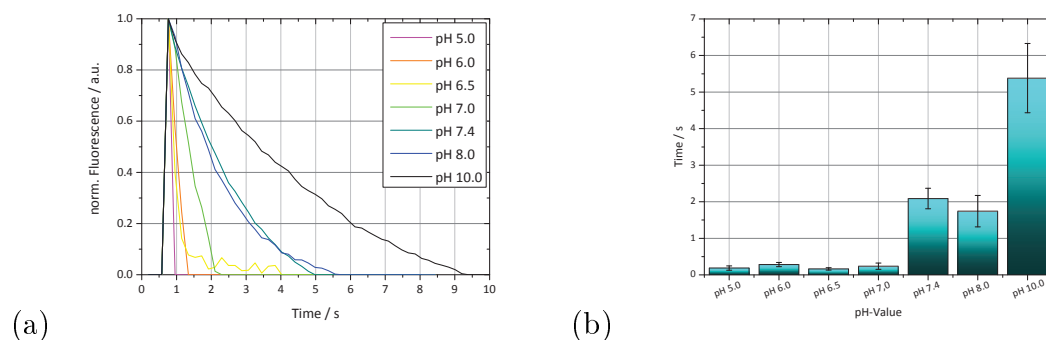


Figure 5.11: **(a)** Normalized OFF-switching curves of cytoplasmic Dreiklang proteins expressed in HEK293 cells at different pH-values by illumination with 405 nm and fluorescence collected through a 570lp filter. **(b)** Histogram showing the OFF-switching time as a function of intracellular pH.

The OFF-switching curves at different pH and calculated times obtained in living HEK293 cells expressing cytoplasmic Dreiklang (Fig. 5.11 (a) and (b)) show the

same behavior and trend for the switching time, as in the purified protein. As described in section 2.3, the switching process is based on a hydration / dehydration of the chromophore, which causes a structural change. In order to explain the effects on the chromophore structure Figure 5.12 shows the chemical structure of the chromophore in the fluorescent equilibrium state and after irradiation with 405 nm in the nonfluorescent OFF-state. In the figure the carbon atoms are given in light grey, nitrogen atoms in blue, oxygen atoms in red and the water molecule is shown in light blue. In the equilibrium state, the chromophore is largely planar and consists of two aromatic rings, a six membered hydroxyphenyl and a five membered imidazolinone ring with the important double bond between a nitrogen (N) and a carbon (C), which are connected through a methine bridge. By irradiation with 405 nm, a hydration of the imidazolinone ring occurs and the chromophore structure is changed. The double bond of the five-membered ring disappears and a new hydroxyl group (-OH) is added.

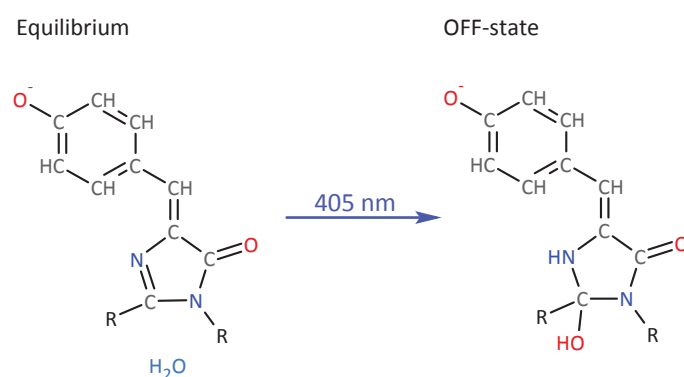


Figure 5.12: Chemical structure of the Dreiklang chromophore in the fluorescent equilibrium state (left) and after irradiation with 405 nm in the nonfluorescent OFF-state (right). Carbons presented in grey, nitrogen in blue, oxygen in red and the water molecule in light blue. Reprinted and extended from [37].

Brakemann *et al.* estimated that this hydration process is due to a nucleophilic addition, since the chromophore is present in a suitable conformation and the C atom is engaged in a double bond. However, the pH-dependent measurements of the OFF-switching time rather suggests an electrophilic addition mechanism. Since water is a poor nucleophile, water addition to alkenes is known to be acid-catalyzed. In this context, a proton serves as a catalyst by attacking the double bond, which leads to formation of a carbocation, which is then sufficiently electrophilic to permit nucleophilic attack by water. This process would fully account for the observed pH dependence of the switching process. In the latter, a water molecule reacts with the double bond and the protonation is thereby the slowest and therefore the rate-determining step of the addition reaction. In this reaction the acid environment

works like a catalyst, resulting in very short OFF-switching times for pH-values between 5.0 and 7.0. Thus, the activation energy in basic solutions is increased for the hydration process and leads to longer switching times. In conclusion, it can be confirmed that the more basic the pH-value, the longer the switching process is.

## 5.7 Discussion

In this chapter, the reversibly photoswitchable protein Dreiklang was characterized dependent on different conditions like temperature or different pH-values. A first introduction about the fluorescent protein was given in section 2.3 and measurements with Dreiklang as a fluorescence marker for diffusion studies were performed in chapter 6.

It can be shown that the fluorescence protein Dreiklang used for this work exhibits two absorption bands, a small one at 412 nm and a main peak at 511 nm, which corresponds to the protonated and deprotonated form of the chromophore. The amplitude of both peaks depends on the pH-value and a clear isosbestic point is apparent at around 455 nm. The fluorescence emission shows a dominant peak at 525 nm with a small shoulder at longer wavelengths. The small shoulder can be explained by a second deprotonated form of the chromophore, which was previously described by Cotlet *et al.* for eGFP [98]. For increasing pH the fluorescence intensity increases. All of these results show that Dreiklang protein used in this study exhibits the same properties in absorption and emission, as described by Brakemann *et al.* [37]. It is also comparable to other fluorescent proteins like GFP, but the pH-dependence is shifted to the neutral range compared to eGFP or the parental Citrine [16, 36, 67, 99].

Furthermore, the lifetime of the purified Dreiklang at different pH-values has been determined and showed that with decreasing pH a fast component increases. The obtained lifetimes (2.7 ns, 740 ps, 80 ps) are in good agreement with lifetimes found for other FPs [98, 100–103]. Lifetime measurements in dependence of the temperature of DRK in glycerol reveal an increase of the average lifetime component with lower temperatures from 2.0 ns at room temperature (291 K) up to 2.7 ns at 250 K. In the same experiment time integrated fluorescence emission spectra were simultaneously taken at 5 K steps. They also exhibit a decrease of the fluorescence signal intensity with decreasing temperature. Measurements under 250 K could not be performed, because the whole fluorescence signal vanished or was too close to the noise level to obtain accurate results. It has to be pointed out, that the fluorescence signal recovers in the same amount after re-heating of the sample, excluding that

irreversible damage of the protein occurs. This effect leads to the assumption that DRK switches in the dark state by freezing under continuous illumination or undergoes some yet uncharacterized photophysical processes. In other words one could say that the equilibrium between the bright and dark population of DRK is affected by temperature. At large temperatures DRK tends to stay in the bright state as confirmed by the switch-ON constant by Brakemann *et al.* [37].

Another property of the photoswitchable protein, which has to be taken into account, was the switching time. Dreiklang exists in three different forms, a fluorescent equilibrium state, a fluorescent ON-state and a nonfluorescent OFF-state. From both fluorescent states the protein can be switched by illumination with 405 nm into the dark state (OFF-state). This switching occurs by a hydration process of the chromophore. The time constant of the switching process from any fluorescent state depends dominantly on the pH. In fact, the switching of DRK in the cytoplasm of living HEK293 cells shows the same dependence as the purified protein in PBS. Indeed, cytoplasm is a more complex environment than PBS, due to the presence of many ion types, different viscosity, refractive index and vesicles. In all cases the switching occurs very fast in a pH range from 5.0 to 7.0. For higher pH-values (7.4 to 10.0) the switching time gets clearly slower. These results can be explained by a nucleophilic or an acid-catalyzed electrophilic addition, which extends the conclusions drawn by Brakemann *et al.* [37]. Furthermore, the switching time in dependence of the used illumination intensity was probed and it was confirmed out that high illumination intensities lead to faster switching times, as expected for a photophysical process.

In conclusion, Dreiklang reveals comparable properties to other fluorescent proteins of the GFP family, but it has major advantages. The benefits of this protein are on the one hand the decoupling of the fluorescence excitation from the optical switching spectrum and the photostability. Additionally, the protein is an excellent pH sensor, which can also be very useful for studies in living cells based on the measurements of the fluorescence signal intensity. However, lifetime measurements or FLIM might be negatively affected by this property especially in living organisms, where the intracellular pH concentration is not under control. Furthermore, Dreiklang as a photoswitchable protein is suitable for the application of optical super-resolution techniques on single molecule level such as stimulated emission depletion microscopy (STED) [32–34], stochastic optical reconstruction microscopy (STORM) [31, 106], photoactivated localization microscopy (PALM) [35, 107] or reversible switchable optical linear fluorescence transitions (RESOLFT) microscopy [108].

# 6 Investigations on the Mobility of the Na,K-ATPase in the Plasma Membrane

## 6.1 Introduction

To clarify the dependence of the mobility of the Na,K-ATPase (NaK) in the cell membrane on the different binding sites to cellular matrix or adapter proteins, e.g. to caveolin-1 and ankyrin B, different mutations of the Na,K-ATPase were generated as described in section 2.4.2. The resulting changes of the protein mobility in living cells was probed by fluorescence correlation spectroscopy (FCS) or by fluorescence recovery after photobleaching (FRAP). FRAP observes the diffusion of chromophores in a photobleached area of some square micrometers and measures the recovery time of the fluorescence signal. In contrast, FCS observes the fluorescence intensity fluctuations of molecules diffusing across a confocal volume of about 1 fL. FCS allows the simultaneous observation of multiple fast-diffusing molecular species, while FRAP is limited to a temporal scale of the diffusion time above 1 ms. Additionally, FRAP requires high laser intensities to bleach the fluorophores, fostering the production of reactive oxygen species (ROS). Both techniques are described in more detail in chapter 3. The solution to the problem of ROS production can be overcome by the use of Dreiklang as fluorescence marker, which is described in detail in section 2.3 and characterized in chapter 5. In all cases one would expect that the fluorescence tag has no influence on the diffusion behavior of the membrane proteins. In order to verify this proposition, all studies in this chapter were performed using Dreiklang as well as the popular eGFP as fluorescence marker and are later on compared.

## 6.2 Fluorescence Correlation Spectroscopy

### 6.2.1 Adjustment and Calibration for FCS Measurements

Intracellular distribution of the fluorescently labeled Na,K-ATPase was visualized by confocal laser scanning microscopy (Fig. 6.1 (a)). FCS experiments of eGFP- or Dreiklang-labeled Na,K-ATPase molecules in the cell were performed at the apical position (upper membrane). To identify the position of the upper cell membrane, the peak of the fluorescence intensity (Fig. 6.1 (b)) was identified by performing a single-point scan in the z-direction with  $0.5 \mu\text{m}$  increments over a distance of  $20 \mu\text{m}$ . Figure 6.1 (a) shows an exemplary z-scan measurement over the cell. The resulting cell profile in z-direction is shown in Fig. 6.1 (b). It is assumed that the plasma membrane is localized at the position with the highest count rate, since Na,K-ATPase is a prototypical plasma membrane protein. Inside the cell cytoplasm, the fluorescence signal has a little bit higher intensity than outside the cell, reflecting the presence of Na,K-ATPase molecules in the endoplasmic reticulum (ER) followed by processing through the Golgi and trans-Golgi network and targeting to the membrane by transport vesicles.

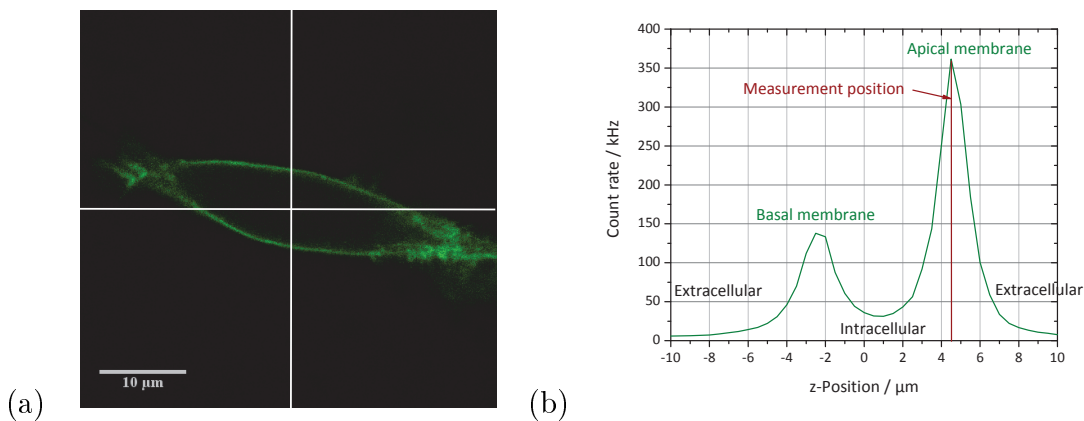


Figure 6.1: **(a)** Confocal image of HEK293T cells expressing eGFP-labeled Na,K-ATPase (green emission) adjusted for measuring the z-profile of the cell (setup parameters are as described above), the scale bar indicates  $10 \mu\text{m}$ . **(b)** A typical z-profile of a cell (abscissa: z-position in  $\mu\text{m}$ , ordinate: count rate in kHz) is illustrated resulting from a z-scan with  $0.5 \mu\text{m}$  increments over a distance of  $20 \mu\text{m}$  across the cell. The peaks in the count rate are attributed to the position of the basal (first peak) and the apical (second peak) plasma membrane, respectively.

For each investigated cell or solution, the autocorrelation curves (ACC) were generated by recording ten or twenty 10 s-long data series. Only curves from selected cells, exhibiting a stable count rate during the whole measurement were taken for analysis. For analysis of the FCS measurements, all autocorrelation curves were normalized to the same amplitude and plotted, according to the following formula:

$$\text{norm. } G(\tau) = \frac{G(\tau) - 1}{G(\tau_{Ref}) - 1} \quad . \quad (6.1)$$

$G(\tau_{Ref})$  is the temporal average of  $G(\tau)$  over the time period from  $5.2 \cdot 10^6$  s to  $4.8 \cdot 10^5$  s. The normalized autocorrelation curves were then averaged, leaving out autocorrelation curves that largely deviated from the majority of the data. In most of the measurements, the first three curves could not be used for calculating the average due to bleaching of immobile molecules in the membrane. Most of these deviating curves relate to bleaching processes or just showed no correlation. The fitting procedure in order to calculate the diffusion times for every measurement was done by using the integrated software of the ConfoCor 3 system from Carl Zeiss with autocorrelation models described in detail in section 3.2.4. These modern FCS analysis software packages developed by microscope manufacturing companies allow to fit autocorrelation curves according to the free diffusion model including triplet transitions and up to  $M$  diffusion components, each with amplitude contribution  $y_i$ :

$$G_{3dim}(\tau) = \frac{1}{N} \cdot \left[ 1 + \frac{T}{1-T} \cdot e^{-\tau/\tau_T} \right] \cdot \left( \sum_{i=1}^M y_i \cdot \left[ 1 + \frac{\tau}{\tau_{D,i}} \right]^{-1} \cdot \left[ 1 + \frac{\tau}{S^2 \cdot \tau_{D,i}} \right]^{-1/2} \right) \quad (6.2a)$$

$$G_{2dim}(\tau) = \frac{1}{N} \cdot \left[ 1 + \frac{T}{1-T} \cdot e^{-\tau/\tau_T} \right] \cdot \left( \sum_{i=1}^M y_i \cdot \left[ 1 + \frac{\tau}{\tau_{D,i}} \right]^{-1} \right) \quad , \quad (6.2b)$$

which apply for three- or two-dimensional diffusion, respectively.

For calibration of the FCS instrument, standard solutions of Rhodamine 6G (R6G) dissolved in water were used. Rhodamine 6G is a dye with a high quantum yield, a known diffusion coefficient and it is used as a molecular diffusion standard due to its extensive use in many applications [109, 110]. As can be seen from Figure 6.2 (a) and (b), the diffusion time for R6G in water is  $(25 \pm 1)$   $\mu\text{s}$  for eGFP settings (PH70) and  $(29 \pm 2)$   $\mu\text{s}$  in DRK settings with PH70 and  $(33 \pm 3)$   $\mu\text{s}$  in DRK settings with PH80, as expected from the properties of this molecule and the solvent. This difference arises from the different size of the confocal volumes at the given settings. Indeed, the beam waist  $r_0$  of the 488 nm laser line was calculated to be

0.17  $\mu\text{m}$  and that of the 514 nm argon line was calculated to be 0.18  $\mu\text{m}$  (PH70) and 0.19  $\mu\text{m}$  (PH80) based on the known diffusion coefficient of R6G in aqueous solution ( $D = 2.8 \cdot 10^{-10} \text{ m}^2/\text{s}$  at 22 °C [111]). The measured autocorrelation curves were evaluated using the model for free three dimensional diffusion (equation 3.23). It has to be noted, that the published values for the diffusion coefficient of R6G in water differ considerably depending on the method used for its determination (see [110] and references therein for an overview about published values). The value used for this work is typically inferred from early FCS studies and comparable with the measurement technique [111, 112]. Recent publications list values for the diffusion coefficient of R6G in aqueous solutions of  $4.14 \cdot 10^{-10} \text{ m}^2/\text{s}$  from dual-focus FCS (see references in [113]), and more recent work using pulsed field gradient NMR spectroscopy found  $4.0 \cdot 10^{-10} \text{ m}^2/\text{s}$  [110].

### 6.2.2 Comparison of Diffusion Studies with Different Fluorescence Labels (eGFP and Dreiklang)

For diffusion studies with FCS, it is essential to use an appropriate fluorescence tag, which needs to match photophysical constraints depending on the required application. Since the photoswitchable fluorescent protein Dreiklang is a promising marker for FCS investigations, this work first of all compared DRK with the conventional, nonswitchable eGFP in FCS applications. Therefore purified proteins of DRK and eGFP both in solution and in the cytoplasm of living cells were measured by FCS. Figure 6.2 (a) and (b) shows the averaged autocorrelation curves for the purified proteins in PBS and for the cytoplasmic proteins expressed in the cytoplasm of HEK293T cells with the resultant standard deviation. For the averaged curves of the cytoplasmic proteins, 26 (DRK) or 17 (eGFP) measurements on cells were taken into account.

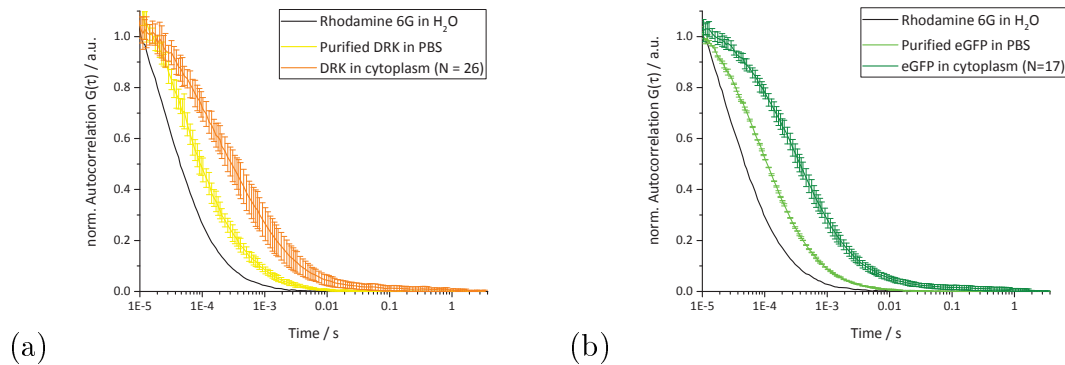


Figure 6.2: **(a)** Normalized autocorrelation curves of Rhodamine 6G in water (black curve), of purified Dreiklang (DRK) proteins in PBS (yellow curve) and of the DRK protein expressed in the cytoplasm of HEK293T cells (orange curve). For both DRK measurements, the curves were generated by averaging ten data acquisitions of 20 s duration at 0.7 % laser intensity. The averaged curve of the cytoplasmically expressed DRK proteins was constructed by measurements on 26 different cells. **(b)** Normalized autocorrelation curves of Rhodamine 6G in water (black curve), of the purified eGFP protein in PBS (light green curve) and of the eGFP expressed in the cytoplasm (dark green curve). For both eGFP measurements, the curves were generated from the average of ten data acquisitions of 20 s duration at 0.5 % laser intensity. For the averaged curve of the cytoplasmically expressed eGFP protein, measurements on 17 different cells were taken into account.

The measured autocorrelation curves were evaluated using the model for free three-dimensional diffusion. In the three-dimensional model, the structure parameter  $S$  must be between 5 and 9 to qualify as a "good" measurement. For the purified DRK in PBS, a diffusion time of  $(106 \pm 22) \mu\text{s}$  was found (Figure 6.2 (a), (b) and Table 6.1). To establish what is the dominant process that gives rise to the measured fluorescence intensity fluctuations, the size of the observation volume element was changed by changing the pinhole size to values above the desired (70 - 80)  $\mu\text{m}$  diameter up to 280  $\mu\text{m}$  and FCS measurements on all samples were performed (measurements on R6G and DRK in PBS are shown in Fig. 6.3). Thereby, it was confirmed that the characteristic decay time of the autocorrelation curve scales with the pinhole area (see eq. 3.24:  $\tau_D \propto r_0^2$ ), which is expected for a diffusion process. As previously described [89], this control is important in order to distinguish whether fluctuations in fluorescence intensity arise from molecular diffusion or from the kinetics of a photophysical or photochemical process occurring on the fluorophore, and that the measured diffusion coefficients are not affected by contributions from other effects, e.g. the well-known pH-independent internal and the pH-dependent external protonation processes of GFP, which exhibit correlation times of 50  $\mu\text{s}$  to 200  $\mu\text{s}$  [16, 114].

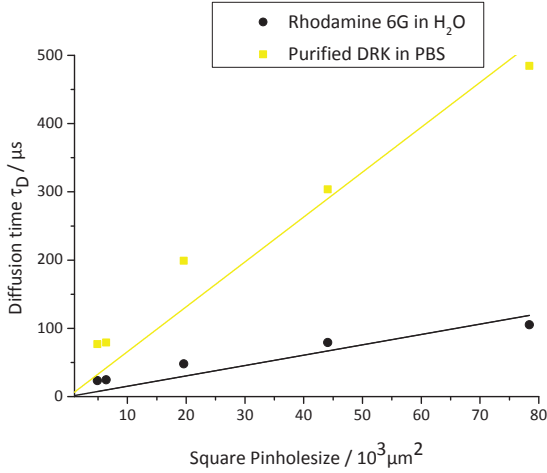


Figure 6.3: shows the change of the diffusion time depending on the pinhole size. The presented data were obtained by Rhodamine 6G in water (black) and purified Dreiklang proteins in PBS (yellow).

The diffusion coefficient  $D$  for DRK in PBS was calculated from equation 3.24 by using the beam waist  $r_0$  and the diffusion time  $\tau_D$  obtained from the autocorrelation curve, yielding a value of  $(8.5 \pm 1.8) \cdot 10^{-11} \text{ m}^2/\text{s}$ . In a different set of experiments the diffusion time of purified eGFP in PBS buffer was determined (see Fig. 6.2 (b)), which yielded a diffusion time of  $(95 \pm 2) \mu\text{s}$  and a diffusion coefficient of  $(7.6 \pm 0.2) \cdot 10^{-11} \text{ m}^2/\text{s}$ .

As shown in Figure 6.2 (a) and (b), diffusion times were also measured upon expression of DRK and eGFP in the cytoplasm of HEK293T cells. Fig. 6.2 (a) and (b) reveal that the diffusion time of the investigated fluorescence proteins in the cytoplasm is longer than the diffusion time of the purified proteins in PBS. Compared to the diffusion time of  $(106 \pm 22) \mu\text{s}$  for the purified DRK protein in PBS, its diffusion time in the cytoplasm of  $(479 \pm 222) \mu\text{s}$  is about 4.5-fold longer, yielding a diffusion constant of  $(1.9 \pm 0.9) \cdot 10^{-11} \text{ m}^2/\text{s}$ . This is about 4.5-fold smaller than in PBS buffer, which reflects the higher viscosity of the cytoplasm and other diffusion barriers present in the cell. Also, the diffusion time of eGFP expressed in the cytoplasm is longer than the one for the purified proteins in PBS, with a diffusion time of  $(376 \pm 69) \mu\text{s}$ , which yields a diffusion constant of  $(1.9 \pm 0.3) \cdot 10^{-11} \text{ m}^2/\text{s}$ .

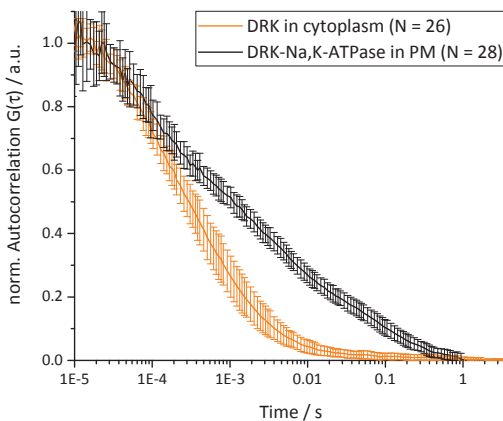


Figure 6.4: Normalized autocorrelation curves of DRK proteins expressed in the cytoplasm and DRK-labeled Na,K-ATPase in the plasma membrane (PM) are shown (0.7 % laser intensity). For each data set, the normalized average of more than 20 measurements on cells were used. The DRK protein expressed in the cytoplasm exhibits a much faster diffusion time than the DRK-labeled Na,K-ATPase in the plasma membrane.

Figure 6.4 shows the ACC of DRK-labeled Na,K-ATPase in the plasma membrane of HEK293T cells (Fig. 6.4, black) as compared to the diffusion of DRK proteins in the cytoplasm. Compared to the cytoplasmic DRK protein, the DRK-labeled Na,K-ATPase exhibits a much slower diffusion time. This is due to the much larger molecular weight of the fusion protein (about 184 kDa) than the isolated fluorophores (27 kDa). Additionally, the dynamic viscosity of lipid membranes is high compared to aqueous media. It is clearly evident from Fig. 6.4 that the autocorrelation curve of DRK-labeled Na,K-ATPase in the plasma membrane exhibits more than one characteristic diffusion time. The simplest model that could be fit to these autocorrelation curve was a two-component two-dimensional diffusion model with singlet-triplet transition (equation 6.2b). The summary of all diffusion time values obtained by fitting this function to the data is listed in Table 6.1.

In order to ensure that the autocorrelation curves are not biased by quenching or photobleaching effects, and to minimize photodamage of the sensitive biological material, the dependency of the measured diffusion curves on the used laser intensity was also studied (Fig. 6.5 (a) and (b)).

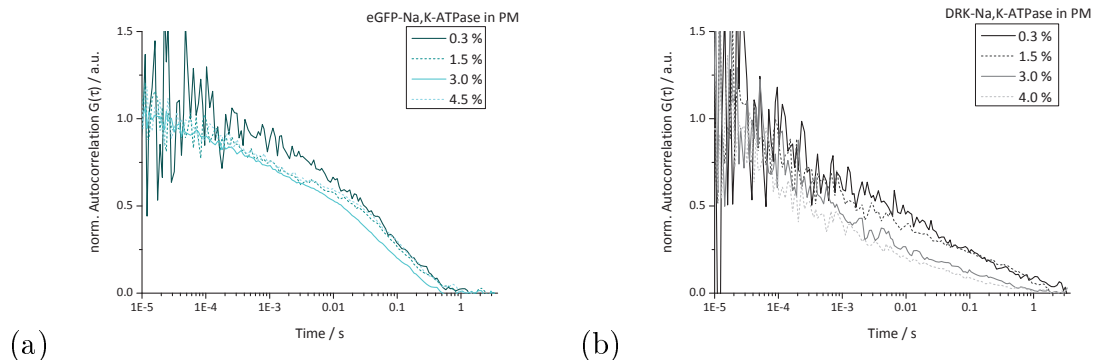


Figure 6.5: Autocorrelation curves of Na,K-ATPase expressed in HEK293T cells carrying a N-terminal eGFP **(a)** or DRK **(b)** label acquired using different laser intensities. Autocorrelation curves normalized to the same amplitude,  $G(\tau) = 1$  at  $\tau = 10 \mu\text{s}$ , show that the characteristic decay times for DRK are strongly dependent on laser intensity.

Fig. 6.5 (a) and (b) shows the ACCs of eGFP- or DRK-labeled Na,K-ATPase at different laser intensities. It is clearly visible that the DRK-labeled construct is much more artificially quenched at high excitation intensities than the construct carrying the eGFP label. However, these results confirmed that the laser intensity of 0.5 % up to 0.7 %, used consistently in all measurements on transfected HEK293T cells does not cause excessive bleaching or photodestruction.

Next, the diffusion behavior of DRK- and eGFP-labeled Na,K-ATPase constructs in the plasma membrane of HEK293T were compared.

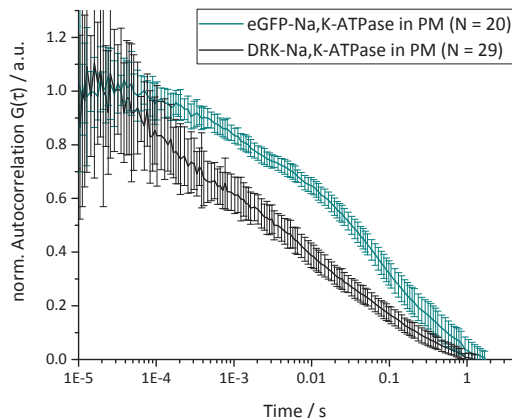


Figure 6.6: Normalized autocorrelation curves of DRK- and eGFP-labeled Na,K-ATPase measured in the plasma membrane of HEK293T cells. The normalized average correlation curve with standard deviation was calculated from 20 measurements on different cells, as indicated. Excitation laser wavelengths were 488 nm (eGFP) and 514 nm (DRK), each at 0.7 % laser intensity. Fluorescence emission was detected with a 505 nm long pass (eGFP) and a 530 nm long pass (DRK) filter, respectively.

Figure 6.6 clearly shows that different autocorrelation curves are obtained depending on the used label. DRK-labeled Na,K-ATPase shows two correlation time components of  $(318 \pm 212) \mu\text{s}$  (amplitude fraction:  $50 \% \pm 7 \%$ ) and  $(44 \pm 14) \text{ms}$  (amplitude fraction:  $50 \% \pm 7 \%$ ), which can be related to diffusion processes. Remarkably, the short time component of DRK-labeled Na,K-ATPase is not significantly larger than the one measured for isolated DRK expressed in the cytoplasm. The eGFP-labeled Na,K-ATPase also exhibits two diffusion times, with the shorter being  $(974 \pm 331) \mu\text{s}$  (amplitude fraction:  $31 \% \pm 4 \%$ ), which is significantly larger than the one measured for eGFP in the cytoplasm, and a longer component of  $(67 \pm 17) \text{ms}$  (amplitude fraction:  $69 \% \pm 4 \%$ ). It was confirmed by a two-sample Student's t-test that the corresponding diffusion time components of eGFP- and DRK-labeled Na,K-ATPase were significantly different ( $P < 0.05$ ). From these correlation time, diffusion coefficients were determined according to equation 3.24, as listed in Table 6.1.

In order to study the photophysical properties and arising differences between the two fluorescence marker DRK and eGFP in more detail, both purified fluorescent proteins were measured by FCS in PBS solvents of different viscosity. Since the molecular weight (26.9 kDa) and structure of both fluorescence proteins should be nearly identical, the fluorescence tag should have no influence on the shape of the autocorrelation curves in FCS measurements. However, this was only true for the isolated FPs. The DRK-labeled Na,K-ATPase showed significantly shorter diffusion times compared with the eGFP-labeled Na,K-ATPase construct, which arises possibly from an, as yet unidentified, photophysical quenching process.

To challenge the hypothesis that the aforementioned quenching process already acts on the isolated DRK molecules, the autocorrelation curves of purified eGFP and DRK protein in sucrose solutions were measured. Sucrose solutions are suitable for this purpose, since it is possible to cover an about 480-fold viscosity increase when using 70 % (w/w) sucrose solutions compared to water (see Table A.4 in the appendix), thereby shifting the diffusion time by the same factor (according to eq. 3.24 and eq. 3.28 in section 3.2.4).

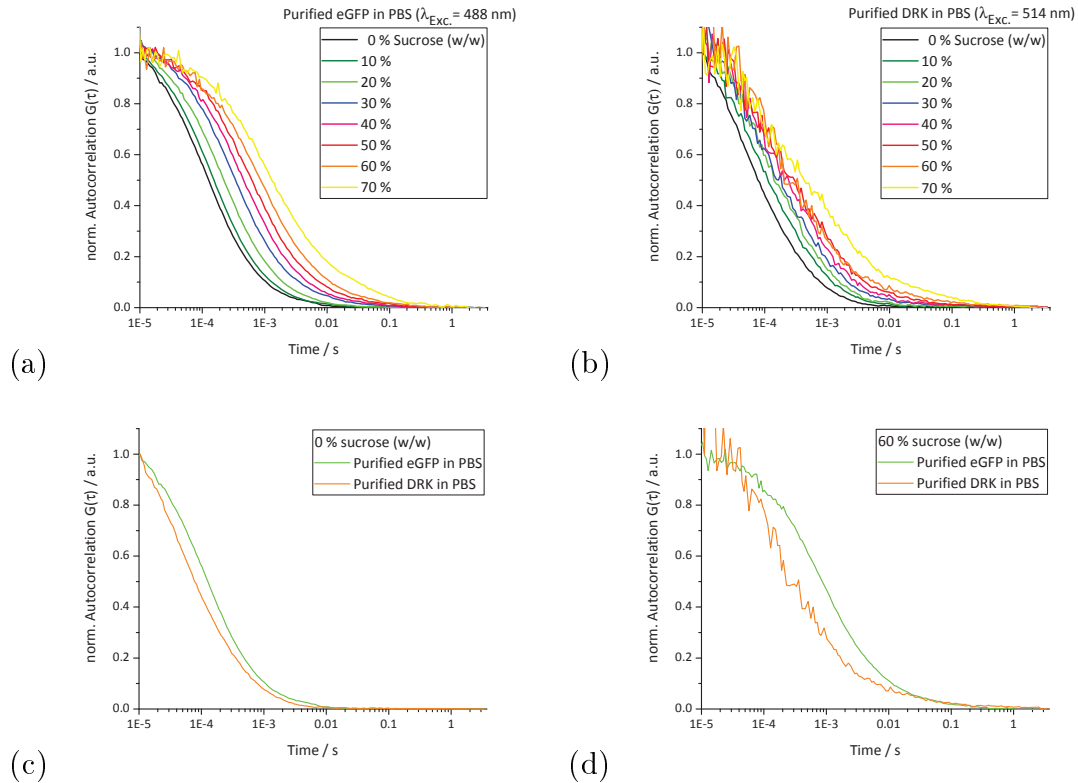


Figure 6.7: Normalized autocorrelation curves of purified eGFP **(a)** and purified Dreiklang **(b)** proteins in different sucrose/PBS solutions indicated by different colors. The curves were generated from the average of three times 20 s data acquisitions of 10 s duration. Direct comparison of normalized and averaged autocorrelation curves of purified Dreiklang (DRK) proteins (using 514 nm excitation) and purified eGFP proteins (using 488 nm excitation) in exemplarily depicted sucrose-free PBS buffer **(c)** and in 60 % sucrose/PBS solution **(d)**

Figure 6.7 (a) and (b) show the normalized autocorrelation curves of purified eGFP and DRK in PBS buffer solutions of different sucrose content and, hence viscosity. For both FPs investigated, the increase of solvent viscosity causes a profound increase of the diffusion times. The shape of the autocorrelation curves of eGFP mostly did not show distortions. The autocorrelation curves of DRK were generally much noisier than those of eGFP and clearly exhibited progressive changes in the slope of the diffusion component with increasing viscosity (Fig. 6.7 (b)). In order to visualize this difference more clearly, Fig. 6.7 (c) and (d) show exemplarily a di-

rect comparison of the mean autocorrelation curves of eGFP and DRK at indicated sucrose solutions (sucrose-free and in 60 % sucrose/PBS). The shape of these mean autocorrelation curves were clearly different.

### 6.2.3 FCS with DRK-/eGFP-labeled Na,K-ATPase on all Mutants

In this section, the dependence of the mobility of the Na,K-ATPase (NaK) in the cell membrane in relation to different interactions with components of the cytoskeleton is demonstrated. The different mutations, as described in detail in section 2.2.4 and section 2.2.5, were measured by FCS in the plasma membrane of living HEK293T cells and analyzed as described in section 6.2.1. This study was performed on all created mutants of the Na,K-ATPase and as well for the Na,K-ATPase wild-type for both available fluorescence labels (Dreiklang and eGFP). The cells used for the FCS measurements were selected within the cell culture according to the expression level of the fluorescent marker. Therefore, a bright-field and a confocal scanning image were acquired before each measurement (see Fig. 6.8).

Another reason for acquiring these pictures was to check whether the cells are grown in a single layer or in multiple cell layers. In the latter case, it is not possible to identify the upper membrane and to measure FCS curves correctly. Picture 6.8 shows different Dreiklang-/eGFP-labeled Na,K-ATPase  $\alpha_2$ -subunit constructs in HEK293T cells, which were used for FCS experiments. The first column of images in Fig. 6.8 (a) and (b), represents the fluorescence signal only, the central column the bright-field images of the same region, and the panels at the last column show an overlay of the fluorescence and the corresponding transmission pictures. HEK293T cells expressing the fluorescence labels DRK and eGFP in the cytoplasm are also illustrated, which show a fluorescence emission signal over the whole cell body, as expected for cytosolic expression.

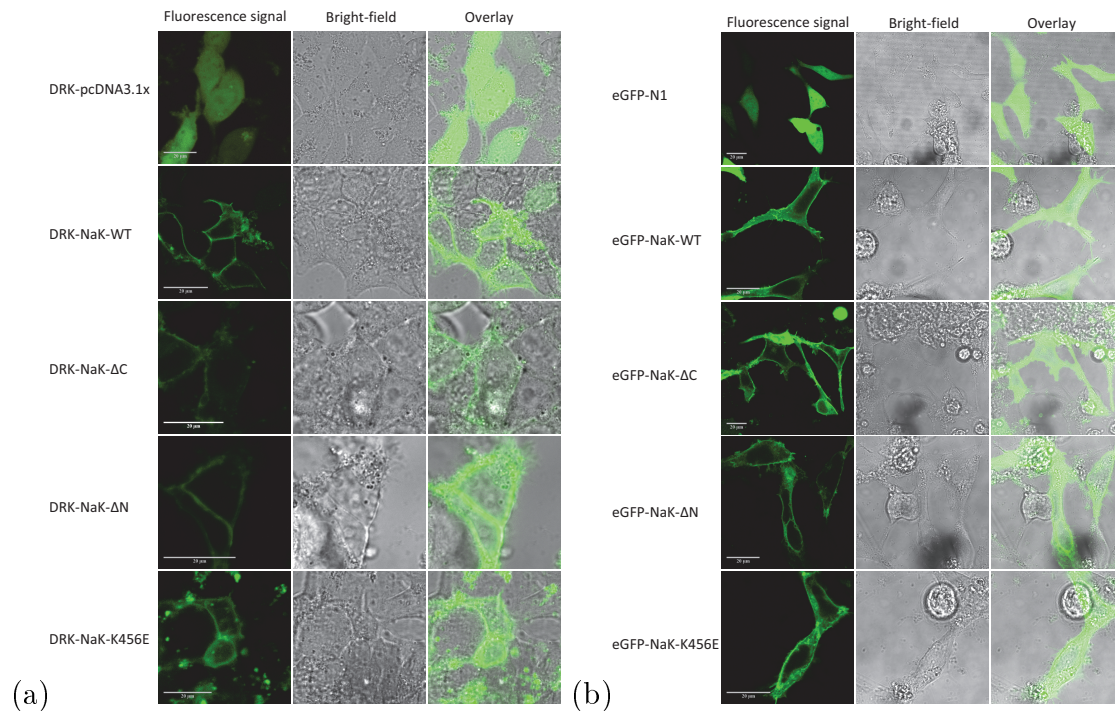


Figure 6.8: **(a)** Visual comparison of the Na,K-ATPase tagged with Dreiklang in HEK293T cells and cytoplasmically expressed Dreiklang. The first column shows the imaged fluorescence upon 514 nm excitation (laser intensity = 10 %) filtered with a 530 nm long-pass filter, the central column the bright-field images of the same region, and the panels at the last column show the overlay of the fluorescence and the transmission picture. As expected, the cytoplasmic protein is expressed in the whole cell and the transporter proteins DRK-NaK-WT, DRK-NaK- $\Delta$ C, DRK-NaK- $\Delta$ N and DRK-NaK-K456E show a clear localization in the plasma membrane. The fluorescence signals from the mutants exhibit also a more diffuse pattern with clear contribution from intracellular proteins in contrast to the wild-type, especially the K456E mutant. **(b)** Visual comparison of the Na,K-ATPase tagged with eGFP in HEK293T cells and eGFP expressed cytoplasmically from the pEGFP-N1 vector. The first column shows the imaged fluorescence under 488 nm excitation (laser intensity = 2 %) filtered with a 505 nm long-pass filter, the central column the bright-field images of the same region, and the panels at the last column show the overlay of the fluorescence and the transmission picture. As expected, eGFP-N1 is expressed in the cytoplasm and the transporter proteins eGFP-NaK-WT, eGFP-NaK- $\Delta$ N, eGFP-NaK- $\Delta$ C and eGFP-NaK-K456E show a prominent localization in the plasma membrane. In some cells, intracellular staining is also visible. The fluorescence signals from eGFP-NaK-K456E expressing cells exhibits a more diffuse pattern with clear contribution from intracellular proteins.

One can also see from Fig. 6.8 (a) and (b) for all DRK-/eGFP-labeled Na,K-ATPase constructs, that a clear fluorescence localization in the plasma membrane is obtained, as expected. A visual comparison between all different DRK-labeled Na,K-ATPase mutants and the DRK-NaK-WT exhibits a diffuse pattern over the cell with a clear contribution from intracellular proteins. This effect is the strongest for the mutant DRK-NaK-K456E. Additionally, it could be observed that the total expression level of the mutants is lower than in cells expressing the Na,K-ATPase wild-type labeled with DRK. This effect is less visible for the eGFP-labeled Na,K-ATPase constructs and the protein is more localized in the plasma membrane. Just the ankyrin B

associated mutant (eGFP-NaK-K456E) shows a more diffuse pattern inside the cell, like the DRK-NaK-K456E mutant. This effect is studied in more detail later on in this work (see section 6.2.4).

To get a quantitative impression of the effects on the autocorrelation curves and the counts per molecule (cpm) dependent on the position in the cell for FCS experiments, a z-scan through a cell was taken while measuring the autocorrelation curve. Thereby, counts per molecule per second is an output parameter of the FCS instrument and is defined as  $\text{cpm} = N^{-1} \cdot \langle F \rangle$ , in which  $\langle F \rangle$  is the mean fluorescence intensity. This was done e.g. for a cell expressing DRK-NaK- $\Delta N$ , as shown in Fig. 6.9.

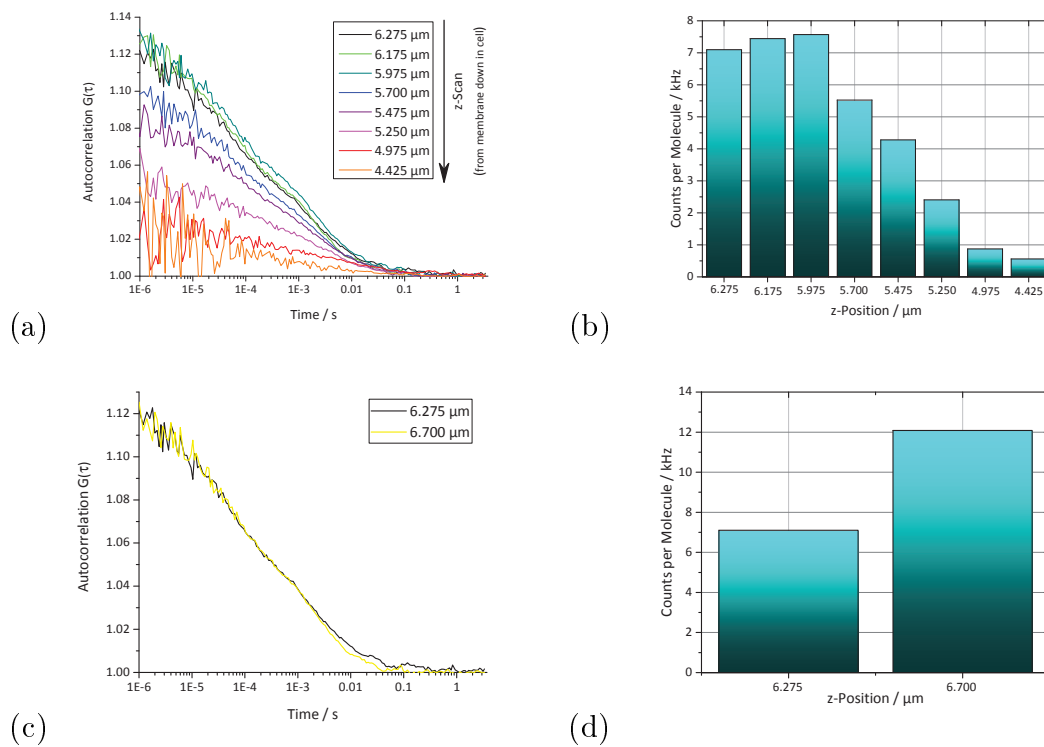


Figure 6.9: **(a)** Autocorrelation curves  $G(\tau)$  of DRK-NaK- $\Delta N$  in dependence of the z-position in the cell and the corresponding counts per molecules **(b)**. **(c)** Autocorrelation curves  $G(\tau)$  of DRK- $\Delta N$  at the plasma membrane before and after the z-scan and the corresponding counts per molecule **(d)**.

Fig. 6.9 (a), represents the measured autocorrelation curves  $G(\tau)$  in dependence of the z-position in the cell. The starting point was set after measuring the z-profile at the position with the highest count rate (here  $z = 6.275 \mu\text{m}$ ) as described in the experimental procedure in section 6.2.1. It is apparent that the first three curves have the same  $G(0)$  level, which is expected since the plasma membrane is placed close to the center of the confocal volume. It is also clear that the amplitudes of the autocorrelation curves decrease when shifting the focus inside the cell. This can be explained by the fact that DRK-NaK- $\Delta N$  is a typical plasma membrane protein

and there is just a little bit of intracellular staining, with very few or no fluorescent diffusing molecules that are not correlated. Additionally, the signal-to-noise ratio decreases by moving inside the cell. Fig. 6.9 (b) shows the counts per molecule as a function of the z-position, which also decreases with the z-position. In addition, the effect of thermal reactivation of Dreiklang is visible in the diagram (see Fig. 6.9 (d)). This is indicated by the higher counts per molecule after scanning through the cell and measuring again at the plasma membrane, whereas the autocorrelation curve is unchanged (Fig. 6.9 (c), yellow curve). The change in the z-position for the highest count rate from  $6.275 \mu\text{m}$  to  $6.7 \mu\text{m}$  could be explained by a not fully stable z-axis and as well by the fact that the confocal volume is smaller than the diameter of the plasma membrane. Another important observation is that after measurements, the cells look brighter than before. The reason for this could be that DRK proteins get switched into the ON-state by measurements with the 514 nm laser line or a pH shift in the cytoplasm occur during measurements, which could lead to a higher fluorescence intensity since DRK is very pH sensitive. See therefore chapter 5.

To make sure that autofluorescence from proteins in the used cell culture medium has no influence on the measurements, FCS measurements were acquired in the cell culture medium above the cells for all constructs (Fig. 6.10 (a)). For the same reason, the measurements were also performed in the cytoplasm of the cells. As an example, the measurements on the eGFP- and DRK-labeled wild-type of the Na,K-ATPase (eGFP-NaK-WT and DRK-NaK-WT) are given in Fig. 6.10 (b).

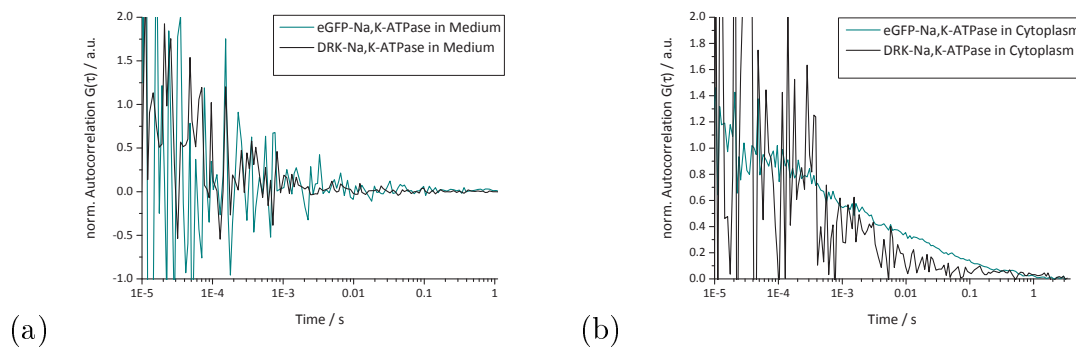


Figure 6.10: **(a)** Normalized autocorrelation curves of eGFP-NaK-WT (cyan curve) and DRK-NaK-WT (black) recorded in the cell culture medium above the cells. **(b)** Autocorrelation curves of eGFP-NaK-WT (cyan curve) and DRK-NaK-WT (black) recorded in the cytoplasm and normalized to the same amplitude.

From Fig. 6.10 (a) one can clearly see that there is no correlation signal in the medium regardless of the sample used. Additionally, the FCS measurements in the cell cytoplasm show a much faster diffusion behavior than the curves in the membrane (Fig. 6.10 (b)). Due to the lower relative fluorescence intensity, which is about 10 times lower than that for the membrane measurements, the influence of the cytoplasmic fluorescence can be neglected.

The goal of this study was to clarify the dependence of the mobility of the Na,K-ATPase in the cell membrane in relation to differential interactions with components of the cytoskeleton. Therefore, the different Na,K-ATPase mutants were measured by FCS in the plasma membrane and analyzed as described above for Figure 6.2. In Fig. 6.11 (a) and (b) the measured normalized averaged autocorrelation curves of all Dreiklang-labeled Na,K-ATPase constructs in HEK293T cells are shown. For all samples, the number of cells used for averaging was larger than 20.

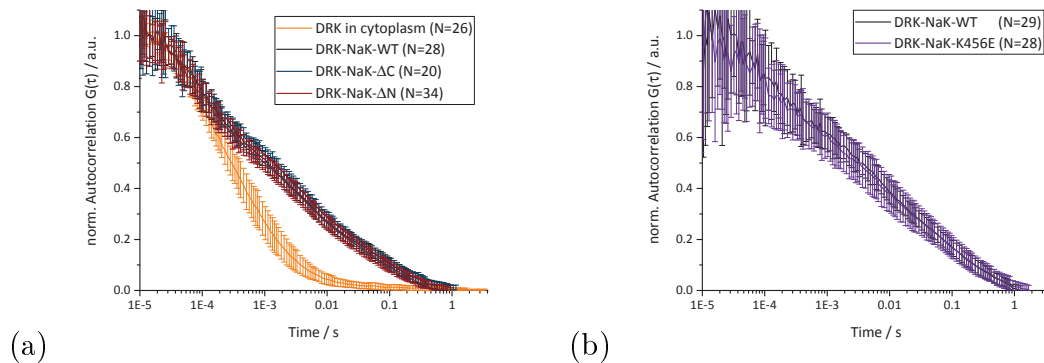


Figure 6.11: **(a)** and **(b)** Normalized autocorrelation curves with standard deviation of the different DRK-labeled Na,K-ATPase  $\alpha_2$ -subunit constructs measured by FCS. For each data set, the measurements on more than 20 cells were averaged. In this set of experiments, the three Na,K-ATPase constructs show the same diffusion behavior compared with the NaK-WT. Only the cytoplasmic DRK protein exhibits a faster diffusion.

No clear differences in diffusion between the different Dreiklang-labeled Na,K-ATPase constructs compared with the wild-type are visible. For this reason, it is not necessary here to give the calculated diffusion times and the associated diffusion coefficients. However, it is clear that all autocorrelation curves exhibit two characteristic diffusion times, as already shown for the Na,K-ATPase WT labeled with both eGFP and DRK in the plasma membrane of HEK293T cells. These results could mean that the disruption of the interaction motifs associated with caveolin-1 (NaK- $\Delta$ C and NaK- $\Delta$ N) or ankyrin B (NaK-K456E) does not affect the interaction of the Na,K-ATPase with the cytoskeleton in the way that differences in the diffusion behavior in the plasma membrane are observed. However, it must be considered that DRK diffusion is biased by photochemical quenching processes, which maybe override the small differences in the diffusion behavior and that, therefore, the fluorescence tag Dreiklang is not a good choice for FCS studies, as already shown in section 6.2.2.

Therefore, the same measurements were performed on identical constructs labeled with eGFP as fluorescence marker. For all constructs more than 30 cells were taken into account for analysis.

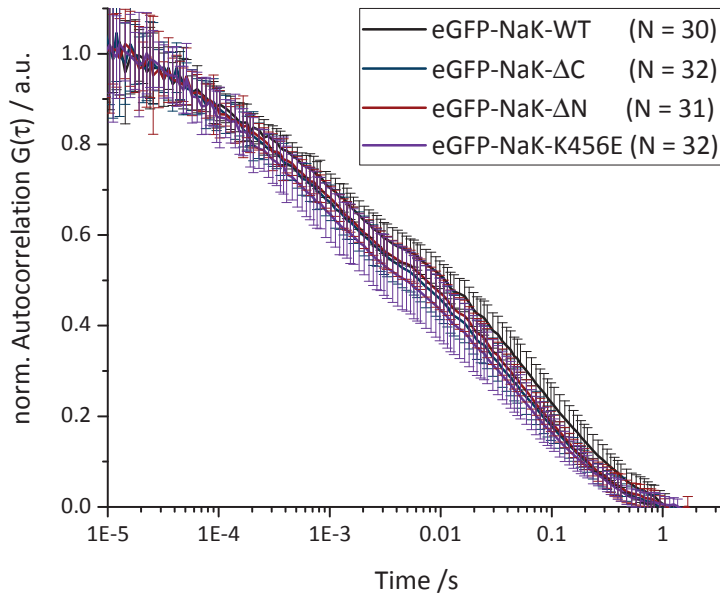


Figure 6.12: Normalized autocorrelation curves of eGFP-labeled Na,K-ATPase constructs measured in the plasma membrane of HEK293T cells. For the data set in the normalized average correlation curve with standard deviation from measurements on more than 30 cells is shown, as indicated. Excitation laser wavelength was 488 nm at 0.5 % laser intensity. Fluorescence emission was detected with a 505 nm long pass filter.

Figure 6.12 shows the normalized autocorrelation curves of eGFP-labeled Na,K-ATPase constructs with corresponding standard deviation. It is clear that different diffusion times are obtained for the different Na,K-ATPase constructs, but all constructs reveal two correlation time components ( $\tau_1$  and  $\tau_2$ ), which can be related to diffusion processes. The Na,K-ATPase wild-type shows the slowest autocorrelation curve with diffusion components  $\tau_1 = (533 \pm 160) \mu\text{s}$  (amplitude fraction:  $41 \% \pm 6 \%$ ) and  $\tau_2 = (63 \pm 18) \text{ms}$  (amplitude fraction:  $59 \% \pm 6 \%$ ). The ankyrin B associated mutant (eGFP-NaK-K456E) exhibits the fastest diffusion times with  $\tau_1 = (334 \pm 132) \mu\text{s}$  (amplitude fraction:  $46 \% \pm 8 \%$ ) and  $\tau_2 = (41 \pm 9) \text{ms}$  (amplitude fraction:  $54 \% \pm 8 \%$ ). The two caveolin-1 associated mutants labeled with eGFP show an intermediate profile with diffusion components of  $(411 \pm 127) \mu\text{s}$  (amplitude fraction:  $43 \% \pm 5 \%$ ) and  $(43 \pm 9) \text{ms}$  (amplitude fraction:  $57 \% \pm 5 \%$ ) for eGFP-NaK- $\Delta\text{C}$ . The Na,K-ATPase eGFP-labeled mutant  $\Delta\text{N}$  exhibits for the shorter component  $(438 \pm 149) \mu\text{s}$  (amplitude fraction:  $42 \% \pm 5 \%$ ) and a longer one being  $(46 \pm 7) \text{ms}$  (amplitude fraction:  $58 \% \pm 5 \%$ ). It was confirmed by a two-sample Student's t-test that the corresponding diffusion time components of Na,K-ATPase wild-type and the three mutants were significantly different ( $P < 0.05$ ). From these diffusion times the corresponding diffusion coefficients  $D$  were calculated according to equation 3.24. The results are listed in Table 6.2.

Additionally, a double and a triple mutant labeled with eGFP (eGFP-NaK- $\Delta$ C $\Delta$ N and eGFP-NaK- $\Delta$ C $\Delta$ NK456E) were also created (see section 2.2.5) and measured under same conditions by FCS. The double mutant carries the two caveolin-1 associated mutations and the threefold mutant comprises the two caveolin-1 associated (NaK- $\Delta$ C and NaK- $\Delta$ N) and also the ankyrin B associated mutation (NaK-K456E).

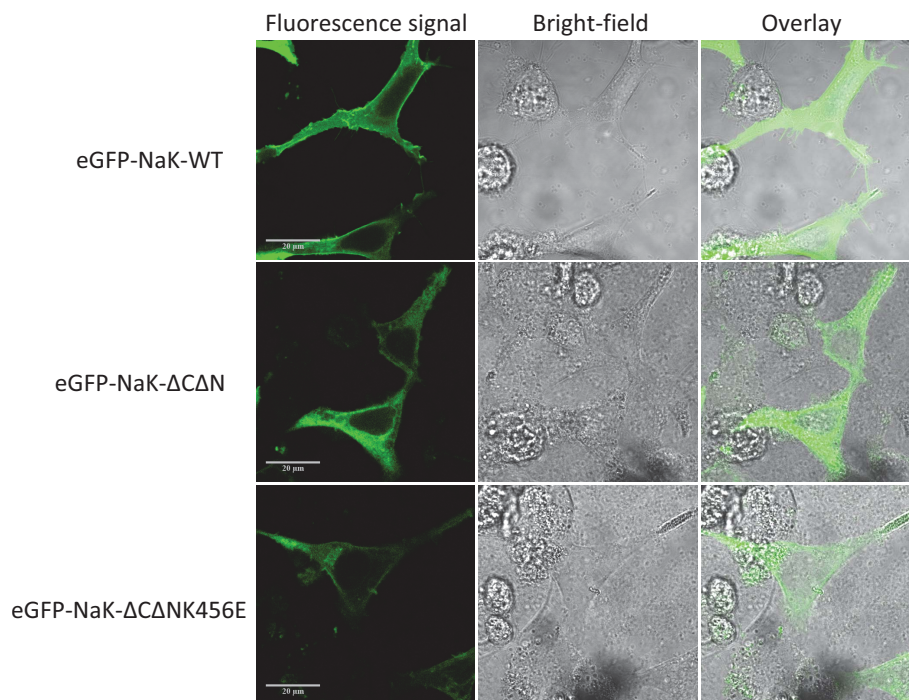


Figure 6.13: Visual comparison of the Na,K-ATPase tagged with eGFP in HEK293T cells. The first column shows the imaged fluorescence signal under 488 nm excitation (laser intensity = 2 %) filtered by a 505 nm long-pass filter. The central column shows the bright-field images of the same region, and the panels at the last column show the overlay of the fluorescence and the transmission pictures. As expected, the transporter proteins eGFP-NaK-WT, eGFP-NaK- $\Delta$ C $\Delta$ N and eGFP-NaK- $\Delta$ C $\Delta$ NK456E show a prominent localization in the plasma membrane. In some cells, intracellular staining is also visible.

Figure 6.13 shows the eGFP-labeled Na,K-ATPase  $\alpha_2$ -subunit double- and threefold mutant as well as the Na,K-ATPase wild-type in HEK293T cells, which were used for the FCS measurements. The first column of images in Fig. 6.13, represents the fluorescence signal only, the central column the bright-field images of the same region, and the third column shows an overlay of the previous two images. From the pictures it is evident that the Na,K-ATPase wild-type exhibits the most prominent fluorescence in the plasma membrane, whereas a strong intracellular staining is visible in the double- (eGFP-NaK- $\Delta$ C $\Delta$ N) and the threefold mutant (eGFP-NaK- $\Delta$ C $\Delta$ NK456E). This could indicate that the transport to the plasma membrane is maybe already disrupted in these mutations.

The diffusion behavior of the double- and threefold mutant is then compared with the Na,K-ATPase wild-type diffusion. FCS curves were averaged over more than 29 cells and are presented in Fig. 6.14.

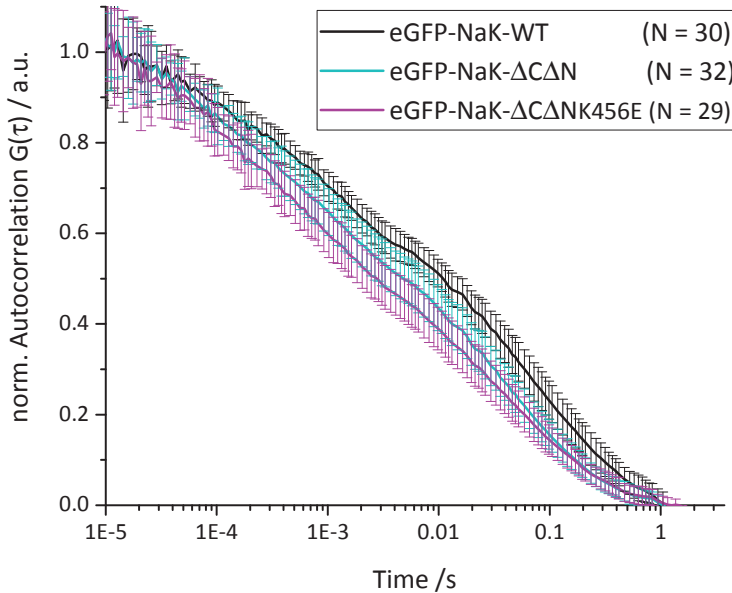


Figure 6.14: Normalized autocorrelation curves of eGFP-labeled Na,K-ATPase wild-type, double- (eGFP-NaK- $\Delta$ C $\Delta$ N) and threefold mutant (eGFP-NaK- $\Delta$ C $\Delta$ NK456E) measured in the plasma membrane of HEK293T cells. For each data set the measurements on more than 29 cells were averaged. Excitation laser wavelength was 488 nm with 0.5 % laser intensity, fluorescence emission was detected with 505 nm long pass filter, respectively.

Figure 6.14 clearly shows that different autocorrelation curves are obtained for the different Na,K-ATPase mutants and also for the wild-type. The two resulting diffusion times for eGFP-NaK-WT were already mentioned above. For the eGFP-labeled Na,K-ATPase double mutant (eGFP-NaK- $\Delta$ C $\Delta$ N) two correlation time components of  $(335 \pm 130) \mu\text{s}$  (amplitude fraction:  $44 \% \pm 6 \%$ ) and  $(38 \pm 9) \text{ms}$  (amplitude fraction:  $56 \% \pm 6 \%$ ) were found, which are comparable with the results for eGFP-NaK-K456E (see also Fig. 6.12 and Table 6.2). The double mutant is therefore also faster than the single mutants associated with caveolin-1 (eGFP-NaK- $\Delta$ C, eGFP-NaK- $\Delta$ N). The threefold mutant eGFP-NaK- $\Delta$ C $\Delta$ NK456E exhibits the fastest diffusion times, with  $\tau_1 = (299 \pm 102) \mu\text{s}$  (amplitude fraction:  $51 \% \pm 6 \%$ ) and  $\tau_2 = (34 \pm 8) \text{ms}$  (amplitude fraction:  $49 \% \pm 6 \%$ ). A two-sample Student's t-test confirms that the measured diffusion times of the Na,K-ATPase wild-type and the two mutants were significantly different ( $P < 0.001$ ).

### 6.2.4 Total Number of Particles in the Observation Volume

To illustrate in more detail the differences in the expression level in the plasma membrane of the different Na,K-ATPase constructs, which was already indicated by the fluorescence images of the cells (Fig. 6.8), the number of particles were analyzed and compared. For all investigated cells, the number of particles were calculated using the ConfoCor 3 integrated software (Carl Zeiss). Therefore, the measured autocorrelation curves were evaluated using a two-component model for two-dimensional diffusion. The model was fit to the data in the time range between  $1 \cdot 10^{-5}$  s and 3.36 s. For all investigated constructs the mean value with corresponding standard deviation is given. For all samples, the number of cells used for averaging was larger than 20 as written in every chart. The data were acquired during different experimental sessions and are therefore not directly comparable to each other in the calculated absolute number of particles, but the trend of the different constructs could be compared. Every histogram was made of data taken within one session (see Fig. 6.15 - 6.17).

Figure 6.15 shows the averaged number of particles ( $N_P$ ) in the observation volume for the different DRK-labeled Na,K-ATPase mutants (DRK-NaK- $\Delta$ C, DRK-NaK- $\Delta$ N) and wild-type (DRK-NaK-WT) in HEK293T cells.

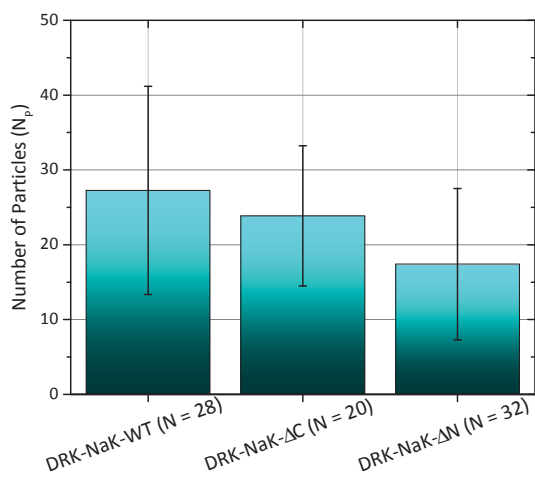


Figure 6.15: Averaged number of particles in the observation volume for the different DRK-labeled Na,K-ATPase constructs (DRK-NaK-WT, DRK-NaK- $\Delta$ C, DRK-NaK- $\Delta$ N) with the corresponding standard deviation and the number of cells taken into account.

The DRK-NaK-WT exhibits with  $N_P = 27 \pm 14$  the highest number of molecules in the observation volume. The mutant DRK-NaK- $\Delta$ C shows a lower number of  $24 \pm 9$  and DRK-NaK- $\Delta$ N exhibits the lowest number with  $N_P = 17 \pm 10$ . This effect was already visible in the taken images of Fig. 6.8, where a clear diffuse intracellular pattern for the DRK mutants is visible. Additionally, these mutants exhibit the smallest fluorescence signal in the plasma membrane. A two-sample Student's t-test confirms that the calculated number of particles ( $N_P$ ) of Na,K-ATPase wild-type and the mutant DRK-NaK- $\Delta$ N was significantly different ( $P < 0.01$ ).

Next, the Na,K-ATPase mutant K456E labeled with Dreiklang (DRK-NaK-K456E) was compared with the Na,K-ATPase wild-type labeled with Dreiklang and, in addition, eGFP-labeled Na,K-ATPase wild-type is shown in the same histogram (see Figure 6.16).

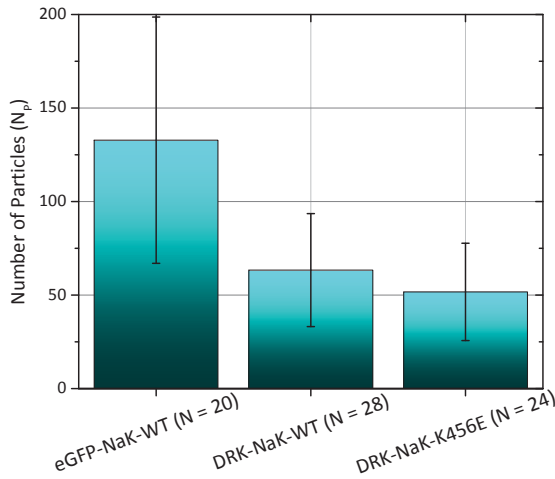


Figure 6.16: Averaged number of particles in the observation volume of one DRK-labeled Na,K-ATPase mutant and the wild-type. In addition for comparison of the used fluorescence label the eGFP-labeled Na,K-ATPase wild-type is shown. All data are given with corresponding standard deviation and the number of cells taken into account.

From the histogram (see Fig. 6.16) one can clearly see that the eGFP-NaK-WT exhibits the highest number of  $N_P = 132 \pm 104$  and the DRK-NaK-K456E mutant ( $N_P = 52 \pm 26$ ) the smallest. The DRK-NaK-WT number of  $N_P = 63 \pm 30$  particles lies between those other two constructs. From the obtained data, it is visible that the mutant DRK-NaK-K456E exhibits a lower expression level in the plasma membrane compared to the wild-type proteins, as already seen in the images in Fig. 6.8. One would expect that the fluorescence tag has no influence on the properties of the protein. But in the diagram it is clearly apparent that there is a profound difference between DRK-NaK-WT and GFP-NaK-WT even if they are measured with the same setup settings (data not shown). A two-sample Student's t-test confirms that  $N_P$  of eGFP-NaK-WT was significantly different from DRK-NaK-WT ( $P < 0.001$ ).

Fig. 6.17 reveals the resulting average number of particles for all Na,K-ATPase constructs labeled with eGFP (eGFP-NaK-WT, eGFP-NaK- $\Delta C$ , eGFP-NaK- $\Delta N$  and eGFP-NaK-K456E) and shows that in this case there is no difference in expression. Also shown in Fig. 6.17 are the double- and threefold mutant (eGFP-NaK- $\Delta C\Delta N$  and eGFP-NaK- $\Delta C\Delta N$ K456E).

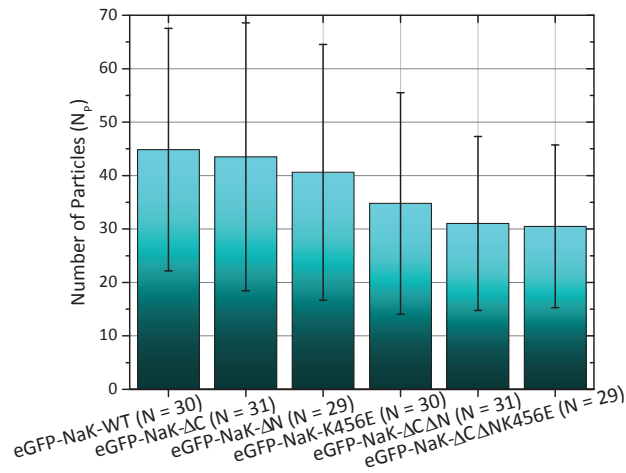


Figure 6.17: Averaged number of particle in the observation volume of the different eGFP-labeled Na,K-ATPase mutants and wild-type with the corresponding standard deviation and number of cells taken into account.

It seems that the number of particles are more similar for some of the eGFP-labeled Na,K-ATPase constructs like the wild-type, the eGFP-NaK-ΔC- and the eGFP-NaK-ΔN mutant. This is underlined by the resulting numbers for eGFP-NaK-WT with  $N_p = 45 \pm 23$  and the two caveolin-1 associated mutants (eGFP-NaK-ΔC, eGFP-NaK-ΔN) with  $N_p = 44 \pm 25$  and  $41 \pm 24$ . But for the ankyrin B associated mutant (eGFP-NaK-K456E) the number of particles is a little bit lower with  $35 \pm 21$  compared with the other constructs, which was already visible for the construct labeled with Dreiklang. Also the images of this mutant show a more prominent intracellular staining than the other ones. The double- and the threefold mutant (eGFP-NaK-ΔCΔN and eGFP-NaK-ΔCΔNK456E) exhibit with  $31 \pm 16$  and  $31 \pm 15$  the lowest number of molecules ( $N_p$ ). A two-sample Student's t-test confirms that the calculated number of particles ( $N_p$ ) of Na,K-ATPase wild-type and the two mutants eGFP-NaK-ΔCΔN and eGFP-NaK-ΔCΔNK456E were significantly different ( $P < 0.01$ ).

## 6.3 Fluorescence Recovery after Photobleaching

### 6.3.1 Image-, Data Analysis and Fitting Procedure

Fluorescence recovery after photobleaching (FRAP) measurements were performed on a commercial Leica microscope setup as described in detail in section 3.3.4. FRAP image sequences from every investigated cell were subsequently analyzed using *ImageJ* software and the *BioFormats* plugin [115]. Figure 6.18 shows an exemplary image sequence of a FRAP measurement. Mean fluorescence intensities  $I(t)$  were read out within a defined region of interest 1 (*ROI1*) in the bleached area on the cell membrane.

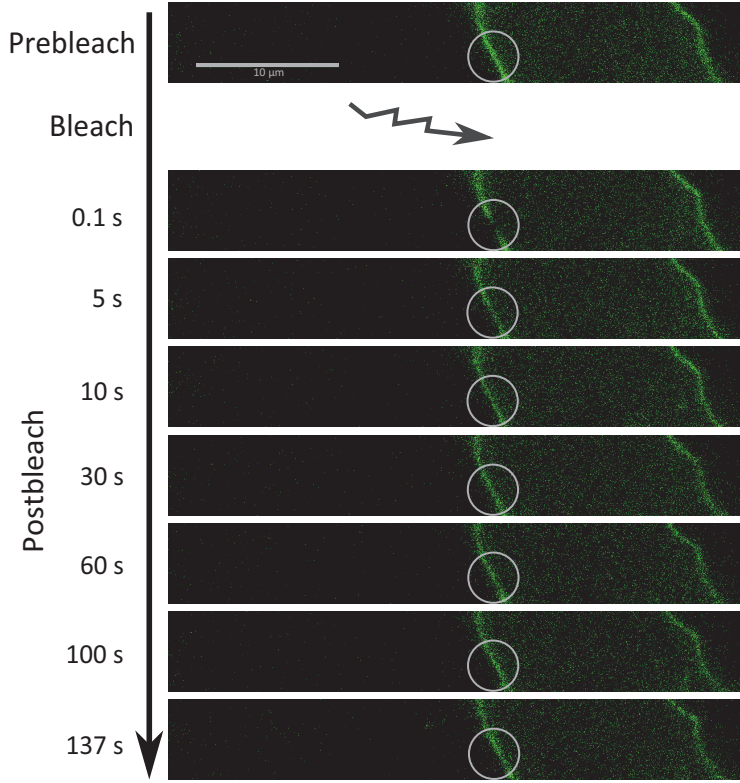


Figure 6.18: Visual comparison of eGFP-NaK-WT fluorescence (green emission) in HEK293T cells at indicated time points before and after photobleaching.

In order to compensate for bleaching effects over the scanning time, the averaged fluorescence intensity  $I_{ref}(t)$  of a reference area ( $ROI2$ , also on the membrane) was taken. For background correction, the fluorescence intensity  $I_{back}(t)$  outside the cell was specified ( $ROI3$ ).

The data were analyzed using the open source software *easyFRAP* [116]. In the first step, the background intensity is subtracted from all measurements and then a double normalization procedure is performed, which scales the data between 0 to 1. This type of normalization accounts for differences in starting intensities in  $ROI1$  and for the fluctuations of the total fluorescence signal during the complete sequence acquisition, due to photobleaching or variations in the laser intensity:

$$I_{double\,norm}(t) = \left[ \frac{\frac{1}{n_{pre}} \cdot \sum_{t=1}^{n_{pre}} I_{ROI2}(t)}{I_{ROI2}(t)} \right] \cdot \left[ \frac{I_{ROI1}(t)}{\frac{1}{n_{pre}} \cdot \sum_{t=1}^{n_{pre}} I_{ROI1}(t)} \right] \quad (6.3)$$

The subscript *pre* symbolizes the time before bleach. The full scale normalization is performed according to:

$$I_{full\,scalenorm}(t) = \frac{I_{double\,norm}(t) - I_{double\,norm}(t_{postbl})}{1 - I_{double\,norm}(t_{postbl})} \quad , \quad (6.4)$$

and corrects additionally for differences in the bleaching depth. These steps were performed for every investigated cell of the same Na,K-ATPase construct. Since the obtained data were not well described with a mono-exponential model, a two-exponential model was used. Thus, the following model was fitted to the data using a non-linear least square minimization algorithm implemented in *MatLAB*:

$$I_{FIT}(t) = I_0(t) - a \cdot e^{-bt} - c \cdot e^{-dt} \quad . \quad (6.5)$$

From these fit functions the mobile fraction  $M$  and the  $t_{1/2}$ -values for all cells were determined. The mobile fraction is given from equation 3.30, but in case of a full scale normalization the formula reduces to the following expression:

$$M = I_\infty \quad . \quad (6.6)$$

The  $t_{1/2}$ -value is given by the time of half-maximal recovery  $I_\infty$  of  $I$  and is determined numerically by the software in case of full scale normalization with a double-exponential model. This procedure was performed for every investigated cell and Na,K-ATPase construct for comparison.

### 6.3.2 FRAP with DRK-labeled Na,K-ATPase

Fluorescence recovery after photobleaching (FRAP), as described in section 3.2.5, requires the irreversible photobleaching of the fluorescent markers in the region of interest (ROI). By the use of Dreiklang as fluorescence marker, reversible FRAP studies are possible, in which the protein is switched into the OFF-state instead of irreversible bleaching. Thus, the process is reversible and can be repeated several times for the same cell and ROI, without any photodamage.

Figure 6.19 shows the normalized averaged fluorescence recovery curves of the various DRK-labeled Na,K-ATPase  $\alpha_2$ -subunit constructs, acquired by reversible or irreversible FRAP measurements. The number of cells used for calculation of the average was larger or equal to 16.

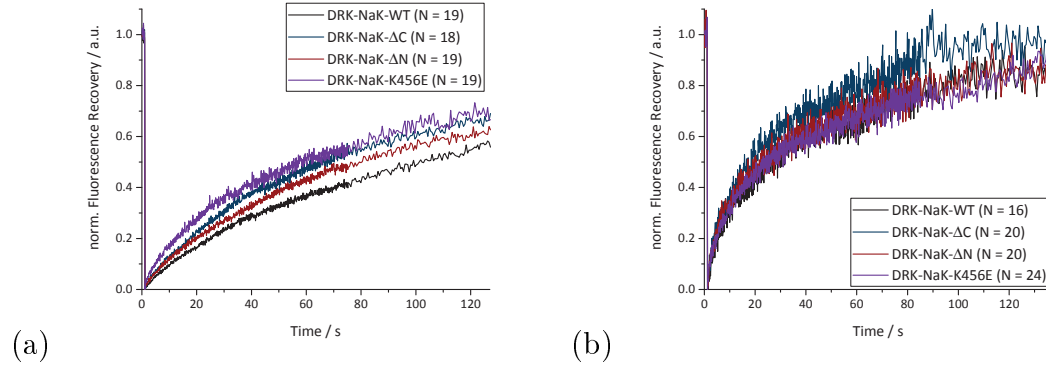


Figure 6.19: **(a)** Normalized averaged reversible fluorescence recovery curves of Dreiklang-labeled Na,K-ATPase mutants and wild-type measured in the plasma membrane of HEK293T cells. **(b)** Normalized averaged irreversible fluorescence recovery curves of DRK-labeled Na,K-ATPase mutants and wild-type measured in the plasma membrane of HEK293T cells. Measurements of 16 and more cells are taken into account, as indicated.

It can be directly seen that the recovery of the fluorescence signal occurs for all investigated Dreiklang-labeled Na,K-ATPase constructs on a very long temporal scale and does not reach a plateau within two minutes observation time, as shown in Fig. 3.8 (a). This usually corresponds to  $I_\infty$  and it is directly proportional to the mobile fraction of fluorophores  $M$ . The determined mobile fraction  $M$  is for all constructs around 81 % to 87 %. Fig. 6.19 (a) shows that DRK-NaK-WT exhibits the slowest  $t_{1/2}$ -value of  $(78 \pm 37)$  s. This corresponds approximately to the FRAP diffusion time. The two caveolin-1 associated mutations result in  $t_{1/2}$ -values of  $(46 \pm 21)$  s for DRK-NaK- $\Delta$ C and  $(52 \pm 23)$  s for DRK-NaK- $\Delta$ N. The ankyrin B associated mutant (DRK-NaK-K456E) exhibits the fastest  $t_{1/2}$ -value of  $(39 \pm 23)$  s. It was confirmed by a two-sample Student's t-test that the corresponding  $t_{1/2}$ -values of the mutants compared with the WT were significantly different ( $P < 0.05$ ).

Next, the behavior of the fluorescence recovery of the DRK-labeled Na,K-ATPase constructs after reversible and irreversible bleaching is compared. Notably, reversible bleaching was obtained by switching the Dreiklang proteins into an OFF-state. Fig. 6.19 (b) clearly shows that different recovery curves are obtained for FRAP experiments with irreversible bleaching than for reversible bleaching measurements (see again Fig. 6.19 (a)).

All averaged normalized recovery curves from Fig. 6.19 (b) exhibit a much faster recovery for all Na,K-ATPase constructs compared to the corresponding curves from reversible bleaching experiments. This is underlined by the determined  $t_{1/2}$ -value for e.g. of DRK-NaK-WT, which is about  $(19 \pm 12)$  s. This is four times faster than the  $t_{1/2}$ -value resulting from the reversible bleaching measurement. The corresponding

mobile fraction  $M$  of the DRK-NaK-WT was calculated to be  $(85 \pm 18) \%$ . For the mutants (DRK-NaK- $\Delta$ C, DRK-NaK- $\Delta$ N and DRK-NaK-K456E), the determined mobile fractions and the  $t_{1/2}$ -values are not significantly different ( $P > 0.05$ ) from those obtained for DRK-NaK-WT (see Table 6.3). These recovery curves do also not reach a plateau within the observed time. All determined mobile fractions  $M$  and  $t_{1/2}$ -values are summarized in Table 6.3. The diffusion constants  $D$  of all constructs were calculated using eq. 3.31 and the determined  $t_{1/2}$ -values are listed in Table 6.3.

### 6.3.3 FRAP with eGFP-labeled Na,K-ATPase

FRAP experiments were also performed on the different eGFP-labeled Na,K-ATPase mutants and wild-type in order to compare the measured diffusion constants with those obtained by FCS. Figure 6.20 presents the normalized averaged fluorescence recovery curves of all eGFP constructs measured in the plasma membrane of HEK293T cells. For the average more than 18 cells were taken into account.

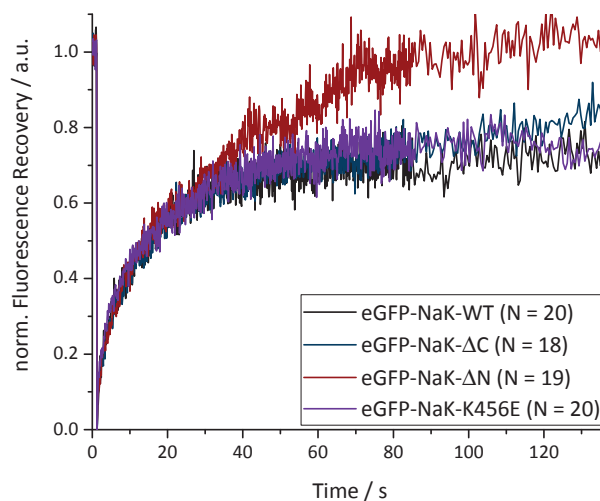


Figure 6.20: Normalized averaged fluorescence recovery curves of eGFP-labeled Na,K-ATPase mutants and wild-type measured in the plasma membrane of HEK293T cells. Measurements of 18 and more cells are taken into account, as indicated.

Fig. 6.20 shows that all constructs show a similar fluorescence recovery compared to those labeled with Dreiklang. The recovery of the fluorescence signal from irreversible photobleaching with eGFP as marker is faster than the recovery from reversible- and irreversible bleaching measurements with the fluorescence tag DRK and each curve reaches the plateau within the observation time of 2 minutes, which corresponds to a partial recovery to initial state. In this set of measurements, the eGFP-NaK-WT exhibits the lowest mobile fraction with  $(75 \pm 22) \%$  and the mu-

tant eGFP-NaK- $\Delta$ N the highest with  $(93 \pm 11)$  %, as clearly visible in Fig. 6.20. The other two mutants do not show significant differences from the wild-type regarding the determined mobile fractions. The calculated  $t_{1/2}$ -values show a similar trend. The wild-type and the mutant eGFP-NaK-K456E possess the fastest fluorescence recovery with a  $t_{1/2}$ -value of  $(8 \pm 6)$  s. The eGFP-NaK- $\Delta$ C mutant has also a very similar recovery time of  $(11 \pm 8)$  s. Only the caveolin-1 associated mutant (eGFP-NaK- $\Delta$ N) shows a significant difference in the  $t_{1/2}$ -value of  $(12 \pm 5)$  s and of the mobile fraction compared to the eGFP-NaK-WT as confirmed by a two-sample t-test ( $P < 0.05$ ). The determined mobile fractions  $M$ ,  $t_{1/2}$ -values and the calculated diffusion constants  $D$  are summarized in Table 6.3 for all FRAP measurements with eGFP-labeled proteins.

## 6.4 Discussion

### 6.4.1 Differences between DRK- and eGFP-labeling for the Diffusion Measurements by FCS

In this section, the diffusion properties of eGFP and Dreiklang as measured by FCS under different experimental situations are compared. When these proteins are measured as purified FPs in PBS buffer, the autocorrelation curves and the estimated diffusion times are very similar (Table 6.1). The resulting diffusion coefficients (Table 6.1) of eGFP agree well with the data published for the fluorophores in aqueous solutions ( $8.7 \cdot 10^{-11}$  m<sup>2</sup>/s [117];  $(9.32 \pm 0.22) \cdot 10^{-11}$  m<sup>2</sup>/s [118]). According to equation 3.28, these diffusion coefficients would yield values for the hydrodynamic radius of 3.0 nm (eGFP) or 2.7 nm (DRK) assuming a dynamic viscosity of water at 22 °C equal to  $\eta_W = 9.5 \cdot 10^{-4}$  Pa · s [113]. These agree with the published results for GFP ( $(2.3 \pm 0.05)$  nm [118]) and are consistent with the dimension of the eGFP  $\beta$ -barrel from crystal structures (barrel diameter  $\sim$ 3 nm, barrel length  $\sim$ 5 nm, PDB structure 1GFL). When expressed in the cytoplasm of HEK293T cells, DRK as well as eGFP yielded one correlation time with 376  $\mu$ s and 479  $\mu$ s, which is attributed to diffusion (Table 6.1). The same diffusion constants of  $(1.9 \pm 0.9) \cdot 10^{-11}$  m<sup>2</sup>/s for DRK and eGFP were obtained. These values are smaller by a factor of about 4 - 4.5 than those measured in PBS buffer and agree fairly well with the range of values of 2.5 to  $3 \cdot 10^{-11}$  m<sup>2</sup>/s reported from FRAP experiments [117]. The smaller diffusion coefficient values reflect the higher viscosity of the cytoplasm and other diffusion barriers located inside the cell, in agreement with [117], in which a 3.2-fold higher viscosity of the cytoplasm compared to water was found. Based on the values of the viscosity of water as an approximation for PBS solution ( $\eta_W = 9.5 \cdot 10^{-4}$  Pa · s

at 22 °C [113]), the viscosity of the cytoplasm can be calculated from the above diffusion times as  $3.8 - 4.3 \cdot 10^{-3} \text{ Pa} \cdot \text{s}$ , which is similar to the viscosity of a ~43 % (w/w) glycerol/water mixture at 20 °C [119].

Table 6.1: Summary of calculated diffusion times and constants.

Sample	Diffusion Time $\tau_D$		Diffusion Constant $D$ in $\text{m}^2/\text{s}$
R6G in eGFP settings, PH70	25 $\mu\text{s} \pm$	1 $\mu\text{s}$	$2.8 \cdot 10^{-10} *$
R6G in DRK settings, PH70	29 $\mu\text{s} \pm$	2 $\mu\text{s}$	$2.8 \cdot 10^{-10} *$
R6G in DRK settings, PH80	33 $\mu\text{s} \pm$	3 $\mu\text{s}$	$2.8 \cdot 10^{-10} *$
Purified DRK in PBS	106 $\mu\text{s} \pm$	22 $\mu\text{s}$	$(8.5 \pm 1.8) \cdot 10^{-11}$
Purified eGFP in PBS	95 $\mu\text{s} \pm$	2 $\mu\text{s}$	$(7.6 \pm 0.2) \cdot 10^{-11}$
DRK in cytoplasm	479 $\mu\text{s} \pm$	222 $\mu\text{s}$	$(1.9 \pm 0.9) \cdot 10^{-11}$
eGFP in cytoplasm	376 $\mu\text{s} \pm$	69 $\mu\text{s}$	$(1.9 \pm 0.3) \cdot 10^{-11}$
DRK-Na,K-ATPase in PM	318 $\mu\text{s} \pm$	212 $\mu\text{s}$	$(2.8 \pm 1.9) \cdot 10^{-11}$
	44 ms $\pm$	14 ms	$(1.8 \pm 0.6) \cdot 10^{-13}$
eGFP-Na,K-ATPase in PM	974 $\mu\text{s} \pm$	331 $\mu\text{s}$	$(0.7 \pm 0.3) \cdot 10^{-11}$
	67 ms $\pm$	17 ms	$(1.1 \pm 0.3) \cdot 10^{-13}$

\*[111, 112]

Both, eGFP- and DRK-labeled Na,K-ATPase in the plasma membrane exhibited a much slower diffusion. This is due to both the larger molecular weight (about 184 kDa) compared to the isolated FPs (27 kDa), and more importantly, the larger dynamic viscosity of the lipid membranes compared to aqueous media. In both cases, the autocorrelation functions exhibited two diffusion components (Table 6.1). Whereas the relative contribution of fast and slowly diffusing fractions was about (50/50) % in case of the DRK-labeled proteins, values of (31/69) % were found for the eGFP-labeled ones.

Formally, the autocorrelation curves indicate the presence of at least two independent fractions with largely different mobility. However, a rationalization of the two temporal components is complicated. The fast diffusion time of the DRK-labeled Na,K-ATPase in the plasma membrane is not significantly larger than that of the isolated DRK protein in the cytoplasm. This is a surprising result even considering the fact that the diffusion coefficient (or diffusion time) is only weakly dependent on the protein molecular weight. From a rough approximation which treats the diffusing molecules as spheres with hydrodynamic radii proportional to the cubic root of the molecular weight (eGFP: 26.9 kDa, eGFP-labeled Na,K-ATPase  $\alpha$ - and glycosylated  $\beta$ -subunit: 183.5 kDa) the diffusion coefficient should increase by a factor of  $\sqrt[3]{\frac{183.5}{26.9}} \approx 1.9$  for the isolated eGFP/DRK proteins compared to eGFP-/DRK-labeled Na,K-ATPase. The fast diffusion time of the eGFP-labeled Na,K-ATPase in the plasma membrane is about 3-fold larger than the diffusion time of eGFP in the cytoplasm, which would be reasonable in comparison with the rough calculation made above. However, diffusion of membrane-intrinsic proteins might encounter

boundary conditions that restrict the effective area, through which diffusion is possible (e.g. fixed macromolecules at high density or "excluded" membrane areas, which - due to different lipid content - might be in a liquid crystalline phase). Under such conditions, the effective area available for particle diffusion might be smaller than the detection volume, which in effect can lead to the observation of artificially short correlation times, i.e. some of the diffusion area is not accessible by the proteins. In any case, the differences between the short diffusion times of the DRK- and eGFP-labeled Na,K-ATPase cannot be due to differences in molecular weight or differential friction caused by the fluorescence tags, since the hydrodynamic properties of eGFP and DRK should be very similar. Different oligomerization or aggregation behavior of DRK- compared to eGFP-labeled Na,K-ATPase is also rather unlikely. Although eGFP and DRK have not been modified to explicitly yield monomeric FPs (e.g. by the most common A206K mutation [120]), it was reported that eGFP and DRK migrate as monomers on semi-native SDS gels [37]. However, even the artificial creation of dimeric or even tetrameric Na,K-ATPase complexes based on FP-mediated assembly would only increase diffusion time by 26 % or 58 %, respectively, nor would one expect to find an increased fraction of slowly diffusing Na,K-ATPase complexes in the case of eGFP-labeling.

From the above correlation times, the calculated diffusion coefficients for DRK- and eGFP-labeled Na,K-ATPase in the plasma membrane are compiled in Table 6.1. The diffusion coefficient associated with the short diffusion time of eGFP-labeled Na,K-ATPase is about 10-fold smaller than that of the isolated eGFP in solution and those from the long diffusion times are about 300-fold (DRK label) or 730-fold (eGFP label) smaller than the ones measured in PBS. In the literature, very little information about the diffusion of Na,K-ATPase is available for a comparison. In fact, only FRAP studies exist, which were carried out several years ago. For Na,K-ATPase in renal proximal tubule epithelial cells, a diffusion constant  $D = 3.3 \cdot 10^{-14} \text{ m}^2/\text{s}$  was found, which increased to  $2.39 \cdot 10^{-13} \text{ m}^2/\text{s}$  upon treatment with cytochalasin A, an agent, which causes actin depolymerization and thus disrupts the cytoskeleton [121]. Vaz and co-workers studied the related  $\text{Ca}^{2+}$ -ATPase (about 100 kDa) from rabbit muscle sarcoplasmic vesicles reconstituted in liquid-crystalline phase bilayers and found  $D = 1.8 \cdot 10^{-12} \text{ m}^2/\text{s}$  (at 36 °C) and  $D = 9.9 \cdot 10^{-13} \text{ m}^2/\text{s}$  (at 13 °C). Other values for comparison can be obtained from a more theoretical viewpoint. Within the model for two-dimensional diffusion developed by Saffman and Delbrück in 1975 [122], membrane proteins are considered as cylindrical inclusions of radius  $R_0$  that diffuse in an infinite two-dimensional bilayer of thickness  $h$  and viscosity  $\eta_m$  within a solvent of viscosity  $\eta_s$ . This results in a weak, logarithmic dependence of

the diffusion constant  $D_{SD}$  on the particle radius:

$$D_{SD} = \frac{k_B \cdot T}{4 \cdot \pi \cdot \eta_m \cdot h} \left( \ln \frac{h \cdot \eta_m}{R_0 \cdot \eta_s} - \gamma \right) \quad , \quad (6.7)$$

where  $\gamma \approx 0.5772$  is the Euler-Mascheroni constant. In a recent systematic study on the diffusion dynamics of membrane proteins with largely varying size (molecular weights between 11.3 kDa (0.7 nm radius) for cytochrome b5 and 345 kDa (3.6 nm radius) for a trimeric ABC transporter, AcrB) reconstituted in black lipid membranes, lateral diffusion coefficients between  $8.5 \cdot 10^{-12}$  m<sup>2</sup>/s and  $10.2 \cdot 10^{-12}$  m<sup>2</sup>/s were reported [123], in compliance with the Saffman-Delbrück model, which was also confirmed by others [124]. However, other authors found a stronger  $1/R_0$  dependence on the radius following Stokes-Einstein behavior [125] according to:

$$D_{SE} = \frac{k_B \cdot T \cdot \lambda}{4 \cdot \pi \cdot \eta_m \cdot h \cdot R_0} \quad . \quad (6.8)$$

Here, the parameter  $\lambda$  is introduced as a characteristic length scale for dimensional reasons. Justifications for the Stokes-Einstein-like behavior were given based on e.g. hydrophobic mismatch or changes in bulk hydrodynamics due to height mismatch between the membrane and the embedded protein [126]. However, the question whether Saffman-Delbrück or Stokes-Einstein behavior governs diffusion of membrane proteins is still a matter of debate and cannot be resolved here.

If, due to the uncertainty of the  $\lambda$  parameter in eq. 6.8, the Saffman-Delbrück formula is used to predict the diffusion coefficient of membrane-embedded Na,K-ATPase (with the radius of the membrane-embedded part of the protein  $R_0 = 2.4$  nm estimated from PDB structure 2ZXE [48], the solvent viscosity  $\eta_s = 4 \cdot 10^{-12}$  Pa · s given by the dynamic viscosity of the cytoplasm determined here, and a membrane thickness = 4 nm), diffusion constants between  $6.0 \cdot 10^{-12}$  m<sup>2</sup>/s and  $2.2 \cdot 10^{-12}$  m<sup>2</sup>/s are obtained, if the extreme values for the membrane viscosity published in the literature ( $3 - 150 \cdot 10^{-3}$  Pa · s [123, 127, 128]) are taken into account. All these comparisons show that theoretical free diffusion models as well as measurements on artificial bilayer systems can only rationalize diffusion times in the range of a few milliseconds for membrane-embedded ATPases, whereas diffusion times in the range of tens to one hundred milliseconds appear to be characteristic for experimental situations in living cells, in which membrane proteins are engaged in molecular interactions or anchoring processes that severely restrict diffusion. For Na,K-ATPase, several interactions with components of the cytoskeleton like ankyrin B [64] or other matrix proteins like caveolin-1 [62] are well established, and it will be addressed in the membrane of native cells (see section 6.2.3 and section 6.4.2), whether the interference

with these interaction motifs changes the dynamic mobility behavior of the enzyme in cellular membranes. Since previous works have also suggested that the diffusion times of e.g. membrane receptors vary according to the density of molecules in the membrane [89], it was also checked, whether a correlation of the obtained diffusion times to the average number of molecules in the confocal volume (calculated from the  $G(0)$  value) existed. However, we found no systematic correlation even though  $N$  values of more than 50 were observed (data not shown). Interestingly, such a density of Na,K-ATPase molecules in the confocal area ( $\sim 0.125 \mu\text{m}^2$ ) would yield a total of about 500,000 molecules in the plasma membrane of a spherical cell of  $20 \mu\text{m}$  diameter, which (given a turnover number of charge transport by Na,K-ATPase of about  $100 \text{ s}^{-1}$  at  $25 \text{ }^\circ\text{C}$  [129]) would result in a whole-cell current of about 10 pA, a typical value for Na,K-ATPase expressed in mammalian cells measured by electrophysiology [130].

This work also shows that photophysical properties of DRK and eGFP are very different, although eGFP and DRK have nearly identical molecular weight and molecular structure. If the photophysical properties of DRK and the parental eGFP were similar, the fluorescence tag should have no influence on the shape of the autocorrelation curves or the diffusion behavior of the fluorescence-tagged proteins in FCS measurements. However, the normalized autocorrelation curves of the DRK-labeled Na,K-ATPase are of lower amplitude compared to eGFP and especially the shorter of the two diffusion times is markedly different. In addition, the same differences were observed for the purified proteins (eGFP, DRK) upon slowing down diffusion velocity by means of viscous media. These results strongly indicate that DRK undergoes some, as yet not clearly identified, photophysical quenching processes. This transition could e.g. be switching to the dark state, for which the true "action spectrum" is not known in detail and clearly necessitates further investigation. This quenching process is apparent on a time scale of hundreds of microseconds to milliseconds and, therefore, has a great influence on the autocorrelation curves of DRK-labeled membrane protein complexes of large molecular mass. It cannot be observed when molecular diffusion is studied in an aqueous medium. Due to the low viscosity of the aqueous medium the diffusion time of purified DRK through the OVE is short. If the diffusion time is shorter comparable to the characteristic decay time of the photophysical switching process, one only observes DRK molecules that are in the "bright" state, but rarely observes switching between these states while the molecule is traversing the OVE. In contrast, when molecular diffusion is slowed down, as is the case in the plasma membrane, and the diffusion time becomes much longer than the characteristic time of the switching process, the molecule switches between photophysical states many times while passing through the observation volume element. Hence, it can be observed. Further support for the notion of an

additional quenching process in DRK as compared to eGFP can be drawn from Figure 6.5 (b), since the normalized autocorrelation curves of DRK-labeled Na,K-ATPase profoundly depend on the intensity of the excitation laser. Regarding other evidence for photobleaching in the literature, the initial work by Brakemann and co-workers found a half-life time of 21 s for irradiation of DRK-expressing *E. coli* colonies at 491 nm with 188 kW/cm<sup>2</sup> intensity [37]. In a recent work that evaluated the usability of DRK for several superresolution microscopy techniques, the authors applied GSDIM (ground-state depletion followed by individual molecule return), a spatially stochastic image reconstruction mode [108]. Using 488 nm laser light at 3 kW/cm<sup>2</sup> intensity to transfer the fluorophores from the singlet ground state ( $S_0$ ) into a long-lived dark state via the excited state  $S_1$ , a switching time of 10 s was reported to obtain sufficiently complete dark-state conversion. Since the excitation power in our FCS experiment (40  $\mu$ W or 12  $\mu$ W at the objective lens for DRK- or eGFP-labeled cells, respectively) is equivalent to about 25 kW/cm<sup>2</sup> (DRK) or 10 kW/cm<sup>2</sup> (eGFP), it is conceivable that dark-state conversion of DRK is an experimental concern for FCS on the time scale typical for the diffusion of membrane-embedded protein complexes. Thus, the fluorescence properties of the DRK chromophore need to be examined in much more detail, especially regarding the action spectra for ON- and OFF-switching or dark state conversion / bleaching and the intensity dependence of these processes in order to understand the effects of these processes on FCS curves better in future investigations.

#### 6.4.2 Mobility in the Plasma Membrane Probed by FCS

In this work, the dependence of the mobility of the Na,K-ATPase  $\alpha_2$ -subunit in the cell plasma membrane of the different binding sites on the cytoskeleton, e.g. in interaction motifs with caveolin-1 (NaK- $\Delta$ C, NaK- $\Delta$ N) and in an interaction motif of ankyrin B (NaK-K456E) labeled with DRK or eGFP were probed by FCS. Since no differences in the diffusion behavior of the Na,K-ATPase mutants and WT labeled by DRK were observed (see Fig 6.11 (a) and (b)), the fluorescence label was changed to the well-known fluorescent protein eGFP. More details about the photoswitching problems observed by FCS for DRK-labeled membrane proteins are given in section 6.4.1. The resulting normalized autocorrelation curves for the different eGFP-labeled Na,K-ATPase constructs (eGFP-NaK- $\Delta$ C, eGFP-NaK- $\Delta$ N, eGFP-NaK-K456E) exhibit a clear difference in diffusion behavior compared to the Na,K-ATPase wild-type (see Fig. 6.12 and Fig. 6.13). In all cases, the autocorrelation curves exhibited two diffusion components, a fast and a slow diffusion time (see Table 6.2). Differences are also clearly visible for the double- and the threefold mutant (eGFP-NaK- $\Delta$ C $\Delta$ N, eGFP-NaK- $\Delta$ C $\Delta$ NK456E).

Table 6.2: Summary of calculated diffusion times and determined diffusion coefficients for different eGFP-labeled Na,K-ATPase constructs.

Sample	Diffusion Time $\tau_D$	Fractional Amplitude in %	Diffusion Constant $D$ in $\text{m}^2/\text{s}$
eGFP-NaK-WT	533 $\mu\text{s} \pm 160 \mu\text{s}$	41 $\pm 6$	$(1.4 \pm 0.4) \cdot 10^{-11}$
	63 ms $\pm 18$ ms	59 $\pm 6$	$(1.1 \pm 0.3) \cdot 10^{-13}$
eGFP-NaK- $\Delta C$	411 $\mu\text{s} \pm 127 \mu\text{s}$	43 $\pm 5$	$(1.8 \pm 0.6) \cdot 10^{-11}$
	43 ms $\pm 9$ ms	57 $\pm 5$	$(1.7 \pm 0.4) \cdot 10^{-13}$
eGFP-NaK- $\Delta N$	438 $\mu\text{s} \pm 149 \mu\text{s}$	42 $\pm 5$	$(1.6 \pm 0.5) \cdot 10^{-11}$
	46 ms $\pm 7$ ms	58 $\pm 5$	$(1.6 \pm 0.2) \cdot 10^{-13}$
eGFP-NaK-K456E	334 $\mu\text{s} \pm 132 \mu\text{s}$	46 $\pm 8$	$(2.2 \pm 0.9) \cdot 10^{-11}$
	41 ms $\pm 7$ ms	54 $\pm 8$	$(1.8 \pm 0.4) \cdot 10^{-13}$
eGFP-NaK- $\Delta C\Delta N$	335 $\mu\text{s} \pm 130 \mu\text{s}$	44 $\pm 6$	$(2.2 \pm 0.9) \cdot 10^{-11}$
	38 ms $\pm 9$ ms	56 $\pm 6$	$(1.9 \pm 0.5) \cdot 10^{-13}$
eGFP-NaK- $\Delta C\Delta N$ K456E	299 $\mu\text{s} \pm 102 \mu\text{s}$	51 $\pm 6$	$(2.4 \pm 0.8) \cdot 10^{-11}$
	34 ms $\pm 8$ ms	49 $\pm 6$	$(2.1 \pm 0.5) \cdot 10^{-13}$

The Na,K-ATPase WT exhibits the slowest mobility of all investigated constructs, with diffusion coefficients of  $D_1 = (1.4 \pm 0.4) \cdot 10^{-11} \text{ m}^2/\text{s}$  and  $D_2 = (1.1 \pm 0.3) \cdot 10^{-13} \text{ m}^2/\text{s}$ . The relative contribution of fast and slow diffusion component is about 41 % and 59 %. The two caveolin-1 associated mutants show significantly different diffusion times compared to the Na,K-ATPase wild-type. The calculated diffusion constants are  $(1.8 \pm 0.6) \cdot 10^{-11} \text{ m}^2/\text{s}$  and  $(1.7 \pm 0.4) \cdot 10^{-13} \text{ m}^2/\text{s}$  for eGFP-NaK- $\Delta C$  and  $(1.6 \pm 0.5) \cdot 10^{-11} \text{ m}^2/\text{s}$  and  $(1.6 \pm 0.2) \cdot 10^{-13} \text{ m}^2/\text{s}$  for eGFP-NaK- $\Delta N$ . The contribution of fast and slow diffusion is very similar for both mutants with (43/57) % for NaK- $\Delta C$  and (42/58) % for NaK- $\Delta N$ . The ankyrin B associated mutant shows a faster diffusion with diffusion coefficients of  $(2.2 \pm 0.9) \cdot 10^{-11} \text{ m}^2/\text{s}$  and  $(1.8 \pm 0.4) \cdot 10^{-13} \text{ m}^2/\text{s}$  (46 % and 54 %).

Furthermore, the double mutant (eGFP-NaK- $\Delta C\Delta N$ ) exhibits a faster diffusion compared to the single mutations associated with caveolin-1 (eGFP-NaK- $\Delta C$ , eGFP-NaK- $\Delta N$ ) and a very similar diffusion behavior like the ankyrin B associated mutant with diffusion coefficients of  $(2.4 \pm 0.8) \cdot 10^{-11} \text{ m}^2/\text{s}$  and  $(1.9 \pm 0.5) \cdot 10^{-13} \text{ m}^2/\text{s}$  (44 % and 56 %). The fastest diffusion is found for the threefold mutant that comprises all single mutations with diffusion coefficients of  $(2.4 \pm 0.8) \cdot 10^{-11} \text{ m}^2/\text{s}$  and  $(2.1 \pm 0.5) \cdot 10^{-13} \text{ m}^2/\text{s}$ . The relative contribution of fast and slow diffusion is now 51 % and 49 %.

In order to understand the measured diffusion times and the calculated diffusion coefficients of the different Na,K-ATPase constructs, the structure of the biological membrane has to be considered (see Fig. 6.21).

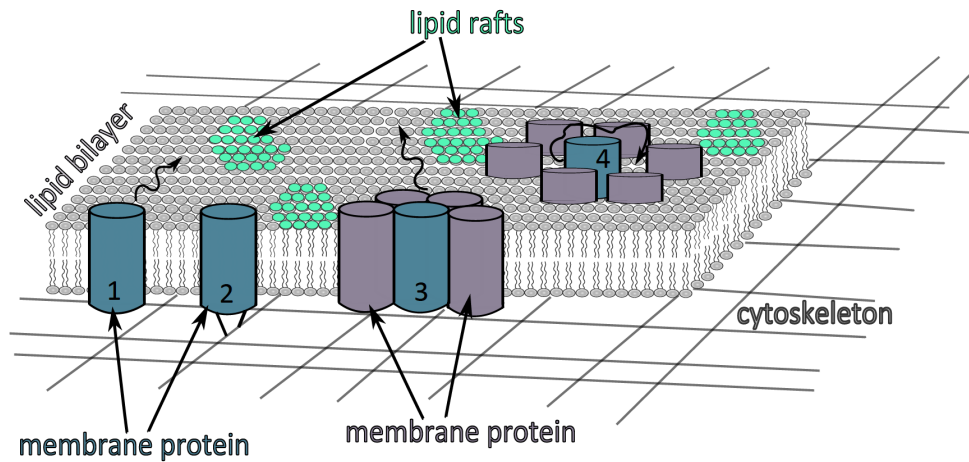


Figure 6.21: Plasma membrane structure with processes that might hinder the free, two-dimensional diffusion of membrane proteins. (1) Free diffusion of a membrane protein through the lipid bilayer. (2) A Membrane protein bound to the cytoskeleton like a transmembrane protein. (3) Multimeric complex of membrane proteins, which lead to a reduced mobility compared to a single membrane protein (1). (4) Corral forming by membrane proteins, that reduces the mobility of the observed protein. Also shown are lipid-rafts (light green), which lead to microdomains in the plasma membrane and are not accessible for most of the transmembrane proteins. The image was reproduced in modified form from [131].

Nowadays, a lot of different models, which try to describe the plasma membrane structure of living cells and the observed diffusion behavior of membrane proteins have been proposed, but the whole system is still not fully understood. The first model was the fluid mosaic model described in 1972 by Singer and Nicolson [132]. In this model, the biological membrane is considered as a two-dimensional liquid, which is highly dynamic. All membrane-embedded proteins and lipids can laterally diffuse freely through the membrane (see Fig. 6.21 (1)). Recent findings points out considerable heterogeneity in the membrane organisation and a more complex structure as initially assumed. In the plasma membrane lipid microdomains exist (shown in light green in Fig. 6.21), also referred as lipid-rafts in the literature, which are enriched in cholesterol content and contain various glyco- and sphingolipids. The increased affinity of certain membrane proteins to those lipids leads to an accumulation in the microdomains (microdomain model) [133]. Therefore, it is clearly evident that diffusion of membrane proteins is hindered by these microdomains, because mostly they can not escape from these compartments of the cell membrane or they do not have access to it. Moreover, interactions with the cellular cytoskeleton and other cellular matrix proteins, as well as integral membrane proteins lead to the forma-

tion of heterogeneous protein complexes (meshwork model). This causes at the same time a complex and dynamic restructuring of the plasma membrane. Thus, the lipid bilayer can be understood as a medium, which allows a dynamic patterning of the membrane protein complexes [134, 135].

Two other models have been also proposed in the literature, the membrane-skeleton "fence" model also termed membrane-skeleton "corralling" model and the anchored-protein "picket" model. The former suggests that a fence is built up at the intracellular interface of the lipid bilayer by the actin filament network and leads therefore, to small compartments. Transmembrane proteins are thus hindered in diffusion, which is then resulting in shortened diffusion times within one compartment. Kusumi *et al.* also assumed that the transmembrane proteins can hop between the different compartments, which lead to a long term hop diffusion for transmembrane proteins. The anchored-protein "picket" model works for all membrane proteins and assumes that different transmembrane proteins are anchored to the membrane-skeleton fence and lined up in there. Therefore, they act like pickets on the membrane-skeleton. For more details about these two models see Kusumi *et al.* [136, 137].

The Na,K-ATPase  $\alpha_2$ -subunit studied in this work is an integral membrane protein with 10 transmembrane segments and several large cytoplasmic loops, as already described in section 2.2. It is clearly evident from Fig. 6.21 and the different plasma membrane structure models, that the diffusion of the Na,K-ATPase in the plasma membrane does not correspond to free Brownian motion in a two-dimensional liquid. Even for Na,K-ATPase WT the diffusion behavior is more complex and can be affected by microdomains or compartments, which might not be accessible by the protein. The enzyme can also be hindered in diffusion by the cytoskeleton meshwork as well as by lipid-rafts. The higher viscosity of the plasma membrane compared to water influences also the diffusion time, as mentioned in section 6.4.1.

Furthermore, the diffusion behavior can be affected by other proteins like caveolin-1, which is a membrane protein and belongs to caveolae, as already mentioned above. Caveolae are invaginations of the plasma membrane that built up microdomains, which are enriched of e.g. cholesterol [60]. Thus, they belong to the lipid-rafts, which are described within the different models for the biological membrane structure. The binding of Na,K-ATPase to caveolae domains has been extensively discussed in the literature. Furthermore, Xie *et al.* assumed that enzymes like the Na,K-ATPase and other signaling proteins tend to concentrate in caveolae, which might then lead to the formation of large signaling complexes [59]. Cai *et al.* showed by FRAP measurements on LLC PK1 cells that cav.-1 is highly immobile within the plasma membrane [62]. From all these hypotheses, it is probable that the disruption of the cav.-1 binding sites (NaK- $\Delta$ C and NaK- $\Delta$ N) on the Na,K-ATPase  $\alpha_2$ -subunit leads

to a faster diffusion compared to the Na,K-ATPase wild-type. This was effectively observed, in the diffusion measurements by FCS as described in section 6.2.3. It is also evident that the double mutant (NaK- $\Delta$ C $\Delta$ N) in which both interaction motifs with caveolin-1 are disrupted, exhibits a faster diffusion compared to the NaK- $\Delta$ C and NaK- $\Delta$ N mutants and the NaK-WT. One can speculate that the double mutant loses the interaction with caveolin-1 and thus the interaction with lipid-rafts or microdomains completely, whereas the single mutants are maybe just untightened on one side of the enzyme.

As already mentioned in section 2.2.4, ankyrin B is a cytoskeleton protein which is involved in the stabilization of the Na,K-ATPase in the plasma membrane [56]. The mutated binding site (NaK-K456E) is also associated to fix the Na,K-ATPase on the cytoskeleton. Therefore, a mutation on this position leads to a partially released or even freely diffusing Na,K-ATPase in the plasma membrane. In comparison, it seems that the binding of the Na,K-ATPase on the cytoskeleton through the ankyrin B interaction motif has a stronger influence on the diffusion behavior than the binding to microdomains by the two single binding sites associated to cav.-1. If both cav.-1 binding sites are disrupted, as it is the case for the double mutant, then the diffusion behavior is comparable to the diffusion of the eGFP-NaK-K456E mutant. The threefold mutant (NaK- $\Delta$ C $\Delta$ NK456E) comprises all three single mutations and exhibits a clearly faster diffusion within the plasma membrane compared to all other Na,K-ATPase mutants and WT. This fact could be explained by no or just a reduced binding to the cytoskeleton (NaK-K456E) and impaired recruitment to lipid-rafts or microdomains (NaK- $\Delta$ C and NaK- $\Delta$ N).

Since the Na,K-ATPase studied here is one enzyme type or even a complex of the  $\alpha_2$ - and  $\beta_1$ -subunits, one would expect that a single characteristic diffusion time would be obtained by FCS measurements. However, the previously described models of the membrane structure would predict a large variance of the mobility for membrane-embedded proteins. Therefore, a single-component model is not sufficient to describe the measured autocorrelation curves for this type of proteins. This has been already shown by other groups for various integral membrane proteins [133, 138]. In literature, the diffusion time is commonly estimated considering the molecular weight of a protein, as already mentioned in section 6.1. The Na,K-ATPase  $\alpha_2$ -subunit together with the  $\beta_1$ -subunit has a molecular weight of about 183.5 kDa, which gives a diffusion time of around 1.8 ms in the case of free diffusion roughly calculated from the molecular weight. If one now assumes that caveolin-1 builds up macrostructures of 14 to 16 monomers with a total weight between 300 kDa up and 400 kDa [60], a diffusion time of 2.6 ms would be expected. It is therefore evident that even the formation of large hetero-oligomeric protein complexes cannot explain the

observed, very long diffusion times [139]. These roughly calculated diffusion times does not fit to the data obtained by FCS measurements (e.g eGFP-NaK-WT  $\tau_1 = (533 \pm 160) \mu\text{s}$  and  $\tau_2 = (63 \pm 18) \text{ms}$ ).

From another point of view, more recent works suggest that membrane proteins undergo an anomalous subdiffusion, instead of free Brownian diffusion. In case of anomalous diffusion, the mean-square displacement (MSD) of molecules is no longer linear with the time  $t$ , as it is the case of normal free diffusion. The MSD is rather proportional to  $t^\alpha$ , with  $0 < \alpha \leq 1$ . If  $\alpha$  corresponds to 1, then the molecules diffuse freely [133, 139–141]. Wawrezynieck *et al.* suggests that FCS measurements within the plasma membrane probed for one size of observation volume element (OVE) are difficult to interpret in presence of microdomains and cytoskeleton meshwork. This is especially true, for the diffusion behavior of different membrane components, like lipids or transmembrane proteins. Therefore, diffusion laws were defined, which describe the diffusion behavior of proteins as a function of the size of the OVE also termed as spot area ( $w^2$ ). Fig. 6.22 shows four different possible diffusion models for the membrane organization, which are presented from Lenne and co-workers and are used for their simulations of the diffusion laws.

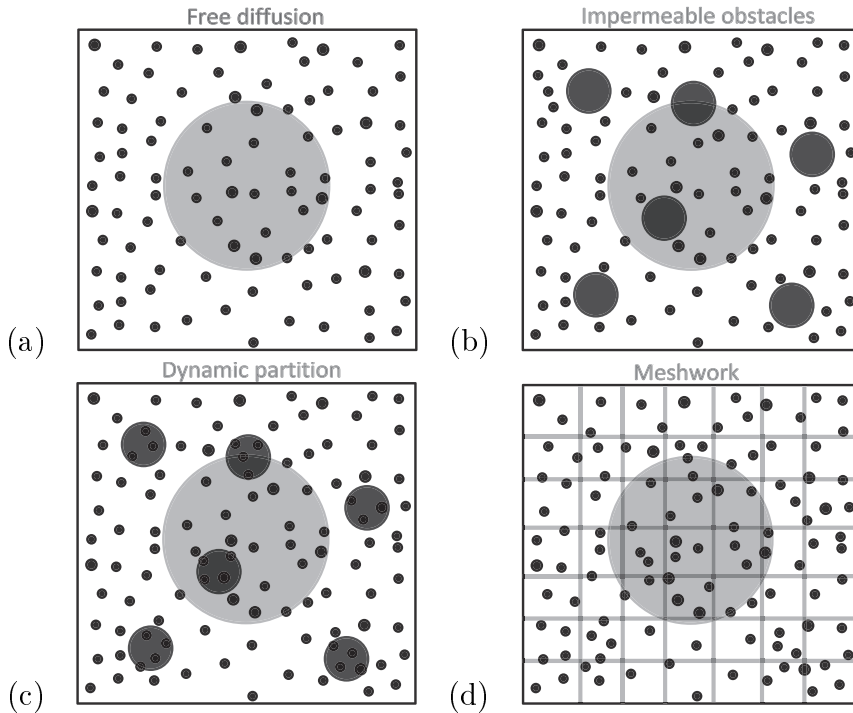


Figure 6.22: Different membrane models used for simulated FCS diffusion laws **(a)** Free diffusing molecules (black dots) showing pure Brownian motion in the OVE (large grey circle). **(b)** Membrane model with impermeable obstacles (dark grey circles) like microdomains, that restricted the diffusion. **(c)** Dynamic partition model suggests that the molecules can diffuse into and out of the microdomains. **(d)** Cytoskeleton meshwork model, associated that the diffusion of molecules is hindered by barriers (light grey grid). Image is reconstructed [135].

Fig. 6.23 shows the diffusion time  $\tau_D$  as a function of the spot area ( $w^2$ ) for the different diffusion membrane models given in Fig. 6.22 (a) - (d). The diffusion laws were tested in simulations for the existence of different barriers and microdomains within the plasma membrane and compared with measurements on living COS-7 cells expressing a lipid and a transmembrane protein [142].

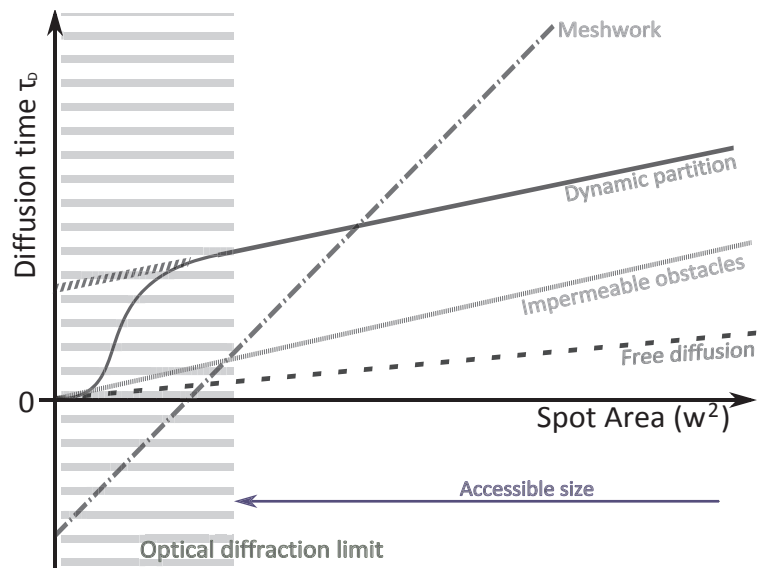


Figure 6.23: Results for the different membrane models of simulated FCS diffusion laws, like free diffusing molecules, impermeable obstacles, dynamic partition or meshwork. The diffusion time  $\tau_D$  as a function of the spot area ( $w^2$ ) is given. Image is reconstructed and extended from [135].

Lenne *et al.* underlined the suggestions of Wawrezynieck *et al.* and showed the same analytical method for various membrane proteins in living COS-7 cells measured by FCS [135]. It is also shown in literature that protein diffusion coefficients vary between different cell lines, as well as for different measurement techniques [140].

In the case of the considered Na,K-ATPase WT and mutants a short diffusion time (299  $\mu$ s - 533  $\mu$ s) was always obtained. This could be explained by an apparently reduced observation volume element induced by a compartmentalization of the plasma membrane, which generates inaccessible regions of the plasma membrane for the Na,K-ATPase. This results in artificial shortened diffusion times. On the other hand, it must be considered that FCS measurements on the plasma membrane contain always a signal contribution from the cytoplasm, which exhibits a shorter diffusion time [141, 143]. The slow diffusion time obtained for all Na,K-ATPase constructs (34 ms - 63 ms) can be explained by the fixation of the observed proteins to the cytoskeleton meshwork. A hop diffusion process also cannot be excluded. The two calculated diffusion coefficients of the Na,K-ATPase constructs are in good agreement with those found in literature. The group of Oshugi *et al.* exhibited for

example very similar diffusion coefficients for membrane-binding fluorescent proteins in COS-7 and HeLa cells ( $D_1 = 2.7 \cdot 10^{-11} \text{ m}^2/\text{s}$  and  $D_2 = 5.6 \cdot 10^{-13} \text{ m}^2/\text{s}$ ). In that paper, the autocorrelation curves were mainly fitted with two-component models for two-dimensional and three-dimensional diffusion. The short diffusion time was associated to free diffusion of molecules near the plasma membrane in the cytoplasm [143].

In conclusion, although a clear statement about the reason for the complex diffusion times can not be given, the data show that clear effects on the characteristic diffusion times of the various eGFP-labeled Na,K-ATPase constructs can be discriminated, when known interaction motifs are disrupted by mutations. Future studies should focus on the mobility of different mutations of the Na,K-ATPase, which are associated to human diseases like FHM, RDP and AHC by FCS. These measurements could give a hint, whether some FHM, RDP or AHC mutations are associated with altered interactions with Na,K-ATPase binding partners, which might show up by differences in diffusion behavior. All of these studies might help to understand the pathophysiology of these diseases more in detail.

### 6.4.3 Total Number of Molecules in the Confocal Volume for Different Na,K-ATPase Constructs

In section 6.2.4, the total number of molecules  $N_P$  in the confocal volume element depending on the measured Na,K-ATPase constructs by FCS was studied. This number of molecules  $N_P$  provides information about the expression level of the Na,K-ATPase protein in the plasma membrane. More precisely, it reflects only the mobile fraction of proteins. The FCS measurements in which Dreiklang was the used fluorescence label show that the number of diffusing molecules is low. As a comparison, Na,K-ATPase wild-type labeled with eGFP (eGFP-NaK-WT) exhibits a higher expression level in the cell membrane than Na,K-ATPase wild-type labeled with DRK (DRK-NaK-WT). This effect is also observable by the acquired images of DKR-labeled cells, which showed a reduced plasma membrane fluorescence signal compared to the eGFP marked cells. The obtained reduced fluorescence signal under the use of Dreiklang could be explained by characteristics of Dreiklang. The physiological pH of living cells is about 7.1 and at this pH 50 % of the Dreiklang chromophores are shifted to the protonated form of the chromophore compared to a pH of 7.4 (see section 5.2). This protonated form has its absorption maximum at 412 nm. Therefore, the Dreiklang-labeled cells give reduces fluorescence signal by excitation at 514 nm.

The different Na,K-ATPase mutants labeled with eGFP compared to the eGFP-NaK-WT show that the two caveolin-1 associated mutants (NaK- $\Delta$ C, NaK- $\Delta$ N) behave similarly to the NaK-WT. This is also visible for the same mutants when Dreiklang is used as fluorescence marker. The ankyrin B associated mutant (NaK-K456E) reveals for both labels a clearly reduced number of particles and the cell images indicate a lot of diffuse intracellular staining. This suggests a disrupted or disordered transport of the membrane protein from the ER to the plasma membrane. The same effect was observed in AAS measurements of section 2.4.6, in which the rubidium uptake was significantly reduced for the NaK-K456E mutant compared to the NaK-WT. The lowest number of molecules was observed for the threefold- (eGFP-NaK- $\Delta$ C $\Delta$ NK456E) and the double (eGFP-NaK- $\Delta$ C $\Delta$ N) mutant, which show values three times smaller compared to the NaK-WT. The same trend was also visible for the rubidium uptake and the images shown exhibit for both mutants a more diffuse intracellular pattern, instead of a clear plasma membrane staining.

The obtained results of the reduced amount of Na,K-ATPase molecules for the different mutants in the plasma membrane can be confirmed in future investigations with a plasma membrane preparation. In order to better understand the reasons of the reduced amount of Na,K-ATPase molecules the question should be solved, if the transport mechanism from ER to the membrane is disrupted in some of the studied Na,K-ATPase mutants or not.

#### 6.4.4 Mobility in the Plasma Membrane Studied by FRAP

In this section different types of FRAP measurements on the Na,K-ATPase constructs are compared and the two used labeling strategies (eGFP and Dreiklang) as well as reversible and irreversible photobleaching are considered.

First of all, the diffusion constants  $D$  for every construct were calculated using eq. 3.31 and the assumption was made that the bleach radius was about 1  $\mu$ m, as previously discussed by [29]. All calculated diffusion constants are summarized in Table 6.3 together with the determined mobile fractions  $M$  and  $t_{1/2}$ -values for all investigated eGFP-/DRK-labeled Na,K-ATPase constructs.

Table 6.3: Summary of determined mobile fractions  $M$ ,  $t_{1/2}$ -values and calculated diffusion constants  $D$  for different eGFP-/DRK-labeled Na,K-ATPase constructs.

Sample	Bleaching Method	Mobile Fraction $M$ in %	$t_{1/2}$ in s	Diffusion Constant $D$ in $\text{m}^2/\text{s}$
DRK-NaK-WT	reversible	$87 \pm 17$	$78 \pm 37$	$(3.2 \pm 1.5) \cdot 10^{-15}$
DRK-NaK- $\Delta\text{C}$	reversible	$83 \pm 22$	$46 \pm 21$	$(5.4 \pm 2.5) \cdot 10^{-15}$
DRK-NaK- $\Delta\text{N}$	reversible	$81 \pm 19$	$52 \pm 23$	$(4.8 \pm 2.1) \cdot 10^{-15}$
DRK-NaK-K456E	reversible	$81 \pm 24$	$39 \pm 23$	$(6.4 \pm 3.8) \cdot 10^{-15}$
DRK-NaK-WT	irreversible	$85 \pm 18$	$19 \pm 12$	$(1.3 \pm 0.8) \cdot 10^{-14}$
DRK-NaK- $\Delta\text{C}$	irreversible	$94 \pm 13$	$17 \pm 9$	$(1.5 \pm 0.8) \cdot 10^{-14}$
DRK-NaK- $\Delta\text{N}$	irreversible	$87 \pm 15$	$18 \pm 11$	$(1.4 \pm 0.9) \cdot 10^{-14}$
DRK-NaK-K456E	irreversible	$85 \pm 17$	$18 \pm 12$	$(1.4 \pm 0.9) \cdot 10^{-14}$
eGFP-NaK-WT	irreversible	$75 \pm 22$	$8 \pm 6$	$(3.1 \pm 2.3) \cdot 10^{-14}$
eGFP-NaK- $\Delta\text{C}$	irreversible	$82 \pm 19$	$11 \pm 8$	$(2.3 \pm 1.7) \cdot 10^{-14}$
eGFP-NaK- $\Delta\text{N}$	irreversible	$93 \pm 11$	$12 \pm 5$	$(2.1 \pm 0.9) \cdot 10^{-14}$
eGFP-NaK-K456E	irreversible	$79 \pm 19$	$8 \pm 6$	$(3.1 \pm 2.3) \cdot 10^{-14}$

Additionally, the photoswitchable Dreiklang protein as fluorescence label offers the opportunity for reversible FRAP measurements with minimal cell damage. This can be achieved by switching the protein in a nonfluorescent OFF-state instead of irreversible bleaching with high laser intensities. These measurements show that the fluorescence recovery exhibits a completely different behavior for reversible bleaching compared to the irreversible one. The recovery of the fluorescence signal of the OFF-switched Na,K-ATPase constructs labeled with DRK took a longer time compared to the irreversible FRAP measurements, which show mostly a fast recovery shortly after photobleaching. The reversible bleaching provided  $t_{1/2}$ -values of  $(39 \pm 23)$  s up to  $(78 \pm 37)$  s, which lead to diffusion coefficients of  $(6.4 \pm 3.8) \cdot 10^{-15}$   $\text{m}^2/\text{s}$  and  $(3.2 \pm 1.5) \cdot 10^{-15}$   $\text{m}^2/\text{s}$  respectively. The calculated mobile fraction  $M$  for this set of data is also not very accurate, because no plateau was reached during the data acquisition. The slow  $t_{1/2}$ -values are explained by the fact that Dreiklang is mostly found in the ON-state at room temperature. Therefore, the OFF-switched chromophores tend to reactivate due to thermal equilibrium and 100 % recovery is always reached for reversible FRAP measurements. Brakemann and co-workers specified that this equilibrium time constant at room temperature is about 400 s [37]. Nevertheless, the different DRK-labeled Na,K-ATPase constructs measured by reversible FRAP show  $t_{1/2}$ -values, which are significantly different ( $P < 0.05$ ), compared to the Na,K-ATPase WT. That means that the three mutants (DRK-NaK- $\Delta\text{C}$ , DRK-NaK- $\Delta\text{N}$  and DRK-NaK-K456E) show a faster recovery time than the Na,K-ATPase WT, which suggests that the diffusion of the mutated Na,K-ATPase constructs is faster, most likely due to disruption of interactions with the respective matrix proteins. The largest deviation from the Na,K-ATPase WT is found for the ankyrin B associated mutant. As previously mentioned, the  $t_{1/2}$ -values are estimated

from the fluorescence recovery curves, which contain contribution both from the thermal reactivation and pure diffusion processes. The contribution of both effects introduces large inaccuracies in the calculated parameters, which make it difficult to derive quantitative conclusions from the data. Additionally, 100 % recovery is always reached after a certain time.

Irreversible FRAP measurements on DRK-labeled Na,K-ATPase constructs show a faster recovery compared to reversible FRAP (see Table 6.3). However, no significant differences between the Na,K-ATPase mutants and the wild-type are observed. Again it needs to be considered that Dreiklang undergoes some reversible photo-physical processes as well on the timescale for FRAP measurements, as already mentioned about the FCS measurements (see section 6.4.1) and underlined by a lower total number of molecules  $N_P$ , which lead to a reduced expression of the membrane protein in the plasma membrane compared to eGFP-labeled cells (see section 6.4.3).

On the other side, a fast component with a large contribution is visible for all fluorescence recovery curves in the irreversible FRAP measurements (see Fig. 6.19 (b) and Fig. 6.20) for both labels (eGFP and DRK). This component has been attributed in literature to a photoswitching process of the chromophores and leads often to an overestimation of the mobility and to false identification of the diffusion behavior. Sinnecker *et al.* showed for different enhanced green fluorescent proteins like eYFP, eCFP and Citrine that they undergo reversible photobleaching under commonly used FRAP settings and lead therefore to significant artifacts in the experiments [38]. It was also shown that this effect has no influence on FCS measurements, since the timescale (above ms to hundreds of s) is not accessible by FCS. Furthermore, Mueller and co-workers showed the same effect for other fluorescent proteins under typical FRAP conditions. They additionally give suggestions how to minimize these effects and presented a mathematical procedure to correct FRAP data for these reversible photobleaching effects [39]. Morisaki *et al.* demonstrated that this photoswitching effect is not present for other fluorophores. The group showed FRAP measurements on GFP-tagged histone H2B and H2B labeled with the organic fluorophore tetramethylrhodamine (TMR) through the genetically encoded HaloTag. They demonstrated that H2B-GFP in FRAP shows an apparent fast component of 15 %, whereas the same measurements with the organic fluorophore (H2B-Halo-TMR) presented only a very small fast component ( $\sim 1$  %) contribution [40]. In summary, the presented FRAP data for eGFP and DRK in this work can also include a fast component from reversible photoswitching and are therefore, may also be biased by the aforementioned FRAP artifact. Furthermore, the reversible FRAP data should be considered as a first qualitative result which only gives a hint about the different diffusion behavior of the various Na,K-ATPase constructs.

The results obtained by the FRAP measurements on eGFP-labeled Na,K-ATPase constructs exhibit, compared to the Dreiklang-labeled constructs, a faster recovery. Furthermore, all the recovery curves reach a plateau region. The calculated mobile fractions for the different Na,K-ATPase constructs yield values between  $(75 \pm 22)$  % for eGFP-NaK-WT and  $(93 \pm 22)$  % for eGFP-NaK- $\Delta$ N. The two other mutants (eGFP-NaK- $\Delta$ C and eGFP-NaK-K456E) exhibit intermediate mobile fraction values. From these data it could only be shown that  $M$  for the eGFP-NaK- $\Delta$ N mutant is significantly different from the Na,K-ATPase wild-type. One can say from these data, that the wild-type has lowest mobility, which means that it is fixed within the plasma membrane or bound to the cytoskeleton, whereas 25 % of the caveolin-1 associated eGFP-NaK- $\Delta$ N mutant are mobile. On the other hand, the second caveolin-1 associated mutant (eGFP-NaK- $\Delta$ C) and the ankyrin B associated mutant (eGFP-NaK-K456E) exhibit similar values of the mobile fractions as the NaK-WT. This could be attributed to an insufficient statistics, and the number of cells should be increased to better discriminate small variations of this parameter. The evaluated  $t_{1/2}$ -values show the same trend as for the mobile fraction of the different Na,K-ATPase constructs. The NaK-WT construct exhibits the fastest recovery or diffusion of  $(8 \pm 6)$  s and the eGFP-NaK- $\Delta$ N mutant the slowest with  $(12 \pm 5)$  s. Those are significantly different according to statistical consideration ( $P < 0.05$ ). Conversely the other Na,K-ATPase mutants show intermediate values which are not significantly different. The estimated  $t_{1/2}$ -values from the measured data greatly deviates from expectations. One would expect a faster recovery for the studied Na,K-ATPase mutants compared to the Na,K-ATPase wild-type. Indeed the disruption of the ankyrin B associated binding site should lead to a more free diffusion and therefore higher mobility. The same assumption could be made for the two caveolin-1 associated mutants of the Na,K-ATPase. However, no of such differences were observed with irreversible FRAP measurements.

The resulting diffusion coefficients  $D$  (Table 6.3) for the different eGFP-labeled Na,K-ATPase mutants and wild-type show values between  $(2.1 \pm 0.9) \cdot 10^{-14}$  m<sup>2</sup>/s and  $(3.1 \pm 2.3) \cdot 10^{-14}$  m<sup>2</sup>/s, which agree well with the data published for Na,K-ATPase in intact renal proximal tubule epithelial cells ( $(3.31 \pm 0.7) \cdot 10^{-14}$  m<sup>2</sup>/s; [121]). Recent publications list values between  $1 \cdot 10^{-16}$  cm<sup>2</sup>/s and  $1 \cdot 10^{-14}$  cm<sup>2</sup>/s for membrane-embedded proteins (see [29]), and a more recent work gives values for membrane proteins studied by FRAP between  $2 \cdot 10^{-14}$  cm<sup>2</sup>/s and  $2.2 \cdot 10^{-13}$  cm<sup>2</sup>/s depending on the number of transmembrane segments [144]. The Na,K-ATPase  $\alpha_2$ -subunit used in this work consists of 10 transmembrane segments, which show a diffusion coefficient that is in good agreements with the data obtained by Kumar *et al.*

Compared to the diffusion coefficients for the Na,K-ATPase labeled with eGFP resulted from FCS experiments (see Table 6.2), a large mismatch between the obtained data is visible. The diffusion coefficients from FRAP experiments are at least one order of magnitude smaller ( $10^{-14}$  m<sup>2</sup>/s) as the one obtained by FCS ( $10^{-11}$  m<sup>2</sup>/s -  $10^{-13}$  m<sup>2</sup>/s). One would expect similar results for both techniques on identical systems or Na,K-ATPase constructs. Other groups observed similar mismatches between the diffusion coefficients measured by FRAP and FCS. For example, Calizo and co-workers found diffusion coefficients in the order of  $10^{-13}$  m<sup>2</sup>/s by FCS and  $10^{-15}$  m<sup>2</sup>/s by FRAP on G-protein coupled receptors [145]. Similar effects were observed by Adkins *et al.* who assumed that the diffusion coefficients determined by FRAP are always one order of magnitude smaller than those observed by FCS. In that case the dopamine transporter tagged with the yellow fluorescent protein (YFP) was studied and compared with a epidermal growth factor receptor and  $\beta$  adrenergic receptor both labeled with eGFP [146]. These authors proposed that the resulting diffusion coefficients or diffusion times depend on the used cell line, which was shown for non-neuronal cells like HEK293 and neuronally derived N2a cell line. Kühn *et al.* also confirmed the work of Adkins and co-workers for different cell lines, for measurements in the cytoplasm and the nucleus and the differences in the diffusion coefficients for FRAP and FCS [26].

Another aspect which has to be taken into account is that FRAP is a complex experiment which requires many parameters to be carefully chosen or accurately determined. As examples, the used bleaching profile (spot, line, disk) and bleaching depth are often assumed, which could lead to large variations in the resulting fluorescence recovery curves [27, 28]. An additional problem for FRAP measurements in living cells is the unexpected phototoxicity, which can arise from the high intensity laser irradiation in the bleaching point and could produce substantial damage around the bleached region of interest [147].

An additional aspect that has to be considered is that a living cell is a complex system, especially the plasma membrane. This membrane is not just a flat fixed skin, but it shows crinkles, invaginations and a lot of enclosed compartments, which could lead to differences in the obtained diffusion times. In fact, one can not distinguish between these regions by FRAP (see also [136]). FRAP is also very insensitive to changes of the protein weight [148].

Weiss and co-workers showed that the diffusion coefficients are underestimated in most typical FRAP studies and FRAP data are highly prone to misinterpretations [149]. In this work, the  $t_{1/2}$ -values were just evaluated for each Na,K-ATPase construct and used as diffusion time in order to calculate the diffusion coefficients. This is valid only as a rough approximation and a more quantitative data analysis for the

diffusion behavior and the mobility of the Na,K-ATPase in the plasma membrane would be required. For a better description of the resulting fluorescence recovery curves, one has to assume a model to correctly simulate the system. This is the only way to distinguish between pure diffusion, binding reactions and mixtures of these processes [24, 148, 149]. In literature, many different fit models have been proposed, which vary widely regarding their underlying hypotheses [150, 151]. Even more so, the quality of the measured curves does not allow a clear identification of the underlying model for the process. This is the reason why only qualitative parameters as  $t_{1/2}$ -values and  $M$  have been estimated from the data.

It is appropriate at this point to speculate and think about the used  $\beta_1$ -subunit, which stabilize the Na,K-ATPase  $\alpha_2$ -subunit as already mentioned in section 2.2. It would be interesting to investigate whether the obtained FRAP curves behave differently with other  $\beta$ -subunits. Finally, one can say that fluorescence recovery after photobleaching technique seems to be not the best choice for studies of the mobility of different Na,K-ATPase constructs in the plasma membrane, while FCS is tentatively preferable as the more accurate method. In fact, it allows for a more accurate estimation of the diffusional mobility of membrane proteins.



## 7 Summary

The aim of this work was the study of the mobility of the Na,K-ATPase  $\alpha_2$ -subunit and various mutations within the plasma membrane of living cells. The two common main techniques for diffusion studies are fluorescence correlation spectroscopy (FCS) and fluorescence recovery after photobleaching (FRAP), which are well described in literature [12, 23].

FCS observes fluorescence intensity fluctuations of molecules diffusing across a confocal volume of about 1 fL. On the other side, FRAP observes the diffusion of chromophores in a photobleached area of some square micrometers and measures the recovery time of the fluorescence signal. FCS allows the simultaneous observation of multiple fast-diffusing molecular species, while FRAP is limited to a temporal scale of the diffusion time above 1 ms. Furthermore, both methods require labeling of the observed proteins with suitable fluorescent markers. Since from the literature it is known that common genetically encoded fluorescent proteins, e.g. eGFP and Citrine, lead to artifacts in diffusion studies by FRAP due to photoswitching of the protein [38–40], the reversibly photoswitchable fluorescent protein Dreiklang (DRK) was used as fluorescent marker for these measurements [37]. In order to study the diffusion of different mutations on the Na,K-ATPase by FCS the well-known fluorescent protein eGFP were utilized as fluorescence marker. For a later on comparison all FCS and FRAP measurements were performed with both fluorescence tags, eGFP and DRK.

Since several mutations in the Na,K-ATPase  $\alpha$ -subunit genes are associated with different diseases, the overall understanding of the integration of the Na,K-ATPase into the plasma membrane is of great interest. By mutational disruption of binding sites of the Na,K-ATPase  $\alpha_2$ -subunit associated with ankyrin B (NaK-K456E) and caveolin-1 (NaK- $\Delta$ C, NaK- $\Delta$ N) it could be expected to observe changes in the plasma membrane targeting of the enzyme, changes of the localization within the plasma membrane and, consequently, of the diffusion behavior of the enzyme [56, 57, 61, 62].

FCS studies on the Na,K-ATPase labeled with DRK lead to the conclusion that DRK is unsuitable for FCS analysis. It seems that DRK undergoes photophysical quenching processes, which are in the same time range as the observed diffusion times and thus small differences in diffusion are not measurable.

The different Na,K-ATPase mutants labeled with eGFP (eGFP-NaK- $\Delta$ C, eGFP-NaK- $\Delta$ N, eGFP-NaK-K456E, eGFP-NaK- $\Delta$ C $\Delta$ NK456E) exhibit significant differences in the diffusion behavior within the plasma membrane compared with the Na,K-ATPase wild-type (eGFP-NaK-WT). All constructs exhibit two diffusion constants, one component for fast diffusion ( $D_1$ ) and a slow diffusion component ( $D_2$ ). Furthermore, the eGFP-NaK-WT shows the slowest diffusion behavior with diffusion coefficients of  $D_1 = (1.4 \pm 0.4) \cdot 10^{-11} \text{ m}^2/\text{s}$  and  $D_2 = (1.1 \pm 0.3) \cdot 10^{-13} \text{ m}^2/\text{s}$ . In contrast, the ankyrin B associated mutant shows the fastest diffusion from all observed Na,K-ATPase mutants with coefficients of  $D_1 = (2.2 \pm 0.9) \cdot 10^{-11} \text{ m}^2/\text{s}$  and  $D_2 = (1.8 \pm 0.4) \cdot 10^{-13} \text{ m}^2/\text{s}$ . The diffusion behavior of the two mutants associated with the binding to caveolin-1 (eGFP-NaK- $\Delta$ C, eGFP-NaK- $\Delta$ N) are located in between the two aforementioned constructs. The fastest diffusion times were found for the threefold mutant (eGFP-NaK- $\Delta$ C $\Delta$ NK456E), which comprises all single mutations and exhibits diffusion coefficients of  $D_1 = (2.4 \pm 0.8) \cdot 10^{-11} \text{ m}^2/\text{s}$  and  $D_2 = (2.1 \pm 0.5) \cdot 10^{-13} \text{ m}^2/\text{s}$ .

FRAP measurements on various Na,K-ATPase constructs labeled with eGFP do not show significant differences, but affirm problems commonly associated with FRAP experiments using genetically encoded fluorophores. DRK as fluorescence marker in standard FRAP settings also exhibits artificial shortened diffusion components, which can be attributed to reversible photoswitching of the fluorescent proteins and therefore these data may be prone to common FRAP artifacts. This problem is overcome by reversible FRAP experiments with DRK as fluorescence marker. However, these reversible FRAP data should be considered as a first qualitative result and only provides a hint for differences in the diffusion behavior of the various Na,K-ATPase constructs, because a thermal reactivation of the OFF-switched proteins into the ON-state is possible which overrides recovery by diffusional entry of fluorescent molecules into the bleached area.

From all investigated constructs in reversible FRAP measurements, the DRK-NaK-WT exhibited the slowest diffusion with a diffusion coefficient of  $D = (3.2 \pm 1.5) \cdot 10^{-15} \text{ m}^2/\text{s}$  and the DRK-NaK-K456E the fastest diffusion with  $D = (6.4 \pm 3.8) \cdot 10^{-15} \text{ m}^2/\text{s}$ . Also in this set of experiments, the two caveolin-1 associated mutants (DRK-NaK- $\Delta$ C, DRK-NaK- $\Delta$ N) are found between the two other constructs with diffusion coefficients of  $D = (5.4 \pm 2.5) \cdot 10^{-15} \text{ m}^2/\text{s}$  and  $D = (4.8 \pm 2.1) \cdot 10^{-15} \text{ m}^2/\text{s}$ .

---

FCS and FRAP experiments reveal for the different Na,K-ATPase constructs the same diffusion trend and differential behavior of the different mutants, but a large mismatch of the resulting diffusion coefficients is visible. The data from FRAP experiments are at least one order of magnitude smaller ( $10^{-14}$  m<sup>2</sup>/s -  $10^{-15}$  m<sup>2</sup>/s) as the one obtained by FCS ( $10^{-11}$  m<sup>2</sup>/s -  $10^{-13}$  m<sup>2</sup>/s). One would expect similar results for both techniques on identical systems or Na,K-ATPase constructs. However, from literature this mismatch is well-known and described by many other working groups in this field [26, 145, 146].

The obtained results for the diffusion behavior of the different Na,K-ATPase  $\alpha_2$ -subunit constructs can be explained well by the microdomain model as well as by the meshwork model. It seems that a combination of both microdomains and meshwork influence the binding of the Na,K-ATPase within the plasma membrane and, therefore, the diffusion behavior.

These measurements open another view on the integration of the Na,K-ATPase within the plasma membrane and provides an opportunity to gain a deeper understanding of the anchoring of this enzyme in the membrane. FCS measurements can be therefore used in future investigations on Na,K-ATPase mutants linked to several diseases.



# Appendix

## Used Buffer for Oocyte Preparation and AAS Measurements:

Table A.1

<b>ORI + Ca<sup>2+</sup></b> <b>(pH 7.5 - 7.6)</b>	110 mM NaCl 5 mM KCl 1 mM MgCl <sub>2</sub> 2 mM CaCl <sub>2</sub> 5 mM HEPES mit NaOH
<b>ORI + Ca<sup>2+</sup></b> <b>(pH 7.5 - 7.6)</b>	110 mM NaCl 5 mM KCl 1 mM MgCl <sub>2</sub> 5 mM HEPES
<b>Na<sup>+</sup>-Buffer</b> <b>(pH 7.4)</b>	100 mM NaCl 1 mM CaCl <sub>2</sub> 5 mM BaCl <sub>2</sub> 5 mM NiCl <sub>2</sub> or 2 mM MgCl <sub>2</sub> 2.5mM MOPS 2.5 mM Tris 10 μM Ouabain
<b>Na<sup>+</sup>-Loading Solution</b> <b>(pH 7.4)</b>	110 mM NaCl 2.5 mM Na <sup>+</sup> -Citrate 2.5 mM MOPS 2.5 mM Tris
<b>NMDG<sup>+</sup>-Buffer</b> <b>(pH 7.4)</b>	100 mM NMDG Cl 1 mM CaCl <sub>2</sub> 5 mM BaCl <sub>2</sub> 5 mM NiCl <sub>2</sub> or 2 mM MgCl <sub>2</sub> 2.5 mM MOPS 2.5 mM Tris 10 μM Ouabain 1 mM RbCl

## Used Buffer for the Cell Culture and pH-Dependent Measurements:

Table A.2

<b>Original PBS (pH 7.4)</b>	137 mM NaCl 2.7 mM KCl 8.1 mM Na <sub>2</sub> HPO <sub>4</sub> · 2H <sub>2</sub> O 1.76 mM KH <sub>2</sub> PO <sub>4</sub>
<b>Original PBS (pH 6.0 - 8.0)</b>	Original PBS HCl or NaOH
<b>Original PBS (pH 5.0 - 5.5)</b>	Original PBS 10 mM CH <sub>3</sub> COO <sub>2</sub> Na · 3H <sub>2</sub> O
<b>PBS equivalent (pH 10.0)</b>	150 mM NaCl 5 mM KCl 5 mM HEPES 5 mM Tris 10 mM CAPS

## Spectral Properties of the Used Fluorescent Proteins:

Comparison of some important spectral properties of the fluorescent proteins WT GFP, eGFP, TagRFP and DRK.  $\epsilon$  is the extinction coefficient at the excitation wavelength ( $\lambda_{Exc}$ ). The brightness is the calculated product of the extinction coefficient  $\epsilon$  and the quantum yield  $Q_y$ . The data for  $\lambda_{Exc}$ ,  $\lambda_{Em}$ ,  $\epsilon$ , and  $Q_y$  were obtained from [37, 67, 69–71].

Table A.3

<b>Fluorescent Protein</b>	$\lambda_{Exc}$ in nm	$\lambda_{Em}$ in nm	$\epsilon$ in M <sup>-1</sup> cm <sup>-1</sup>	$Q_y$	<b>Brightness (<math>\epsilon \cdot Q_y</math>)</b> in M <sup>-1</sup> cm <sup>-1</sup>
wild-type GFP	396 475	504	25,000 - 30,000 9,500 - 14,000	0.79	19,750 - 23,700 7,505 - 11,060
eGFP	488	507 - 509	55,000 - 57,000	0.60	33,000 - 34,200
TagRFP	555	584	100,000	0.48	48,000
DRK	511	529	83,000	0.41	34,030

---

## Viscosity of Aqueous Solutions of Sucrose:

Sucrose solutions were prepared at indicated percentages (in % w/w) in PBS buffer and the physicochemical properties of aqueous sucrose solutions are given [152].

Table A.4

% sucrose (w/w)	viscosity ratio ( $\eta/\eta_w$ )
0	1.000
10	1.333
20	1.941
30	3.181
40	6.150
50	15.400
60	58.370
70	480.600



# List of Abbreviations

<b>AAS</b>	Atomic absorption spectrophotometry
<b>ACC</b>	Autocorrelation curve
<b>ADC</b>	Analog-to-digital converter
<b>ADP</b>	Adenosine diphosphate
<b>AHC</b>	Alternating hemiplegia of childhood
<b>ATP</b>	Adenosine triphosphate
<b>BSA</b>	Bovine serum albumin
<b>cav.-1</b>	Caveolin-1
<b>cav.-2</b>	Caveolin-2
<b>CLSM</b>	Confocal laser scanning microscopy
<b>CNS</b>	Central nervous system
<b>DAS</b>	Decay associated spectra
<b>DMEM</b>	Dulbecco's Modified Eagle Medium
<b>DNA</b>	Deoxyribonucleic acid
<b>DRK</b>	Dreiklang
<b>DYT12</b>	Rapid dystonia parkinsonism
<b>eGFP</b>	Enhanced green fluorescent protein
<b>ER</b>	Endoplasmic reticulum
<b>FBS</b>	Fetal bovine serum
<b>FCS</b>	Fluorescence correlation spectroscopy
<b>FHM</b>	Familial hemiplegic migraine
<b>FLIM</b>	Fluorescence lifetime imaging microscopy
<b>FWHM</b>	Full width at half maximum
<b>FRAP</b>	Fluorescence recovery after photobleaching
<b>FRET</b>	Förster resonance energy transfer
<b>HEK293</b>	Human embryonic kidney 293 cell line
<b>IC</b>	Internal conversion
<b>IHS</b>	International headache society
<b>IRF</b>	Instrument response function
<b>ISC</b>	Intersystem crossing
<b>LQT4</b>	Long-QT syndrome type 4
<b>MPLC</b>	Medium pressure liquid chromatography
<b>MSD</b>	Mean-square displacement
<b>NA</b>	Numerical aperture
<b>NaK</b>	Na,K-ATPase
<b>NCX</b>	Na,Ca-exchanger
<b>OVE</b>	Observation volume element
<b>PALM</b>	Photoactivated localization microscopy
<b>PBS</b>	Phosphate buffered saline
<b>PCR</b>	Polymerase chain reaction
<b>PM</b>	Plasma membrane
<b>QA</b>	Quadrant anode
<b>RESOLFT</b>	Reversible switchable optical linear fluorescence transitions (microscopy)
<b>RNA</b>	Ribonucleic acid
<b>ROI</b>	Region of Interest
<b>ROS</b>	Reactive oxygen species
<b>RPD</b>	Rapid dystonia parkinsonism
<b>SNR</b>	Signal-to-noise ratio
<b>SPAD</b>	Single-photon avalanche photodiode
<b>STED</b>	Stimulated emission depletion (microscopy)
<b>STORM</b>	Stochastic optical reconstruction microscopy
<b>TAC</b>	Time-to-amplitude-converter
<b>tagRFP</b>	Tag red fluorescent protein
<b>TCSPC</b>	Time-correlated single photon counting
<b>THGF</b>	Transversely heated graphite furnace
<b>TM</b>	Transmembrane
<b>WT</b>	Wild-type



# List of Figures

2.1	Components of a typical animal/human cell. ....	10
2.2	Illustration of different compartments in living HEK293 cells. The different areas are marked with the fluorescent protein Dreiklang. As expected, the fluorescence in the cytoplasmically labeled cells is distributed over the entire cell <b>(a)</b> . The middle image shows the mitochondria and the nucleus is also clearly recognizable, which occupies more than half of the cell <b>(b)</b> . <b>(c)</b> A typical transmembrane protein, the Na,K-ATPase, is shown. A typical membrane staining and some intracellular staining from moving vesicles are visible. ....	12
2.3	The pictures show an untransfected HEK293T cell culture under a microscope with 20x magnification <b>(a)</b> and the same cell culture by bright-field microscopy at a higher resolution <b>(b)</b> .....	15
2.4	The Na,K-ATPase enzyme located in the plasma membrane with the mode of active ion transport upon hydrolysis of ATP. ....	16
2.5	X-ray crystal structure of the Na,K-ATPase in E <sub>2</sub> conformation and at 2.4 Å resolution (reconstructed from PDB entry 3A3Y) [48]. The α-subunit consists of ten transmembrane segments (purple) and contains intracellular the N- (orange), P- (green) and A domain (light red). The two bound K <sup>+</sup> ions in the transmembrane segments of the α-subunit (red) are also illustrated. The β-subunit with one transmembrane cylinder and the corresponding extracellular domain are painted in cyan. The γ-subunit is depicted in black. ....	17
2.6	The topological arrangement of the Na,K-ATPase α-, β- and γ-subunits is shown. The purple cylinders represent the ten transmembrane segments (M1 - M10) of the α-subunit, which are located in the transmembrane domain. The small extracellular and the larger intracellular loops with the three cytoplasmic domains (A, P and N) are also shown. The β-subunit (cyan cylinder) comprises only one transmembrane segment, like the γ-subunit painted in dark grey. ....	19
2.7	Scheme of the Na,K-ATPase α <sub>2</sub> -subunit with the positions of the desired mutations (orange points). ....	23

---

2.8	X-ray crystal structure of the Na,K-ATPase in E <sub>2</sub> conformation at 2.4 Å resolution (reconstructed from PDB entry 3A3Y) [48] with the positions of the two interaction motifs associated with caveolin-1 (NaK-ΔC, NaK-ΔN) and the interaction motif associated to ankyrin B (NaK-K456E). .	24
2.9	Structure of the green fluorescent protein (GFP) and the chromophore formed within. The picture is reconstructed from PDB entry 1GFL. The β-barrel and the α-helices are shown in cartoon representation and the chromophore as sticks. Carbons are displayed in light grey, nitrogen in blue and oxygen in red. ....	26
2.10	Structure of the fluorescent protein TagRFP (reconstructed from PDB entry 3M22). The β-barrel and the α-helices are shown in cartoon representation and the chromophore as sticks. ....	27
2.11	Structure of the photoswitchable fluorescent protein Dreiklang in the equilibrium state (reconstructed from PDB entry 3ST2). The β-barrel and the α-helices are shown in cartoon representation and the chromophore as sticks. ....	27
2.12	Scheme of the Dreiklang chromophore in different states and with the different switching wavelengths. a) shows the equilibrium, b) the OFF-state and c) the ON-state (all chromophores are reconstructed from PDB entry 3ST2, 3ST3 and 3ST4). The chromophore is represented as sticks. ....	28
2.13	The received purified Dreiklang protein after MPLC in a glass tube illuminated with UV light. ....	32
2.14	Pictures of a female clawed frog <i>Xenopus laevis</i> <b>(a)</b> and digested oocytes <b>(b)</b> . ....	33
2.15	<b>(a)</b> Normalized Rb <sup>+</sup> uptake of the caveolin-1 associated mutants labeled with Dreiklang (DRK-NaK-ΔC, DRK-NaK-ΔN) in comparison with the DRK-NaK-WT, human Na,K-ATPase wild-type, water injected and uninjected oocytes. The number N of measured oocytes is also shown. Data are given as means ± S.D. <b>(b)</b> Normalized Rb <sup>+</sup> uptake of the mutant DRK-NaK-K456E compared with eGFP-NaK-WT and DRK-NaK-WT. ....	35
2.16	Normalized Rb <sup>+</sup> uptake of all eGFP-labeled Na,K-ATPase mutations in comparison with the eGFP-labeled Na,K-ATPase wild-type and uninjected oocytes. Also the number N of measured oocyte is shown in each bar. Data are given as means ± S.D. ....	36

---

3.1	The Jablonski diagram shows the different electronic states of a molecule (singlet state S, triplet state T) with possible transitions between them. Radiative transitions are indicated by solid arrows in dark grey. Light grey dashed lines represent nonradiative transitions, such as intersystem crossing (ISC) and internal conversion (IC).....	40
3.2	Scheme of the Franck-Condon principle. The vibrational levels of the electronic ground state and the first excited state as a function of the nuclear coordinates are plotted. ....	41
3.3	Scheme of the optical pathway of a wide-field fluorescence microscope. The dashed blue line shows the effect, when the observed signal is shifted from the optical axis. ....	43
3.4	Scheme of the light beam path from a confocal microscope. The dashed blue line shows the effect, when the observed signal is shifted from the optical axis. ....	44
3.5	Working principle of time-correlated single photon counting (TCSPC) measurements. The photon arrival times of multiple cycles are summed up in a histogram (reconstructed from [80]). ....	46
3.6	Scheme of a confocal volume element with freely diffusion molecules. ...	49
3.7	Schematic representation of a common FRAP experiment with an intense laser beam in a living cell. ....	51
3.8	Typical monitored fluorescence recovery curve before ( $I_I(t)$ ) and after bleaching ( $I_\infty(t)$ ) in a region of interest over the time $t$ . ....	52
3.9	Scheme of the whole fluorescence microscopy setup ....	53
3.10	The PML-16C setup with the different available lasers is shown. ....	55
4.1	Comparison between the different mutations of Na,K-ATPase labeled with eGFP and TagRFP in living HEK293 cells (P979L, WT and FS) at different incubation temperatures. In the first row, bright-field pictures, then eGFP channel, the TagRFP channel and at least an overlay of eGFP and TagRFP is shown. ....	61
4.2	Ratio of fluorescence intensities between the green fluorescence of eGFP-labeled Na,K-ATPase constructs (WT: wild-type, PL: mutant P979L, FS: S966fs frame shift mutant) and the red fluorescence intensity of TagRFP in the cytoplasm, which is used as expression standard. For measuring the green fluorescence, either the intensity in the plasma membrane (blue columns) or in the cytoplasm (red columns) was taken. Also the number of sample cells measured is given. ....	62
4.3	Ratio of the normalized eGFP-Na,K-ATPase signal (TagRFP fluorescence used for normalization) in the membrane vs. the signal in the cytoplasm. ....	63

5.1	Normalized absorption and fluorescence emission spectra of purified Dreiklang proteins in PBS at pH 7.4. ....	68
5.2	Absorption- <b>(a)</b> and emission spectra <b>(b)</b> of purified Dreiklang protein in PBS at various pH-values. Fluorescence emission spectra were taken with excitation at 470 nm. ....	68
5.3	Overlay of the excitation spectrum of Dreiklang taken at an emission wavelength of 525 nm and the absorption spectrum. Both spectra were taken at physiological pH and have been normalized to a maximal amplitude of 1. ....	70
5.4	Steady-state emission spectra of purified Dreiklang protein at various pH-values for excitation with 412 nm <b>(a)</b> and 505 nm <b>(b)</b> . ....	71
5.5	Normalized emission spectra to their respective maximum of Dreiklang protein at various pH-values for excitation with 412 nm <b>(a)</b> and 505 nm <b>(b)</b> . ....	72
5.6	<b>(a)</b> Fluorescence decay curves of purified Dreiklang proteins at different pH-values and the measured IRF. <b>(b)</b> Decay associated spectra with lifetimes and respective amplitudes of Dreiklang as a function of the pH. ....	73
5.7	<b>(a)</b> FLIM images of living HEK293 cells expressing cytoplasmic DRK after illumination at 470 nm and emission selection above 565 nm at various pH-values. The color scale bar encode the average lifetime. Lower panel shows the corresponding normalized measured lifetime decay curves <b>(b)</b> . ....	74
5.8	<b>(a)</b> Normalized fluorescence emission spectra of purified DRK proteins (pH 7.4) in dependence of the temperature after excitation with 470 nm. <b>(b)</b> The obtained DAS spectra from DRK at room temperature (291 K) and 250 K after excitation with 470 nm and fitting with a single exponential model are shown on the right. ....	76
5.9	<b>(a)</b> Normalized OFF-switching process of Dreiklang protein diluted with PBS at a pH of 7.4 by illumination with different intensities of 405 nm and fluorescence collected through a 570lp filter. <b>(b)</b> Calculated switching times at different intensities. ....	78
5.10	<b>(a)</b> Normalized OFF-switching curves of purified Dreiklang protein at different pH-values by illumination with 405 nm and fluorescence collected through a 570lp filter. <b>(b)</b> OFF-switching time in dependence of the pH estimated with an exponential fit. ....	79

5.11	(a) Normalized OFF-switching curves of cytoplasmic Dreiklang proteins expressed in HEK293 cells at different pH-values by illumination with 405 nm and fluorescence collected through a 570lp filter. (b) Histogram showing the OFF-switching time as a function of intracellular pH. ....	79
5.12	Chemical structure of the Dreiklang chromophore in the fluorescent equilibrium state (left) and after irradiation with 405 nm in the non-fluorescent OFF-state (right). Carbons presented in grey, nitrogen in blue, oxygen in red and the water molecule in light blue. Reprinted and extended from [37]. ....	80
6.1	(a) Confocal image of HEK293T cells expressing eGFP-labeled Na,K-ATPase (green emission) adjusted for measuring the z-profile of the cell (setup parameters are as described above), the scale bar indicates 10 $\mu\text{m}$ . (b) A typical z-profile of a cell (abscissa: z-position in $\mu\text{m}$ , ordinate: count rate in kHz) is illustrated resulting from a z-scan with 0.5 $\mu\text{m}$ increments over a distance of 20 $\mu\text{m}$ across the cell. The peaks in the count rate are attributed to the position of the basal (first peak) and the apical (second peak) plasma membrane, respectively. ....	84
6.2	(a) Normalized autocorrelation curves of Rhodamine 6G in water (black curve), of purified Dreiklang (DRK) proteins in PBS (yellow curve) and of the DRK protein expressed in the cytoplasm of HEK293T cells (orange curve). For both DRK measurements, the curves were generated by averaging ten data acquisitions of 20 s duration at 0.7 % laser intensity. The averaged curve of the cytoplasmically expressed DRK proteins was constructed by measurements on 26 different cells. (b) Normalized autocorrelation curves of Rhodamine 6G in water (black curve), of the purified eGFP protein in PBS (light green curve) and of the eGFP expressed in the cytoplasm (dark green curve). For both eGFP measurements, the curves were generated from the average of ten data acquisitions of 20 s duration at 0.5 % laser intensity. For the averaged curve of the cytoplasmically expressed eGFP protein, measurements on 17 different cells were taken into account. ....	87
6.3	shows the change of the diffusion time depending on the pinhole size. The presented data were obtained by Rhodamine 6G in water (black) and purified Dreiklang proteins in PBS (yellow). ....	88

6.4	Normalized autocorrelation curves of DRK proteins expressed in the cytoplasm and DRK-labeled Na,K-ATPase in the plasma membrane (PM) are shown (0.7 % laser intensity). For each data set, the normalized average of more than 20 measurements on cells were used. The DRK protein expressed in the cytoplasm exhibits a much faster diffusion time than the DRK-labeled Na,K-ATPase in the plasma membrane. . . . .	88
6.5	Autocorrelation curves of Na,K-ATPase expressed in HEK293T cells carrying a N-terminal eGFP ( <b>a</b> ) or DRK ( <b>b</b> ) label acquired using different laser intensities. Autocorrelation curves normalized to the same amplitude, $G(\tau) = 1$ at $\tau = 10 \mu\text{s}$ , show that the characteristic decay times for DRK are strongly dependent on laser intensity. . . . .	89
6.6	Normalized autocorrelation curves of DRK- and eGFP-labeled Na,K-ATPase measured in the plasma membrane of HEK293T cells. The normalized average correlation curve with standard deviation was calculated from 20 measurements on different cells, as indicated. Excitation laser wavelengths were 488 nm (eGFP) and 514 nm (DRK), each at 0.7 % laser intensity. Fluorescence emission was detected with a 505 nm long pass (eGFP) and a 530 nm long pass (DRK) filter, respectively. . . . .	90
6.7	Normalized autocorrelation curves of purified eGFP ( <b>a</b> ) and purified Dreiklang ( <b>b</b> ) proteins in different sucrose/PBS solutions indicated by different colors. The curves were generated from the average of three times 20 s data acquisitions of 10 s duration. Direct comparison of normalized and averaged autocorrelation curves of purified Dreiklang (DRK) proteins (using 514 nm excitation) and purified eGFP proteins (using 488 nm excitation) in exemplarily depicted sucrose-free PBS buffer ( <b>c</b> ) and in 60 % sucrose/PBS solution ( <b>d</b> ) . . . . .	91

- 
- 6.8 **(a)** Visual comparison of the Na,K-ATPase tagged with Dreiklang in HEK293T cells and cytoplasmically expressed Dreiklang. The first column shows the imaged fluorescence upon 514 nm excitation (laser intensity = 10 %) filtered with a 530 nm long-pass filter, the central column the bright-field images of the same region, and the panels at the last column show the overlay of the fluorescence and the transmission picture. As expected, the cytoplasmic protein is expressed in the whole cell and the transporter proteins DRK-NaK-WT, DRK-NaK- $\Delta$ C, DRK-NaK- $\Delta$ N and DRK-NaK-K456E show a clear localization in the plasma membrane. The fluorescence signals from the mutants exhibit also a more diffuse pattern with clear contribution from intracellular proteins in contrast to the wild-type, especially the K456E mutant. **(b)** Visual comparison of the Na,K-ATPase tagged with eGFP in HEK293T cells and eGFP expressed cytoplasmically from the peGFP-N1 vector. The first column shows the imaged fluorescence under 488 nm excitation (laser intensity = 2 %) filtered with a 505 nm long-pass filter, the central column the bright-field images of the same region, and the panels at the last column show the overlay of the fluorescence and the transmission picture. As expected, eGFP-N1 is expressed in the cytoplasm and the transporter proteins eGFP-NaK-WT, eGFP-NaK- $\Delta$ N, eGFP-NaK- $\Delta$ C and eGFP-NaK-K456E show a prominent localization in the plasma membrane. In some cells, intracellular staining is also visible. The fluorescence signals from eGFP-NaK-K456E expressing cells exhibits a more diffuse pattern with clear contribution from intracellular proteins..... 93
- 6.9 **(a)** Autocorrelation curves  $G(\tau)$  of DRK-NaK- $\Delta$ N in dependence of the z-position in the cell and the corresponding counts per molecules **(b)**. **(c)** Autocorrelation curves  $G(\tau)$  of DRK- $\Delta$ N at the plasma membrane before and after the z-scan and the corresponding counts per molecule **(d)**..... 94
- 6.10 **(a)** Normalized autocorrelation curves of eGFP-NaK-WT (cyan curve) and DRK-NaK-WT (black) recorded in the cell culture medium above the cells. **(b)** Autocorrelation curves of eGFP-NaK-WT (cyan curve) and DRK-NaK-WT (black) recorded in the cytoplasm and normalized to the same amplitude. .... 95

6.11	(a) and (b) Normalized autocorrelation curves with standard deviation of the different DRK-labeled Na,K-ATPase $\alpha_2$ -subunit constructs measured by FCS. For each data set, the measurements on more than 20 cells were averaged. In this set of experiments, the three Na,K-ATPase constructs show the same diffusion behavior compared with the NaK-WT. Only the cytoplasmic DRK protein exhibits a faster diffusion. . . . .	96
6.12	Normalized autocorrelation curves of eGFP-labeled Na,K-ATPase constructs measured in the plasma membrane of HEK293T cells. For the data set in the normalized average correlation curve with standard deviation from measurements on more than 30 cells is shown, as indicated. Excitation laser wavelength was 488 nm at 0.5 % laser intensity. Fluorescence emission was detected with a 505 nm long pass filter. . . . .	97
6.13	Visual comparison of the Na,K-ATPase tagged with eGFP in HEK293T cells. The first column shows the imaged fluorescence signal under 488 nm excitation (laser intensity = 2 %) filtered by a 505 nm long-pass filter. The central column shows the bright-field images of the same region, and the panels at the last column show the overlay of the fluorescence and the transmission pictures. As expected, the transporter proteins eGFP-NaK-WT, eGFP-NaK- $\Delta C\Delta N$ and eGFP-NaK- $\Delta C\Delta NK456E$ show a prominent localization in the plasma membrane. In some cells, intracellular staining is also visible. . . . .	98
6.14	Normalized autocorrelation curves of eGFP-labeled Na,K-ATPase wild-type, double- (eGFP-NaK- $\Delta C\Delta N$ ) and threefold mutant (eGFP-NaK- $\Delta C\Delta NK456E$ ) measured in the plasma membrane of HEK293T cells. For each data set the measurements on more than 29 cells were averaged. Excitation laser wavelength was 488 nm with 0.5 % laser intensity, fluorescence emission was detected with 505 nm long pass filter, respectively. . . . .	99
6.15	Averaged number of particles in the observation volume for the different DRK-labeled Na,K-ATPase constructs (DRK-NaK-WT, DRK-NaK- $\Delta C$ , DRK-NaK- $\Delta N$ ) with the corresponding standard deviation and the number of cells taken into account. . . . .	100
6.16	Averaged number of particles in the observation volume of one DRK-labeled Na,K-ATPase mutant and the wild-type. In addition for comparison of the used fluorescence label the eGFP-labeled Na,K-ATPase wild-type is shown. All data are given with corresponding standard deviation and the number of cells taken into account. . . . .	101

6.17	Averaged number of particle in the observation volume of the different eGFP-labeled Na,K-ATPase mutants and wild-type with the corresponding standard deviation and number of cells taken into account. . . .	102
6.18	Visual comparison of eGFP-NaK-WT fluorescence (green emission) in HEK293T cells at indicated time points before and after photobleaching.	103
6.19	<b>(a)</b> Normalized averaged reversible fluorescence recovery curves of Dreiklang-labeled Na,K-ATPase mutants and wild-type measured in the plasma membrane of HEK293T cells. <b>(b)</b> Normalized averaged irreversible fluorescence recovery curves of DRK-labeled Na,K-ATPase mutants and wild-type measured in the plasma membrane of HEK293T cells. Measurements of 16 and more cells are taken into account, as indicated. . . .	105
6.20	Normalized averaged fluorescence recovery curves of eGFP-labeled Na,K-ATPase mutants and wild-type measured in the plasma membrane of HEK293T cells. Measurements of 18 and more cells are taken into account, as indicated. . . . .	106
6.21	Plasma membrane structure with processes that might hinder the free, two-dimensional diffusion of membrane proteins. (1) Free diffusion of a membrane protein through the lipid bilayer. (2) A Membrane protein bound to the cytoskeleton like a transmembrane protein. (3) Multimeric complex of membrane proteins, which lead to a reduced mobility compared to a single membrane protein (1). (4) Corral forming by membrane proteins, that reduces the mobility of the observed protein. Also shown are lipid-rafts (light green), which lead to microdomains in the plasma membrane and are not accessible for most of the transmembrane proteins. The image was reproduced in modified form from [131]. . . . .	114
6.22	Different membrane models used for simulated FCS diffusion laws <b>(a)</b> Free diffusing molecules (black dots) showing pure Brownian motion in the OVE (large grey circle). <b>(b)</b> Membrane model with impermeable obstacles (dark grey circles) like microdomains, that restricted the diffusion. <b>(c)</b> Dynamic partition model suggests that the molecules can diffuse into and out of the microdomains. <b>(d)</b> Cytoskeleton meshwork model, associated that the diffusion of molecules is hindered by barriers (light grey grid). Image is reconstructed [135]. . . . .	117
6.23	Results for the different membrane models of simulated FCS diffusion laws, like free diffusing molecules, impermeable obstacles, dynamic partition or meshwork. The diffusion time $\tau_D$ as a function of the spot area ( $w^2$ ) is given. Image is reconstructed and extended from [135]. . . . .	118



# List of Tables

2.1	Primer and Sequences .....	24
2.2	Used PCR protocol. ....	29
2.3	Temperature protocol for THGF-AAS measurements with rubidium....	34
6.1	Summary of calculated diffusion times and constants.....	108
6.2	Summary of calculated diffusion times and determined diffusion coefficients for different eGFP-labeled Na,K-ATPase constructs. ....	113
6.3	Summary of determined mobile fractions $M$ , $t_{1/2}$ -values and calculated diffusion constants $D$ for different eGFP-/DRK-labeled Na,K-ATPase constructs. ....	121



# Publications

**Parts of this work has been published in the following journal articles:**

1. Junghans, C., Schmitt, F.-J., Vukojević, V. and Friedrich, T., Monitoring the diffusion behavior of Na,K-ATPase by fluorescence correlation spectroscopy (FCS) upon fluorescence labelling with eGFP or Dreiklang, *De Gruyter Optofluidics, Microfluidics and Nanofluidics* **2** (1), 1-13 (2015).

**Contributions to other journal articles:**

1. Schmitt, F.-J., Maksimov, E., Junghans, C., Weißenborn, J., Hätti, P., Paschenko, V. Z., Allakhverdiev, S. I., and Friedrich, T., Structural Organization and Dynamic Processes in Protein Complexes Determined by Multiparameter Imaging, *Signpost Open Access J. NanoPhotoBioSciences* **1** , 1-53 (2013).
2. Schmitt, F.-J., Thaa, B., Junghans, C., Vitali, M., Velt, M. and Friedrich, T., eGFP-pHsens as highly sensitive fluorophore for pH determination in cells by fluorescence lifetime imaging microscopy (FLIM), *BBA* **1837** (9), 1581-1593 (2014).
3. Vitali, M., Bronzi, D., Krmpot, A. J., Nikolić, S., Schmitt, F.-J., Junghans, C., Tisa, S., Friedrich, T., Vukojević, V., Terenius, L., Zappa, F. and Rigler, R., A Single-Photon Avalanche Camera for Fluorescence Lifetime Imaging Microscopy and Correlation Spectroscopy, *IEEE J. Selected Topics in Quantum Electronics* **20** (6), 344-353 (2014)
4. Schmitt, F.-J., Junghans, C., Sturm, M., Keuer, C., Eichler, H. J. and Friedrich, T., Laser switching contrast microscopy to monitor free and restricted diffusion inside the cell nucleus, *De Gruyter Optofluidics, Microfluidics and Nanofluidics* **3**, 1-12 (2016).

## Poster contributions:

1. Hätti, P., Schmitt, F.-J., Junghans, C., Vitali, M. and Friedrich, T., Determination of the hydrodynamic radius of GFP-tagRFP FRET-Constructs with Fluorescence Correlation Spectroscopy, *Frühjahrstagung der DPG*, Berlin, Germany (25. - 30. March 2012).
2. Schmitt, F.-J., Junghans, C., Vitali, M. and Friedrich, T., Dual emission GFP as highly sensitive fluorophore for the determination of intracellular pH with fluorescence lifetime imaging microscopy (FLIM), *Frühjahrstagung der DPG*, Berlin, Germany (25. - 30. March 2012).
3. Weißenborn, J., Schmitt, F.-J., Hätti, P., Junghans, C., Schöps, O., Woggon, U. and Friedrich, T., Time- and spectrally resolved investigation of switchable and non-switchable tagRFP-Molecules *Frühjahrstagung der DPG*, Berlin, Germany (25. - 30. March 2012).
4. Junghans, C., Schmitt, F.-J., Hätti, P., Reis, M., Vitali, M. and Friedrich, T., Multi-parameter fluorescence techniques for combined confocal and wide-field observations, *Annual Meeting of the German Biophysical Society*, Göttingen, Germany (23. - 26. September 2012).
5. Schmitt, F.-J., Junghans, C., Vitali, M., Weißenborn, J. and Friedrich, T., Dual emission GFP as highly sensitive fluorophore for the determination of intracellular pH with fluorescence lifetime imaging microscopy (FLIM), *Annual Meeting of the German Biophysical Society*, Göttingen, Germany (23. - 26. September 2012).
6. Junghans, C., Schmitt, F.-J., Vitali, M., Tavraz, N., Vukojević, V. and Friedrich, T., Fluorescence microscopic techniques to assay cellular targeting, localization and diffusion behavior of human Na,K-ATPase  $\alpha_2$  subunit expressed in HEK293 cells, *The ASBMB Special Symposium, entitled Na, K-ATPase and Related Transport ATPases Structure, Mechanism, Cell Biology, Health and Disease*, Lunteren, Netherlands (30. August - 4. September 2014).

# Bibliography

- [1] M. Khalid, F. Cornelius, and R. J. Clarke. Dual mechanisms of allosteric acceleration of the Na<sup>+</sup>,K<sup>+</sup>-ATPase by ATP. *Biophysical Journal*, 98(10):2290–2298, 2010.
- [2] M. de Fusco, R. Marconi, L. Silvestri, L. Atorino, L. Rampoldi, L. Morgante, A. Ballabio, P. Aridon, and G. Casari. Haploinsufficiency of ATP1A2 encoding the Na<sup>+</sup>/K<sup>+</sup> pump  $\alpha$ 2 subunit associated with familial hemiplegic migraine type 2. *Nature genetics*, 33(2):192–196, 2003.
- [3] N. N. Tavraz, T. Friedrich, K. L. Dürr, J. B. Koenderink, E. Bamberg, T. Freilinger, and M. Dichgans. Diverse functional consequences of mutations in the Na<sup>+</sup>/K<sup>+</sup>-ATPase  $\alpha$ 2-subunit causing familial hemiplegic migraine type 2. *The Journal of biological chemistry*, 283(45):31097–31106, 2008.
- [4] J. P. Morth, H. Poulsen, M. S. Toustrup-Jensen, V. Rodacker Schack, J. Egebjerg, J. P. Andersen, B. Vilsen, and P. Nissen. The structure of the Na<sup>+</sup>,K<sup>+</sup>-ATPase and mapping of isoform differences and disease-related mutations. *Philosophical transactions of the Royal Society of London. Series B, Biological sciences*, 364(1514):217–227, 2009.
- [5] N. N. Tavraz, K. L. Dürr, J. B. Koenderink, T. Freilinger, E. Bamberg, M. Dichgans, and T. Friedrich. Impaired plasma membrane targeting or protein stability by certain ATP1A2 mutations identified in sporadic or familial hemiplegic migraine. *Channels*, 3(2):82–87, 2009.
- [6] D. P. Calderon, R. Fremont, F. Kraenzlin, and K. Khodakhah. The neural substrates of rapid-onset Dystonia-Parkinsonism. *Nature neuroscience*, 14(3):357–365, 2011.
- [7] de Carvalho Aguiar, P., K. J. Sweadner, J. T. Penniston, J. Zaremba, L. Liu, M. Caton, G. Linzasoro, M. Borg, Tijssen, M. A. J., S. B. Bressman, W. B. Dobyns, A. Brashear, and L. J. Ozelius. Mutations in the Na<sup>+</sup>/K<sup>+</sup> -ATPase alpha3 gene ATP1A3 are associated with rapid-onset dystonia parkinsonism. *Neuron*, 43(2):169–175, 2004.

- [8] E. L. Heinzen, A. Arzimanoglou, A. Brashear, S. J. Clapcote, F. Gurrieri, D. B. Goldstein, S. H. Jóhannesson, M. A. Mikati, B. Neville, S. Nicole, L. J. Ozelius, H. Poulsen, T. Schyns, K. J. Sweadner, van den Maagdenberg, A., and B. Vilsen. Distinct neurological disorders with ATP1A3 mutations. *The Lancet Neurology*, 13(5):503–514, 2014.
- [9] M. K. Demos, van Karnebeek, C. D., C. J. Ross, S. Adam, Y. Shen, S. H. Zhan, C. Shyr, G. Horvath, M. Suri, A. Fryer, S. J. Jones, and J. M. Friedman. A novel recurrent mutation in ATP1A3 causes CAPOS syndrome. *Orphanet journal of rare diseases*, 9:15, 2014.
- [10] X. Liu, Z. Špicarová, S. Rydholm, J. Li, H. Brismar, and A. Aperia. Ankyrin B Modulates the Function of Na,K-ATPase/Inositol 1,4,5-Trisphosphate Receptor Signaling Microdomain. *Journal of Biological Chemistry*, 283(17):11461–11468, 2008.
- [11] P. J. Mohler, J.-J. Schott, A. O. Gramolini, K. W. Dilly, S. Guatimosim, W. H. duBell, L.-S. Song, K. Haurogné, F. Kyndt, M. E. Ali, T. B. Rogers, W. J. Lederer, D. Escande, H. Le Marec, and V. Bennett. Ankyrin-B mutation causes type 4 long-QT cardiac arrhythmia and sudden cardiac death. *Nature*, 421(6923):634–639, 2003.
- [12] D. Magde, E. Elson, and W. W. Webb. Thermodynamic fluctuations in a reacting system-measurement by fluorescence correlation spectroscopy. *Physical Review Letters*, 29:705–708, 1972.
- [13] S. R. Aragón. Fluorescence correlation spectroscopy as a probe of molecular dynamics. *The Journal of Chemical Physics*, 64(4):1791, 1976.
- [14] G. Bonnet, O. Krichevsky, and A. Libchaber. Kinetics of conformational fluctuations in DNA hairpin-loops. *Proceedings of the National Academy of Sciences USA*, 95(15):8602–8606, 1998.
- [15] M. Ehrenberg and R. Rigler. Rotational brownian motion and fluorescence intensity fluctuations. *Chemical Physics*, 4(3):390–401, 1974.
- [16] U. Haupts, S. Maiti, P. Schwille, and W. W. Webb. Dynamics of fluorescence fluctuations in green fluorescent protein observed by fluorescence correlation spectroscopy. *Proceedings of the National Academy of Sciences*, 95(23):13573–13578, 1998.
- [17] P. Kask, P. Piksarv, M. Pooga, Ü. Mets, and E. Lippmaa. Separation of the rotational contribution in fluorescence correlation experiments. *Biophysical journal*, 55(2):213–220, 1989.

- 
- [18] D. Magde. Chemical Kinetics and Fluorescence Correlation Spectroscopy. *Quarterly Reviews of Biophysics*, 9(01):35, 1976.
- [19] B. Rauer, E. Neumann, J. Widengren, and R. Rigler. Fluorescence correlation spectrometry of the interaction kinetics of tetramethylrhodamin  $\alpha$ -bungarotoxin with Torpedo californica acetylcholine receptor. *Biophysical Chemistry*, 58(1-2):3–12, 1996.
- [20] J. Widengren, R. Rigler, and Ü. Mets. Triplet-state monitoring by fluorescence correlation spectroscopy. *Journal of Fluorescence*, 4:255–258, 1994.
- [21] J. Widengren, U. Mets, and R. Rigler. Fluorescence correlation spectroscopy of triplet states in solution: a theoretical and experimental study. *The Journal of Physical Chemistry*, 99(36):13368–13379, 1995.
- [22] E. Haustein and P. Schwille. Ultrasensitive investigations of biological systems by fluorescence correlation spectroscopy. *Methods*, 29(2):153–166, 2003.
- [23] D. Axelrod, D.E Koppel, J. Schlessinger, E. Elson, and W. W. Webb. Mobility measurement by analysis of fluorescence photobleaching recovery kinetics. *Biophysical Journal*, 16(9):1055–1069, 1976.
- [24] B. L. Sprague and J. G. McNally. FRAP analysis of binding: proper and fitting. *Trends in Cell Biology*, 15(2):84–91, 2005.
- [25] A. Diaspro, editor. *Optical Fluorescence Microscopy: From the Spectral to the Nano Dimension*. Springer-Verlag Berlin Heidelberg, 1 edition, 2011.
- [26] T. Kühn, T. O. Ihalainen, J. Hyväluoma, N. Dross, S. F. Willman, J. Langowski, M. Vihinen-Ranta, and J. Timonen. Protein Diffusion in Mammalian Cell Cytoplasm. *PLoS ONE*, 6(8):1–12, 2011.
- [27] C. Klein and F. Waharte. Analysis of Molecular Mobility by Fluorescence Recovery After Photobleaching in Living Cells. *Microscopy: Science, Technology, Applications and Education*, pages 772–783, 2010.
- [28] J. Braga, J.M.P. Desterro, and M. Carmo-Fonseca. Intracellular Macromolecular Mobility Measured by Fluorescence Recovery after Photobleaching with Confocal Laser Scanning Microscopes. *The American Society for Cell Biology*, 15:4749–4760, 2004.
- [29] N. Klonis, M. Rug, I. Harper, M. Wickham, A. Cowman, and L. Tilley. Fluorescence photobleaching analysis for the study of cellular dynamics. *European Biophysics Journal*, 31(1):36–51, 2002.

- [30] O. Shimomura, F. H. Johnson, and Y. Saiga. Extraction, Purification and Properties of Aequorin, a Bioluminescent Protein from the Luminous Hydromedusan, Aequorea. *Journal of Cellular and Comparative Physiology*, 59(3):223–239, 1962.
- [31] M. J. Rust, M. Bates, and X. Zhuang. Sub-diffraction-limit imaging by stochastic optical reconstruction microscopy (STORM). *Nature methods*, 3(10):793–795, 2006.
- [32] S. W. Hell and J. Wichmann. Breaking the diffraction resolution limit by stimulated emission: stimulated-emission-depletion fluorescence microscopy. *Optics Letters*, 19(11):780, 1994.
- [33] T. A. Klar and S. W. Hell. Subdiffraction resolution in far-field fluorescence microscopy. *Optics Letters*, 24(14):954, 1999.
- [34] T. A. Klar, S. Jakobs, M. Dyba, A. Egner, and S. W. Hell. Fluorescence microscopy with diffraction resolution barrier broken by stimulated emission. *Proceedings of the National Academy of Sciences*, 97(15):8206–8210, 2000.
- [35] S. T. Hess, T.P.K. Girirajan, and M. D. Mason. Ultra-High Resolution Imaging by Fluorescence Photoactivation Localization Microscopy. *Biophysical Journal*, 91(11):4258–4272, 2006.
- [36] F. V. Subach, L. Zhang, T.W.J. Gadella, N. G. Gurskaya, K. A. Lukyanov, and V. V. Verkhusha. Red Fluorescent Protein with Reversibly Photoswitchable Absorbance for Photochromic FRET. *Chemistry & Biology*, 17(7):745–755, 2010.
- [37] T. Brakemann, A. C. Stiel, G. Weber, M. Andresen, I. Testa, T. Grotjohann, M. Leutenegger, U. Plessmann, H. Urlaub, C. Eggeling, M. C. Wahl, S. W. Hell, and S. Jakobs. A reversibly photoswitchable GFP-like protein with fluorescence excitation decoupled from switching. *Nature Biotechnology*, 29(10), 2011.
- [38] D. Sinnecker, P. Voigt, N. Hellwig, and M. Schaefer. Reversible Photobleaching of Enhanced Green Fluorescent Proteins. *Biochemistry*, 44(18):7085–7094, 2005.
- [39] Florian Mueller, Tatsuya Morisaki, Davide Mazza, and James G. McNally. Minimizing the Impact of Photoswitching of Fluorescent Proteins on FRAP Analysis. *Biophysical Journal*, 102(7):1656–1665, 2012.

- 
- [40] T. Morisaki, J. G. McNally, and M. Akaaboune. Photoswitching-Free FRAP Analysis with a Genetically Encoded Fluorescent Tag. *PLoS ONE*, 9(9):e107730, 2014.
- [41] K. Dose and A. Bieger-Dose. *Biochemie: Eine Einführung ; mit 22 Tabellen*. Springer-Lehrbuch. Springer, Berlin [u.a.], 4., vollst. überarb. aufl edition, 1994.
- [42] B. Alberts and L. Nover. *Lehrbuch der molekularen Zellbiologie*. Wiley-VCH, Weinheim, 4., vollst. überarb. aufl edition, 2012.
- [43] F. L. Graham, J. Smiley, W. C. Russell, and R. Nairn. Characteristics of a Human Cell Line Transformed by DNA from Human Adenovirus Type 5. *Journal of General Virology*, 36(1):59–72, 1977.
- [44] L. Aiello, R. Guilfoyle, K. Huebner, and R. Weinmann. Adenovirus 5 DNA sequences present and RNA sequences transcribed in transformed human embryo kidney cells (HEK-Ad-5 or 293). *Virology*, 94(2):460–469, 1979.
- [45] J. C. Skou. The influence of some cations on an adenosine triphosphatase from peripheral nerves. *Biochimica et Biophysica Acta*, 23(0):394–401, 1957.
- [46] J. H. Kaplan. Biochemistry of Na,K-ATPase. *Annual Review of Biochemistry*, 71:511–535, 2002.
- [47] J. P. Morth, B. P. Pedersen, M. S. Toustrup-Jensen, T. L-M Sørensen, J. Petersen, J. P. Andersen, B. Vilsen, and P. Nissen. Crystal structure of the sodium-potassium pump. *Nature*, 450(7172):1043–1049, 2007.
- [48] T. Shinoda, H. Ogawa, and Cornelius, F. and Toyoshima, C. Crystal structure of the sodium-potassium pump at 2.4 Å resolution. *Nature*, 459(7245):446–450, 2009.
- [49] S. Spiller. *Struktur-Funktionsbeziehungen der Na<sup>+</sup>/K<sup>+</sup>-ATPase anhand elektrophysiologischer Untersuchungen C-terminaler und Migräne-assoziiierter Mutationen*. PhD thesis, TU Berlin, Berlin, 27.03.2013.
- [50] K. Geering. The Functional Role of  $\beta$  Subunits in Oligomeric P-Type ATPases. *Journal of Bioenergetics and Biomembranes*, 33(5):425–438, 2001.
- [51] A. G. Therien, R. Goldshleger, Karlsh, S. J. D., and R. Blostein. Tissue-specific Distribution and Modulatory Role of the Subunit of the Na,K-ATPase. *Journal of Biological Chemistry*, 272(51):32628–32634, 1997.

- [52] H. Rosewich, H. Thiele, A. Ohlenbusch, U. Maschke, J. Altmüller, P. Frommolt, B. Zirn, F. Ebinger, H. Siemes, P. Nürnberg, K. Brockmann, and J. Gärtner. Heterozygous de-novo mutations in ATP1A3 in patients with alternating hemiplegia of childhood: a whole-exome sequencing gene-identification study. *The Lancet Neurology*, 11(9):764–773, 2012.
- [53] IHS. The International Classification of Headache Disorders, 3rd edition (beta version). *Cephalalgia*, 33(9):629–808, 2013.
- [54] F. Riant, E. Roze, C. Barbance, A. Méneret, L. Guyant-Maréchal, C. Lucas, P. Sabouraud, A. Trébuchon, C. Depienne, and E. Tournier-Lasserre. PRRT2 mutations cause hemiplegic migraine. *Neurology*, 79(21):2122–2124, 2012.
- [55] K. Jurkat-Rott, T. Freilinger, J. P. Dreier, J. Herzog, H. Göbel, G. C. Petzold, P. Montagna, T. Gasser, F. Lehmann-Horn, and M. Dichgans. Variability of familial hemiplegic migraine with novel A1A2 Na<sup>+</sup>/K<sup>+</sup>-ATPase variants. *Neurology*, 62(10):1857–1861, 2004.
- [56] Z. Zhang, P. Devarajan, A. L. Dorfman, and J. S. Morrow. Structure of the Ankyrin-binding Domain of  $\alpha$ -Na,K-ATPase. *Journal of Biological Chemistry*, 273(30):18681–18684, 1998.
- [57] P. J. Mohler, J. Q. Davis, and V. Bennett. Ankyrin-B Coordinates the Na/K ATPase, Na/Ca Exchanger, and InsP3 Receptor in a Cardiac T-Tubule/SR Microdomain. *PLoS Biology*, 3(12):2158–2167, 2005.
- [58] P. R. Stabach, P. Devarajan, M. C. Stankewich, S. Bannykh, and J. S. Morrow. Ankyrin facilitates intracellular trafficking of  $\alpha$ 1-Na<sup>+</sup>-K<sup>+</sup>-ATPase in polarized cells. *American journal of physiology. Cell physiology*, 295(5):C1202–14, 2008.
- [59] Z. Xie and T. Cai. Na<sup>+</sup>-K<sup>+</sup>-ATPase-mediated signal transduction: from protein interaction to cellular function. *Molecular interventions*, 3(3):157–168, 2003.
- [60] T. M. Williams and M. P. Lisanti. The Caveolin genes: from cell biology to medicine. *Annals of Medicine*, 36(8):584–595, 2004.
- [61] P. Liu, M. Rudick, and Anderson, R. G. W. Multiple functions of caveolin-1. *The Journal of biological chemistry*, 277(44):41295–41298, 2002.
- [62] T. Cai, H. Wang, Y. Chen, L. Liu, W. T. Gunning, L.E.M. Quintas, and Z.-J. Xie. Regulation of caveolin-1 membrane trafficking by the Na/K-ATPase. *JCB*, 182(6):1153–1169, 2008.

- 
- [63] H. Wang, M. Haas, M. Liang, T. Cai, J. Tian, S. Li, and Z. Xie. Ouabain assembles signaling cascades through the caveolar Na<sup>+</sup>/K<sup>+</sup>-ATPase. *The Journal of biological chemistry*, 279(17):17250–17259, 2004.
- [64] C. Jordan, B. Püschel, R. Koob, and D. Drenckhahn. Identification of a Binding Motif for Ankyrin on the  $\alpha$ -Subunit of Na<sup>+</sup>,K<sup>+</sup>-ATPase. *Biological Chemistry*, 250(50):29971–29975, 1995.
- [65] E. M. Price and J. B. Lingrel. Structure-function relationships in the sodium-potassium ATPase .alpha. subunit: Site-directed mutagenesis of glutamine-111 to arginine and asparagine-122 to aspartic acid generates a ouabain-resistant enzyme. *Biochemistry*, 27(22):8400–8408, 1988.
- [66] R. Ando, H. Mizuno, and A. Miyawaki. Regulated fast nucleocytoplasmic shuttling observed by reversible protein highlighting. *Science (New York, N.Y.)*, 306(5700):1370–1373, 2004.
- [67] R. Y. Tsien. The Green Fluorescent Protein. *Annual Review of Biochemistry*, 67:509–544, 1998.
- [68] M. Ormö, A. B. Cubitt, K. Kallio, L. A. Gross, R. Y. Tsien, and S. J. Remington. Crystal Structure of the *Aequorea victoria* Green Fluorescent Protein. *Science*, 273(5280):1392–1395, 1996.
- [69] B. P. Cormack, R. H. Valdivia, and S. Falkow. FACS-optimized mutants of the green fluorescent protein (GFP). *Gene*, 173(1):33–38, 1996.
- [70] G. Zhang, V. Gurtu, and S. R. Kain. An enhanced green fluorescent protein allows sensitive detection of gene transfer in mammalian cells. *Biochemical and Biophysical Research Communications*, 227(3):707–711, 1996.
- [71] E. M. Merzlyak, J. Goedhart, D. Shcherbo, M. E. Bulina, A. S. Shcheglov, A. F. Fradkov, A. Gaintzeva, K. A. Lukyanov, S. Lukyanov, Gadella, T. W. J., and D. M. Chudakov. Bright monomeric red fluorescent protein with an extended fluorescence lifetime. *Nature methods*, 4(7):555–557, 2007.
- [72] N. N. Tavraz. *Charakterisierung Migräne-relevanter Mutationen anhand Struktur-Funktions-Untersuchungen der Na<sup>+</sup>/K<sup>+</sup>-ATPase  $\alpha$ 2-Untereinheit*. PhD thesis, TU Berlin, 2010.
- [73] N. D. Eljack, H.-Y. M. Ma, J. Drucker, C. Shen, T. W. Hambley, E. J. New, T. Friedrich, and R. J. Clarke. Mechanisms of cell uptake and toxicity of the anticancer drug cisplatin. *Metallomics : integrated biometal science*, 6(11):2126–2133, 2014.

- [74] G. Hilken, F. Iglauer, and H. J. Richter. *Der Krallenfrosch Xenopus laevis als Labortier: Biologie, Haltung, Zucht und experimentelle Nutzung*. Ferdinand Enke Verlag, Stuttgart, 1997.
- [75] J. N. Dumont. Oogenesis in *Xenopus laevis* (Daudin). I. Stages of oocyte development in laboratory maintained animals. *Journal of Morphology*, 136(2):153–179, 1972.
- [76] M. Minsky. Memoir on inventing the confocal scanning microscope. *The Journal of Scanning Microscopies*, 10:128–138, 1988.
- [77] A. Gräslund, R. Rigler, and J. Widengren. *Single molecule spectroscopy in chemistry, physics and biology: Nobel Symposium*, volume 96 of *Springer series in chemical physics*. Springer, Heidelberg [Germany] and New York, 2010.
- [78] W. Becker. The B&H TCSPC Handbook, 2008.
- [79] D. V. O'Connor and D. Phillips. *Time-Correlated Single Photon Counting*. Academic Press Inc. (London) Ltd, 1984.
- [80] W. Becker. *Advanced Time-Correlated Single Photon Counting Techniques*. Springer Series in Chemical Physics, 2005.
- [81] R. Rigler, Ü. Mets, J. Widengren, and P. Kask. Fluorescence correlation spectroscopy with high count rate and low background: analysis of translational diffusion. *European Biophysics Journal*, 22:169–175, 1993.
- [82] C. Eggeling, J. Widengren, R. Rigler, and C.A.M. Seidel. Photobleaching of fluorescent dyes under conditions used for single-molecule detection: evidence of two-step photolysis. *Analytical Chemistry*, 70:2651–2659, 1998.
- [83] J. R. Lakowicz. *Principles of Fluorescence Spectroscopy*. Springer, New York, 3rd edition, 2006.
- [84] D. M. Soumpasis. Theoretical analysis of fluorescence photobleaching recovery experiments. *Biophysical Journal*, 41(1):95–97, 1983.
- [85] W. W. Webb. LUMINESCENCE MEASUREMENTS OF MACROMOLECULAR MOBILITY. *Annals of the New York Academy of Sciences*, 366(1 Luminescence):300–314, 1981.
- [86] J. Yguerabide, J. A. Schmidt, and E. E. Yguerabide. Lateral mobility in membranes as detected by fluorescence recovery after photobleaching. *Biophysical Journal*, 40(1):69–75, 1982.

- 
- [87] F.-J. Schmitt. *Picobiophotonics for the investigation of pigment-pigment and pigment-protein interactions in photosynthetic complexes*. PhD thesis, TU Berlin, 2011.
- [88] V. Vukojević, Y. Ming, C. D’Addario, M. Hansen, Ü. Langel, R. Schulz, B. Johansson, R. Rigler, and L. Terenius.  $\mu$ -opioid receptor activation in live cells. *FASEB journal : official publication of the Federation of American Societies for Experimental Biology*, 22(10):3537–3548, 2008.
- [89] V. Vukojević, M. Heidkamp, Y. Ming, B. Johansson, L. Terenius, and R. Rigler. Quantitative single-molecule imaging by confocal laser scanning microscopy. *Proceedings of the National Academy of Sciences of the United States of America*, 105(47):18176–18181, 2008.
- [90] A. Ciechanover. The ubiquitin-proteasome proteolytic pathway. *Cell*, 79(1):13–21, 1994.
- [91] D. Nandi, P. Tahiliani, A. Kumar, and D. Chandu. The ubiquitin-proteasome system: Journal of Biosciences. *J Biosci*, 31(1):137–155, 2006.
- [92] D. Boujard, B. Anselme, C. Cullin, C. Raguénès-Nicol, and S. Lechowski. *Zell- und Molekularbiologie im Überblick*. Springer Berlin Heidelberg, 2014.
- [93] H. Will. *Molekularbiologie kurz und bündig*. Springer Berlin Heidelberg, 2014.
- [94] L. Hicke and H. Riezman. Ubiquitination of a Yeast Plasma Membrane Receptor Signals Its Ligand-Stimulated Endocytosis. *Cell*, 84(2):277–287, 1996.
- [95] M. V. Coppi and G. Guidotti. Ubiquitination of Na,K-ATPase  $\alpha$ 1 and  $\alpha$ 2 subunits. *FEBS Letters*, 405(3):281–284, 1997.
- [96] S. H. Yoshimura and K. Takeyasu. Differential Degradation of the Na<sup>+</sup>/K<sup>+</sup>-ATPase Subunits in the Plasma Membrane. *Annals of the New York Academy of Sciences*, 986(1):378–381, 2003.
- [97] M. Cherniavsky-Lev, O. Golani, S. J. Karlsh, and H. Garty. Ouabain-induced internalization and lysosomal degradation of the Na<sup>+</sup>/K<sup>+</sup>-ATPase. *The Journal of biological chemistry*, 289(2):1049–1059, 2014.
- [98] M. Cotlet, J. Hofkens, M. Maus, T. Gensch, Van der Auweraer, M., J. Michiels, G. Dirix, M. van Guyse, J. Vanderleyden, Visser, A. J. W. G., and De Schryver, F. C. Excited-State Dynamics in the Enhanced Green Fluorescent Protein Mutant Probed by Picosecond Time-Resolved Single Photon Counting Spectroscopy. *The Journal of Physical Chemistry B*, 105(21):4999–5006, 2001.

- [99] G. T. Hanson, T. B. McAnaney, E. S. Park, Rendell, M. E. P., D. K. Yarbrough, S. Chu, L. Xi, S. G. Boxer, M. H. Montrose, and S. J. Remington. Green Fluorescent Protein Variants as Ratiometric Dual Emission pH Sensors. 1. Structural Characterization and Preliminary Application. *Biochemistry*, 41(52):15477–15488, 2002.
- [100] G. Striker, V. Subramaniam, Seidel, C. A. M., and A. Volkmer. Photochromicity and Fluorescence Lifetimes of Green Fluorescent Protein. *The Journal of Physical Chemistry B*, 103(40):8612–8617, 1999.
- [101] H. Lossau, A. Kummer, R. Heinecke, F. Pöllinger-Dammer, C. Kompa, G. Bieser, T. Jonsson, C. M. Silva, M. M. Yang, D. C. Youvan, and M. E. Michel-Beyerle. Time-resolved spectroscopy of wild-type and mutant Green Fluorescent Proteins reveals excited state deprotonation consistent with fluorophore-protein interactions. *Chemical Physics*, 213(1–3):1–16, 1996.
- [102] J. W. Borst, M. A. Hink, A. van Hoek, and Visser, A. J. W. G. Effects of Refractive Index and Viscosity on Fluorescence and Anisotropy Decays of Enhanced Cyan and Yellow Fluorescent Proteins. *Journal of Fluorescence*, 15(2):153–160, 2005.
- [103] Visser, A. J. W. G., S. P. Laptinok, N. V. Visser, A. van Hoek, D.J.S. Birch, J.-C. Brochon, and J. W. Borst. Time-resolved FRET fluorescence spectroscopy of visible fluorescent protein pairs. *European Biophysics Journal*, 39(2):241–253, 2010.
- [104] F.-J. Schmitt, B. Thaa, C. Junghans, M. Vitali, M. Veit, and T. Friedrich. eGFP-pHsens as a highly sensitive fluorophore for cellular pH determination by fluorescence lifetime imaging microscopy (FLIM). *Biochimica et Biophysica Acta*, 1837(9):1581–1593, 2014.
- [105] M. Vitali. *Long-term observation of living cells by wide-field fluorescence lifetime imaging microscopy*. PhD thesis, Technische Universität Berlin, 2011.
- [106] B. Huang, W. Wang, M. Bates, and X. Zhuang. Three-dimensional super-resolution imaging by stochastic optical reconstruction microscopy. *Science (New York, N.Y.)*, 319(5864):810–813, 2008.
- [107] S.-H. Lee, J. Y. Shin, A. Lee, and C. Bustamante. Counting single photoactivatable fluorescent molecules by photoactivated localization microscopy (PALM). *Proceedings of the National Academy of Sciences USA*, 109(43):17436–17441, 2012.

- 
- [108] N. A. Jensen, J. G. Danzl, K. I. Willig, F. Lavoie-Cardinal, T. Brakemann, S. W. Hell, and S. Jakobs. Coordinate-targeted and coordinate-stochastic super-resolution microscopy with the reversibly switchable fluorescent protein Dreiklang. *ChemPhysChem*, 15(4):756–762, 2014.
- [109] C. Barta, T. Kálai, I. Vass, K. Hideg, and È. Hideg. Dansyl- and rhodamine-based fluorescent sensors for detecting singlet oxygen and superoxide production in plants in vivo. *Acta Biologica Szegediensis*, 46(3-4):149–150, 2002.
- [110] G. Majer and J. P. Melchior. Characterization of the fluorescence correlation spectroscopy (FCS) standard rhodamine 6G and calibration of its diffusion coefficient in aqueous solutions. *The Journal of chemical physics*, 140(9):94201, 2014.
- [111] D. Magde, E. L. Elson, and W. W. Webb. Fluorescence correlation spectroscopy. II. An experimental realization. *Biopolymers*, 13(1):29–61, 1974.
- [112] R. Rigler, P. Grasselli, and M. Ehrenberg. Fluorescence Correlation Spectroscopy and Application to the Study of Brownian Motion of Biopolymers. *Physica Scripta*, 19(4):486–490, 1979.
- [113] P. Kapusta. Absolute Diffusion Coefficients: Compilation of Reference Data for FCS Calibration: Application Note: Rev.1. Rev.1, 2010.
- [114] J. Widengren, Ü. Mets, and R. Rigler. Photodynamic properties of green fluorescent proteins investigated by fluorescence correlation spectroscopy. *Chemical Physics*, 250(2):171–186, 1999.
- [115] T. J. Collins. ImageJ for microscopy. *Biotechniques*, 43(1 Suppl.):25–30, 2007.
- [116] M. A. Rapsomaniki, P. Kotsantis, I.-E. Symeonidou, N.-N. Giakoumakis, S. Taraviras, and Z. Lygerou. easyFRAP: an interactive, easy-to-use tool for qualitative and quantitative analysis of FRAP data. *Bioinformatics (Oxford, England)*, 28(13):1800–1801, 2012.
- [117] R. Swaminathan, C. P. Hoang, and A. S. Verkman. Photobleaching recovery and anisotropy decay of green fluorescent protein GFP-S65T in solution and cells: cytoplasmic viscosity probed by green fluorescent protein translational and rotational diffusion. *Biophysical Journal*, 72(4):1900–1907, 1997.
- [118] M. A. Hink, R. A. Griep, J. W. Borst, A. van Hoek, M. H. Eppink, A. Schots, and A. J. Visser. Structural dynamics of green fluorescent protein alone and fused with a single chain Fv protein. *The Journal of biological chemistry*, 275(23):17556–17560, 2000.

- [119] Glycerine Producers' Association and others. *Physical properties of glycerine and its solutions*. Glycerine Producers' Association, 1963.
- [120] D. A. Zacharias, J. D. Violin, A. C. Newton, and R. Y. Tsien. Partitioning of lipid-modified monomeric GFPs into membrane microdomains of live cells. *Science (New York, N.Y.)*, 296(5569):913–916, 2002.
- [121] M. S. Paller. Lateral mobility of Na,K-ATPase and membrane lipids in renal cells. Importance of cytoskeletal integrity. *The Journal of Membrane Biology*, 142(1):127–135, 1994.
- [122] P. G. Saffman and M. Delbrück. Brownian motion in biological membranes. *Proceedings of the National Academy of Sciences*, 72(8):3111–3113, 1975.
- [123] K. Weiß, A. Neef, Q. Van, S. Kramer, I. Gregor, and J. R. Emanuel. Quantifying the diffusion of membrane proteins and peptides in black lipid membranes with 2-focus fluorescence correlation spectroscopy. *Biophysical Journal*, 105(2):455–462, 2013.
- [124] S. Ramadurai, A. Holt, V. Krasnikov, van den Bogaart, G., J. A. Killian, and B. Poolman. Lateral diffusion of membrane proteins. *Journal of the American Chemical Society*, 131(35):12650–12656, 2009.
- [125] Y. Gambin, R. Lopez-Esparza, M. Reffay, E. Sieracki, N. S. Gov, M. Genest, R. S. Hodges, and W. Urbach. Lateral mobility of proteins in liquid membranes revisited. *Proceedings of the National Academy of Sciences of the United States of America*, 103(7):2098–2102, 2006.
- [126] A. Naji, A. J. Levine, and P. A. Pincus. Corrections to the Saffman-Delbruck mobility for membrane bound proteins. *Biophysical Journal*, 93(11):L49–51, 2007.
- [127] P. Cicuta, S. L. Keller, and S. L. Veatch. Diffusion of liquid domains in lipid bilayer membranes. *The journal of physical chemistry. B*, 111(13):3328–3331, 2007.
- [128] W. L.C. Vaz, F. Goodsaid-Zalduondo, and K. Jacobson. Lateral diffusion of lipids and proteins in bilayer membranes. *FEBS Letters*, 174(2):199–207, 1984.
- [129] T. Friedrich, E. Bamberg, and G. Nagel. Na<sup>+</sup>,K<sup>+</sup>-ATPase pump currents in giant excised patches activated by an ATP concentration jump. *Biophysical Journal*, 71(5):2486–2500, 1996.

- 
- [130] J. Kockskämper, G. Gisselmann, and H. G. Glitsch. Comparison of ouabain-sensitive and -insensitive Na/K pumps in HEK293 cells. *Biochimica et Biophysica Acta (BBA) - Biomembranes*, 1325(2):197–208, 1997.
- [131] J. Lippincott-Schwartz, E. Snapp, and A. Kenworthy. Studying protein dynamics in living cells. *Nature Reviews Molecular Cell Biology*, 2:444–456, 2001.
- [132] S. J. Singer and G. L. Nicolson. The Fluid Mosaic Model of the Structure of Cell Membranes. *Science*, 175:720–731, 1972.
- [133] S. Chiantia, J. Ries, and P. Schwille. Fluorescence correlation spectroscopy in membrane structure elucidation. *Biochimica et Biophysica Acta*, 1788(1):225–233, 2009.
- [134] G. Vereb, J. Szöllosi, J. Matkó, P. Nagy, T. Farkas, L. Vigh, L. Mátyus, T. A. Waldmann, and S. Damjanovich. Dynamic, yet structured: The cell membrane three decades after the Singer-Nicolson model. *Proceedings of the National Academy of Sciences of the United States of America*, 100(14):8053–8058, 2003.
- [135] P.-F. Lenne, L. Wawrezynieck, F. Conchonaud, O. Wurtz, A. Boned, X.-J. Guo, H. Rigneault, H.-T. He, and D. Marguet. Dynamic molecular confinement in the plasma membrane by microdomains and the cytoskeleton meshwork. *The EMBO journal*, 25(14):3245–3256, 2006.
- [136] A. Kusumi, H. Ike, C. Nakada, K. Murase, and T. Fujiwara. Single-molecule tracking of membrane molecules: plasma membrane compartmentalization and dynamic assembly of raft-philic signaling molecules. *Seminars in immunology*, 17(1):3–21, 2005.
- [137] A. Kusumi, Y. M. Shirai, I. Koyama-Honda, K. G. N. Suzuki, and T. K. Fujiwara. Hierarchical organization of the plasma membrane: investigations by single-molecule tracking vs. fluorescence correlation spectroscopy. *FEBS Letters*, 584(9):1814–1823, 2010.
- [138] P. Schwille, J. Korlach, and W. W. Webb. Fluorescence correlation spectroscopy with single-molecule sensitivity on cell and model membranes. *Cytometry*, 36(3):176–182, 1999.
- [139] E. L. Elson. Fluorescence Correlation Spectroscopy Measures Molecular Transport in Cells. *Traffic*, 2(11):789–796, 2001.
- [140] T. J. Feder, I. Brust-Mascher, J. P. Slattery, B. Baird, and W. W. Webb. Constrained diffusion or immobile fraction on cell surfaces: A new interpretation. *Biophysical Journal*, 70(6):2767–2773, 1996.

- [141] P. Schwille, U. Haupts, S. Maiti, and W. W. Webb. Molecular Dynamics in Living Cells Observed by Fluorescence Correlation Spectroscopy with One- and Two-Photon Excitation. *Biophysical Journal*, 77(4):2251–2265, 1999.
- [142] L. Wawrezinieck, H. Rigneault, D. Marguet, and P.-F. Lenne. Fluorescence correlation spectroscopy diffusion laws to probe the submicron cell membrane organization. *Biophysical Journal*, 89(6):4029–4042, 2005.
- [143] Y. Ohsugi, K. Saito, M. Tamura, and M. Kinjo. Lateral mobility of membrane-binding proteins in living cells measured by total internal reflection fluorescence correlation spectroscopy. *Biophysical Journal*, 91(9):3456–3464, 2006.
- [144] M. Kumar, M. S. Mommer, and V. Sourjik. Mobility of cytoplasmic, membrane, and DNA-binding proteins in *Escherichia coli*. *Biophysical journal*, 98(4):552–559, 2010.
- [145] R. Calizo and S. Scarlata. Discrepancy between fluorescence correlation spectroscopy and fluorescence recovery after photobleaching diffusion measurements of G-protein-coupled receptors. *Analytical Biochemistry*, 440:40–48, 2013.
- [146] E. M. Adkins, D. J. Samuvel, J. U. Fog, J. Eriksen, L. D. Jayanthi, C. Bjerregaard Vaegter, S. Ramamoorthy, and U. Gether. Membrane mobility and microdomain association of the dopamine transporter studied with fluorescence correlation spectroscopy and fluorescence recovery after photobleaching. *Biochemistry*, 46(37):10484–10497, 2007.
- [147] J. W. Dobrucki, D. Feret, and A. Noatynska. Scattering of Exciting Light by Live Cells in Fluorescence Confocal Imaging: Phototoxic Effects and Relevance for FRAP Studies. *Biophysical Journal*, 93(5):1778–1786, 2007.
- [148] B. L. Sprague, R. L. Pego, D. A. Stavreva, and J. G. McNally. Analysis of Binding Reactions by Fluorescence Recovery after Photobleaching. *Biophysical Journal*, 86:3473–3495, 2004.
- [149] M. Weiss. Challenges and artifacts in quantitative photobleaching experiments. *Traffic (Copenhagen, Denmark)*, 5(9):662–671, 2004.
- [150] J. N. Molk, S. C. Schuyler, J. Y. Liu, J. G. Evans, E. D. Salmon, D. Pellman, and K. Bloom. The differential roles of budding yeast Tem1p, Cdc15p, and Bub2p protein dynamics in mitotic exit. *Molecular biology of the cell*, 15(4):1519–1532, 2004.

- [151] H. Kimura and P. R. Cook. Kinetics of Core Histones in Living Human Cells: Little Exchange of H3 and H4 and Some Rapid Exchange of H2b. *The Journal of Cell Biology*, 153(7):1341–1354, 2001.
- [152] Table - sucrose solutions, composition, viscosity, density: <http://lclane.net/text/sucrose.html>, 14.04.2013.



# Acknowledgments

Creating a PhD thesis is not an individual experience it rather takes places in a social context and includes a lot of persons that attended me on the way and whom I would like to thank.

Firstly, I would like to express my sincere gratitude to my supervisor Prof. Dr. T. Friedrich for the continuous support of my PhD study and related research studies, for his patience and motivation. His guidance helped me in all the time. Secondly, I would like to thank Prof. Dr. J. Koenderink for the support of the present work.

I would especially like to thank Marco, for his guidance, which helped me in all the time. Without his help this work would not be the same and he made that jonathan can fly higher and faster. In addition, I want to thank present and past members of the Bioenergetic group. Especially, Kirstin and Susan my friends, which never give up to help me in understanding biology, molecular biology and cell treatment. Also Mario has to be named here for being such a good colleague and always sharing lab time and lab cleaning with me. Furthermore, I acknowledge my friends from my former physics group and the members of Sicoya (Alex, Aws, Basti, Chris, Christoph, Danilo, David, Dawid, Hanjo, Haro, Jan, Julia, Milan, Moritz, Oli, Stefan, Tara, Torsten and everyone I forgot to mention here) for all the help and discussions about science and meaning of life. As well as for the many interesting and fancy activities in spare time.

My sincere thanks also goes to Dr. Vladana Vukojević and her group at the Karolinska Institute in Stockholm, who provided me an opportunity to join their team as intern, and who gave access to the laboratory and research facilities. Without their precious support it would not be possible to conduct this research. I also acknowledge here Werner Zuschratter and Oliver Kobler from IFN Magdeburg for the opportunity to use the microscopy systems for FRAP measurements and the technical support.

Last but not the least, I would like to thank my parents and my friends for supporting me spiritually throughout writing this thesis and my life in general.

Another special thanks goes to my personal monster Dreiklang, which brought me over the PhD time by his behavior again and again to new challenges and made sure that never boredom aroses.

